

Redox electrolytes for non-flow electrochemical energy storage

Dissertation

zur Erlangung des Grades

des Doktors der Naturwissenschaften

der Naturwissenschaftlich-Technischen Fakultät

der Universität des Saarlandes

von

Juhan Lee

Saarbrücken

2018

Tag des Kolloquiums: 04.10.2018

Dekan: Prof. Dr. G. Kickelbick

Berichterstatter: Prof. Dr. V. Presser
Prof. Dr. -Ing. F. Mücklich
Prof. Dr. T.A. Hatton

Vorsitzender: Prof. Dr. T. Kraus

Akad. Mitarbeiter: Dr.-Ing. F. Aubertin

Table of Contents

Acknowledgements	1
Zusammenfassung	3
Abstract	4
List of symbols and abbreviations	5
1. Introduction	8
1.1. Distinctions between batteries, capacitors, and hybrids.....	17
1.2. Type of redox electrolytes.....	21
1.3. Design considerations for REHES systems.....	23
1.3.1. Selection of redox couples.....	23
1.3.2. Prevention of redox shuttling.....	27
1.4. Critical characterization for redox electrolyte systems.....	29
1.4.1. Energy and power performance.....	29
1.4.2. Determination of system stability.....	33
1.4.3. Time-dependent potential decay.....	39
1.5. Diffusion, adsorption, and kinetics for REHES.....	42
1.5.1. Self-discharge and time-dependent potential decay.....	42
1.5.2. Redox kinetics and mass transport for redox electrolyte systems.....	50
2. Approach and overview	54
3. Results and discussions	58
3.1. Use of Surfactants for Continuous Operation of Aqueous Electrochemical Flow Capacitors.....	59
3.2. High Performance Hybrid Energy Storage with Potassium Ferricyanide Redox Electrolyte.....	77
3.3. Sub-micrometer Novolac-Derived Carbon Beads for High Performance Supercapacitors and Redox Electrolyte Energy Storage.....	97
3.4. Tin/vanadium redox electrolyte for battery-like energy storage capacity combined with supercapacitor-like power handling.....	122
3.5. Asymmetric tin–vanadium redox electrolyte for hybrid energy storage with nanoporous carbon electrodes.....	141
3.6. Porous carbon as a quasi-reference electrode in aqueous electrolytes.....	159
3.7. Nanoconfinement of redox reactions enables rapid zinc iodide energy storage with high efficiency.....	166
4. Conclusions and outlook	191
References	195
Curriculum vitae	202

Acknowledgements

This PhD thesis work was carried out from November 2014 to December 2017 at the INM - Leibniz Institute for New Materials, Saarbrücken, in the Energy Materials Group. The work was funded by the German Federal Ministry for Research and Education (BMBF) in support of the nanoEES^{3D} project (award number 03EK3013) as part of the strategic funding initiative energy storage framework; I sincerely thank those financial supports.

I am very grateful to acknowledge my supervisor Prof. Volker Presser, head of the Energy Materials Group, and I also thank Prof. Frank Mücklich for being my scientific co-advisor, his optimism during the study, and his kind and warm support.

I also owe a great debt of gratitude to my colleagues to complete my thesis in a pleasant atmosphere. I would thank Anna Schreiber, our laboratory chef, for her help for searching for chemicals, designing devices, and for maintaining the laboratory with reliable and safe environments. To Dr. Mesut Aslan, I owe my deepest gratitude for his warm and continuous advice and discussions about the analytical and synthesis approaches. My special thanks are due to Pattarachai Srimuk for his enthusiastic support, advice, and discussion regarding the electrochemistry from fundamentals to sharing new ideas. Sylvain Badie, Daekyu Kim, and Alexander Ridder deserve my sincere gratitude for their active research activities which significantly supported my PhD work. I thank Mathias Widmaier, Dr. Sathyamoorthi Sethuraman, Dr. Daniel Weingarth, and Dr. Soumyadip Choudhury for the fruitful discussions about the electrochemistry and my Ph.D. work despite the short period to stay together. I also thank Simon Fleischmann, Aura Tolosa, Benjamin Krüner, Nicolas Jäckel, Dr. Ingrid Grobelsek, and Andrea Jung for useful discussions and technical advice. I also appreciate the collaborators at KOREATECH, Dr. Kum-Hee Seo, Prof. Yoon-Chae Nah, and Prof. Haiwoon Park. I want to acknowledge Dr. Marco Zeiger for his contribution to maintaining the laboratory facilities as well his support for particle size measurements, pycnometer analyses, and transmission electron micrographs. Finally, I want to acknowledge that my PhD work was only possible with the support from our workshop; especially, I thank Stefan Altpeter for manufacturing the electrochemical measurement cell, Herbert Beermann, and Uwe Magar for the cell design.

Most of all, I wish to thank my father, mother, sister, and Anne-Kathrin for their unconditional love, support, and understanding during my work.

Zusammenfassung

Die Forschung der letzten Jahrzehnte hat eine neue Art der elektrochemischen Energiespeicherung hervorgebracht, bei der elektrische Ladung nicht nur an der Grenzfläche zwischen der Elektrode und dem Elektrolyten gespeichert wird, sondern auch im Elektrolyten selbst durch dessen Redoxaktivität. Diese Redox-Elektrolyte sind für hybride Energiespeichersysteme ohne extern-mechanische Bewegung des Elektrolyten (REHES) vielversprechend, insbesondere, wenn hochporöse Kohlenstoffmaterialien als Elektroden verwendet werden. In dieser Doktorarbeit wurden verschiedene REHES-Systeme hinsichtlich der Diffusion, der elektrochemischen Kinetik und der Adsorption von Redox-Ionen untersucht, um grundlegende Effekte und Prozesse aufzuklären. Die Kombination grundlegender Elektrochemie und Materialcharakterisierung ermöglichte es, die Leistungsparameter von REHES im Vergleich zum Stand der Technik deutlich zu verbessern. Die Energiespeicherkapazität des herkömmlichen wässrigen elektrischen Doppelschichtkondensators ohne Redoxelektrolyt von 4 Wh/kg (entspricht 80 F/g) wurde zum Beispiel im ZnI_2 System auf bis zu 226 Wh/kg gesteigert, während die spezifische Leistung von 1.3 kW/kg auf 20 kW/kg verbessert werden konnte. Als Ergebnis zeigt sich, dass REHES ein besonders vielversprechender Ansatz zur Darstellung hochleistungsfähiger elektrochemischer Energiespeicher ist. Weitere Vorteile von REHES sind ein vereinfachtes Zellkonzept und die Verwendung von potentiell kostengünstige Einzelkomponenten.

Abstract

In recent decades, a new type of electric energy storage system has emerged with the principle that the electric charge can be stored not only at the interface between the electrode and the electrolyte, but also in the electrolyte by the redox activities of the bulk electrolyte itself. Such redox electrolytes are promising for non-flow energy storage (redox electrolyte aided hybrid energy storage systems, REHES) particularly when they are combined with electrodes made of nanoporous carbon. In this PhD work, I have established a fundamental understanding regarding ion diffusion, process kinetics, and adsorption of redox ions. For that, different REHES systems have been investigated including tetrapropylammonium iodide, zinc iodide, potassium iodide, potassium ferricyanide, vanadyl sulfate, tin sulfate, and tin fluoride. The basic understanding of REHES systems enabled the targeted improvement of the device performance throughout this PhD work. Compared to the energy storage capacity of a conventional (non-redox) electrical double layer capacitor of 4 Wh/kg (ca. 80 F/g), the use of the ZnI_2 redox electrolyte yielded significantly higher performance of up to 226 Wh/kg. Furthermore, the specific power was also enhanced from 1.3 kW/kg to 20 kW/kg. As a key conclusion, this PhD work demonstrates the high attractiveness of REHES systems not only from a performance point of view, but also regarding low cost and simplicity of the system.

List of symbols and abbreviations

Symbols

A	Area of the planar electrode in cm^2
a_{Ox}	Activity of oxidized species in the electrolyte
a_{Re}	Activity of reduced species in the electrolyte
C	Capacitance in F
C_d	Device specific capacitance in F/g
C_ϕ	Potential-dependent capacitance in F
c	Concentration in mol/cm^3
c_0	Initial molar concentration of the impurity redox reaction in mol/cm^3
c_R	Molar concentration of the redox species mol/cm^3
D	Diffusion coefficient in cm^2/s
E_{char}	Energy invested during charging
E_{dis}	Energy restored during discharging
E_s	Specific energy in Wh/kg
F	Faraday constant (96,485.33 C/mol)
I	Discharging current
i_0	Exchange current density in A/cm^2
i_{Diff}	Diffusion-limited redox current in cyclic voltammogram
i_{EDL}	Current from the double-layer formation in cyclic voltammogram
i_p	Redox peak current
i_s	Leakage current
i_{TLE}	Redox current under thin-layer condition in cyclic voltammetry
l	Distance from the electrode surface in cm
m_a	Mass of the active electrodes in the device
n	Electron transfer number
n_0	Number of electrons transferred before the rate handling step
P_s	Specific power in kW/kg
Q	Accumulated electric charge during the cell operation
Q_a	Charge accumulated due to the anodic current
Q_c	Charge accumulated due to the cathodic current
q_1	Charge for the formation or desorption of a monolayer of the intermediate
R	Universal gas constant (8.31 J/K·mol)
R_s	Short-circuiting resistance element in Ohm
S_a	S-value for the anodic limit

S_c	S-value for the cathodic limit
T	Temperature in Kelvin
t_{dis}	Discharging time
t_0	Integration constant
U_t	Volume of the thin layer in cm ³
V_a	Applied potential
V_c	Cell voltage
V_i	Initial potential
V_t	Time-dependent OCP
v	Scan rate in V/s
x	Charge state of the redox species
$[Ox]$	Concentration of the oxidized species at the electrode surface
$[Re]$	Concentration of the reduced species at the electrode surface
α	Transfer coefficient
Γ	Fractional surface coverage
$\Delta\varphi_p$	Peak-to-peak separation determined by cyclic voltammetry
ε_E	Energy efficiency
η	Overpotential
θ	Areal fractional coverage
φ_0	Standard electrode potential
φ_e	Potential of the half-cell
φ_f	Formal potential
φ_{V0}	Electrode potential at cell voltage of zero
φ_+	Potentials of the positive electrode
φ_-	Potentials of the negative electrode

Abbreviations

AC	Activated carbon
BQ	Benzoquinone
CEM	Cation exchange membrane
CV	Cyclic voltammogram
EDL	Electrical double-layer
EDLC	Electrical double-layer capacitor
EES	Electric energy storage
EIS	Electrochemical impedance spectroscopy
GCPL	Galvanostatic cycling with potential limitation
GITT	Galvanostatic intermittent titration technique
HER	Hydrogen evolution reaction
HQ	Hydroquinone
HVBr ₂	1,1'-Diheptyl-4,4'-bipyridinium dibromide
IHP	Inner Helmholtz layer
LTO	Lithium titanate
MC	Microporous carbon (i.e., pores <2 nm)
MVCl ₂	Methyl viologen dichloride
OCP	Open-circuit potential
OER	Oxygen evolution reaction
PFC	Potassium ferricyanide
Q	Quinone
REHES	Redox electrolyte aided hybrid energy storage
TLE	Thin-layer electrochemistry

1. Introduction

Electrochemical energy storage (EES) devices are increasingly becoming important in our daily life. They are applied to small devices such as laptops, tablets, and cell phones to bigger devices like electric cars to provide efficient and reliable use of energy.[1] Furthermore, EES systems are promising for large-scale energy storage to stabilize the power supply of future grids which heavily rely on energy produced from renewable sources, such as solar and wind energy.[2-4] Batteries are one of the most popular EES types which are broadly applied in our world. By redox reactions at the positive and negative electrodes, either by conversion-type or insertion/intercalation type reactions, batteries provide a stable operating potential with high specific charge storage capacity.[5] State-of-the-art intercalation-type lithium-ion batteries, for instance, offer a nominal cell voltage of 3.6 V with a specific charge capacity of 100-300 mAh/g.[4, 6, 7] The main disadvantage of batteries are the long charging time due to its intrinsically low power handling capability (<1 kW/kg, normalized by the device mass) and the short cycle life.[8-10] Intensive research activities have increased the specific power of modern batteries; however, the cost of those advanced batteries are high, and they still do not fulfill the power demands in many applications (especially regarding electric vehicles). For high power energy storage applications, supercapacitors are more appropriate with values typically >10 kW/kg, normalized by the device mass.[11] In general, they provide high cyclic stability ($>10,000$ cycles) whereas the low energy storage capacity (<10 Wh/kg, normalized by the device mass) is a severe limitation.[11] According to the charge storage mechanism and device configuration, supercapacitors are further classified as electrical double-layer capacitors (EDLC) or pseudocapacitors and hybrids thereof.

The different performance of EES systems originates from different charge storage mechanisms. In principle, four different mechanisms can be identified, as schematically shown in **Fig. 1A** (after Ref. [12]): i) electrical double-layer formation (EDL), ii) bulk redox reaction of the electrode, iii) redox reaction at the near electrode surface, and iv) the redox activity of the bulk electrolyte. EDL formation is the dominant principle for the electrical double-layer capacitor (EDLC, **Fig. 2A**), which is the most common type of supercapacitor. When the electrode is charged, oppositely charged ions are adsorbed on the electrode surface to balance the charge while the ions are released during discharging (**Fig. 1A**, type-i mechanism). This fast electrostatic sorption process of dissolved ions allows high

power handling performance of EDLCs since it occurs without chemical reactions or solid-state diffusion. Accordingly, EDL formation is a non-Faradaic process which does not involve an electron transfer process from the electrode to the electrolyte (or in reverse) during energy storage and recovery. Since the ion sorption process does (ideally) not involve significant structural changes of the electrode materials, high cyclic stability can be achieved. By contrast, batteries (**Fig. 2C**) employ Faradaic reactions of the bulk electrode material which can be conversion or insertion/intercalation type (**Fig. 1A**, type-ii mechanism). For instance, lithium-ion batteries store energy by the insertion or intercalation of lithium ions into the bulk electrode material. Because of the structural damage to the bulk electrode material through the insertion/intercalation process, the cyclic stability of the EES device based on the bulk redox reaction of the electrode material is limited.

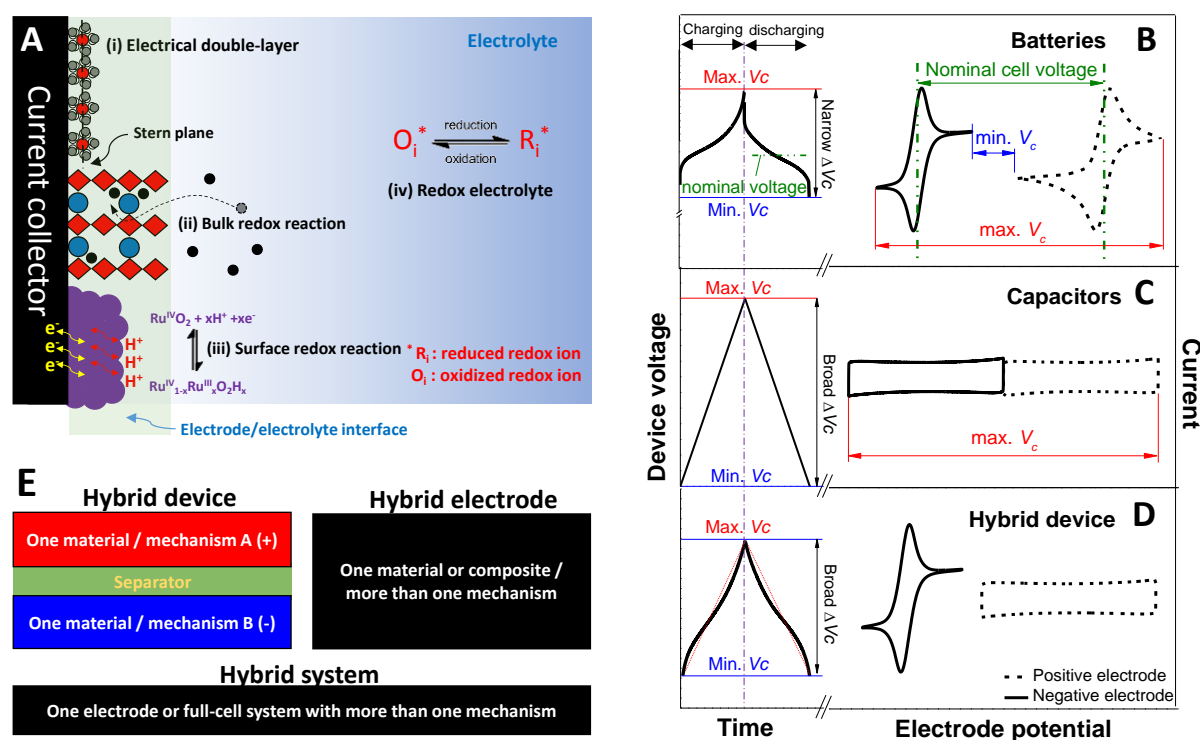


Figure 1 Charge storage mechanisms for electric energy storage (EES) devices and the types of EES devices with their characteristic electrochemical behavior. (A) Schematic descriptions of the four major mechanisms: the electrical double-layer formation, the bulk redox reaction, the surface near redox reaction, and the redox activity of the electrolyte. Adapted from Ref. [12] - Published by The Royal Society of Chemistry. (B-D) Cyclic voltammograms of various materials and galvanostatic charging/discharging curves of various devices. (E) The definitions for the hybrid device, hybrid electrode, and hybrid system.

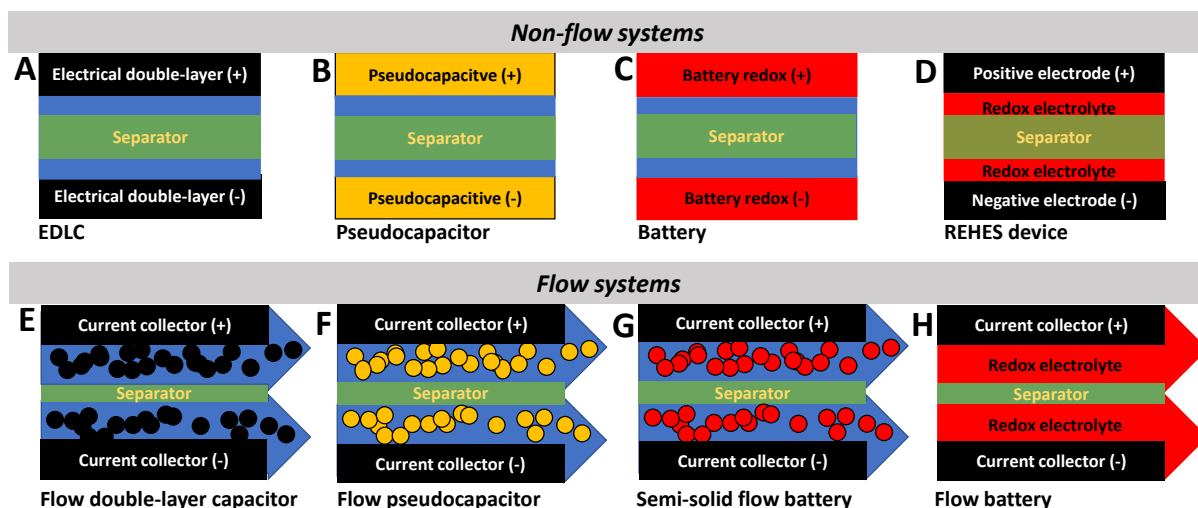


Figure 2: Device configurations of various electric energy storage (EES) systems under flow and non-flow condition: (A) electrical double-layer capacitor (EDLC), (B) pseudocapacitor, (C) battery, (D) redox electrolyte aided hybrid energy storage (REHES) device, (E) flow double-layer capacitor, (F) flow pseudocapacitor, (G) semi-solid flow battery, and (H) flow battery.

When a Faradaic reaction occurs only near the electrode surface (**Fig. 1A**, type-iii mechanism), the reaction is less diffusion-controlled but more surface-controlled which leads to fast redox kinetics.[13] The type of those reactions can be i) underpotential deposition and ii) Faradaically adsorbed ions near the surface of the material. In case of underpotential deposition, a metal is deposited on the other metal, but this process requires less energy (underpotential) than the redox potential of the metal for deposition; an example is the underpotential deposition of lead on gold.[14] In case of hydrous RuO_2 in aqueous solution, a proton can be Faradaically adsorbed near the surface of the electrode.[15] Despite its Faradaic reaction origin, the hydrous RuO_2 material exhibits a capacitor-like behavior.[16] For this reason, this type of electrode materials is classified as *intrinsic* pseudocapacitive materials.[13, 17] The capacitor-like features can also be observed from the electrode with bulk redox reaction when the size of the reaction layer in the electrode reduces into nanometer range. Those materials can be classified as *extrinsic* pseudocapacitive materials.[17, 18] When pseudocapacitive materials are used to build a device, the device is classified as pseudocapacitor (**Fig. 2B**).

Unlike the three charge storage mechanisms described above, the charge storage capacity of the bulk redox electrolyte system is not limited by the electrode/electrolyte interface (**Fig. 1A**, type-iv mechanism). After the electron transfer occurred from the electrode to the redox active ions dissolved in the electrolyte, the ions diffuse away from the fluid/solid interface and back to the bulk electrolyte volume. Thereby, the oxidation state of the electrolyte changes. Redox flow batteries (**Fig. 2H**) rely on this charge storage

mechanism. Their main advantage is that the redox electrolyte can be separately stored in a scalable reservoir after charging in the cell with the aid of pumping device.[19-21] Thereby, a facile scalability is enabled by adjusting the number of cell stack and the size of the electrolyte reservoir because of their close relations to the power and the energy storage capacity of the system, respectively.[19] Furthermore, for electric vehicle applications, the charged electrolyte can be quickly replaced instead of charging for a long time at the recharging station. The main drawback of redox flow batteries is the lower specific energy as compared to modern batteries and the lower specific power as compared to supercapacitors.[22] Thereby, no practical application to the electric vehicle is available in the market considering the limited space for the energy storage device. Nonetheless, redox flow battery technologies have been employed by large-scale energy storage for grid-level applications since volume and size of the individual devices are less of a concern.[23]

The different electrochemical performances originate from different charge storage mechanisms. Accordingly, EES devices can be classified into capacitors, batteries, and their hybrids.[24] For instance, a battery device (**Fig. 1B**) provides stable operating cell voltage (reported regarding nominal cell voltage) due to the strong bulk redox activities at the positive and negative electrodes. The redox activities of battery materials can be seen in cyclic voltammograms (CV) as characterized by reduction and oxidation peaks (**Fig. 1B, right**). During charging of a battery device, the negative electrode is being reduced while the positive electrode is being oxidized. The potential difference between both electrodes corresponds to the device potential, or cell voltage (**Fig. 1B, left**). In case of an ideal capacitor (**Fig. 1C**), the device exhibits a linear relationship between the cell voltage and the accumulated charge which also corresponds to potential independent constant current response in CVs. Therefore, for capacitors and capacitor-like devices, it is reasonable to report the charge storage capacity as capacitance (F) which is, by definition, the slope in the voltage and the accumulated charge profile.[8, 11] Along with capacitance value, a relatively broad cell voltage window ($\Delta V > 0.8$ V) is provided for a capacitor device in comparison to the narrow operating cell voltage of battery device.[25]

For the continuing development of EES systems, key target parameters are: i) high specific energy, ii) high specific power, iii) long cycle life, iv) low cost, and v) environmental friendliness. For that, the most recent research activities have focused on the developments of nano-engineered materials for batteries and supercapacitors.[1, 4, 26, 27]

As an alternative solution, hybrid devices have also emerged to provide desired specific power and energy by combining two different negative and positive electrode materials with different charge storage mechanisms (**Fig. 1E**). For instance, a lithium-ion capacitor combines a porous carbon positive electrode and a negative electrode with battery-type redox reaction (i.e., insertion, intercalation, or conversion reaction).[28] In general, the cell voltage of lithium-ion capacitors is mostly controlled by the capacitive potential change at the positive electrode, while the negative battery electrode provides only a slight change in potential (**Fig. 1D**). Thereby, the galvanostatic (constant current) potential profile exhibits a linear-like feature. Because of this nearly linear correlation between voltage and charge, the system can be called capacitor-like.

Hybridization can also be realized on the electrode level instead of the device level. A hybrid electrode (**Fig. 1E**) may consist of one homogeneous material or inhomogeneous mixture material (composite) which capitalizes on more than one charge storage mechanism. For instance, a composite of porous carbon and battery material like lithium titanium oxide (LTO) yields, in regards to performance, a hybrid electrode which shows the characteristics of both batteries and capacitors.[29, 30] In contrast, a composite of LTO and the conductive additive is not considered as a hybrid electrode since it relies mostly on just one charge storage mechanism (lithium intercalation).

In general, the term hybrid device has been used regarding device hybridization whereas the term hybrid electrode arises from the perspective on hybridization of mechanisms at one electrode. For a clear distinction, in this dissertation, hybrid *device* is defined as a device consisting of one electrode material with one charge storage mechanism and the other electrode material with different charge storage mechanism (**Fig. 1E**). Further, a hybrid *system* is defined as a system consisting of one electrode or full-cell system (device) containing more than one charge storage mechanism. Hence, the term *hybrid system* can be applied to both a single hybrid electrode and a hybrid device. For instance, the LTO-microporous carbon (MC) hybrid electrode and the hybrid device consisting of LTO-MC hybrid electrode and graphite negative electrode can be both seen as hybrid systems. Unlike hybrid devices, a hybrid system with a hybrid electrode exhibits much complicating electrochemical behavior. While lithium-ion capacitors (hybrid device) show a capacitor-like behavior, graphite|LTO-MC hybrid systems exhibit both capacitor-like and battery-like regime in different potential ranges due to the hybridized feature of LTO-MC electrode.[29]

Various new types of hybrid systems have been introduced in the last decades, and several new types of EES systems have emerged using flowable electrodes/electrolytes for batteries and supercapacitors (**Fig. 2E-G**). On the one hand, semi-solid flow batteries and flow capacitors share with redox flow batteries that the active electrode materials are not confined to the cell but can be pumped through the cell. On the other hand, semi-solid flow batteries and flow capacitors differ from redox flow batteries by the physical state of the active material. For redox flow batteries, the active materials are liquid, while dispersed phases such as slurry or suspension are being used in semi-solid flow batteries and flow capacitors. According to the origin of the charge storage mechanisms, flow capacitors can be further classified into flow double-layer capacitors[31, 32] and flow pseudocapacitors[33]. Critical issues for slurry or suspension based flow EES systems are i) the high resistance of the cell by particle-particle contact resistance, ii) the membrane contamination by carbon particles, and iii) the reduction of pumping energy.[31, 34]

Among other hybrid systems, redox electrolyte aided hybrid energy storage (REHES) systems are particularly promising for next-generation EES technologies.[11, 24, 35-37] Most hybrid systems focus on mixing two different materials or coupling electrodes with different charge storage mechanisms at the electrode/electrolyte interface. REHES systems further extend the concept of hybridization by adding charge storage capacity beyond the electrode/electrolyte interface through the redox activity of the electrolyte.[35] For enabling the redox activities of the electrolyte, the only requirement is an electrically conductive electrode to accomplish the electron transfer between the electrode and electrolyte (**Fig. 2D**). Therefore, REHES can be adapted to other EES systems, for example, to battery systems or porous carbon electrodes (EDLC).

Once a redox electrolyte has been hybridized with another EES system, the total charge storage capacity is the synergistic sum of both charge storage mechanisms. For instance, when a redox electrolyte containing potassium ferricyanide (PFC) is combined with a symmetric (MC|MC) electrical double-layer capacitor (**Fig. 3A**), the system exhibits characteristics of both redox reaction of PFC (a current peak pair) and EDL formation (a rectangular shape current response).[38] The latter occurs by the reversible adsorption and desorption of cations (potassium) at the negative electrode and anions (ferrocyanide/ferricyanide) at the positive electrode during cell charging and discharging.

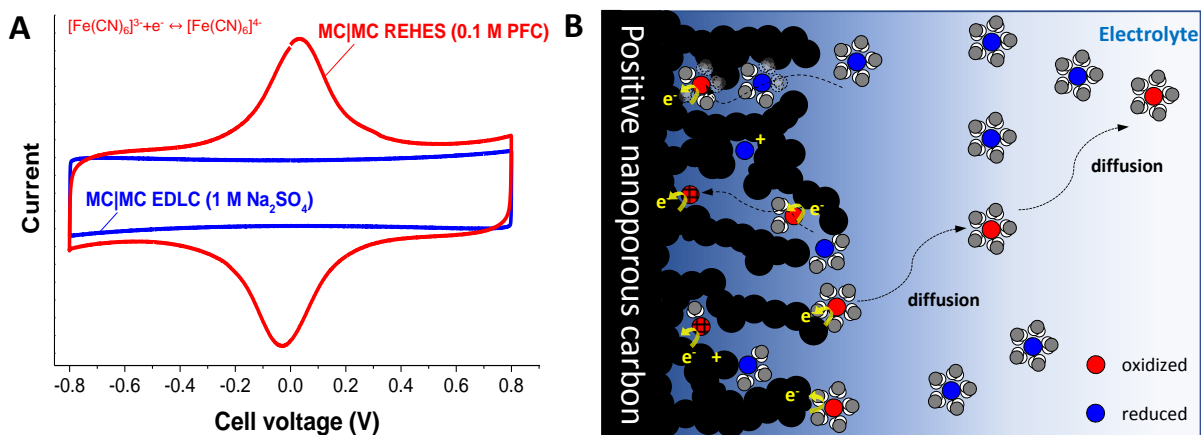


Figure 3: Working principles of the redox electrolyte aided hybrid energy storage systems. Adapted with permission from Ref. [38]. Copyright (2017) American Chemical Society. (A) Cyclic voltammograms of the symmetric microporous carbon electrodes (MC|MC) systems in potassium ferricyanide (PFC) and sodium sulfate aqueous solutions. (B) Schematic illustration of the working principles of the redox electrolyte aided hybrid energy storage system with a porous carbon electrode.

Fig. 3B schematically illustrates the adsorption process of ferrocyanide at the positive electrode during cell charging. When the redox potential is reached, the electrons are transferred from the electrolyte to the MC electrode, and ferrocyanide is oxidized to ferricyanide. Since the oxidized ferricyanide can diffuse to the bulk electrolyte, the charge storage capacity of the system has contributions not only of EDL formation at the electrode/electrolyte interface, but also of the bulk electrolyte beyond the interface. The latter is effectively enabled by the high pore volume of the MC electrode. By contrast, charge storage capacity of the conventional hybrid electrodes like LTO-MC electrode is limited by the electrode/electrolyte interface. For instance, when the battery-like feature is intensified by increasing the relative amount of LTO, the capacitor-like feature is weakened because of the reduced portion of MC of the hybrid electrode.

The use of MC electrodes for REHES systems is beneficial not only for providing the reservoir of the redox electrolyte, but also for effective charge transfer.[26, 38, 39] First, the high specific surface area of MC provides a high number of active sites for the electron transfer reactions at the electrode/electrolyte interface. Second, the redox reactions of the electrolyte occur in confined space of carbon micropores. Thereby, in contrast to conventional electrochemistry on flat electrodes, the REHES systems with MC exhibit diffusion-less electrochemical kinetics for the reaction of the redox electrolyte in carbon micropores.[40] This diffusion-less kinetic is essential for the fast reaction during cell charging and discharging. In virtue of the unique redox kinetics of the electrolyte in carbon micropores, REHES systems with MC electrodes do not only provide the enhanced specific energy (10-200 Wh/kg, normalized by the electrode mass), but also high specific

power (>1 kW/kg, normalized by the electrode mass).[12, 40-43] Furthermore, they could provide almost same cyclic stability as that of EDLCs when the applied redox electrolyte is electrochemically stable in the operating cell voltage window.[38, 41]

One of the essential features of the REHES systems is the charge storage capacity beyond the electrode/electrolyte interface by redox reactions of the bulk electrolyte. Therefore, the precise definition of REHES systems can be:

REHES is a non-flow hybrid system, where charge storage is accomplished both by the electrode material and the redox electrolyte. The oxidation state of the latter changes in the liquid phase through electron transfer between the electrode and electrolyte.

According to this definition, deposition-type transition metal redox couples should not be classified as a REHES system. For instance, the $\text{Zn(s)}/\text{Zn}^{2+}$ redox couple does not tremendously change the oxidation state of the zinc-containing redox electrolyte when applied at the negative electrode, but only a small change in formal potential by the change in concentration of dissolved zinc is observed. Therefore, the energy storage capacity is limited by the electrode/electrolyte interface, where the boundary of the interface changes during the reaction through the deposition/dissolution of zinc. For that reason, unlike other redox flow batteries, the capacity of zinc bromide flow batteries is limited by the cell volume at the negative electrode where deposited zinc can be confined.

Following the above definition, the first REHES system seems to be the zinc iodide battery from Yamamoto in 1981.[44] This work focused on polymer-iodine adducts as a positive electrode with the ZnI_2 electrolyte for primary batteries.[44-46] Additionally, the MgI_2 electrolyte was investigated for secondary batteries.[44] Later in 1984, Yamamoto et al. investigated the $\text{Zn}|\text{ZnI}_2|\text{polymer}$ system in more detail while focusing on the performance as a secondary battery.[47] The latter work avoided redox shuttling of iodides by use of a cation exchange membrane (CEM) in the cell. Thereby, the oxidation state of iodide in the electrolyte changes only at the positive electrode compartment during cell charging and discharging while the oxidation state of zinc in the electrolyte is always Zn^{2+} . Based on the change in the oxidation state of iodide in the electrolyte, the $\text{Zn}|\text{ZnI}_2|\text{polymer}$ system can be classified as a REHES system. Polyaniline electrodes for polymer-based REHES have been further investigated by Mengoli et al. by comparing zinc iodide and zinc bromide electrolytes.[48-50] The zinc halide systems were benchmarked for different positive electrode materials, such as conducting clay/porous carbon

composite with the approximate pore diameter of 1 μm ,[51] polyether,[52] 6-nylon,[52] polyacrylamide-carbon composite,[53] and ferrocene-deoxycholic acid based inclusion compounds[54]. The zinc halide REHES works from 1981 to 1993 focused on the use of polymer-based electrodes; yet, the latter has significant drawbacks due to the poor cycle life and high resistance as compared to carbon-based electrodes.[40, 55, 56]

The first REHES work published after 1993 was the 2007 study using highly porous carbon electrodes (specific surface area $>2500 \text{ m}^2/\text{g}$, Brunauer-Emmett-Teller theory) and employing a $\text{Fe}^{2+}/\text{Fe}^{3+}$ redox electrolyte combined with $\text{Cu(s)}/\text{Cu}^{2+}$ redox reactions.[57] The application of porous carbon re-energized the REHES research; follow-up works revisited the earlier halides systems[58, 59] and explored new systems, such as the hydroquinone/quinone (HQ/Q) redox couple,[60, 61] vanadium complexes,[12, 42, 43] and ferrocyanide/ferricyanide.[38, 62, 63] The choice of the electrolytes has also been broadened from aqueous to non-aqueous systems, including organic solutions and ionic liquids. In 2009, Tachibana et al. reported an organic REHES system (propylene carbonate and γ -butyrolactone) containing redox active $\text{N,N}'$ -diphenyl-phenylene-diamine.[64] In 2010, Sun et al. introduced a REHES system with copper-containing ionic liquid where the oxidation state of the copper in the ionic liquid changes from $\text{Cu}^+/\text{Cu}^{2+}$.[65]

The following sub-sections **Section 1.1** and **Section 1.2** will discuss the terminology and classifications of REHES systems. Afterwards, the critical design considerations will be given in **Section 1.3**. In **Section 1.4**, electrochemical characterization techniques will be discussed which are particularly useful for the REHES research. In **Section 1.5**, the theoretical backgrounds and the summary of the recent research activities will be given, particularly, with the perspectives on the electrochemical kinetics, diffusion, and adsorption of the redox ions. In **Chapter 2**, a brief overview will be given about the structure of the PhD work which contains seven peer-reviewed papers (details in **Chapter 3**). Finally, **Chapter 4** concludes with a summary and provides an outlook.

1.1. Distinctions between batteries, capacitors, and hybrids

Fundamentally, a cathode is defined as the electrode where a chemical reduction occurs, while at the anode, oxidation is encountered. Therefore, the fundamental definition of cathode and anode is according to the direction of electron flow in the system. For instance, electrolysis is a non-spontaneous reaction which requires an energy input or electric charging process. Once the cell is being charged, one positively polarized electrode is oxidized (anodic) while the one negatively polarized electrode is reduced (cathodic). Since this charging process is of importance for the products, the cathode and anode assignment is made during the charging process.

The research of batteries historically had started with the primary batteries, where the reaction is spontaneous while discharging the cell. For that reason, the cathode and the anode are defined based on the discharging process. Thereby, the cathodic reaction occurs at the positively polarized electrode, while the anodic reaction occurs at the negative polarized electrode. However, the direction of electrons during the discharging process is opposite to that of the non-spontaneous reaction of electrolysis. After the development of the secondary batteries, this nomenclature remained unchanged even though the cathode, in fact, becomes anode and anode becomes cathode during the charging process when applying the primary definition for the electrode assignment.

An issue arises in case of electrical double-layer capacitors where energy storage is accomplished by the reversible electrosorption of ions without chemical reduction or oxidation. Furthermore, the terminology of cathode and anode becomes problematic when describing energy storage systems during charging, because the terminology was initially based on discharging processes. Therefore, in this PhD thesis, it is preferred to use the terms “positive electrode” and “negative electrode” to describe the positively polarized electrode (the conventional cathode for a battery system) and negatively polarized electrode (the conventional anode for a battery system). For the description of the fundamental electrochemistry, the term anodic and cathodic will be still used to express the oxidation and reduction, respectively.

Capitalizing on Faradaic reactions of the electrolyte, REHES devices often exhibit battery-like features which can be distinctly seen from redox peaks during electrochemical voltage sweeping. Identifying battery-like or capacitor-like behavior is vital for clear

target applications and data comparison. In many cases, battery-like systems are treated as a capacitive device.[24, 66-68] However, clear differentiation between battery-like and capacitor-like behavior may be complicated due to the following reasons:

- i) System behavior depends on the applied potential window.
- ii) No clear criteria have been established for linearity of the capacitor-like system.

First, the electrochemical behavior of REHES systems depends on the applied cell voltage window. In case of the bromide and viologen-based redox electrolytes combined with highly porous activated carbon (AC) electrodes (**Fig. 4A**),[68] a clear capacitive regime can be seen at a low cell voltage range (0-1 V). By comparison, a strong potential plateau can be observed around 1.2 V. If the device operates only at 0-1 V, it will appear as a capacitor, while characterization in the range from 1.0-1.4 V will lead to an interpretation that the device is a battery. In that regard, clear application criteria should be mentioned according to the electrochemical features of REHES devices. For instance, the device (**Fig. 4A**) should be operated in the potential window from 0-1 V for capacitive application, while for the battery application 1.0-1.4 V. Otherwise, one could conclude that the device is for hybrid energy storage in the potential range from 0 to 1.4 V.

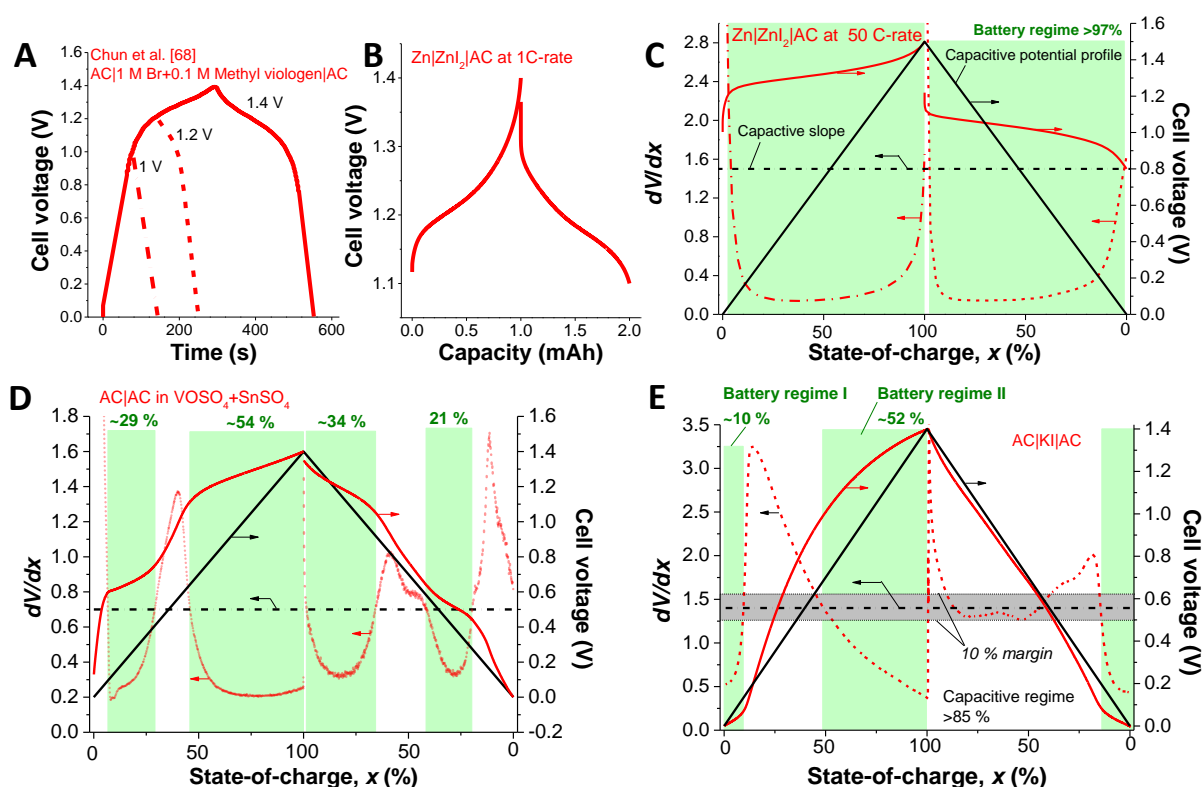


Figure 4 Galvanostatic profiles of AC|AC in KBr + methyl viologen dichloride (MVCl₂) system (A) and Zn|ZnI₂|AC system (B). Derivative analysis (dV/dx) for Zn|ZnI₂|AC system (C), AC|AC in VOSO₄+SnSO₄ system (D), and AC|KI|AC system (E).

The definition of capacitive behavior is the linear relation between the cell voltage and the accumulated charge (quantifiable by the unit of Farad = Coulomb/Volt). Often, the potential plateau from the battery material is interpreted as pseudocapacitive behavior because one could see a linear-like behavior from the potential plateau in a narrow window. For instance, when the ZnI₂ system with Zn negative electrode and AC positive electrode, or Zn|ZnI₂|AC (**Fig. 4B**) is operated in a narrow cell voltage window of 1.1-1.4 V, the potential plateau appears to be capacitor-like. The potential plateau is governed by the Nernst equation which is a non-linear function of the natural log of (1-x)/x, where x is the state-of-charge of the redox species at the electrode/electrolyte interface. In general, the potential variation in the plateau regime is around 100-200 mV for one battery electrode and 200-400 mV for the cell with two battery electrodes. Hence, for the precise characterization of the potential plateau regime, the cell voltage range for the test should be larger than 500 mV. Furthermore, the cell voltage window lower than 500 mV is not attractive for practical supercapacitor applications due to low specific energy. Therefore, the cell voltage window for the capacitor-like device should be investigated over 500 mV.

In several recent works, the differentiation between capacitor-like and battery-like behavior has been discussed.[24, 36, 37] However, no clear quantitative criteria have been established how one should distinguish capacitor-like behavior and battery-like behavior. For the identification of battery-like or capacitor-like behavior, an analysis can be carried out by considering the derivative of the cell voltage with respect to the state-of-charge. For the capacitive feature in the cell voltage window of 1.4 V, for instance, the derivative, or the slope of the potential and the state-of-charge, is 1.4 (**Fig. 4C**). In general, the slope of a capacitor with a maximum cell voltage of a V will be a . When a Faradaic reaction occurs, the derivative will be lower than 1.4 (**Fig. 4C**) due to the enhanced charge capacity in the system, while a slope higher than 1.4 will be most probably due to the capacitive contribution. When the derivative (dV/dx) is plotted versus the state-of-charge in a hybrid device, for instance, the Zn|ZnI₂|AC system,[40] two regimes can be distinguished from the intersection between the derivative curve and the line with a constant value of 1.4 (**Fig. 4C**). Matching with the potential plateau range in the cell voltage versus the state-of-charge plot, the regime with the derivative lower than 1.4 represents the range that is dominated by the battery-like Faradaic reaction. Applying this way of differentiation, we can quantify that the system behaves over 97 % battery-like in

the tested cell voltage window. Therefore, the Zn|ZnI₂|AC REHES system can be classified as a battery with a nominal cell voltage of ca. 1.2 V.

When a hybrid device contains more than two potential plateaus, the dV/dx analyses can be effectively applied. In case of AC|AC in VOSO₄+SnSO₄ REHES system (**Fig. 4D**),[12] the device can be classified as battery-like because it shows over 50% contribution of battery-like Faradaic reactions in the tested cell voltage window. In case of the AC|KI|AC REHES system (**Fig. 4E**),[41] higher linearity can be observed during discharging. Despite the Faradaic contribution in the potential range from 0.6 V to 1.0 V, the discharging profile appears linear with a slope close to 1.4. It is reasonable to assume a $\pm 10\%$ error range for the determination of linear-like behavior; thereby, the AC|KI|AC REHES system (**Fig. 4E**) can be classified as capacitor-like based on its discharging profile. With these criteria, many of the hybrid devices can be quantitatively classified as capacitor-like devices despite their battery-like Faradaic origin. In short, the criteria for the capacitor-like and battery-like behavior are suggested in this dissertation:

- i) For the capacitor-like system, the linear regime in the cell voltage window should be larger than 0.5 V.
- ii) Even if the slope is lower than the ideal capacitive slope, the regime can still be considered as linear when the value is within $\pm 10\%$ error range of the capacitive slope.
- iii) Battery-like Faradaic behavior occurs when the slope is lower than the capacitive slope (including a $\pm 10\%$ error range).

From these suggested criteria, an explicit assignment to capacitor or battery devices can be made. When a device has 90 % of capacitor-like contribution with a continuous linear-like slope and 10 % battery-like contribution, for instance, the device can be considered to be a capacitor. In that case, the operating potential should not cross the battery-like regime. Otherwise, the device should be labelled as a hybrid energy storage unit for the entire cell voltage window, including the capacitor-like and battery-like regimes. Similarly, when a device contains 90 % battery-like and 10 % capacitor-like regimes, the device can be considered as a battery while the nominal cell voltage should be given. This is exactly how commercial batteries work when the cell voltage of a phone is close to the capacitive regime, the “empty” sign will be indicated on display. The rapid potential change below or above the operating potential is not appropriate for battery applications.

1.2. Types of redox electrolytes

Three different types of redox electrolytes can be identified according to the use of solvent: i) aqueous redox electrolytes, ii) organic redox electrolytes, and iii) ionic liquid redox electrolytes. In earlier works, Senthilkumar et al. classified the redox electrolyte systems into i) redox active liquid electrolytes, ii) redox additive liquid electrolytes, and iii) redox-polymer electrolytes.[36] Accordingly, the redox additive liquid electrolytes were defined as the electrolytes in which redox additives or compounds are added. However, the definition of redox additive liquid electrolytes is rather ambiguous. For instance, potassium ferricyanide with KOH aqueous solution[69] would be a redox additive liquid electrolyte, whereas potassium ferricyanide aqueous solution[38, 63] would be a redox active liquid electrolyte. In fact, potassium ferricyanide can be used without additives since its cations and anions enable sufficient ionic conductivity and EDL formation along with the redox reaction of ferrocyanide/ferricyanide.[38] The performance of REHES systems employing the ferrocyanide/ferricyanide redox couple can be further modified in basic media, with the latter acting quasi as an additive.[70] Therefore, a more suitable classification would be based on the state-of-charge of redox ions[24]:

- i) Cationic redox electrolytes (e.g., $\text{Cu}^+/\text{Cu}^{2+}$).
- ii) Anionic redox electrolytes (e.g., ferrocyanide/ferricyanide).
- iii) Neutral redox electrolytes (e.g., quinone/hydroquinone).

Unlike the cationic and anionic redox electrolytes, redox species in neutral redox electrolytes, such as quinone/hydroquinone and *p*-phenylenediamine, do not contribute to the electrical double-layer formation. Furthermore, their charge neutrality is responsible for poor ionic conductivity leading to the necessity of ionic additives such as H_2SO_4 , KOH, and KNO_3 . Besides, for the prevention of redox shuttling of the neutral redox species, proton exchange membranes are required. Cation or anion exchange membranes can provide selective diffusions for the anionic or the cationic redox electrolytes, respectively.

Often, polymers are applied for liquid, gel, or solid type electrolytes where the energy storage can be enhanced by the redox activities of the conducting polymers. An essential aspect of those redox active polymer gel or solid electrolytes is that the charge transfer is enabled through the solid phase components in the electrolyte.[24] In that regard, the

primary distinction between polymer based redox electrolytes and conventional redox electrolytes is the location of the boundary for the electron charge transfer in the system. In case of conventional redox electrolyte systems, the charge transfer occurs at the electrode and electrolyte interface and the redox ions diffuse to the bulk electrolyte. In case of polymer gel or solid electrolytes, the charge transfer boundary depends on how the electrically conductive network was established in the system. Even if there is a clear charge transfer boundary at the electrode/electrolyte interface, the diffusion of redox species to the bulk electrolyte in a gel or solid phase is fairly slow. In case of continuous charge transfer network by solid phase conducting polymer in the electrolyte, the separator is a practical boundary only if the polymer network is not connected through the pore structure of the separator. If the separator does not block the electron charge transfer, the cell will suffer from excessive self-discharge. For that reason, semi-permeable or non-porous separators are necessary.[71] The aspect of the charge transfer boundary raises the question whether one sees solid or gel electrolytes as a part of the electrode. In this PhD work, the solid or gel type redox electrolyte system will not be considered as a REHES system, and the focus will be on the conventional liquid type redox electrolytes.

1.3. Design considerations for REHES systems

1.3.1. Selection of redox couples

The first step for REHES system design is to select the redox electrolyte. The standard redox potentials of the known redox couples (**Fig. 5A**) determine which redox couples can be used.[68] Yet, the actual redox potentials of the redox couples can deviate from that of determined at standard conditions. The key factors for this deviation in aqueous media are the pH value and the concentration of the electrolyte. For instance, the VO^{2+}/VO_2^+ reaction can occur in a stable potential window at low pH value even though the standard redox potential of the VO^{2+}/VO_2^+ couple is above the water stability window (**Fig. 5B**). The reason for this phenomenon is the potential up-shift of the oxygen evolution potential at low pH value (OER, **Fig. 5C**).[72] Accordingly, the Pourbaix diagram, or E_h -pH diagram, which shows the dependency on pH value and concentrations, considerably helps for the selection of the redox couples. Depending on the pH value of the aqueous electrolyte, the redox species can have different phase even with the same oxidation state. For instance, Fe^{3+} is soluble in the electrolyte at low pH value while it exists as a solid phase in Fe_2O_3 form despite having the same oxidation state (**Fig. 5C**). The influence of the concentration on the redox potential should also be considered and can be assessed by use of the Nernst equation:

$$\varphi_e = \varphi_f(Ox/Re) + \frac{RT}{nF} \ln \left(\frac{[Ox]}{[Re]} \right) \quad \text{Equation (1)}$$

In this equation, φ_e is the potential of the half-cell with a redox couple having the oxidized form Ox and the reduced form Re , R is the universal gas constant (8.31 J/K·mol), T is the temperature in Kelvin, n is the electron transfer number, F is the Faraday constant (96,485.33 C/mol), $[Ox]$ and $[Re]$ are the concentrations of the reduced and oxidized species at the electrode surface. The formal potential (φ_f) is defined as:

$$\varphi_f = \varphi_0(Ox/Re) + \frac{RT}{nF} \ln \left(\frac{a_{Ox}}{a_{Re}} \right) \quad \text{Equation (2)}$$

where φ_0 is the standard electrode potential, a_{Ox} and a_{Re} are the activities of oxidized and reduced species, respectively. Depending on the activities of the oxidized and reduced species in the electrolyte, the formal potential shifts when the ionic strength of the electrolyte changes. For instance, the formal potential for Fe^{2+}/Fe_2O_3 (**Fig. 5C**) up-shifts at a fixed pH value when the concentration decreases according to Equation (2).

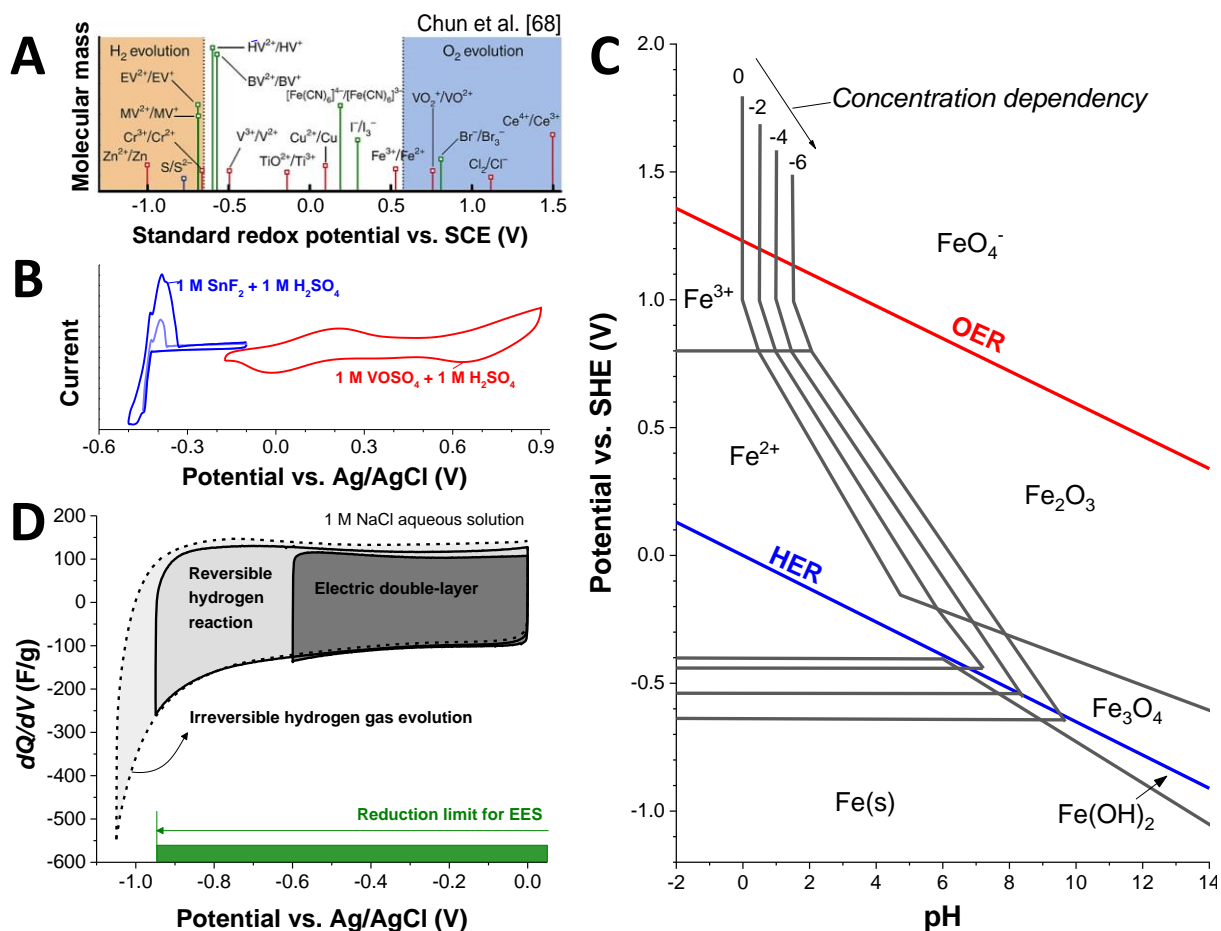


Figure 5 Several essential aspects of the selection of redox couples for the REHES systems. (A) Standard redox potentials for various redox couples. Reproduced from Ref. [68] (B) Cyclic voltammograms of SnF₂ and VOSO₄ systems at low pH value. Adapted from Ref. [42] with permission from The Royal Society of Chemistry. (C) Pourbaix diagram for the aqueous iron system. (D) Cyclic voltammograms for microporous carbon electrode in NaCl aqueous solution. Adapted from Ref. [73] with permission from John Wiley and Sons.

The standard redox potentials for oxygen and hydrogen also depend on the pH value. As the pH values increases, the OER and the hydrogen evolution reaction (HER) potentials shift towards more negative potentials (**Fig. 5C**). To understand the redox potential of hydrogen and oxygen reactions, one must consider catalytic effects as well. The following reported activity orders are useful for the HER and OER to understand the phenomena:

- i) HER: Pb>Sn>Zn>Cd>Cu>Ti>Fe>Ag>Ni>Al>Co>Pd>Pt in alkaline media.[74]
- ii) OER: Ru>Pd>Rh>Pt>Au>Nb>Zr~Ti~Ta in acidic media.[75, 76]

A higher catalytic activity of the electrodes leads to a lower stable operating potential for the actual EES device. Therefore, not only the catalytic effects of pure metals should be considered for designing REHES systems, but also for other materials such as metal oxides, and heteroatom-doped carbons, and composite materials. For instance, heteroatom-doped carbons (e.g., doped with S, P, B, and N)[77] and MoS₂[78] have been recently

reported as promising catalysts to modify the HER and OER activities. The OER activity is also catalytically changed by FeO_x , CoO_x , MnO_x , or Fe-Ni alloys.[75]. Hence, when electrode materials known for catalytic activities for the HER or OER are applied for REHES systems, the electrochemical stability window of the redox electrolyte must be carefully investigated. Under any circumstances, the desired redox reaction should occur without crossing the actual OER and HER potentials in the system.

Another important aspect of REHES design is to adjust the charge balance between the positive and negative electrodes. In case of a device with one redox species, the potential development of the individual electrodes can be significantly different. The charge storage capacity of one electrode may be much larger than that of the other electrode when the majority of the redox reaction occurs at one electrode. Limited to the potential range of the positive electrode, systems like Cu/Cu^{2+} ,[79] ferricyanide/ferrocyanide,[62] and multiple redox reactions with iodide[58] capitalize on the reversible hydrogen reaction at the negative microporous carbon electrode.[80-86] Due to their redox activities at the positive electrode, the potential at the negative electrode rapidly increases until reaching the potential for the $\text{H}_2(\text{g})/2\text{H}^+$ reaction. Within carbon nanopores, the carbon surface can efficiently adsorb the dihydrogen intermediate through $\text{C-H}_{\text{ad}}/\text{H}^+$ reaction which can be reversibly back-oxidized to protons.[82, 84, 87] As thoroughly investigated by electrochemical and in-situ gas analyses,[12, 34, 81, 84, 88] hydrogen can be reversibly stored in carbon micropores until actual gas evolution at higher voltages (**Fig. 5D**, AC in 1 M NaCl aqueous solution). This reversible hydrogen reaction is the fundamental origin for high potential aqueous supercapacitors which operate in the cell voltage range from 1.2-1.8 V.[89-93] While contributing to the charge storage capacity, the central issue of reversible electrochemical hydrogen storage is the reduced energy efficiency of the overall process.[94]

Another critical aspect for the selection of redox couples is the maximization of specific energy, which should be distinguished from the specific capacity. As initially demonstrated by Roldan et al.,[61] the HQ/H system has a high specific capacity of around 63 mAh/g (converted from 901 F/g, since Farad is an incorrect unit to quantify a battery-like system). However, due to the redox reaction occurring at the cell voltage around 0 V, the energy enhancement of this system is ineffective since the specific energy measured during discharging is the area underneath the galvanostatic discharging curve (**Fig. 6**). Despite the three-fold enhancement of the specific capacity, the specific energy is barely

doubled after introducing HQ/H redox couple into the system; the values in **Fig. 6** are recalculated based on the discharging profiles from Ref. [61]. For an effective enhancement of specific energy, the redox couples should be selected to provide a maximum potential difference between the redox potentials of the electrolytes at the negative and positive electrodes. Chun et al. and Evanko et al. carefully chose bromide and pentyl viologen which could give a redox potential difference over 1 V exhibiting a cell voltage plateau at 0.9-1.1 V (**Fig. 6**). [67, 68] One can clearly see the difference in specific energy by comparing the area underneath the cell voltage profile in **Fig. 6**.

In short, for the selection of redox couples, a standard redox potential (**Fig. 5A**) can guide us to balance redox activities of the electrolytes of the positive and negative electrodes. For the comprehensive selection of the redox couples, the concentration and pH influence should be considered with the Pourbaix diagrams (**Fig. 5C**). After the selection of redox couples, the redox potential and the thermodynamic limits (such as precipitation and corrosions) should be experimentally determined. Particularly, the unique conditions of nanoconfinement in micropores may vary the redox reactions compared to theory. Additionally, issues considering the toxicity, safety, material costs, and environmental influences should also be considered.

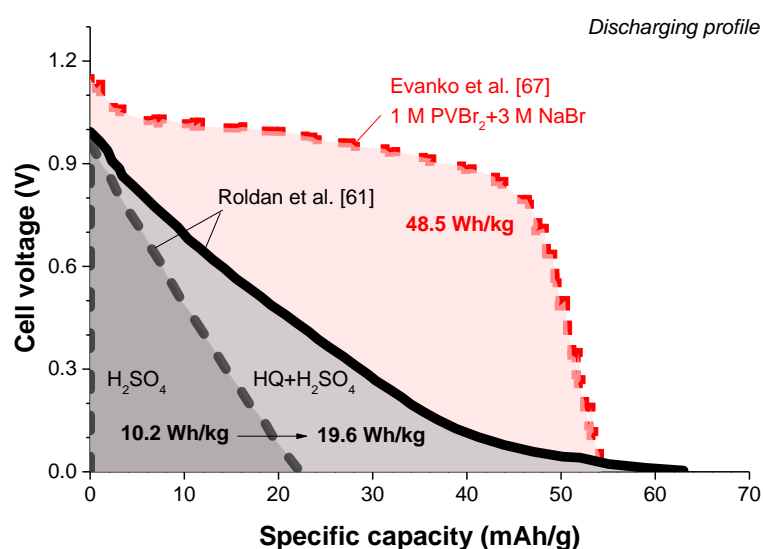


Figure 6 Discharging galvanostatic profiles of the HQ/H REHES system and of the REHES system containing pentyl viologen (PVBr₂) and sodium bromide in AC|AC configuration.

1.3.2. Preventing redox shuttling

The high mobility of soluble redox species may cause severe self-discharge of a REHES device. As demonstrated by Tachibana et al., the cell voltage of the REHES system with acetylferrocene rapidly approaches 0 V within just a few hours after having been charged (Fig. 7A).[95] To suppress the self-discharge process, Tachibana et al. used an anion exchange membrane as it effectively hinders the mobility of ferrocenium cations from the positive electrode to the negative electrode. The latter case is known as redox shuttling, and it causes the reduction of ferrocenium cations which are oxidized initially during charging. In Fig. 7B, the self-discharge process by redox shuttling is schematically described as exemplified by HQ/*p*-benzoquinone (BQ) redox couple. After being oxidized from HQ during charging, BQ diffuses through the porous separator to the other compartment leading to self-discharge by reduction back to HQ.

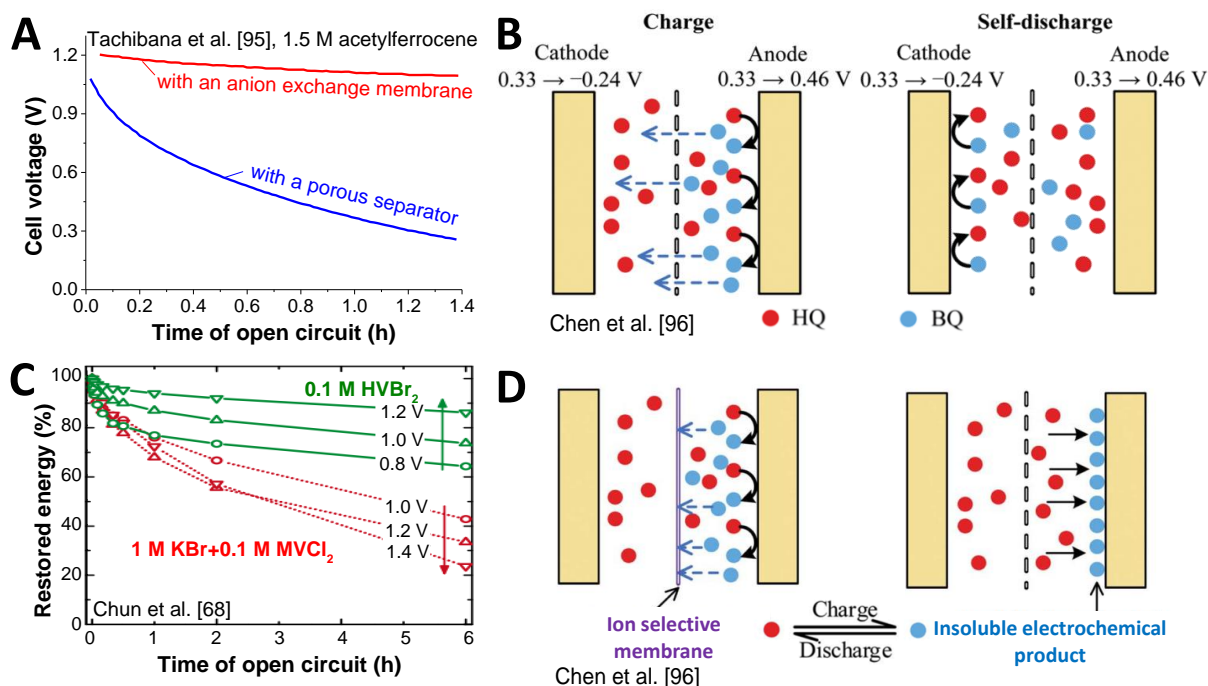


Figure 7 Redox shuttling phenomenon of the REHES systems and the known methods for the prevention. (A) High rate of self-discharge by the redox shuttling of ferrocenium cations for a porous separator and its prevention by an anion exchange membrane. Redox shuttling phenomenon by the hydroquinone/*p*-benzoquinone (BQ) redox couple for a porous separator (B) and the prevention of redox shuttling by introducing an ion selective membrane or an insoluble redox couple (D). Adapted from Ref. [96] - Published by The Royal Society of Chemistry. (C) Prevention of redox shuttling by the adsorption of bromide and viologen ions at the porous carbon material. The restored energy values are obtained from the AC|AC cells in 0.1 M 1,1'-Diheptyl-4,4'-bipyridinium dibromide (HVBr₂) and 1 M KBr+0.1 M MVCl₂. Adapted from Ref. [68]

Since self-discharge is closely related to the energy efficiency of the system, prevention or suppression of redox shuttling is one of the most critical requirements for the design of REHES systems. If the origin of the self-discharge is the diffusion of the redox species from one compartment to the other, the only way to reduce redox shuttling is to inhibit the diffusion of the soluble species. One approach is to apply ion-selective membranes to suppress the diffusion of the reduced/oxidized ions or molecules after charging the cell (**Fig. 7D, left**).

To prevent cation diffusion such as VO_2^+ and VO^{2+} , [12, 42] anion exchange membranes can be applied; and cation exchange membranes for anions such as iodide and bromide. [41] In case of the presence of both cation and anion species or neutrally charged molecules such as HQ, proton exchange membranes can be used. [43] Another approach is to apply soluble redox species having solid phase conversion during charging as demonstrated by Chen et al. (**Fig. 7D, right**) with $\text{Cu(s)}/\text{Cu}^{2+}$ redox couple. As the conversion into solid phase prevents the chance for the diffusion, the self-discharge rate can be effectively reduced. Nevertheless, the redox electrolytes with solid phase conversion do not fit the definition of REHES given in **Chapter 1**.

Alternatively, the diffusion of soluble redox species can also be reduced when the soluble redox species are adsorbed on the electrode surface. As reported by Chun et al., [68] the strong adsorption behavior of bromide in carbon micropores significantly suppress the diffusion rate of oxidized bromide ions from the positive electrode to the negative electrode (**Fig. 7C**). However, the reported bromide system shows still an energy loss of 10-20 % 6 h after charging. Although this is a higher rate as compared to conventional batteries, the bromide REHES system is still promising for the applications where fast charge/discharge is required (5-10 h intervals). Albeit very important from an application point of view, discharge rates of REHES systems have been investigated only by a few.

1.4. Critical characterization of redox electrolyte systems

1.4.1. Energy and power performance

For EES devices, the specific energy (E_s in Wh/kg) is one of the most critical performance metrics. The specific energy of any EES system can be calculated by Equation (3).

$$E_s = \frac{1}{3600 \cdot m_a} \int V_c I dt \quad \text{Equation (3)}$$

where m_a is the mass of the active electrodes in the device, which actively contributes to the charge storage capacity, V_c is the cell voltage, and I is the discharging current. Typically, the specific energy is reported according to the discharging period, and energy efficiency (ε_E) can be additionally calculated according to Equation (4).

$$\varepsilon_E = \frac{E_{dis}}{E_{char}} \quad \text{Equation (4)}$$

where E_{char} is the energy invested during charging, and E_{dis} is the energy restored during discharging.

According to Equation (3), the specific energy is the area underneath the cell voltage profile by galvanostatic measurement (**Fig. 6**). Since the shape of the voltage profile is triangular for supercapacitors, Equation (3) can be simplified to:

$$E_{s,cap} = \frac{C_d V_c^2}{2 \cdot 3600} \quad \text{Equation (5)}$$

where the device specific capacitance C_d is defined as:

$$C_d = \frac{Q}{m_a \Delta V} \quad \text{Equation (6)}$$

where Q is the accumulated electric charge during the cell operation in the cell voltage window (ΔV). For batteries, the specific energy is roughly the multiple of operating potential, specific current, and discharging time by galvanostatic measurement.

For REHES and many hybrid EES systems, the performance values are often incorrectly calculated by use of Equation (5) despite the non-capacitive behavior of the device.[24, 38, 94] When a Faradaic activity of the redox electrolyte enhances the specific capacity of the REHES system, an apparent potential plateau can appear in the voltage profile.[24] If the potential plateau is in a low cell voltage range, the use of Equation (5) may result in a severe overestimation of the actual performance. For instance, the area underneath the

cell voltage profile of the REHES system with 1.2 M PFC (**Fig. 8A**) is apparently smaller than the area depicted by Equation (5). Even more critical, in some cases, the specific energy has been reported by calculating the slope from a certain cell voltage range and inserting the capacitance value to Equation (5). For example, when being calculated at the potential plateau in **Fig. 8A**, a large capacitance of 2389 F/g (normalized by m_a) is obtained. Furthermore, by assuming the 1.23 V width of the theoretical potential window and applying Equation (5), the specific energy can be evaluated to be 120 Wh/kg (normalized by m_a) which is far beyond the actual value of 5.6 Wh/kg.[38]

Often, the specific energy of the REHES devices is determined by sweeping the cell voltage from positive to negative values.[97-99] However, this approach does not bring a practical sense since the negative polarization below 0 V does not survey energy recovery but constitutes energy consumption. In fact, for the understanding of the systems, the potential of the cell can be swept from negative to positive values; however, the data thereof should not be used for the calculation of the specific energy.[97-99] The possible exception is for the symmetric capacitor systems where the slope in the galvanostatic plot does not change. Likewise, reporting the specific energy based on the half-cell data of the hybrid EES systems should be prevented.[100, 101] If one would report the specific energy of a hybrid electrode, an ideal opposite electrode with a known electrochemical behavior may be assumed for the calculation. For instance, the specific energy of a lithium-ion battery can be estimated from the half-cell data for the positive electrode by assuming the redox potential of the graphite negative electrode with infinite capacity.

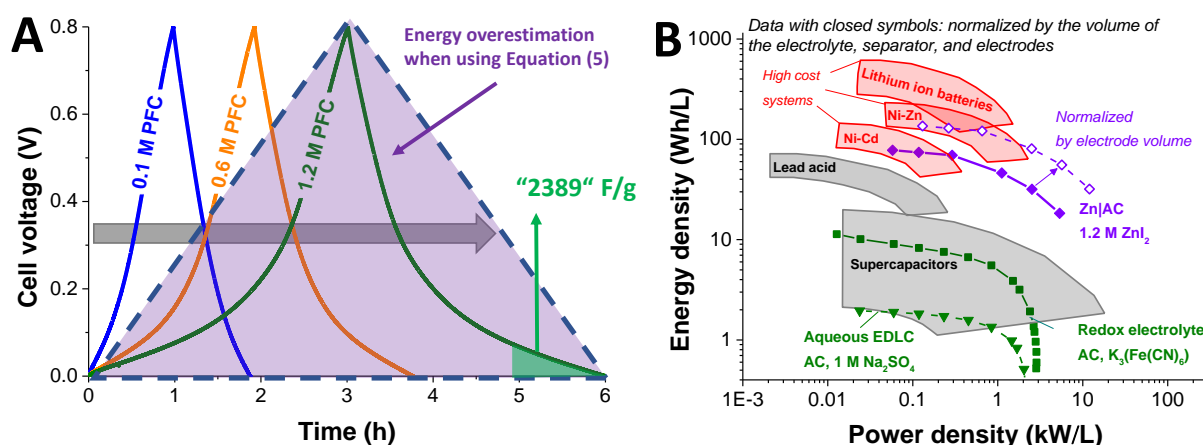


Figure 8 Performance report for the REHES systems. (A) An example of the performance overestimation by applying inappropriate equations. Adapted with permission from Ref. [38] Copyright (2017) American Chemical Society. (B) Energy and power density values are normalized by the volume. Adapted from Ref. [40] with permission from The Royal Society of Chemistry.

Another important performance parameter reflects the charging/discharging rate capability. The specific power (P_s in kW/kg) is often reported by applying Equation (7):

$$P_s = \frac{3600 \cdot E_s}{\Delta t_{dis}} \quad \text{Equation (7)}$$

where Δt_{dis} is the duration of the discharging process. In case of batteries, the multiplication of the operating cell voltage and the discharging current often corresponds with an approximation of the electric power of the device. Hence, batteries supply roughly a stable power since their operating potential window is typically very narrow. By comparison, the electric power of supercapacitors significantly drops as the cell voltage decreases during discharging.

Most adequately, the specific power (kW/kg) is calculated from the data obtained during discharge. However, often the specific power has been derived from charging process, which may result in misleading and incorrect data. For higher resistance values, we will see a lower specific power; vice-versa. However, we see an artificial enhancement of the specific power when the specific power is calculated from the charging energy by Equation (7). For instance, when two devices provide the same specific power during discharging, the one with a higher resistance will consume more energy during charging, leading to a higher specific power value calculated from Equation (7). Thus, the high specific power during charging does not necessarily indicate a rapid charging process. For the claim of fast charging capability, either high specific current or high upper limit potential can be reported; the latter enables higher charging voltage than the nominal voltage in case of batteries.

For a comparison of different EES devices, it is convenient to present the performance in a Ragone (pronounced "ru-GO-nee") diagram, where energy storage capacity and electric power values are plotted. In such diagrams, the performance values are conveniently normalized by the mass or by the volume of the device (**Fig. 8B**).[40] Normalization by the volume is of particular importance to space-sensitive applications, like in the case of electric vehicles or mobile computing. Porous carbon materials are much lighter than metals and metal oxides; however, their low density is a drawback for the volumetric performance. When comparing data in Ragone diagrams, a key issue is a distinction between normalization on a device level and data normalized just by the active material. Ragone himself normalized by device mass because the purpose was the facile

comparison of technologies (in contrast to comparing materials). The mass (or volume) of just the electrodes is much smaller compared to assembled cells, whereby a comparison between different technologies (and different devices) becomes complex. For instance, the data of commercial (well-engineered) devices are often compared with electrodes assembled in a laboratory, where only the electrodes (not the optimized cell) are measured. To ensure comparability, at least one should only compare data that were normalized by the same way (e.g., just electrode data or just device data).

As shown in **Fig 8B** for the Zn|ZnI₂|AC REHES system, the normalization only to the electrode mass can be misleading when compared to the performance of commercial devices with device normalization. Hence, for the fair comparison with the other reported systems, the way of normalization must clearly be outlined. In the case of the REHES systems, not only the electrode material is contributing the charge storage capacity, but also the electrolyte. The contribution of the latter can lead to the performance overestimation, particularly, for the device containing a relatively large volume of the redox electrolyte as compared to that of the small electrode. For this reason, normalization of the performance by the volume or mass of the electrolyte, separator, and electrode (**Fig. 8B**) can provide a more realistic comparison with that of the commercial products with device normalization. Thereby, a volume limited cell is recommended to confine the electrolyte to space through the electrode and separator.[38, 68, 96] In case of reporting laboratory scale systems, the outer housing and current collectors are often way larger than the electrode, electrolyte, and separators.

1.4.2. Determination of electrochemical stability

The electrochemical stability is a crucial requirement for the robust cycle life of EES systems. In most cases, the electrochemical stability is limited by irreversible decomposition reactions of the electrodes or electrolytes. For REHES systems, the electrochemical stability of the electrolyte is particularly important due to the additional redox activities of the dissolved redox ions. At a certain pH value, the electrochemical stability window is not only limited by irreversible oxygen or hydrogen evolution, but also by the irreversible phase transition of the dissolved ions into solid or gas phases. For instance, in case of the REHES systems with bromide and ferrocyanide/ferricyanide, the corrosive and volatile feature of bromide or the high toxicity of hydrogen cyanide can bring severe health and safety issues. Therefore, the electrochemical stability window must be carefully determined.

For the investigation of undesired phase transitions of the redox ions, in-situ techniques such as Raman and electrochemical mass spectroscopy can be effectively applied. As demonstrated, for example, by Fic et al.,[88] electrochemical sorption of hydrogen of microporous carbon can be studied by in-situ Raman for C-H bond. He et al. carried out thorough in-situ gas analyses by online electrochemical mass spectrometry and cell pressure measurements (**Fig. 9A**).[81, 84] They measured ion-current profiles for O₂, H₂, CO, and CO₂ during the electrochemical operation of the cell. Their approach provided a unique interpretation regarding the mechanisms of the electrolyte decomposition and the side reactions at the carbon surface.

Still, advanced electrochemical analyses without in-situ or in-operando measurements can also enable detailed investigations regarding the undesired phase transitions in the REHES systems. Conventionally, galvanostatic charge/discharge with potential limitation (GCPL) is applied to report the cyclic stability and the reversibility of the device or individual electrode. The capacity, Coulombic efficiency, equivalent series resistance, and the potential profile at each cycle provide information which could correlate with the undesired phase transitions. However, the data from the galvanostatic cycling with potential limitation (GCPL) test are often not sufficient to identify the precise origin of the stability degradation. For additional information, other electrochemical analyses such as electrochemical impedance spectroscopy (EIS) can be carried out at specified cycle intervals.[80]

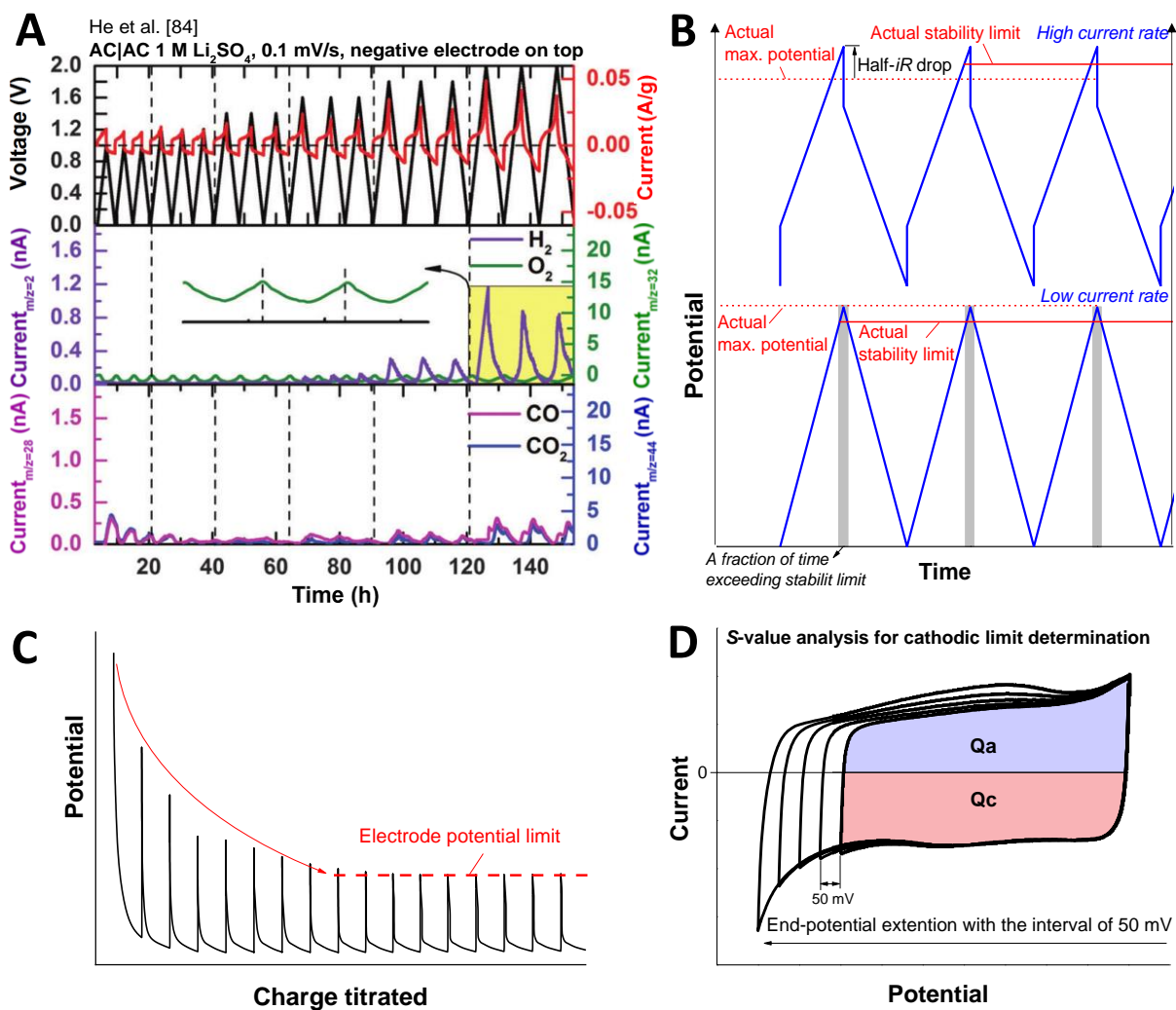


Figure 9 Advanced characterization techniques for the determination and the investigation of the electrochemical stability of the EES systems. (A) In-situ gas and pressure analysis for the detailed degradation mechanisms of the porous carbon electrodes and aqueous electrolytes. Adapted from Ref. [84.] - Published by The Royal Society of Chemistry. (B) Limitations of galvanostatic cycle test (C) Galvanostatic intermittent titration technique for the determination of electrolyte decomposition potential. (D) *R*-value (also known as *S*-value) analysis with cyclic voltammetry.

During the GCPL cycling, the potential of the system exceeds the stability limit in a fraction of time compared to the entire charging/discharging period (**Fig. 9B**); therefore, the stability limit can be overestimated.[102] Furthermore, GCPL often employs large currents to shorten the measuring time, but this may lead to an overestimation of the apparent cyclic stability. High currents can cause a rather large *iR* drop which prevents the system to reach the targeted maximum potential for the test. For that reason, voltage floating test can be applied for a more realistic determination of electrochemical stability of the device.[102] For the voltage floating test, a constant potential, also referred to as floating potential, is applied, and the system is supplied with a sufficient current (floating current) for maintaining the potential. The detailed analysis on floating current will be given in **Section 6.1**. Complementary electrochemical measurements are carried out with

a certain interval of time such as EIS, CV, and GCPL test; after these tests, the floating potential is re-established and maintained for a pre-defined duration until the next set of complementary measurements will be carried out (e.g., every 10 h). These allow investigating the change in electrochemical properties regarding irreversible phase transitions such as electrolyte decomposition. If there is an irreversible phase transition, the capacity will fade rapidly under the harsh floating condition.

While important for benchmarking of practical voltage limits, one floating experiments only yields data for one pre-set potential value. For the survey of the potential dependency of the on-setting electrochemical instability, multiple sets of data at different upper potential limits are required, or other methods can be applied. For instance, the galvanostatic intermittent titration (GITT) analysis requires only one set of data in a relatively short time frame (10-40 h) for identifying the potential limits for individual electrodes.[88] For this method, a given amount of charge is titrated to the electrode with a certain time interval while the potential of the electrode is being measured (**Fig. 9C**). Exceeding the potential of the irreversible reaction, the electrode potential stagnates despite the continuous titration process due to the charge consumption for the irreversible reaction. Yet, GITT does not provide detailed information about the origin of the potential limit; hence, other electrochemical analyses such as CVs are required as a complementary data.

Another helpful electrochemical analytical tool to quantify stability limits is a determination of the *R*-value, or also known as *S*-value analysis. The *R*-value analysis was initially suggested by Xu et al. based on Butler-Volmer equation that the kinetic current for Faradaic reaction increases exponentially with the potential increase.[103] The criteria for Faradaic decomposition were further refined by Weingarth et al.[104] who assigned the name of “*S*-value analysis” (*S* for “stability”). Instead of the initial criterion of *R*-value exceeding 0.1 for the onset of decomposition, a new criterion was suggested that the second derivative of *S*-value ($d^2S/d\phi^2$) exceeding 0.05 indicates the onset of Faradaic decomposition. *S*-value and *R*-value analyses can be simply carried out by cyclic voltammetry; the maximum potential is extended from a fixed starting potential with the certain potential interval (**Fig. 9D**). The *S*-values (equal to *R*-values) can be obtained as:

$$S_a = \frac{Q_a}{Q_c} - 1 \quad \text{Equation (8)}$$

$$S_c = \frac{Q_c}{Q_a} - 1 \quad \text{Equation (9)}$$

where S_a is the S -value for the anodic limit, S_c is the S -value for the cathodic limit, Q_a is the charge accumulated due to the anodic current, and Q_c due to the cathodic current. The main advantages of the S -value analysis are: i) only one set of data is required in a relatively short time frame (1-3 d), ii) complementary analyses are available by CVs, and iii) reversibility of the reaction can be quantitatively evaluated.

Establishing a universal S -value criterion is a challenging task since the electrochemical behavior differs from system to system. For instance, applying the R -value criterion ($S > 0.1$) or S -value criterion ($d^2S/d\phi^2 > 0.05$) can lead to the misinterpretation regarding the cathodic limit of porous carbon in aqueous solution (**Fig. 10A**).^[73] In general, the onset of substantial cathodic current increase in cyclic voltammogram is interpreted as the cathodic limit by hydrogen gas evolution. This approach cannot be applied to porous carbon electrodes because of the reversible C-H_{ad}/H⁺ redox reaction (**Fig. 5D**). The latter also contributes to the cathodic current increase which does not necessarily mean an irreversible reaction. Hence, the S -value analysis is particularly useful for the quantitative evaluation of the reversibility regarding the hydrogen reaction at the porous carbon electrode (**Fig. 10A**, AC in 1 M NaCl aqueous solution). A linear slope in S -value plot from 0.60 to -0.95 V vs. Ag/AgCl implies the regime where hydrogen can be reversibly stored while the exponent increase below -0.95 V vs. Ag/AgCl indicates the irreversible hydrogen gas evolution. Those results correspond to the studies with high voltage aqueous EDLCs (1.6-1.8 V) and in-situ gas analyses.^[34, 80, 84, 89, 90, 92, 93] For reversible electrochemical hydrogen storage, the cathodic limit can be overestimated for R -value criterion and underestimated when benchmarking the S -value criterion (**Fig. 10A**).

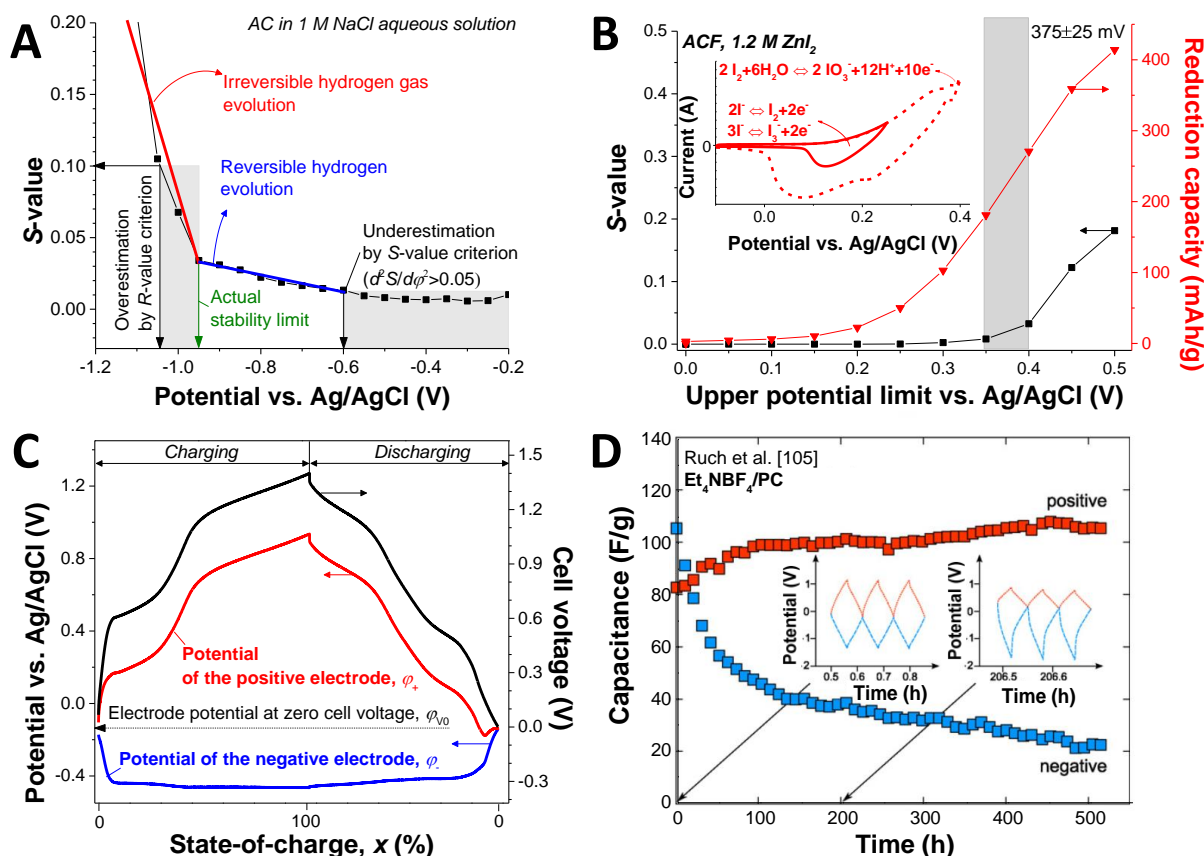


Figure 10 Advanced electrochemical analyses for the system stability. (A) The evaluation of S -value for the reduction limit in aqueous solution. Reproduced from Ref. [73] with permission from John Wiley and Sons. (B) The S -value analysis of the activated carbon fiber electrode (ACF) in 1.2 M ZnI₂ aqueous solution. The inset shows redox activities of the ZnI₂ solution in cyclic voltammogram. Adapted from Ref. [40] with permission from The Royal Society of Chemistry. (C) The cell and cable configuration with a spectator reference electrode allow tracing the individual potentials for the positive and negative electrodes while operating the device voltage. Adapted from Ref. [67] - Published by The Royal Society of Chemistry. (D) Long-term stability test for a double-layer capacitor (AC|AC) with 1 M tetraethylammonium tetrafluoroborate (Et₄NBF₄) in propylene carbonate (PC). The inset shows the potential profiles of the positive and negative electrodes in the device. Reprinted from Ref. [105], Copyright (2018), with permission from Elsevier.

The S -value analysis can be effectively applied even in the presence of multiple redox activities whose redox potentials are close to each other. In case of AC electrodes with an iodide-containing electrolyte, the main limitation for the positive potential limit seems to be not by OER, but by the low Coulombic efficiency through the conversion to iodate.[40] Since the S -values are obtained from each cyclic voltammogram at each potential step, they provide complementary information such as specific capacity and the types of redox reactions. Thereby, the potential limit of the activated carbon fiber (ACF) electrode operated in aqueous 1.2 M ZnI₂ is determined to be 0.35-0.40 V vs. Ag/AgCl according to the exponential increase in S -value (**Fig. 10B**). The origin of the latter can be identified as the iodine/iodate reaction based on the redox peak around 0.40 V vs. Ag/AgCl in the CV (**Fig. 10B, inset**). By comparison, the redox reactions with polyiodide in the range of 0.10-

0.35 V vs. Ag/AgCl are reversible in terms of stable S -values. Up to the cathodic limit of 0.35 V vs. Ag/AgCl, the charge storage capacity significantly increases up to 200 mAh/g (normalized by m_a).

In contrast to supercapacitors, the voltage limits of REHES devices cannot be estimated merely based on the cathodic and anodic limits determined from half-cell experiments. During charging/discharging of a REHES device, redox activities contribute to charge storage capacities differently at each electrode which brings difficulties to predict the potential development of individual electrode. Therefore, the device stability still must be evaluated in full-cell configuration even when the potential limits are carefully determined for the individual electrode in half-cell configuration. Only by this way, it is possible to obtain data based on the actual device performance for practical EES applications. For the investigation on how the individual electrode potential develops in a device, it is convenient to add a spectator reference electrode to a full-cell setup to observe the potential of the counter electrode while operating the cell voltage (**Fig. 10C**).^[12, 67] By this way, the cell works like the actual application as a device for energy storage while still basic electrochemical benchmarking is enabled. The working electrode potential is obtained by subtracting the counter electrode potential from the cell voltage. For the analysis, the electrode potential at zero cell voltage, φ_{v0} , the potentials of the positive (φ_+) and the negative electrode (φ_-) at various state-of-charge are particularly important. First, the most critical point is that the φ_+ and φ_- do not cross the stability limits. Second, the shift of φ_{v0} is also vital since it could lead to the situation that φ_+ or φ_- cross the stability limit. Furthermore, if the capacity fades differently for each electrode (**Fig. 10D**), the device could exceed the stability limit because the potential at the electrode with more capacity fade will develop more rapidly than that of the other electrode (**Fig. 10D, inset**).^[105] Therefore, careful evaluation of each electrode is still of high importance for full-cell devices.

1.4.3. Time-dependent potential decay

Despite the importance of the self-discharge by redox shuttling for efficient energy storage of REHES systems, the self-discharge rate of the REHES systems remains ill-explored. Instead of investigating the energy efficiency, mostly high Coulombic efficiency values (>90 %) are reported to validate efficient energy storage performance. However, the Coulombic efficiency values at high current rate do not adequately represent the self-discharge characteristics of the system. For instance, when a system has a high self-discharge rate caused by redox shuttling, the Coulombic efficiency values increase as a function of the specific current. The latter occurs because the time frame of the charging/discharging is getting shorter with respect to the amount of self-discharge current at a higher current rate (Fig. 11A).

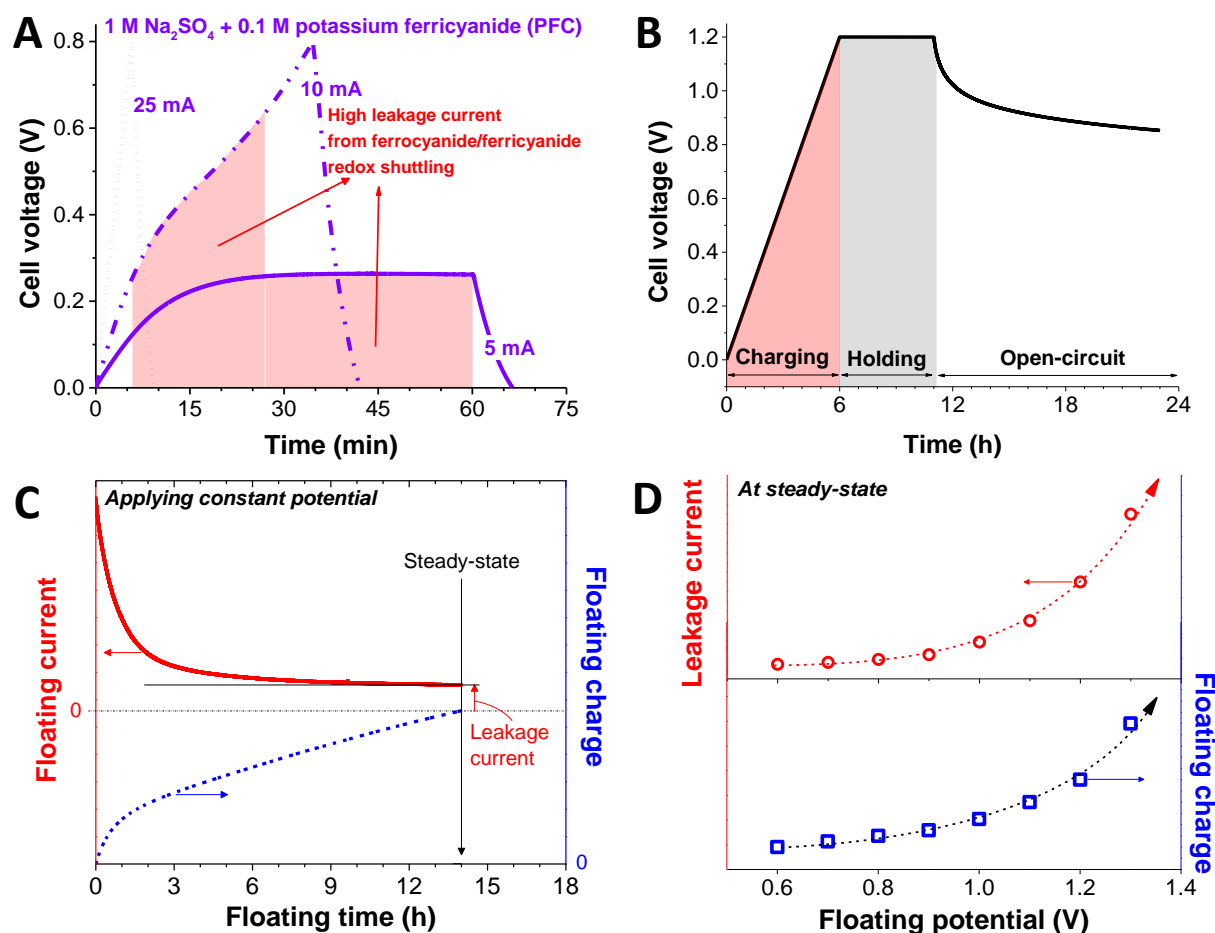


Figure 11 Electrochemical analyses for self-discharge phenomena. (A) Galvanostatic charging/discharging profiles of the REHES system with AC electrodes in potassium ferricyanide at various applied currents. Adapted with permission from Ref. [38]. Copyright (2017) American Chemical Society. (B) Open-circuit potential measurement. (C-D) The analyses with the floating current and floating charge.

For the characterization and the analysis of self-discharge behavior, either full-cell or half-cell configuration can be applied. The full-cell configuration allows characterizing a more application-realistic performance of the entire system, while the detailed analyses about the individual influences of each electrode are challenging. Often, full-cells with a spectator reference electrode are applied. Such setups enable the operation with a full-cell configuration and still allow us measuring the individual potential of each electrode. For a detailed analysis of the self-discharge behavior of one electrode, the half-cell configuration is still necessary. The combined studies with the half-cell and the full-cell can provide a comprehensive understanding of the self-discharge behavior of redox electrolyte systems.[106]

The two most common methods to quantify and investigate self-discharge are the open-circuit potential (OCP) measurement (**Fig. 11B**) and floating current analysis (**Fig. 11C-D**). Monitoring the open-circuit potential may be the method closest to the actual application; furthermore, it conveniently allows analyzing the underpinning mechanisms when implementing modeling. For the comparison and the interpretation of the OCP profile, the characteristic differences between batteries and capacitors must be correctly considered and reflected to describe the self-discharge. In case of capacitors and capacitor-like devices (**Fig. 1C**), the potential is linear to the total accumulated charge; hence, the OCP loss can be seen as a self-discharge (loss in stored charge) in the absence of the charge redistribution (Details in **Section 1.5.1**). In case of batteries (**Fig. 1B**), the loss in charge is not linearly correlated to the OCP loss. For that reason, restored electric charge as a function of resting time is much more representative for the self-discharge rate; the restored electric charge can be obtained by discharging the cell after the resting period.

Instead of plotting the OCP change over time, one can also calculate the restored energy to evaluate how much energy was lost due to cell self-discharge and voltage decay. Such values are only meaningful when benchmarking full-cell devices and not half-cells. The specific energy must be understood as the combined data for both positive and negative electrodes. For the interpretation, the decrease in specific energy should not be directly interpreted as the sole result of self-discharge, because the cell resistivity can also contribute to the energy loss. Reporting a restored energy without resting time can help to identify the energy loss by the cell resistance (**Fig. 7C**). For a comprehensive understanding of the self-discharge process, it is important to report i) restored electric

charge, ii) restored energy, and iii) the actual OCP profile; conveniently, all three parameters can be obtained from one experimental setup.

The floating current analysis can be carried out by measuring the current response after the desired potential is reached and held (**Fig. 11C**). This current response indicates that the system is still being charged because of the electrochemical kinetics, and that the system consumes current by self-discharge. Therefore, a constant current response at the steady-state (no reversible charging current is flowing) is interpreted as the leakage current of the system (**Fig. 11D, top**). Integrating the measured floating current over floating time till the steady-state is reached yields the total accumulated charge, or floating charge (**Fig. 11D, bottom**) which is helpful to identify and characterize the discharge mechanisms.[107]

Based on these considerations, we see that thorough characterization of self-discharge is necessary for redox electrolyte aided hybrid energy storage systems (as it is for any other EES system, too). For a practical application, it is crucial to quantify the self-discharge rate and to compare it with reference systems such as commercially available double-layer capacitors. Further improvements of REHES systems will then require a firm understanding of the self-discharge mechanism(s). More discussion on the state of the art of theoretical and modeling work regarding self-discharge is found in **Section 1.5.1**.

1.5. Diffusion, adsorption, and kinetics of REHES

The use of highly porous carbon electrodes allows the design of REHES systems with attractive performance values. For a comprehensive understanding of the latter, it is necessary to study fundamental aspects of redox kinetics, ion diffusion, and adsorption of redox ions under the unique conditions of nanoconfinement inside carbon pores. The redox kinetics in carbon micropores are known to be different from processes occurring on flat surfaces, where we can assume semi-infinite planar diffusion.[108-114] The works of Narayanan, Bandaru, and coworkers explained the high power handling performance of REHES systems by adopting key concepts of thin-layer electrochemistry (TLE).[26, 39] The TLE theory, initially developed by Hubbard and Anson in the 1960s, addresses electrochemical processes in the confined diffusion length, or thin layer.[108, 109] The core aspect of the theory is the concept of diffusion-less reaction under thin-layer condition. Further fundamental studies with advanced simulations and models indicate that the diffusion-less TLE behavior is an intrinsic feature. Hence, it should not be interpreted as a kinetic enhancement leading to the conclusion of catalytic effect.[111, 112, 114] Nonetheless, the TLE behavior is considered as a critical factor for the high power performance of REHES systems with microporous carbon electrodes.

The diffusion of redox ions is an important aspect not only for the redox kinetics but also for efficient energy storage. The diffusion of redox ions may lead to severe energy loss by ion shuttling from one electrode compartment to the other.[38, 68, 96] While the use of ion selective membranes can be recommended to prevent the redox shuttling, a unique solution is alternatively the implementation of strong halides adsorption in carbon micropores.[66-68, 88] Thereby, an effective immobilization of otherwise mobile redox ions can be achieved. In the following sections, the diffusion, adsorption, and redox kinetics on REHES systems will be discussed.

1.5.1. Self-discharge and time-dependent potential decay

Self-discharging performance is an important performance parameter with impact on energy and charge efficiency, life time of the system, and safety issues.[106, 107, 115-118] The theories and models about the self-discharge mechanisms for supercapacitors have been pioneered by Conway et al.[107, 119] and its recent progress is well summarized by Andreas et al.[106] or I. Ike et al.[120] In this section, the current progress on the state of

the art knowledge of the time-dependent potential decay and the self-discharge will be reviewed. Which can be categorized as follows:

- i) Self-discharge due to short-circuit leakage between the electrodes interface.
- ii) Self-discharge due to activation-controlled Faradaic process.
- iii) Self-discharge due to diffusion-controlled Faradaic process.
- iv) Potential decay due to non-uniformity of the charge.

Type-(i) self-discharge occurs due to the imperfect sealing of the positive and negative electrodes which causes short-circuit between the electrodes. Therefore, it is often considered to be a trivial origin of self-discharge which is not related to the electrochemistry.[106, 107] To prevent this type of self-discharge, one needs to fabricate a cell with complete insulating and perfect sealing between the electrodes. The time-dependent OCP, V_t , can be derived from a simple RC circuit model where the short-circuiting resistance element, R_s , is introduced (**Fig. 12A**).[107, 121] The characteristic of this mechanism is that $\ln(V_t)$ has a linear relationship with time (t).

$$\ln\left(\frac{V_t}{V_i}\right) = -\frac{t}{R_s C} \quad \text{Equation (10)}$$

where V_i is the initial potential and C is the double-layer capacitance.

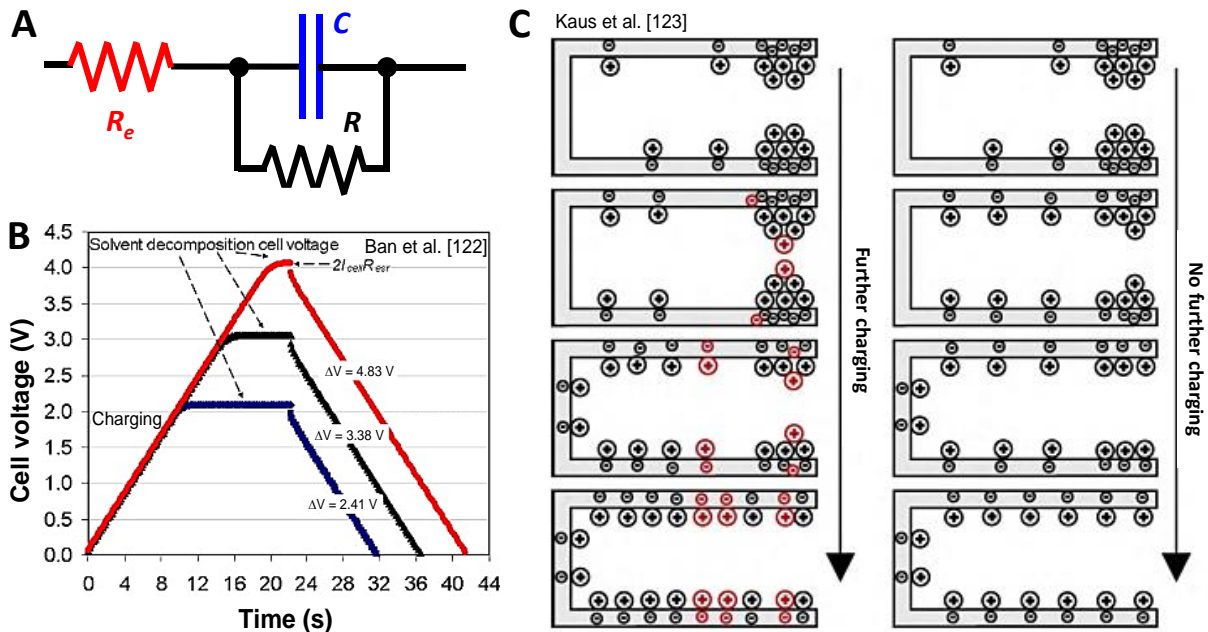


Figure 12 Various models and simulations for self-discharge mechanisms of supercapacitors. (A) A simple RC model for the self-discharge mechanisms with the short-circuiting element in the cell. (B) Self-discharge mechanisms due to the solvent decomposition. Reprinted from Ref. [122], Copyright (2018), with permission from Elsevier. (C) Charge redistribution theory for double-layer capacitors. Reprinted from Ref. [123], Copyright (2017), with permission from Elsevier.

At equilibrium, the leakage current (i_s) at an applied potential (V_a) can be defined as:

$$i_s = \frac{V_a}{R_s} \quad \text{Equation (11)}$$

The type-(ii) mechanism originates from the non-diffusion controlled reaction with electrode or electrolyte and exhibits no transport limitation. The latter is enabled when the reaction species are the part of the electrode or highly concentrated;[116, 121] for instance, a decomposition of a solvent (**Fig. 12B**). In the case of the activated-controlled Faradaic process, the OCP has a linear relationship with $\ln(t)$. [107, 121]

$$V_t = \frac{RT}{\alpha F} \ln\left(\frac{RTC}{\alpha F i_0}\right) - \frac{RT}{\alpha F} \ln\left(t + \frac{Ct_0}{i_0}\right) \quad \text{Equation (12)}$$

where i_0 is the exchange current density in A/cm^2 which passes reversibly in both anodic and cathodic direction, t_0 is an integration constant, and α is the transfer coefficient. The leakage current of this type follows the Tafel equation which is a function of overpotential (η):[121]

$$i_s = i_0 e^{\frac{\alpha n F}{RT}} \quad \text{Equation (13)}$$

Since the leakage current strongly relies on the overpotential of the reaction, any catalytic influence of the system must be considered.

This model can be further advanced by introducing potential-dependent capacitance (C_θ) which arises due to the partially reversible Faradaic reaction on carbon surface in addition to the electrical double-layer capacitance. For instance, Faradaic adsorption of hydrogen on the electrode surface leads to the potential-dependent additional charge storage capacity to the electrode.[121] In that case, C_θ is defined by the areal fractional coverage θ by Faradaically electroadsorbed species:

$$C_\theta = q_1 \left(\frac{d\theta}{dV}\right) \quad \text{Equation (14)}$$

where q_1 is the charge for the formation or desorption of a monolayer of the intermediate (e.g., adsorbed H). Unlike what is shown in Equation (12), more than one slope can arise in the case of Faradaically electroadsorbed species described in Equation (14); that is, one slope for small θ and another slope for $\theta > 1$. [87] This theoretical consideration is expected to play a critical role in the REHES systems with reversible hydrogen reaction. [80-82] For the REHES systems, not only the solvent decomposition reaction (e.g., H_2 or O_2 gas evolution), but also the decomposition of highly concentrated redox ions must be

considered. One such example is a ferricyanide-containing acidic solution, where hydrogen cyanide gas evolution may occur.[124]

The main difference between type-(iii) and type-(ii) is that the activation-controlled self-discharge arises from the Faradaic reaction via the overcharge beyond the specific activation potential. By comparison, the diffusion-controlled self-discharge occurs through the Faradaic reaction within the operating potential window at the electrode/electrolyte interface where the reactants should diffuse to the interface. For instance, in the presence of Fe ion impurities, the leakage current arises by the redox shuttling of the Fe²⁺/Fe³⁺ couple which attributes to its characteristic diffusion-controlled feature.[125] Considering the diffusion of the redox shuttling process by Fick's law and the semi-infinite diffusion of the planar electrodes, the time-dependent potential of the system can be derived as:

$$V_t = V_i - \frac{2nFA\sqrt{D}c_0}{c\sqrt{\pi}}\sqrt{t} \quad \text{Equation (15)}$$

where D and c_0 are the diffusion coefficient in cm²/s and the initial molar concentration of the impurity redox reaction in mol/cm³, respectively. A is the area of the planar electrode in cm².

The diffusion-controlled leakage current is defined as:

$$i_s = nFD \left(\frac{dc_R}{dl} \right) \quad \text{Equation (16)}$$

where c_R is the molar concentration of the redox species in mol/cm³ and l is the distance from the electrode surface to the electrolyte in cm. As clearly distinguished from the activation-controlled leakage current by Equation (13), Equation (16) shows how diffusion coefficient and the concentration of redox species influence the leakage current of the system. In the case of semi-infinite diffusion of flat capacitor electrodes, the time-dependent leakage current is defined as:

$$i_s = nFA \sqrt{\frac{D}{\pi t}} c_0 \quad \text{Equation (17)}$$

The linear relationship between the concentration term for the redox species and the leakage current can be seen.

The cell voltage decay as a function of time does not necessarily originate from the leakage current. Non-uniform charge distribution, or type-(iv), mechanism, can also cause a potential decay of the cell as the potential drops through charge redistribution.[107, 121] For that reason the term 'self-discharge' may be improper to describe the phenomena regarding the potential decay by charge redistribution.[125, 126] The non-uniform charge distribution occurs either through the double-layer formation in porous carbons[107, 123, 127-129] or the conversion type Faradaic electrodes.[107, 115, 121] As originally suggested by De Levie, the equivalent circuit of a porous electrode should be established by considering the series of resistance and capacitive components along the pore.[128] According to the model developed by De Levie, also known as RC ladder circuit or transmission line model, electrochemical interaction for double-layer formation is higher at the pore entrance and lower as the depth of the pore increases. The length of the electrical double-layer response, or penetration depth, is a square root function of angular frequency. At high frequency, the electrode behaves just like a flat electrode with its geometric surface area.[128] De Levie also found that the impedance phase angle of the porous electrode can be 45 °, similar to that of Warburg diffusion. This, however, should not mean that it has the same origin or underpinning mechanism as the latter. When the electrode is rapidly charged, the electrical double-layer will be formed more at the entrance of the pores and the potential of the cell drops at resting condition due to the charge redistribution in the pores (**Fig. 12C**).

The charge redistribution can also be caused by Faradaic reactions of the electrode material like, for instance, RuO₂. Conway et al. reported that the oxidation state of a RuO₂ electrode is non-uniform during the charging process and when the electrode is resting, the oxidation state of the electrode redistributes to reach the uniform state in the bulk electrode.[115] As a result of this redistribution process, the potential decays in the resting period after the charging process.

Initially discussed by Conway et al. and Black et al.,[107, 116] the potential profile by charge redistribution was reported to follow a linear relation with respect to $\log(t)$. Later, Kowal et al. reported that the potential decay of commercially available supercapacitors fits better by two exponential terms with two time constants.[129] However, adopting a suitable mathematical representation of the voltage decay for the charge redistribution is challenging due to the presence and concurrence of other self-discharge mechanisms in the system. The process of charge redistribution can be identified from its strong

dependency on the applied current and the voltage holding time (**Fig. 13A**); in contrast, the other self-discharge mechanisms do not show these dependencies.[116] Additionally, the charge redistribution mechanisms can be identified by the potential recovery after discharging of the cell (**Fig. 13B**). These intrinsic features of charge redistribution are critical for the investigation of a system containing more than one potential decay mechanism. For example, a sufficiently extended voltage holding time can exclude the contribution of charge redistribution.

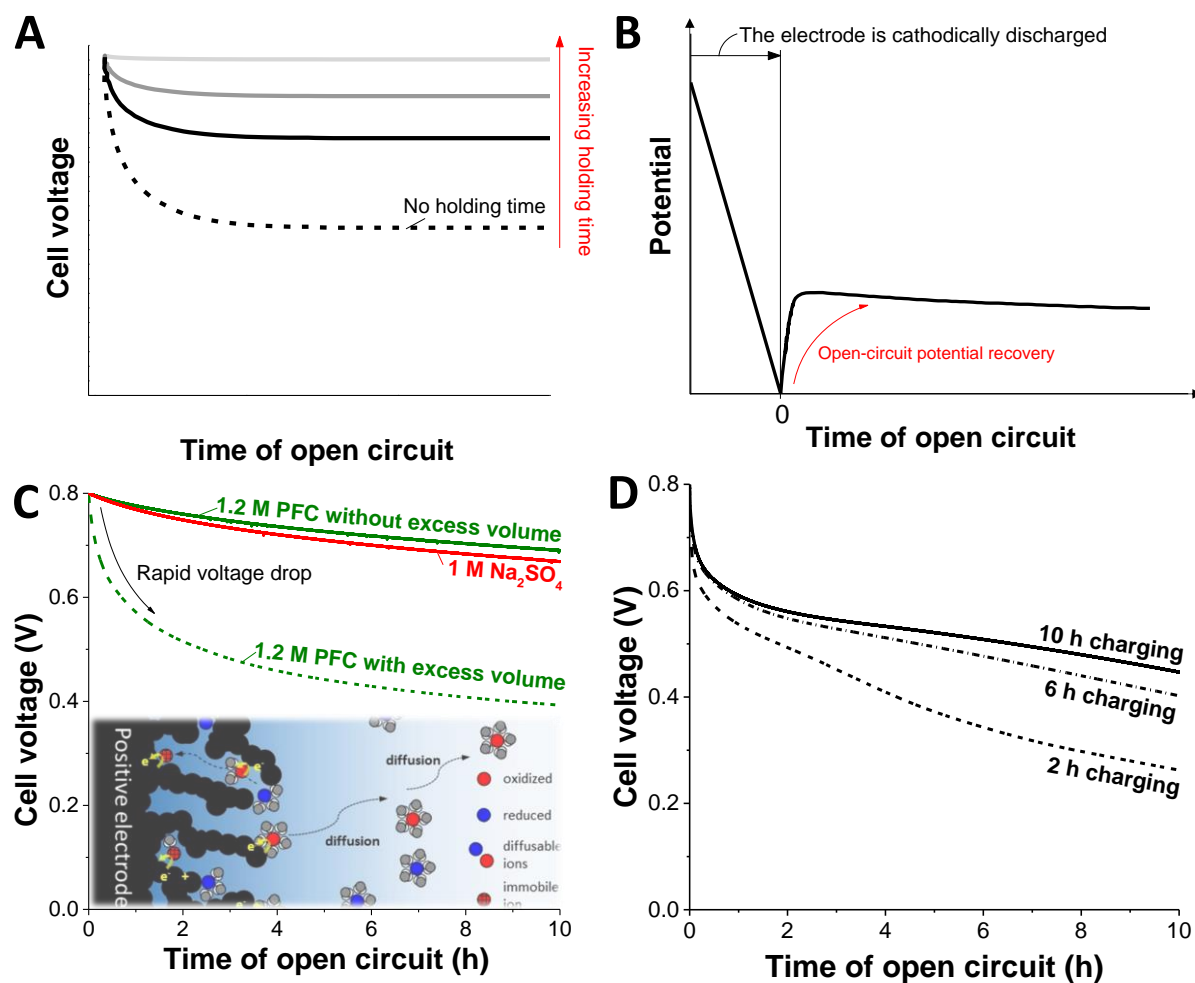


Figure 13 Open-circuit potential during charge redistribution. (A) The charge redistribution is strongly dependent on the charging history. (B) Slow potential recovery after discharging the system is a unique feature of the charge redistribution. The diffusion-limited charge redistribution throughout the redox electrolyte in REHES systems (C) which depends on the charging time (D). Adapted with the permission from Ref. [38]. Copyright (2017) American Chemical Society.

In case of REHES systems, a similar potential decay behavior can be observed while the charge redistribution occurs not at the electrode/electrolyte interface but mainly in the bulk electrolyte solution. As our work demonstrated for potassium ferricyanide (1.2 M) in a symmetric AC|AC cell configuration,[38] a rapid cell voltage drop occurs over a period of hours (**Fig. 13C**). This voltage drop does not originate from redox shuttling since the diffusion of ferricyanide from the negative electrode to the positive electrode is effectively hindered by a cation exchange membrane. The substantial reduction in voltage arises from the incomplete oxidation of ferrocyanide due to the diffusion limit from the bulk electrolyte to the electrode during charging. After charging, the oxidized ferricyanide ions are diffusing from the electrode to the bulk electrolyte (**Fig. 13C, schematic illustration**). Thereby, the state-of-charge in the electrolyte is redistributed, and therefore the cell voltage decays, particularly, when being charged in a short period (**Fig. 13D**).

For minimizing the effect of the diffusion-limited charge redistribution, the cell can be charged either by potential holding for a longer time or by a lower current. However, these approaches are not practical for actual applications because they require a longer charging time for a device. Considering that the level of redistribution decreases when the size of the bulk electrolyte volume is reduced (**Fig 13C**), confining the electrolyte only in the narrow carbon pores can be a more realistic solution. Otherwise, adsorption of redox ions can be considered as an alternative. By assuming porous carbon as a flat electrode, a simple mathematical model can be applied to describe this potential decay phenomenon by combining the Nernst equation and solving Fick's equation. Yet, a more appropriate model should be developed reflecting the porous feature of the electrode for an adequate description of the process.

The models introduced for the self-discharge and the potential decay behavior have mostly been developed for supercapacitors.[106, 116, 120] Since many REHES systems do not behave like a capacitor in a strict sense, Equation (10), (12), and (15) are not preferred because they assume constant capacitance. Theoretical calculations for the electrochemical and diffusion behavior of the redox species in porous electrodes are complex.[120] Therefore, the interpretation of self-discharge and potential decay of REHES systems should be carefully approached with the conventional models. Nonetheless, these models are of great help, particularly when combined with the use of other analytical tools.

When a REHES system suffers from redox shuttling, the leakage current starts to dominate as soon as the redox potential is reached at the electrode (**Fig. 11A**). Hence, the potential profile for highly concentrated REHES systems at low current density looks like that of activation-controlled self-discharge (**Fig. 12B**) despite its diffusion-controlled feature. Therefore, complementary analyses are necessary for the adequate interpretation of self-discharge mechanisms while investigating the system in the range of cell voltage where redox reaction occurs. Our previous work examined the redox shuttling behavior by comparing the potential profile in a resting condition with other electrochemical analyses such as EIS and CV techniques.[38] When a system suffers from severe self-discharge caused by redox shuttling, a distorted cyclic voltammogram is obtained (**Fig. 14A**, AC|AC with potassium ferricyanide, PFC). In contrast, when suppressing the redox shuttling, a cell with a CEM exhibits a rectangular current response outside of the redox potential window of PFC (e.g., 0.5-0.8 V). In this case, the sign of the current changes from positive to negative when the direction of the cell polarization changes from positive to negative. This indicates that the current is consumed during charging and restored during subsequent discharging. In contrast, because of high self-discharge current, the cell without CEM shows no change in the sign of the current even though the scan direction is reversed. Therefore, the level of offset current (**Fig. 14A**) can be assigned to redox shuttling.

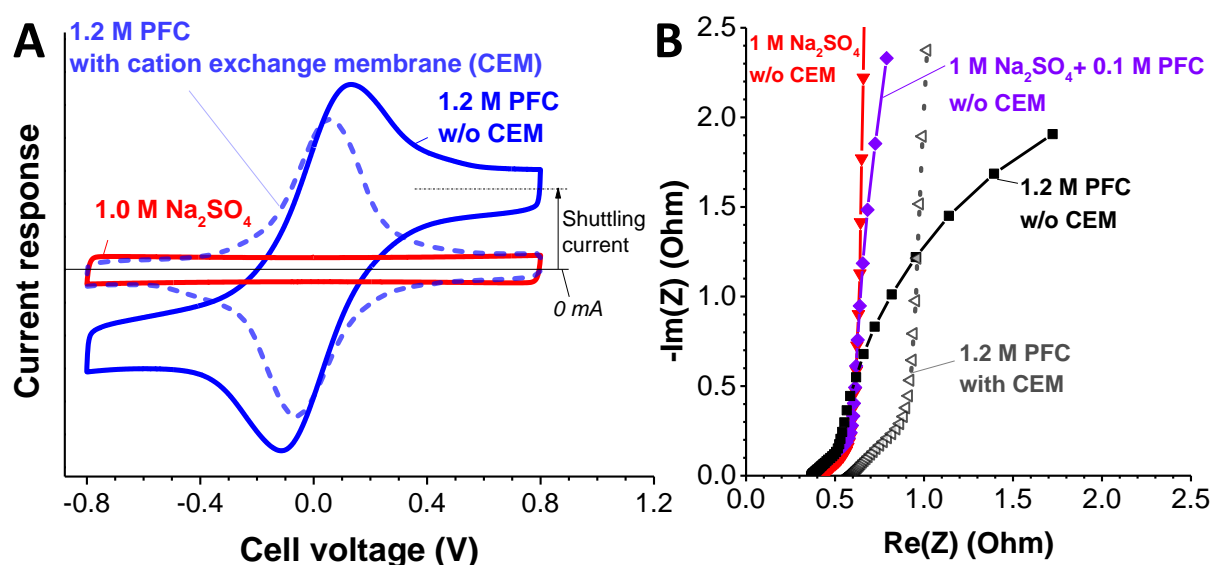


Figure 14 New characterization methods for the investigation of the self-discharge rate by redox shuttling in REHES systems. The cyclic voltammogram (A) and Nyquist plot (B) indicate significant redox shuttling. Adapted with permission from Ref. [38]. Copyright (2017) American Chemical Society.

The redox shuttling can also be identified in a Nyquist plot (**Fig. 14B**, measured at 0 V with a potential amplitude of 5 mV). In general, EDLCs exhibit a regime with a slope close to 90° which originates from the capacitive component in the system: for example, a symmetric AC|AC cell in 1 M Na₂SO₄ (**Fig. 14B**). In case a low concentrated PFC solution (1 M Na₂SO₄+0.1 M PFC), a slight bend occurs, leading to a deviation from a straight line (with a slope close to 90°) of the EDLC. At high concentration (1.2 M PFC), the cell without CEM exhibits a much clearer bending. In contrast, the same cell with CEM shows no sign of a bending in the curve. Considering that the presence of CEM significantly suppresses the redox shuttling, the bending at low-frequency regime (where 90° slope appears for EDLCs) can be an indication of the redox shuttling. The possible origin of the bending can be the resistive component of a chemical short-circuit through redox shuttling because the curve bends toward the phase angle of resistive impedance (0°).

1.5.2. Redox kinetics and mass transport for redox electrolyte systems

As reported in previous work,[38, 40] REHES systems provide not only enhanced energy storage capacity but may also excel in power handling. For the understanding of the enhanced power performance, the thin-layer electrochemistry (TLE) is an excellent theoretical basis. The development of the theories for TLE was initiated by Anson[110] and Hubbard[109] in the 1960s in support to their experimental work with a confined thin-layer electrolyte (40-140 μm) on a flat electrode. In general case of cyclic voltammetry, the redox peak current, i_p , is governed by the Randles-Ševčík equations; Equation (18) for reversible processes and Equation (19) for irreversible processes:[130-132]

$$I_{p,rev} = \pm 0.446nFAc \sqrt{\left(\frac{nFDv}{RT}\right)} \quad \text{Equation (18)}$$

$$I_{p,irr} = \pm 0.496nFAc \sqrt{\left(\frac{\alpha n_0 FDv}{RT}\right)} \quad \text{Equation (19)}$$

In these equations, the plus-minus symbol indicates anodic or cathodic current, respectively, A is the geometric area of the electrode in cm², c is the concentration in mol/cm³, v is the scan rate in V/s, n_0 is the number of electrons transferred before the rate determining step. The Randles-Ševčík theory is based on the model that the

electrochemical reaction is not only controlled by the charge transfer kinetic near the electrode surface (ca. 1 nm), but also by the mass transport in the diffusion layer. **Fig. 15A** depicts the schematic representation of molecular arrangements at the interface between electrode and electrolyte which consists of i) a compact layer with Inner Helmholtz layer (IHP) and outer Helmholtz layer (OHP), ii) Gouy-Chapman diffuse layer, and iii) diffusion layer.[130] According to the model by Hubbard and Hubbard & Anson,[108, 109] the redox peak current for reversible ($I_{p,rev}$) and irreversible processes ($I_{p,irr}$) can be described by the following equation when the diffusion layer thickness is reduced (40 μm).

$$I_{p,rev} = \pm 0.250nFU_t c \left(\frac{nFv}{RT} \right) \quad \text{Equation (20)}$$

$$I_{p,irr} = \pm 0.368nFU_t c \left(\frac{\alpha n_0 Fv}{RT} \right) \quad \text{Equation (21)}$$

where U_t is the volume of the thin layer in cm^3 .

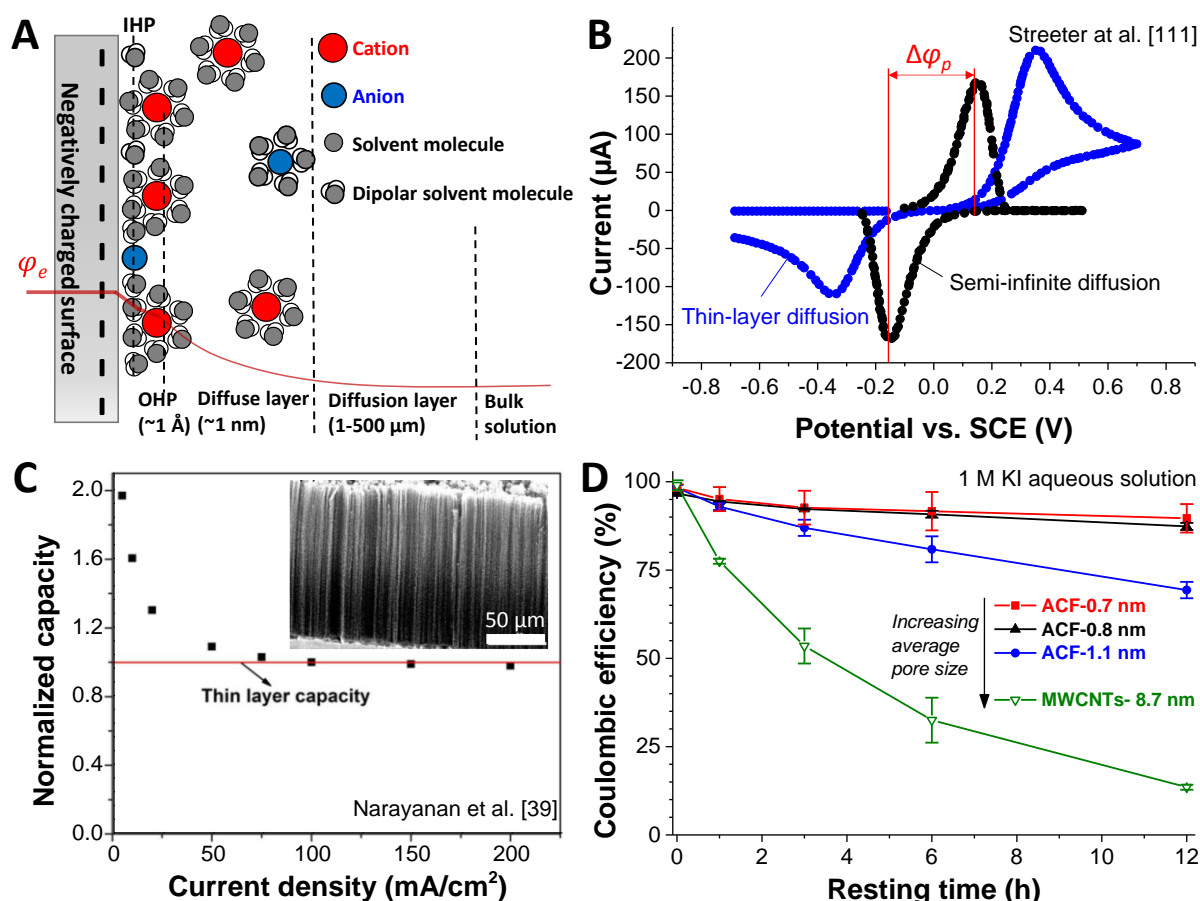


Figure. 15 (A) Schematic illustration of the molecular arrangements and the diffusion in the case of a flat electrode. (B) Simulation work based on the model with the thin-layer electrochemistry from Ref. [111], (C) Identification of the thin-layer capacity with vertically aligned carbon nanotubes. Inset shows the scanning electron micrograph of the vertically aligned carbon nanotubes. Republished with permission of Electrochemical Society, from Ref. [39], Copyright (2017); permission conveyed through Copyright Clearance Center, Inc. (D) Self-discharge rate is different in case of redox ion adsorption which depends on the carbon pore size. Adapted from Ref. [40] with permission from The Royal Society of Chemistry.

It is important to note that the peak current is not a function of the square root of the scan rate, \sqrt{v} , but a linear function of v . This has often been observed in recent papers for the high power performing redox enhanced energy storage systems.[38, 133] After the TLE theories were established, further developments have been made by Compton's group with numerical simulations.[111, 112, 114] Their simulation works indicate that the electrochemical analysis regarding the charge transfer kinetics should be carefully carried out with cyclic voltammetry. As presented in **Fig. 15B**, the peak-to-peak separation, $\Delta\phi_p$, was simulated by semi-infinite diffusion and thin-layer diffusion model applying the same value of the heterogeneous rate constant. The results imply that the smaller $\Delta\phi_p$ value for the electrode modified with the carbon nanotube array should not be interpreted as electrocatalysis by enhanced electron transfer kinetics. Instead, it should be understood as the intrinsic feature of TLE formed in the confined space of the electrode. The TLE simulation has been further extended for cylinder arrays[112] and cylindrical pores[114].

Most of the theoretical works have been developed to investigate fundamental aspects. In extension, recent studies by Narayanan et al.[39] applied TLE theory to energy storage aspects for vertically aligned carbon nanotubes (**Fig. 15C, inset**) with a spacing between nanotubes of around 350 nm (macropore range). They concluded that the enhanced electrochemical reaction is based on the relative absence of diffusion as the electrolyte is confined to thin layers on the carbon nanotubes. The uniqueness of their work is that the individual redox charge storage capacity by a thin layer (or thin-layer capacity) and by diffusion contribution was experimentally determined. They assumed that the redox charge storage capacity through diffusion disappears and the thin-layer capacity predominates at high galvanostatic currents (**Fig. 15C**). The redox kinetics in carbon micropores were further investigated in our team with potassium ferricyanide[40] by comparing the reduction peak currents in cyclic voltammograms. We observed a thin-layer behavior in the case of microporous carbon, while diffusion-controlled redox kinetic was found for the flat glassy carbon electrode. Our work implies that the electrochemical analysis by peak current versus scan rate for microporous carbons should be carried out carefully since the contribution of double-layer current is not negligible. The peak current is the contribution of i) double-layer formation, i_{EDL} , ii) diffusion-limited redox current, i_{Diff} , and iii) redox current under TLE condition, i_{TLE} .

$$i_p = i_{EDL} + i_{Diff} + i_{TLE} \quad \text{Equation (22)}$$

In the presence of a significant electrical double-layer current, plotting the peak current against the scan rate may lead to an incorrect data interpretation. Hence, the electrical

double-layer current should be quantified and be subtracted or limited by modifying, if possible, the experimental condition. An alternative is a kinetic analysis with rotating disk electrode at a fixed scan rate by varying the diffusion condition by rotating the electrode. Thereby, the electrical double-layer contribution will be constant at fixed scan rate while kinetics of the redox species can be studied at various rotating speeds.[40]

However, there are further aspects that need to be considered. As reported by Chathoth et al.,[134] the diffusion coefficients of ionic liquids are higher in confined carbon mesopores than in a bulk liquid. On the contrary, lower diffusion coefficients in porous carbon for biredox ionic liquids were suggested by Mourad et al.[135] Whether the diffusion of the ions is faster or slower in the confined carbon pores, we see that the diffusion coefficients might not be constant for the pores with different shapes, sizes, and functional groups. For the TLE theories and models, the diffusion coefficients were assumed to be constant. Another difficulty is to distinguish the thin-layer diffusion from the adsorption effects since the electrochemical reaction with adsorbed species shows a similar mass transport feature with the TLE condition.[112] For instance, the peak current of a reversible process can be described by introducing the surface covered adsorbed species:[130]

$$I_{p,ads} = \pm 0.250nF\Gamma A \left(\frac{nFv}{RT} \right) \quad \text{Equation (23)}$$

where Γ is the fractional surface coverage. The similarity between Equation (20) and (23) can be seen; particularly, the peak current is a linear function of v .

As demonstrated by our work (**Fig. 15D**, ACF in 1 M KI aqueous solution),[40] the iodide diffusion and adsorption behavior is closely related to the size of the carbon pores. We found that iodide shows stronger adsorption in smaller pores and weaker adsorption in bigger pores leading to the faster diffusion behavior. The latter causes higher self-discharge rates by redox shuttling. Furthermore, the concentration of the ions in the carbon pores is expected to be different as the diffusion layer can be overlapped.[136] This unique aspect is neither reflected by recent theory nor simulation work. New theories and simulations are necessary considering the influence of pore size and functional groups on the adsorption energy, diffusion coefficients, and local concentrations. Thereby, the understanding of the redox kinetics and ion diffusion in porous carbon electrodes can be advanced including further performance improvement of the REHES systems.

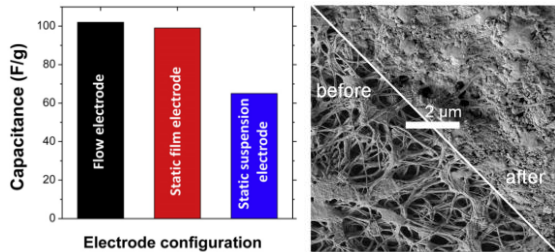
2. Approach and overview

As introduced in the previous chapter, the REHES systems have emerged as a promising new generation of energy storage systems. In this PhD work, the aqueous REHES systems with tetrapropylammonium iodide, potassium ferricyanide, potassium iodide, vanadyl and tin sulfate, tin fluoride, and zinc iodide have been investigated. The focus of the work was set on the enhancement of device performance by design of redox electrochemistry and material optimization as well as the fundamental understandings of diffusion, electrochemical kinetics, and adsorption of redox ions.

The first part of the PhD work was dedicated to understanding the basics of EDLCs and flow electrode capacitors (**Fig. 16, Chapter 3.1**).[31, 34] The latter show critical technical issues such as clogging and membrane contaminations as well as intrinsically high electric resistance by poor particle-particle contact resistance. The primary disadvantage of the EDLC was found to be the low specific energy. Even when an iodide-containing redox active surfactant (tetrapropylammonium iodide) was used in the non-flow EDLC, only a minor capacity enhancement was observed due to its low concentration (5 mM). Hence, for the second part of the work (**Fig. 16, Chapter 3.2**), an intense Faradaic reaction was introduced to the conventional EDLC cell configuration by applying a highly concentrated (1.2 M) potassium ferricyanide redox electrolyte. Thereby, the intrinsically low charge storage capacity of the EDLC was significantly enhanced through the intense reaction of soluble ferrocyanide/ferricyanide redox couple.[38] However, the redox shuttling of ferrocyanide/ferricyanide couple was found to cause a high self-discharge rate. As a solution, the porous separator was replaced with a cation exchange membrane which effectively suppressed the redox shuttling. Nonetheless, the cell still suffered from the initial rapid voltage loss in the resting condition, particularly, after fast charging process. The reason for this phenomenon was the diffusion-controlled potential loss through the charge redistribution of redox ions in the electrolyte which was prevented by confining the electrolyte mostly to the carbon microporous. Additionally, the origin of the high power performance of the ferrocyanide/ferricyanide based REHES systems was investigated. By applying the Randles-Ševčík equation, the principle behind the high power performance was identified as the diffusion-less fast reactions of the redox ions which are confined to carbon micropores.

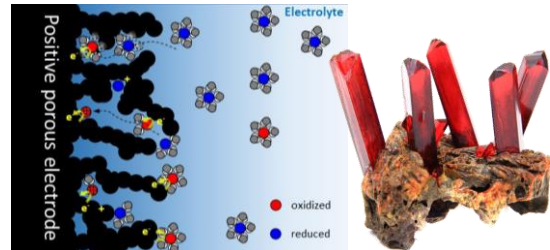
3.1 Understanding basics of flow and non-flow EDLCs and its limitations

- ▶ Low specific energy of EDLCs
- ▶ High resistance of flow EDLC due to particle-particle contact resistance
- ▶ Membrane contaminated by carbon particles



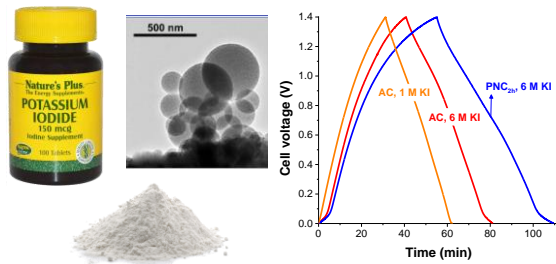
3.2 Understanding basics of REHES with potassium ferricyanide and microporous carbon

- ▶ Diffusion-controlled potential loss in resting condition by the diffusion of redox ions
- ▶ High specific energy by charge balance via reversible hydrogen storage
- ▶ High specific power due to the diffusion-less electrochemistry in carbon micropores



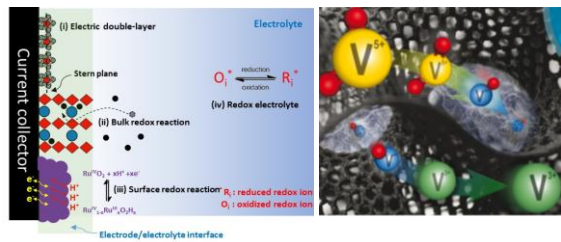
3.3 Enhanced specific energy of REHES system with potassium iodide by pore design optimization

- ▶ High concentrated KI solution increases the specific energy
- ▶ Enhancement of specific energy by the use of Novolac-derived carbon with high total pore volume with the majority of micropores
- ▶ The CO₂ activation at 1000°C for 2 h showed the optimized performance



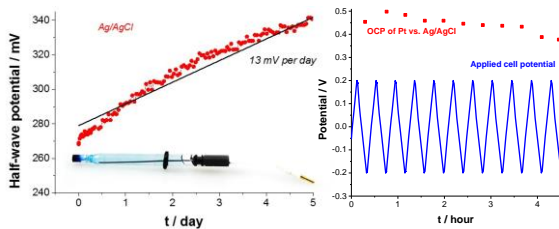
3.4-3.5 A new REHES system with the balanced charge by vanadium and tin redox activities

- ▶ Facile charge balance by the concentration adjustment between vanadium and tin
- ▶ Tin oxides reduce the pore volume at the positive electrode
- ▶ Asymmetric electrolytes prevent the tin oxides formation at the positive electrode



3.6 Porous carbon as a quasi-reference electrode for aqueous electrochemistry

- ▶ Cross contamination between the cell with redox electrolyte and the reference electrode
- ▶ Highly porous carbon with less functional groups could be applied as quasi-reference electrode
- ▶ A new testing method is introduced to investigate the potential of QREs



3.7 Nanoconfinement of iodide in carbon micropores for REHES systems with zinc negative electrode

- ▶ Strong iodide adsorption in sub-nanometer carbon pores
- ▶ Low level of self-discharge by iodide adsorption without ion selective membrane
- ▶ New analytical method with rotating disk electrode for thin-layer electrochemistry

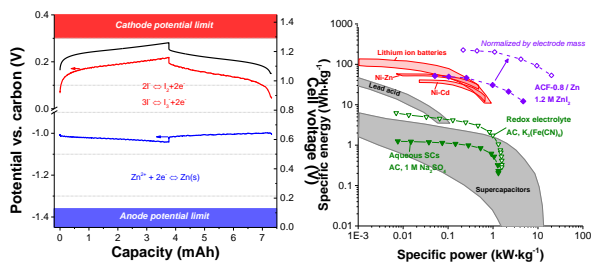


Figure 16 Approach and overview of this PhD work for the fundamental understanding and further optimization of REHES systems. (3.1) The image (left) is reprinted from Ref. [31], Copyright (2017), with permission from Elsevier. The image (right) is reproduced from Ref. [34] with permission from John Wiley and Sons. (3.2) Reprinted with permission from Ref. [38]. Copyright (2017) American Chemical Society. (3.3) Reprinted with permission from Ref. [41]. Copyright (2017) American Chemical Society. (3.4-3.5) Adapted from Ref. [12] - Published by The Royal Society of Chemistry. (3.6) Reprinted from Ref. [137], Copyright (2017), with permission from Elsevier. (3.7) Reproduced from Ref. [40] with permission from the Royal Society of Chemistry.

The third part of the work (**Fig. 16, Chapter 3.3**) is about the optimization of carbon pore structure. Accordingly, carbon beads with sub-micrometer diameter were synthesized by a self-emulsifying novolac-ethanol-water system and further activated by CO₂ gas as a part of PhD work of Benjamin Krüner (Saarland University). By varying the activation time, a high total pore volume of 1.7 cm³/g with a high level of micro-porosity was obtained at optimized activation conditions at 1000 °C for 2 h. By high specific surface area (2237 m²/g, quenched-solid density functional theory) of the optimized Novolac-derived carbon beads, the redox electrolyte based on iodide redox couples effectively enhanced the specific energy performance (33 Wh/kg, normalized by m_a), while also providing the high specific power of up to 11 kW/kg (normalized by m_a).

In case of previous studies with iodide and ferrocyanide/ferricyanide redox electrolytes, reversible hydrogen storage was critical to consider for charge balancing between positive and negative electrodes. Against the significantly enhanced charge capacity at the positive electrode, the capacity at the negative electrode can be balanced by the reversible hydrogen reaction. However, the main disadvantage of the reversible hydrogen storage is the large overpotential which leads to low energy efficiency. Hence, the fourth part of the work (**Fig. 16, Chapter 3.4**) designed a REHES system with the biredox activities of the Sn(s)/Sn²⁺ redox couple and the redox activities of the vanadium complex. The charge between positive and negative electrodes was balanced by adjusting the concentration ratio of tin and vanadium contents in the electrolyte. Since the charge storage capacity was significantly enhanced and balanced at both positive and negative electrodes by two-step vanadium redox couples and tin redox activities, respectively, a significant enhancement of the specific energy was achieved up to 75 Wh/kg (normalized by m_a).

The main drawback of the previous REHES system with tin and vanadium redox activities was relatively low power performance (1.5 kW/kg, normalized by m_a) as well as low cyclic stability (ca 4500 cycles for 80 % capacity retention). Therefore, the fifth part of the work (**Fig. 16, Chapter 3.5**) identifies the origin of low power performance and the improvement of power performance. Through material characterization and postmortem analyses, the reduction in pore volumes at the negative electrode was identified as the reason for the low power performance of the cell. Since the tin dioxide formation at the positive electrode caused this reduction in pore volume, a tin-containing solution (1 M SnF₂) was separately introduced to the negative electrode, while 3 M vanadyl sulfate was applied at the positive electrode. The use of an anion ion exchange membrane enabled the

separation of the tin cations. Thereby, the formation of tin dioxide was substantially suppressed, and the specific power was enhanced to 3.8 kW/kg (normalized by m_a) while providing still a high specific energy up to 58.4 Wh/kg (normalized by m_a).

While investigating REHES systems with the previously introduced redox electrolytes, the cross-contamination of the reference electrode was found to be a challenging issue, particularly, for the long-term measurements. For that reason, the sixth part of the work (**Fig. 16, Chapter 3.6**) establishes a suitable quasi-reference electrode (QRE) for aqueous systems. Highly porous carbons with a low level of functional groups were found to be sufficiently stable (potential shift <1 mV/day with the reproducible potential of ± 10 mV). Also, a new analytical method was introduced to measure the potential of the QREs since the implementation of the conventional internal reference such as ferricyanide/ferrocyanide couple could influence the redox potential of the QREs.

With the aid of carbon QRE, the last part of the work (**Fig. 16, Chapter 3.7**) explored the highly promising ZnI_2 redox electrolyte. The focus of this work was the design of a REHES system without the use of ion selective membranes which leads to a significant cost increase of the entire system. Without any ion selective membrane, the confinement of adsorbed iodide in carbon micropores (<1 nm) greatly suppressed the redox shuttling of iodide. The strong redox activity of the iodide at the positive electrode (activated carbon fiber) was effectively coupled with $\text{Zn(s)}/\text{Zn}^{2+}$ redox couple at the negative electrode (zinc foil). As a result, the specific energy of 226 Wh/kg (normalized by m_a) was achieved while providing high specific power up to 20 kW/kg (normalized by m_a). Additionally, the origin of high power performance had been thoroughly investigated by rotating disk electrode. The diffusion-less fast redox reaction by the adsorbed iodide at the confined space of the carbon micropores was found to be the major contribution of high power performance.

3. Results and discussions

3.1 Use of surfactants for continuous operation of aqueous electrochemical flow Capacitors

3.2 High performance hybrid energy storage with potassium ferricyanide redox electrolyte

3.3 Sub-micrometer novolac-derived carbon beads for high performance supercapacitors and redox electrolyte energy storage

3.4 Tin/vanadium redox electrolyte for battery-like energy storage capacity combined with supercapacitor-like power handling

3.5 Asymmetric tin-vanadium redox electrolyte for hybrid energy storage with nanoporous carbon electrodes

3.6 Porous carbon as a quasi-reference electrode in aqueous electrolytes

3.7 Nanoconfinement of redox reactions enables rapid zinc iodide energy storage with high efficiency

3.1. Use of surfactants for continuous operation of aqueous electrochemical flow capacitors

Juhan Lee,^{1,2} Daniel Weingarth,¹ Ingrid Grobelsek,¹ and Volker Presser^{1,2}

¹ INM - Leibniz Institute for New Materials, Campus D2 2, 66123 Saarbrücken, Germany

² Saarland University, Campus D2 2, 66123 Saarbrücken, Germany

Citation:

Lee, J.; Weingarth, D.; Grobelsek, I.; Presser, V., Use of surfactants for continuous operation of aqueous electrochemical flow capacitors. *Energy Technology* **2016**, 4 (1), 75-84.

Own contributions:

Design, planning, writing, cell design, experimental setup, viscosity measurements, electrochemical analyses, and optical microscopy

Abstract

The electrochemical flow capacitor (EFC) is a novel design for supercapacitor technologies. To avoid misinterpretation arising from non-flow analytical methods, we have investigated an EFC system under continuous flow conditions. Several different surfactants were introduced as modifiers to activated carbon in an aqueous electrolyte with sodium sulfate (Na₂SO₄). A significant reduction in viscosity was found by adding sodium lignosulfonate, and as a consequence, a maximum volumetric capacitance of 26 F/cm³ was achieved for the EFC system. A steady performance of the EFC system was observed for 200 h in terms of specific capacitance (90±5 F/g); however, degradation in the power performance was observed. Membrane fouling was confirmed to be the major contribution to the power degradation, and a cleaning process using water was developed to partially restore the initial performance (~70 %).



Use of Surfactants for Continuous Operation of Aqueous Electrochemical Flow Capacitors

Juhan Lee,^[a, b] Daniel Weingarth,^[b] Ingrid Grobelsek,^[b] and Volker Presser*^[a, b]

The electrochemical flow capacitor (EFC) is a novel design for supercapacitor technologies. To avoid misinterpretation arising from non-flow analytical methods, we have investigated an EFC system under continuous flow conditions. Several different surfactants were introduced as modifiers to activated carbon in an aqueous electrolyte with sodium sulfate (Na_2SO_4). A significant reduction in viscosity was found by adding sodium lignosulfonate, and as a consequence, a maxi-

mum volumetric capacitance of 26 F cm^{-3} was achieved for the EFC system. A steady performance of the EFC system was observed for 200 h in terms of the specific capacitance ($90 \pm 5 \text{ F g}^{-1}$); however, degradation in the power performance was observed. Membrane fouling was confirmed to be the major contributor to the power degradation, and a cleaning process using water was developed to partially restore the initial performance ($\approx 70\%$).

Introduction

Efficient, scalable energy storage systems have become a technological bottleneck for the utilization of common renewable energy sources such as solar and wind energy, considering their intermittent nature.^[1] Electrochemical energy storage (EES) systems, such as batteries, are particularly attractive because they are dynamically scalable to meet certain local requirements. Electrical double-layer capacitors (EDLCs, also known as supercapacitors) have particular advantages exhibiting 10–100 times greater power density than that of batteries and extended long cycle lives ($> 100\,000$ cycles).^[2] However, the typical energy densities of supercapacitors are only approximately $5\text{--}8 \text{ Wh kg}^{-1}$ which is notably lower than that of Li-ion batteries, for instance (180 Wh kg^{-1}).^[3] Therefore, current research activities are dedicated to increasing the cell energy (E) density by either boosting the capacitance ($E \sim C$) or by increasing the maximum stable cell voltage ($E \sim V^2$).

Recently, we have introduced the so-called electrochemical flow capacitor (EFC) as a new concept to provide flexible scalability of the energy and power performance, while potentially maintaining a long cycle lifetime.^[4] Instead of using static film electrodes, as known from conventional supercapacitors, an EFC system utilizes a flowable carbon suspension (Figure 1A). The EFC technology finds itself in the long tradition of flow electrode research, dating back almost one hundred years,^[5] with especially noteworthy contributions of Bertel Kastening^[6] and Ora Kedem.^[7] By virtue of a semisolid energy-storage material, the energy capacity of the system can be scaled by adjusting the size of the suspension reservoirs, and the power handling will scale with the geometry and total number of electrochemical charge/discharge cells. Therefore, the EFC concept is expected to bring benefits for reducing the material cost for the insulating and outer housing. On a system level, EFC systems operate similar to semisolid lithium flow batteries (SLFB);^[8] however,

these technologies employ different charge storage and recovery mechanisms. EFC systems rely on electric double-layer (EDL) formation as an essential energy storage mechanism whereas SLFBs rely on reversible Faradaic reactions.

The operation of an EFC can be fully continuous^[9] as schematically depicted in Figure 1B. As the carbon suspension enters the cell consisting of two flow channels partitioned by a separator (Figure 1A), the carbon particles become charged as a certain voltage is applied to the current collectors. Charge storage is accomplished by ion electrosorption at the surface of such charged carbon particles. The dynamic movement of the particles allows further propagation of the charge carriers through random contacts of the particles; and therefore, EDL charge storage is possible even in particles distant to the current collectors.^[10] The net charge neutrality of the electrolyte is balanced as an ion-permeable separator permits ion exchange between two compartments, either by using a porous separator or an ion-exchange membrane.

So far, most EFC studies have focused on studying electrochemical properties and exploring promising approaches to

[a] J. Lee, Prof. Dr. V. Presser
Department of Materials Science and Engineering
Saarland University
Campus D2 2
66123 Saarbrücken (Germany)
E-mail: volker.presser@leibniz-inm.de

[b] J. Lee, Dr. D. Weingarth, Dr.-Ing. I. Grobelsek, Prof. Dr. V. Presser
INM - Leibniz Institute for New Materials
Campus D2 2
66123 Saarbrücken (Germany)

Supporting information for this article is available on the WWW under <http://dx.doi.org/10.1002/ente.201500243>.

This publication is part of a Special Issue on the "Energy, Science & Technology" conference in Karlsruhe, Germany. To view the complete issue visit:

<http://dx.doi.org/10.1002/ente.v4.1>

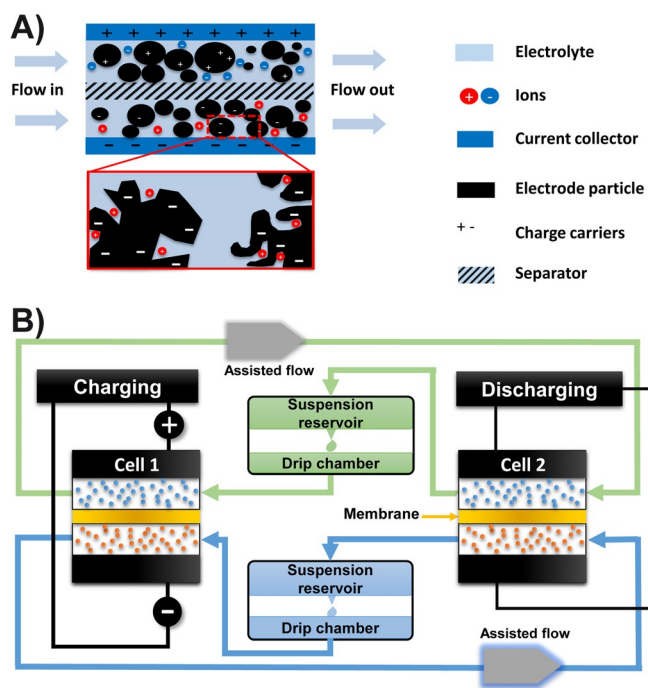


Figure 1. (A) Schematic description of double layer formation inside of an electrochemical flow capacitor. (B) Schematic depiction of a full EFC system for continuous operation.

improve the energy storage capacity.^[11–14] The increased specific capacitance was reported as the surface area of the carbon sphere was increased by activation at high temperature.^[13] Significantly improved energy ratings were reported upon adding redox agents, such as hydroquinone^[15] or *p*-phenylenediamine,^[16] known from pseudocapacitors.^[17,18] These results were very promising, but so far it remains unclear how redox additives or an increased pore volume may impact on the overall and long-term rheological behavior.

A key challenge to advance the EFC technology is to simultaneously optimize both the electrochemical and rheological flow electrode properties. Particularly sedimentation, aggregation, and viscosity are of great importance also for the total pumping energy needed for system operation and this impacts the maintenance cost. A major obstacle is that although some parameters may positively impact the electrochemical properties, they are rather detrimental to the rheological properties. For instance, a high carbon mass loading enables high volumetric energy density of the suspension, but also leads to increased viscosity and higher energy consumption for pumping (or even clogging).^[19] From the point of view of maximizing the energy density, a very high mass loading with carbon particles is desirable; yet, a low viscosity, as found for low carbon concentrations, benefits from a low pumping energy and helps to maximize the system energy efficiency.^[20,21] In consequence, strategies to lower the flow electrode viscosity are of high interest, for example by adding surfactants.

With the virtue of amphiphilic molecular structures, surfactants can be grafted or adsorbed on the particle surface to effectively reduce the interfacial tension between the particles

and the solvent, and therefore, possibly lead to a capacitance enhancement through improved wettability at carbon/electrolyte interface.^[22,23] Additionally, adsorbed or grafted surfactant molecules may also act as a physical barrier to hinder the interparticle interactions (i.e., steric hindrance). Besides modifying the viscosity, functional surface groups may also benefit the electrochemical performance by facilitating additional energy storage through reversible redox reactions, such as is possible using phenylpropane groups from liginosulfonate.^[24] Thus, using surfactants to modify carbon suspensions may be promising to reduce the viscosity of the carbon suspension and to enhance the energy density at the same time. A few studies have reported a positive influence of surfactants on the electrochemical properties of supercapacitors while also reporting negative influences when the concentration of the surfactants exceeds the critical micelle concentration (CMC).^[22,23] As far as we know, no systematic studies have been published so far regarding the use of surfactants in EFC systems.

The best characterized EFC property so far is the electrochemical response of carbon flow electrodes under non-flow conditions in either aqueous or organic electrolytes. In such studies, the effect has been studied of enabling redox reactions through adding metal oxides,^[25] redox electrolytes, or adding conductive additives such as carbon black^[25] or graphene.^[26] Non-flow operation, however, may lead to over- or underestimation of the actual EFC system performance, especially when we consider the possible sedimentation of micrometer-sized carbon particles.^[9] Particularly, the power performance in EFC system may easily be overestimated under non-flow conditions when the system resistance is measured after the sedimentation of the carbon particles.

As demonstrated by Mengying Li et al.,^[12] using volume-averaging theory for porous electrodes and the Gouy–Chapman–Stern model for the electrical double-layer, non-capacitive charging/discharging behavior can be expected when an EFC system is characterized under static conditions. In other words, the charge accumulated near the current collector surface may not correlate linearly with the cell voltage under static conditions because the state-of-charge has a non-linear gradient in space and changes over time.^[10] Consequently, seemingly non-capacitive (i.e., non-linear) charging/discharging curves can be observed when using galvanostatic cycling.^[9] However, a linear, and thus, capacitive behavior can be observed after the particles have settled.^[9] Therefore, the resistance values measured by galvanostatic cycling under non-flow conditions may not adequately represent the actual performance of a continuously operating EFC system. This can be further supported upon comparing a very low system resistance (0.35–1.5 Ω) in a non-flow configuration with values in the range of 35–75 Ω for semi-continuous operation,^[10] or with 26 Ω during fully continuous operation, even though the investigated electrochemical cells were of similar size.^[13,25]

Herein, we investigate the electrochemical properties of an EFC system including a 200 h stability test. To avoid particle sedimentation and non-capacitive behavior under non-

flow conditions, all measurements were performed in the continuous flow operation of the EFC system as described in Ref. [9]. Our study investigates several surfactants to optimize the electrochemical and the rheological properties of carbon suspensions. Additionally, measurements using a conventional film electrode configuration were employed to complement the electrochemical characterization of the investigated carbon material as well as the surfactants. We also provide data on the so-called self-discharge (voltage loss) and compare data for the EFC with a conventional film electrode of the same material. Finally, we report on the issue of power degeneration over time.

Results and Discussion

Rheological properties of surfactant-modified flow electrodes

The rheological behavior of carbon flow electrodes is characterized by shear thinning.^[19,20] As shown in Figure 2A, the apparent viscosity of 20 wt% carbon suspension decreases with increasing shear rate for all samples, and significant differences can be observed for different types of surfactants. This effect is exemplified in Figure 2A at a constant concentration of 20 mM for sodium lignosulfonate (SLS, anionic), tetrapropylammonium iodide (TPAI, cationic), a 50:50 mixture of SLS and TPAI (T5S5), and (ferrocenylmethyl) dodecyldimethyl-ammonium bromide (FDAB, redox active). The viscosity was also measured for octyl phenol ethoxylate

which is known as Triton X-100 (TX, non-ionic) and the viscosity behavior of TX is almost identical to that of FDAB (Figure S2, Supporting Information). A dramatic decrease in viscosity was observed for 20 mM SLS, giving the suspension an almost Newtonian feature (i.e., the viscosity is independent of the shear rate). Hydrophobic lignin groups of SLS are expected to adsorb onto hydrophobic sites on the carbon surface, whereas hydrophilic groups (e.g., acidic sulfonate and hydroxylic groups) will be oriented towards the water; thus, the initially hydrophobic carbon particles will effectively become more hydrophilic.^[27] Adsorbed SLS molecules may also exert repulsive forces between the carbon particles through steric hindrance. As SLS is an anionic surfactant, an additional electrostatic repulsion is expected as extra cations are attracted to the SLS molecules. A lower viscosity after adding SLS is in agreement with the literature on SLS-modified coal-water slurries.^[28,29]

The influence of different amounts of surfactant (ranging from 1 mM to 100 mM) was studied for a constant carbon mass loading of 20 wt% in 1 M aqueous Na₂SO₄. The corresponding viscosity profiles were measured from 10 s⁻¹ to 4000 s⁻¹ and, for better comparability, the apparent viscosities at 1000 s⁻¹ are shown in Figure 2B (the data for the shear rate of 100 s⁻¹ can be found in Supporting Information, Figure S2). In case of SLS, the lowest value of 12 MPa s was reached at a concentration of 20 mM, and no further reduction of viscosity was found for concentrations higher than 20 mM. A similar trend can be observed for T5S5, a mixture of two surfactants for which the contribution of SLS is believed to be dominating the viscosity. Thus, the optimized concentration is approximately 5 mM as no noticeable reduction in viscosity was observed at concentrations higher than 5 mM at both high (1000 s⁻¹) and low shear rates (100 s⁻¹). High molar concentration may even lead to a detrimental effect: a concentration above 1 wt% of the copolymer with sulfonate groups has been reported to increase the viscosity of a coal-water slurry, and excessive sodium-ion adsorption was suggested as a reason for reduced electrostatic repulsive forces.^[30]

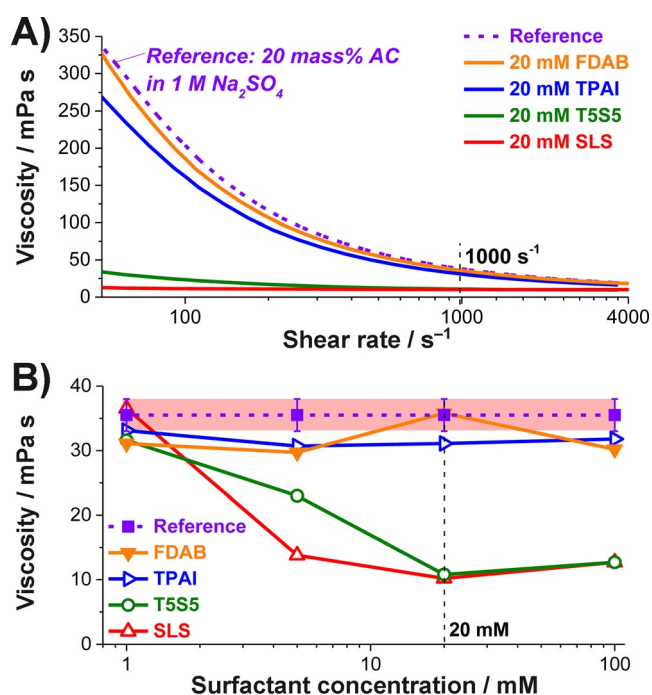


Figure 2. A) Apparent viscosity of 20 wt% carbon suspension was measured as a function of shear rate as various types of surfactants were introduced with 20 mM concentration. A dramatic reduction in viscosity was found as the carbon suspension was modified by sodium lignosulfonate. B) Apparent viscosity of the 20 wt% carbon suspension is shown as a function of surfactant concentration at shear rate 1000 s⁻¹.

Electrochemical behavior of surfactant-modified carbon film electrodes

As presented, surfactants may effectively minimize the flow electrode viscosity. Eliminating the influence of dynamic flow, we first investigated the influence of the surfactants on the electrochemical performance of the studied activated carbon by using conventional film electrodes. We deem this approach more reliable than resorting to non-flow EFC operation because we eliminate issues of particle sedimentation and will later on move directly to continuous EFC operation. From Figure 2B, it is evident that the surfactant concentration of 20 mM presents a maximum rheological improvement and onset of viscosity saturation (most probably due to micelle formation of the surfactant molecules). Therefore, we only investigated film electrode cells with the surfactant concentration in the range of 5–20 mM in the electrolyte.

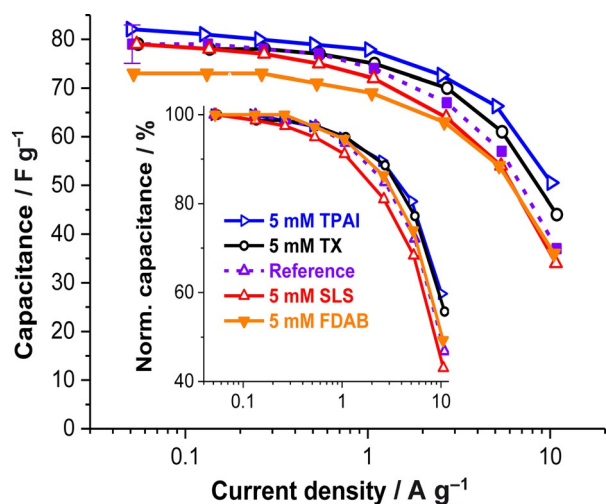


Figure 3. Specific capacitance derived from galvanostatic charge/discharge in the voltage range from 0 to 0.6 V at current density from 0.05 to 10 A g^{-1} . In the inset, the capacitance values were normalized to the maximum capacitance measured at 0.05 A g^{-1} .

In Figure 3, the specific capacitance is plotted versus the current density for data obtained from galvanostatic charging/discharging with potential limitation (GCPL); here, the data for T5S5 is not shown because the curve obtained for T5S5 showed no statistical difference in comparison to the case of 5 mM SLS, TX, TPAI, and the reference. The reference showed specific capacitance values of approximately 78 F g^{-1} from galvanostatic charging/discharging in voltage range 0–0.6 V at the low current density of 50 mA g^{-1} (Figure 3). A slightly higher specific capacitance of 81 F g^{-1} was obtained for 5 mM TPAI, which might be due to the iodide/iodine redox reaction as their redox peaks were observed in the cyclic voltammograms (Figure S3, Supporting Information); however, this value is within the statistical scatter of the method, and statistically indistinguishable from the performance of the reference. Therefore, the redox reaction observed for TPAI from cyclic voltammetry does not significantly increase the capacitance values, perhaps due to the low concentration of TPAI.

The lowest capacitance value (73 F g^{-1}) was obtained for FDAB, possibly because of micelle formation which may effectively block the entrance to the pore volume.^[22] This is supported by the optical observation of micelle formation at a molar concentration of 5 mM in $1 \text{ Na}_2\text{SO}_4$ (Figure S2, Supporting Information). In all other cases, no visible micelle formation was observed. Contrary to the reported positive influence of TPAI and TX surfactants on the rate performance of EDLCs in the 6 M KOH aqueous electrolyte,^[22,23] we have found no specific effect of the surfactants on the rate handling performance for TPAI and TX or for any of the other surfactants. In all cases, approximately 50% of the initial capacitance was lost upon transitioning to a high current density of 10 A g^{-1} .

Figure 4A shows the change of the electrochemical impedance response after cycling conditioning (i.e., cyclic voltammetry for 40 cycles in 0–0.6 V sweep range). In the initial

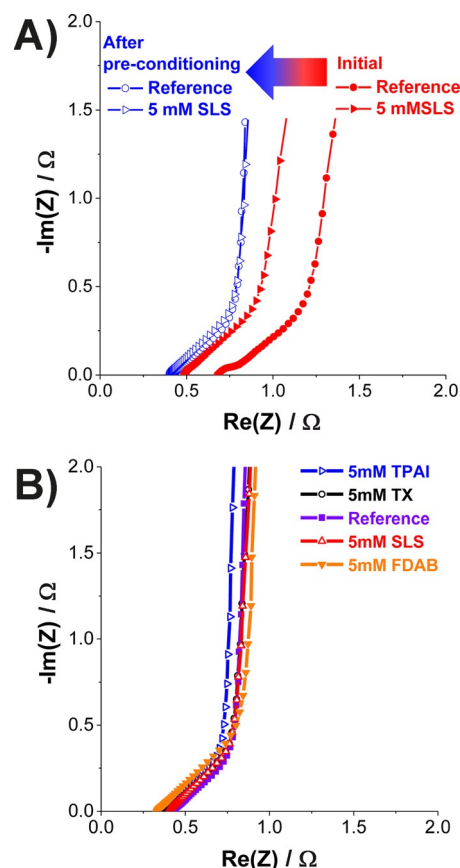


Figure 4. A) Nyquist plots obtained before and after the pre-conditioning procedure using cyclic voltammetry in the case of 5 mM SLS and the reference without surfactant. B) After applying the pre-conditioning procedure, no significant difference was found in the shape and the position of EIS curves as various surfactants were added to the Na_2SO_4 aqueous electrolyte.

state, the cell with an electrode modified by 5 mM SLS showed a lower equivalent series resistance (ESR) of approximately 0.49Ω compared to the ESR of 0.69Ω from the reference without surfactant. The improved performance may be related to enhanced wetting in the presence of SLS. After cycling, the resistance values for the system with and without surfactant modification were virtually indistinguishable, as seen from the Nyquist plot. This aligns well with the absence of differences of electrodes with and without surfactant as presented in Figure 3, which were also derived after initial cyclic voltammetry as a pre-conditioning procedure to overcome wetting-related run-in effects. After the pre-conditioning, the equivalent series resistance (ESR) at low frequency ($\approx 1 \text{ kHz}$) was measured to be $0.48 \pm 0.04 \Omega \text{ cm}^{-2}$ normalized to the membrane area (1.13 cm^2).

Due to the decomposition of water beyond 1.23 V at 25°C , the operation voltage in most aqueous supercapacitors is limited to below 1 V. Extending the operation voltage window, however, is possible by the use of pH neutral electrolytes such as Na_2SO_4 (Ref. [31]) and Li_2SO_4 (Ref. [32]), or by combining two different active materials.^[33] Recently, an extended applicable voltage window up to 1.6 V has been reported after 5 mM TX had been added to the 6 M KOH aqueous electrolyte.^[22]

To investigate the possible voltage window extension, we have applied S -value analysis^[34] with cyclic voltammetry. The stability-related S -value is defined in Equation (1)^[34]

$$S = \frac{Q_{\text{char}}}{Q_{\text{dis}}} - 1 \quad (1)$$

in which Q_{char} is the charge accumulated during charging, and Q_{dis} is the amount of charge released during discharging. The contribution to the total leakage current can be related a constant background current ($dS \cdot dV = 0$), unwanted leakage currents ($dS \cdot dV^{-1} \neq 0$, but $dS^2 \cdot dV^{-2} = 0$), and Faradaic currents ($dS^2 \cdot dV^{-2} \neq 0$). A rather exponential increase in S -value vs. maximum applied voltage plot can be interpreted as the onset of water decomposition. The S -values are practical stability indicators where the second derivate of S vs. voltage should be $< 5\%$.^[34]

In Figure 5A, S -values obtained from cyclic voltammetry for the various types of surfactants are plotted against the voltage maxima of the cycle. The characteristics of the curves can be classified into three sections: Section I from 0 to 1.2 V, Section II from 1.2 V to 1.45 V, and Section III above 1.45 V cell voltage. Section I represents the voltage window with stable performance, whereas in Section II, the thermodynamic equilibrium threshold for water stability is approached. A gradual increase of the S -value of approximate-

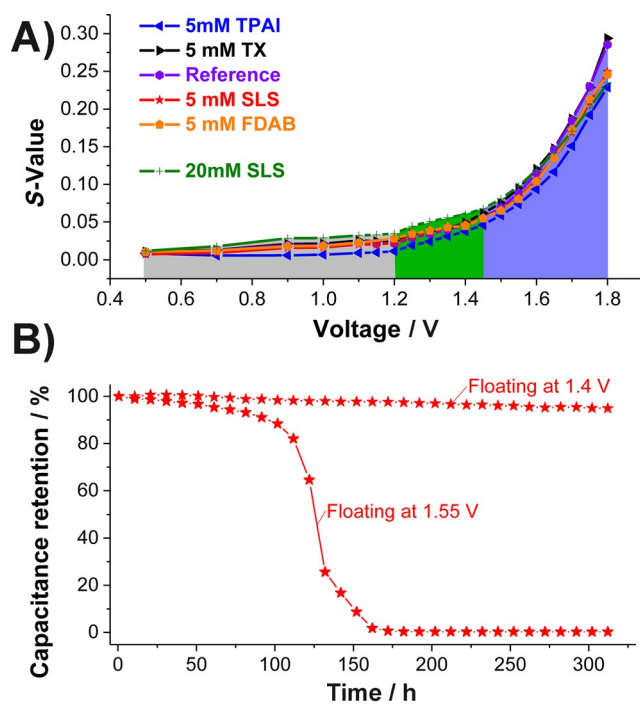


Figure 5. A) Even though no significant influence of the surfactants was observed, the S -values increase as the sweeping voltage window extends from 0.5 to 1.8 V. Three sections can be defined: Section I (gray colored) with the slope lower than 0.05, Section II (green colored) with the slope higher than 0.05 but the increase in the second derivative is lower than 5%, and Section III with higher than 5% increase in the second derivative. B) Voltage floating for 5 mM SLS: The capacitance values are obtained from the floating test at 1.4 and 1.55 V, normalized to the initial capacitance values, and plotted vs. floating time.

ly 5% is seen in this range and, as shown in Ref. [32], reversible hydrogen formation and storage is possible. The non-reversibility of the latter process is finally reached in Section III, where all samples show a very steep increase in the second derivative. No significant difference between the unmodified reference and the surfactant-functionalized electrodes is seen in Sections II and III whereas minor variations can be identified in Section I.

Stability information derived from S -value testing can be effectively complemented by data from voltage floating.^[35] This method applies a certain maximum cell voltage over an extended period of time as a highly demanding stress test in alignment with industry standards. By using voltage floating at 1.4 V (Figure 5B) a small loss ($< 10\%$) of initial capacitance appears after 300 h. In contrast, voltage floating at 1.55 V leads to a severe loss in electrochemical performance on-setting after 50 h and a complete loss of capacitive behavior after approximately 160 h.

Electrochemical behavior of surfactant-modified carbon flow electrodes under continuous EFC operation

To avoid the influence of particle sedimentation during EFC operation under static conditions,^[9] all electrochemical analyses described in the text below were performed under continuous flow operation in a closed loop circulatory system (Figure 1B). As we observed a significant viscosity reduction in the case of applying SLS to the carbon suspension, the main focus will remain on SLS-modified carbon suspensions for the characterization of the EFC system. By charging at a constant voltage of 0.6 V and discharging to 0 V, a stable cyclic performance was obtained for 200 h of non-stop operation when using a suspension with 20 wt% carbon concentration (Figure 6A).

From the chronoamperometric data, the specific capacitance and the Coulombic efficiency were derived for each cycle and plotted versus time (Figure 6B). Adding 5 mM SLS yielded no significant difference to the unmodified activated carbon flow electrode, namely, $90 \pm 3 \text{ F g}^{-1}$, and the Coulombic efficiency (Figure 6B inset) was decreased by approximately 8%. This decrease is in contrast to a very high Coulombic efficiency for 5 mM SLS when using film electrodes instead of the flowing carbon suspension. As compared to the 79 F g^{-1} capacitance value of the film electrode configuration, the initial capacitance values derived from our EFC system were approximately 14% higher. This aligns well with our recent study on continuous EFC operation in which we also reported higher specific capacitances normalized to the dry carbon mass for flow electrodes as compared to film electrodes.^[9] As no polymer binder is being used for flow electrodes, the absence of pore blocking and the more effective usable total pore volume can explain why film electrodes show a lower performance.^[36]

Figure 7 shows the initial power performance (normalized to the membrane area) measured from the EFC system as the electrolyte was modified with 5 mM SLS or 20 mM TX. A reduced power performance occurs when any surfactant is

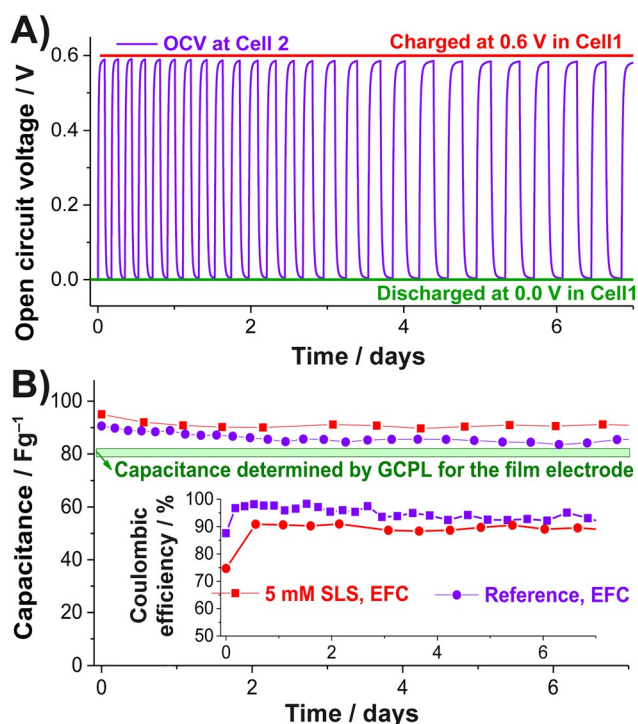


Figure 6. A) Cell voltage measured in one cell while a constant voltage was applied for charging (0.6 V) and discharging (0 V) in the other cell (see the detailed description in the Experimental Section). B) Specific capacitance derived from each cycle displayed in Figure 6A.

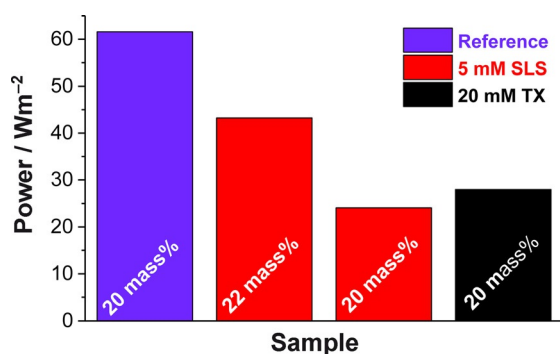


Figure 7. Power performances of the EFC system with various types of surfactants were calculated from the system resistance assuming the maximum applicable voltage of 1.2 V. The values were normalized to the actual membrane area in the flow channel.

added to the carbon suspension. An almost complete loss in power performance is observed when using 20 mM SLS whereas 20 mM TX lowered the power performance by approximately 54% compared to that of the reference (i.e., carbon without any surfactant). The increased resistance of the system by adding surfactants is likely related to the rheological behavior of the carbon suspension. An increased power performance by adding SLS with a lower concentration of 5 mM further supports the relation between viscosity and the system resistance. It is reasonable to assume that, when using surfactants, well-dispersed carbon particles have less contact to each other and/or to current collectors as

steric hindrance is considered to play an important role for charge transfer. Another important parameter to consider is the concentration of the carbon suspension, as the compactness of the particles in the suspension may be a critical factor for the charge percolation through particles. The system power was nearly doubled by increasing the carbon concentration from 20 to 22 wt% in the case of a carbon suspension with 5 mM SLS. A decreased resistance after increasing the carbon loading has also been found for flow electrodes used for capacitive deionization.^[21]

There is a large difference in system resistance between the values derived from our system in continuous flow operation and some values reported with non-flow operations, mostly measured in GCPL mode. As reported using an in situ method^[10] and mathematical modeling,^[12] the state-of-charge is expected to vary over time and the position of particles along the channel depth. Therefore, ESR characterization using GCPL mode is not practical because non-linear charge/discharge behavior (non-capacitive) is expected when the particles are well dispersed. Linearity is representative for a capacitive response and can be obtained only when the particles have fully settled. The use of electrochemical impedance spectroscopy (EIS) is complicated as long as the particles are highly and dynamically dispersed. Therefore, in situ flow investigation^[10] and using continuous flow operation^[9] are more practical measures to investigate the system resistance for EFC systems.

Self-discharge is another important performance value for electrochemical energy storage systems. In Figure 8, the cell voltage of the EFC system is plotted as a function of time (blue lines) as the system was at resting condition to investigate the voltage decay behavior; additionally, the results from the film electrode cells (red lines) are also shown for comparison. For the EFC system, the carbon suspensions were charged at constant voltage (0.6 V) until the system had reached 0.58 V. The film electrode cells were charged by GCPL with 2 h of voltage holding.

There are three general major mechanisms governing voltage decay: i) leakage currents coming from the resistive link between the positive and negative electrodes due to imper-

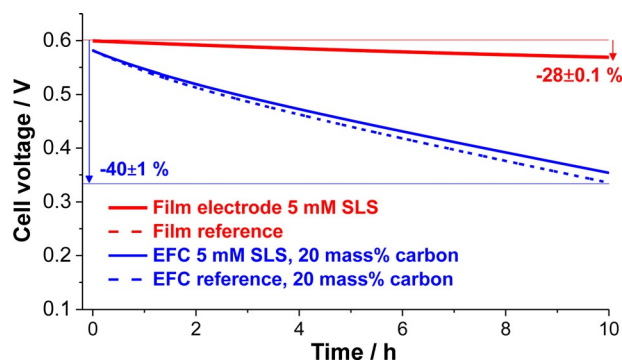


Figure 8. Cell voltage of the EFC system with 5 mM sodium lignosulfonate and the reference (without surfactant) measured as a function of resting time. The data are shown also for the film electrode with and without 5 mM SLS functionalization in comparison to the EFC system.

fections in the insulating materials,^[37] ii) leakage currents due to parasitic Faradaic reactions, and iii) voltage losses through ion-redistribution.^[38,39] An exponential decay of the cell voltage, especially leading to a large initial voltage drop, would be indicative of a dominant ion-redistribution mechanism. Yet, with a long charging duration for an EFC or film electrode setup, a more linear voltage decrease is encountered. The cell voltage of the EFC system dropped by 41 % after 10 h resting while the carbon suspension without surfactant was continuously circulating through the system. The cell voltage of the film electrode configuration dropped by approximately 28 % in the absence of surfactant. The much higher voltage decay in flow mode may be related to the much higher resistance of the EFC system. A slightly lower voltage decay can be observed in the EFC system with the addition of 5 mM SLS whereas adding SLS did not influence the voltage decay over time for the film electrodes. Contrary to our results, a significantly reduced voltage decay has been reported upon adding TX and TPAI in 6M KOH aqueous solution.^[22,23] This indicates that the influence of TX and TPAI on the voltage decay behavior may depend on the type of the electrolyte and concentration. As mentioned,^[4] the self-discharging behavior of EFC systems may be further improved by separately storing polarized carbon suspensions after charging them to reduce a possible leakage current through a separator.

Power degeneration

As shown in Figure 6A, a continuous increase in charging time was required to maintain the target cell voltage of 0.58 V. This implies an increase of the system resistance with the total operating time. As shown in Figure 9, the system resistance increases over time as exemplified for a system using 20 wt% carbon suspension without surfactant and an Omnipore (ONP) separator. A possible mechanism for this power degeneration is membrane fouling. The latter can be confirmed by electron micrographs (Figure 10A), which show obstruction of the ONP separator pores by small carbon particles after 200 h of continuous flow operation. The cross-sectional SEM images reveal that small chunks of carbon particles were deposited on the surface of the membrane, forming a thin layer with a few tens of nanometers thickness (Supporting Information, Figure S5A). Yet, the cumulative particle size distribution of the carbon suspension remains largely unchanged (Figure 10B) during 115 h of continuous operation, which shows that particle agglomeration and chipping are only of minor magnitude. The power degeneration, however, is not caused by blocked pores in the separator directly. As almost the same level of degenerated power performance was observed in the case of a non-porous anion exchange membrane (FAA-3, Fumatech), the major contribution to the cake formation (formation of a thin layer foulants) is believed to be the deposited carbon particles with sub-micrometer size onto the membrane surface. The volume fraction of sub-micrometer particles accounts for approximately 5% of the flow electrode's solid

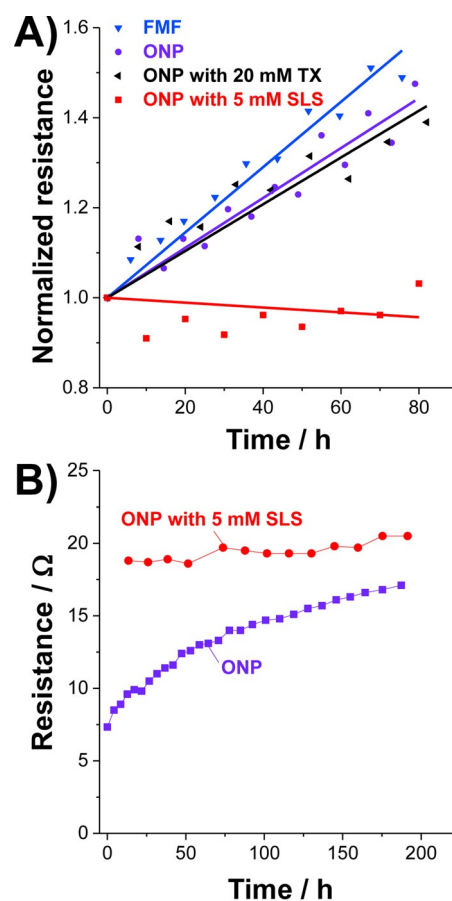


Figure 9. A) System resistance values of the EFC system using different configurations were obtained from each cycle as described in Figure 6A and plotted as a function of operation time. The values are normalized to initial resistance. B) Non-normalized resistance values obtained from 200 h operation for the carbon suspensions with and without 5 mM sodium lignosulfonate

mass, as determined by laser-aided centrifugal sedimentation analysis (Figure 10B).

As the major contribution to the degenerating power performance seems to be the cake formation on the membrane surface, a cleaning process (detailed in the Experimental Section) was introduced to the cells to remove the cake formation from the membrane. After a cleaning process was applied, the system resistance was restored to approximately 76% of the initial performance (Figure 11) for both non-porous (FAA-3) and porous (ONP) separators. Further regeneration and restoring more of the initial performance may be possible by sonication or chemical cleaning (or the combination of both).

Stable power performance was observed over 200 h as the 20 wt% carbon suspension was modified by 5 mM SLS (Figure 9A). Adding 20 mM TX showed no significant difference in normalized resistance values when comparing to the results from non-modified carbon suspensions. We found no significant difference between the SEM images from ONP separators operated for 200 h with and without 5 mM SLS modification (Figure S5, Supporting Information). An accelerated cake formation caused by 5 mM SLS is supported by

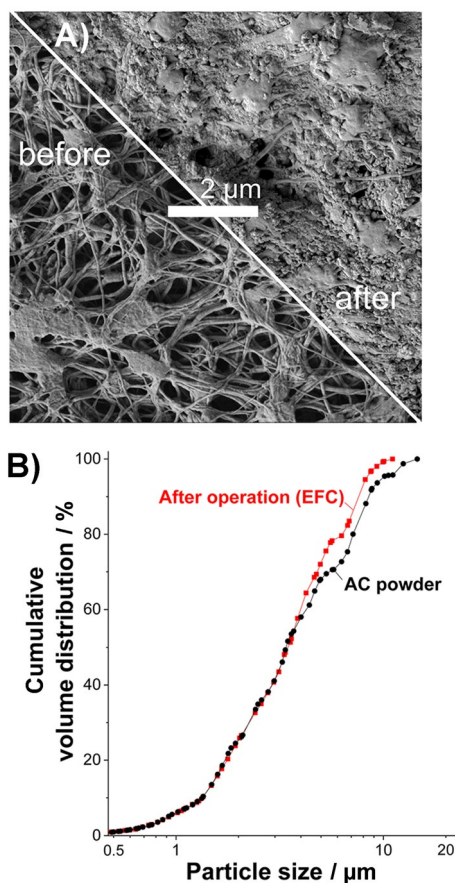


Figure 10. A) SEM images of the Omnipore separators taken before and after 115 h continuous flow operation in the EFC system. B) Cumulative particle size distribution of the activated carbon powder obtained before and after 115 h continuous flow operation in the EFC system.

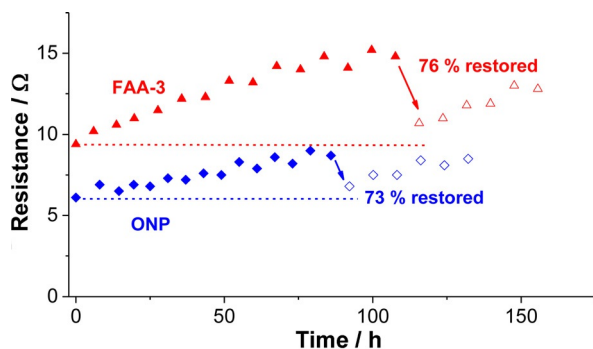


Figure 11. System resistance of the EFC system with the porous separator and anion exchange membrane measured for 6 days of continuous flow operation. The system resistance was restored to more than 70% as a cleaning process with deionized water was introduced (shown using the arrows).

the absolute resistance data obtained for 200 h (Figure 9B). A saturating trend can be observed around the resistance value of 20 Ω. Namely, the cake might have been rapidly formed in the case of adding 5 mM SLS whereas rather slow cake formation might have occurred in the case of a non-modified carbon suspension. This consideration is important for the different initial power performances of the various

carbon suspensions as shown in Figure 7. There, a low initial power observed for the SLS-modified carbon suspensions may be explained by accelerated cake formation on the separator as well as by the viscosity-related charge percolation in the carbon suspension.

Conclusions

Our work presents long-term testing of continuous EFC operation. A stable performance was observed in terms of specific capacitance versus operating time ($90 \pm 5 \text{ F g}^{-1}$) with even higher values compared to those of the film electrodes (normalized to the carbon mass). The main contribution to the higher capacitance is believed to be the improved pore access to electrolyte as compared to film electrodes. In contrast to the low system resistance of EFC systems known for non-flow operation, a notably higher resistance ($58\text{--}149 \text{ } \Omega \text{ cm}^{-2}$) was obtained in continuous flow operation. The different results for non-flow and flow operation relate to particle sedimentation and the charge gradient in space as a function of time.

The use of surfactants for EFC systems effectively enhanced the volumetric energy density of the system; however, as the viscosity reduction is closely related to the decreased power performance, a careful balance between the viscosity and system resistance is required as a function of carbon concentration. The highest volumetric capacitance (26 F cm^{-3}) was achieved after adding 5 mM SLS; this was enabled by a dramatic reduction in viscosity of the carbon suspension. However, a high concentration of surfactant was found to cause visible micelles formation.

We also investigated degeneration of the EFC power performance. Our data indicate that membrane fouling is the major contribution to the degenerating power performance. As the power performance was restored by introducing a simple cleaning process with deionized water, further restoration may be achieved by additional sonication and/or chemical cleaning process.

Experimental Section

Materials

For the preparation of carbon suspensions and film electrodes, YP50 activated carbon (Kuraray, $1614 \text{ m}^2 \text{ g}^{-1}$ specific surface area, $\approx 1 \text{ nm}$ average pore size) was used without further modification. Following the procedure outlined in Ref. [40], the as-received activated carbon powder was blended with polytetrafluoroethylene (5 wt %, Sigma–Aldrich). We used hot rolling to produce self-standing film electrodes, from which we cut out discs with areas of 1.13 cm^2 and a thicknesses of $142 \pm 4 \text{ } \mu\text{m}$.

A $1 \text{ M Na}_2\text{SO}_4$ (Sigma–Aldrich) aqueous solution was prepared, and four different types of surfactants were used as electrolyte additives with 5 mM and 20 mM concentrations: Sodium lignosulfonate (SLS, Sigma–Aldrich) as anionic surfactant, tetrapropylammonium iodide (TPAI, Sigma–Aldrich) as cationic surfactant, octyl phenol ethoxylate or commercially known as Triton-X 100 (TX, Carl Roth) as non-ionic surfactant, and (ferrocenylmethyl) dodecyltrimethyl-ammonium bromide (FDAB, Tokyo Chemical

Industry) as a redox-active surfactant. For the carbon suspension, activated carbon was dispersed in the electrolytes, mixed using a shake mixer (Willy A. Bachofen AG Maschinenfabrik) for 20 min, and then sonicated for 10 min at a power of 40 W and 50% duty cycle.

As separators, a conventional porous separator, Omnipore (ONP, Merck Millipore, 20 μm thickness) and FAA-3 type anion exchange membrane (Fumatech, 20 μm thickness) were applied for the flow electrode configuration and only ONP was used for the film electrode configuration. The FAA-3 membrane was conditioned in an 0.5 M NaCl (Sigma–Aldrich) aqueous solution for 72 h at room temperature, rinsed in demineralized water to remove any additive from the membrane, and stored in 1 M Na_2SO_4 aqueous solution prior to the cell assembly for the flow electrode configuration.

Cell design and system configurations

For the electrochemical analysis of the film electrodes, spring-loaded two-piston cells (custom-built, Figure S1, Supporting Information) were utilized using a two-electrode setup. To trace the redox reactions observed for TPAI (5 mm), an extra cell with a three-electrode configuration was prepared using an Ag/AgCl reference electrode. The ONP separator was placed between two film electrodes, and platinum foils (Dukatshop, 200 nm thickness) were placed between the titanium current collector and the film electrode to optimize the contact resistance. As the film electrode cells were assembled, 1 M Na_2SO_4 aqueous electrolytes, with and without being modified by the surfactants, were injected using syringe back-filling to apply a negative pressure and holding it for 30 min for the optimized penetration of the electrolytes to the film electrodes.

For the flow electrode configuration, a closed-loop EFC system was designed for the continuous flow operation, employing a peristaltic pump (Gilson), suspension reservoirs, and electrochemical cells (Figure 1B). A fixed flow rate of 16 mL min^{-1} was applied using a peristaltic pump to transport the carbon suspension in a closed-loop circulatory flow system. To separate the electrical connection between the two cells, a special drip chamber was introduced using a similar mechanism to intravenous drips in hospitals. The cell was assembled with two graphite current collectors (10 mm thickness) partitioned by the ONP separator or the FAA-3 membrane, and two sheets of silicone gasket (0.56 mm thickness) were placed between the separator and the graphite plate (Figure S1, Supporting Information). This particular layer structure was designed to provide a 1 cm width flow channel with a chamber volume of 0.47 cm^3 in each compartment. For each measurement, 8 mL carbon suspension was injected through the syringe into each compartment.

Structural characterization

SEM images were obtained using a JSM-7500F field emission system at an accelerate voltage of up to 5 kV to investigate the ONP membranes before and after the operation with flow electrode configuration. The OPN taken after the EFC operation was cleaned by water prior to SEM analysis. A thin platinum layer was sputtered onto the sample surface to reduce the surface charging.

To measure the effective particle size of the activated carbon, a laser-aided sedimentation analysis technique was applied using a Lumisizer (LUM GmbH). Prior to the measurements, the

carbon suspension was diluted to 0.01–0.1 wt% carbon concentration in 1 M Na_2SO_4 electrolytes.

Rheological analysis

A Physica MCR 300 rheometer (Anton-Paar GmbH) was used to investigate the rheological properties of the carbon suspension in a double gap concentric cylinder (DG45, Anton-Paar GmbH) at 25 °C. The apparent viscosity of each sample was measured as the shear rate varied from 10 to 4000 s^{-1} .

Electrochemical analysis

A VSP300 and VMP300 potentiostat/galvanostat (Bio-Logic) was used to characterize the electrochemical performance of the EFC system and the film electrode cells. The film electrode cells were placed in a climate chamber at 25 °C during the analysis.

The film electrode cells were initially activated implementing 3 cycles of cyclic voltammetry in a voltage range from -0.2 V to $+0.2$ V at a scan rate of 10 mVs^{-1} for the optimized performance. Then, electrochemical impedance spectroscopy measurements were performed by applying an alternating voltage (5 mV amplitude) over a frequency range of 10^{-2} to 10^6 Hz. To investigate the influence of the electrochemical conditioning on the wettability related property change, cyclic voltammetry was applied in a 0–0.6 V sweep range with various scan rates from 5 to 1000 mVs^{-1} for 40 cycles in total. Subsequently, galvanostatic charging/discharging cycles with potential limitation were applied by varying the current density from 0.05 to 10 A g^{-1} in a voltage range of 0–0.6 V introducing a resting time of 10 s. Specific capacitance values were calculated based on the discharging current obtained using GCPL and the cell voltage measured after a resting time of 10 s to take the IR drop into consideration. For the normalization, only the dry carbon mass was considered, that is, excluding the mass of the binder from the total mass of the film electrode.

To study the time-dependent voltage loss of the film electrode cells, each cell was charged up to 0.6 V at 500 mA g^{-1} ; then, the voltage was held at 0.6 V for 15 min, and the cell voltage was measured under resting conditions for 10 h. In case of the EFC system, the system was charged under constant voltage (0.6 V) until the measured cell voltage reached approximately 0.58 V, and then, the cell voltage under resting conditions was measured for 10 h while the carbon suspension was continuously circulated in the system.

For the determination of the maximum applicable voltage window, cyclic voltammetry was performed over the voltage window from 0.5 to 1.8 V for 3 cycles at each step with a scan rate of 1 mVs^{-1} . By integrating the current with respect to time at a charging/discharging step, S -values were derived from Equation (1).

To test the long-term stability of the film electrode cells, we employed a floating test by applying a constant voltage of 1.4 or 1.55 V for 300 h. To determine the capacitance, three galvanostatic cycles were applied for every 10 h in the voltage range of 1.2 V with 500 mA current density.

In case of the EFC system, chronoamperometry was applied to one cell while the open-circuit voltage was simultaneously being measured at the other cell. The EFC system was charged under a constant voltage of 0.6 V until the system reached almost equilibrium state, and then the system was discharged at 0 V. The drip chamber design prevented the influence of the charge/discharge current on the open-circuit voltage measurement. The

equivalent specific capacitance was derived from the discharge current (Figure S4, Supporting Information) by subtracting the leakage current, and the achieved voltage was considered for the calculation instead of the voltage applied. As exemplified in Figure S4 (Supporting Information), the leakage current during charging accounts for approximately 0.15 and 0.04 mA cm⁻² during discharging. The Coulombic efficiency values were obtained by dividing the charge obtained during discharging by the charge invested during charging; for this calculation, the leakage current was subtracted from measured currents. Assuming a simple equivalent circuit consisting of a capacitive element and an ESR, the ESR value of the EFC system was determined by the slope in the discharged current versus achieved open-cell voltage plot (Figure S4, Supporting Information).

As a solution to membrane fouling, a cleaning process was introduced to the EFC system. First, the carbon suspension was flushed out of the system. Then, the entire flow line in the system was washed out by deionized water at 48 mL min⁻¹ for an hour. To dry the water inside the system, nitrogen gas was blown through the flow line for two hours. Finally, a fresh carbon suspension was injected to the system and the electrochemical analysis was resumed.

Acknowledgements

We acknowledge funding from the German Federal Ministry for Research and Education (BMBF) in support of the nano-EES^{3D} project (award number 03EK3013) as part of the strategic funding initiative energy storage framework. The authors thank Prof. Eduard Arzt (INM) for his continuing support, FuMA-Tech for kindly providing membranes, and Marco Zeiger (INM) for the particle size measurements.

Keywords: capacitance • electrochemical flow capacitors • energy storage • sodium sulfate • surfactants

- [1] B. Dunn, H. Kamath, J.-M. Tarascon, *Science* **2011**, *334*, 928–935.
- [2] S. Faraji, F. N. Ani, *J. Power Sources* **2014**, *263*, 338–360.
- [3] J. R. Miller, A. F. Burke, *Electrochem. Soc. Interface* **2008**, *17*, 53.
- [4] V. Presser, C. R. Dennison, J. Campos, K. W. Knehr, E. C. Kumbur, Y. Gogotsi, *Adv. Energy Mater.* **2012**, *2*, 895–902.
- [5] E. Müller, K. Schwabe, *Z. Elektrochem. Angew. Phys. Chem.* **1928**, *34*, 170–185.
- [6] B. Kastening, T. Boinowitz, M. Heins, *J. Appl. Electrochem.* **1997**, *27*, 147–152.
- [7] O. Kedem, T. Robinson, Vol. US4226688 A, Yeda Research And Development Co. Ltd., **1980**.
- [8] M. Duduta, B. Ho, V. C. Wood, P. Limthongkul, V. E. Brunini, W. C. Carter, Y.-M. Chiang, *Adv. Energy Mater.* **2011**, *1*, 511–516.
- [9] S. Porada, J. Lee, D. Weingarth, V. Presser, *Electrochem. Commun.* **2014**, *48*, 178–181.
- [10] C. R. Dennison, Y. Gogotsi, E. C. Kumbur, *Phys. Chem. Chem. Phys.* **2014**, *16*, 18241–18252.
- [11] T. J. Petek, N. C. Hoyt, R. F. Savinell, J. S. Wainright, *J. Electrochem. Soc.* **2015**, *163*, A5001–A5009.
- [12] M. Li, H. H. Hu, H. H. Bau, *Phys. Chem. Chem. Phys.* **2015**, *17*, 7181–7195.
- [13] M. Boota, K. B. Hatzell, M. Beidaghi, C. R. Dennison, E. C. Kumbur, Y. Gogotsi, *J. Electrochem. Soc.* **2014**, *161*, A1078–A1083.
- [14] S. Sasi, A. Murali, S. V. Nair, A. S. Nair, K. R. V. Subramanian, *J. Mater. Chem. A* **2015**, *3*, 2717–2725.
- [15] M. Boota, K. B. Hatzell, E. C. Kumbur, Y. Gogotsi, *ChemSusChem* **2015**, *8*, 835–843.
- [16] K. B. Hatzell, M. Beidaghi, J. W. Campos, C. R. Dennison, E. C. Kumbur, Y. Gogotsi, *Electrochim. Acta* **2013**, *111*, 888–897.
- [17] S. Roldán, M. Granda, R. Menéndez, R. Santamaría, C. Blanco, *J. Phys. Chem. C* **2011**, *115*, 17606–17611.
- [18] Z. Liu, H. Zhou, Z. Huang, W. Wang, F. Zeng, Y. Kuang, *J. Mater. Chem. A* **2013**, *1*, 3454–3462.
- [19] S. Porada, D. Weingarth, H. V. M. Hamelers, M. Bryjak, V. Presser, P. M. Biesheuvel, *J. Mater. Chem. A* **2014**, *2*, 9313–9321.
- [20] J. W. Campos, M. Beidaghi, K. B. Hatzell, C. R. Dennison, B. Musci, V. Presser, E. C. Kumbur, Y. Gogotsi, *Electrochim. Acta* **2013**, *98*, 123–130.
- [21] K. B. Hatzell, M. C. Hatzell, K. M. Cook, M. Boota, G. M. Housel, A. McBride, E. C. Kumbur, Y. Gogotsi, *Environ. Sci. Technol.* **2015**, *49*, 3040–3047.
- [22] K. Fic, G. Lota, E. Frackowiak, *Electrochim. Acta* **2012**, *60*, 206–212.
- [23] K. Fic, G. Lota, E. Frackowiak, *Electrochim. Acta* **2010**, *55*, 7484–7488.
- [24] G. Milczarek, *Langmuir* **2009**, *25*, 10345–10353.
- [25] K. B. Hatzell, L. Fan, M. Beidaghi, M. Boota, E. Pomerantseva, E. C. Kumbur, Y. Gogotsi, *ACS Appl. Mater. Interfaces* **2014**, *6*, 8886–8893.
- [26] M. Boota, K. B. Hatzell, M. Alhabeab, E. C. Kumbur, Y. Gogotsi, *Carbon* **2015**, *92*, 142–149.
- [27] Ł. Klapiszewski, J. Zdzarta, T. Szatkowski, M. Wysokowski, M. Nowacka, K. Szwarz-Rzepka, P. Bartczak, K. Siwińska-Stefańska, H. Ehrlich, T. Jesionowski, *Cent. Eur. J. Chem.* **2014**, *12*, 719–735.
- [28] D. Yang, X. Qiu, M. Zhou, H. Lou, *Energy Convers. Manage.* **2007**, *48*, 2433–2438.
- [29] A. Slaczka, A. Wasilczyk, *Physicochem. Probl. Miner. Process.* **2012**, *48*, 141–148.
- [30] J. Huang, J. Xu, D. Wang, L. Li, X. Guo, *Ind. Eng. Chem. Res.* **2013**, *52*, 8427–8435.
- [31] L. Demarconnay, E. Raymundo-Pinero, F. Béguin, *Electrochem. Commun.* **2010**, *12*, 1275–1278.
- [32] Q. Gao, L. Demarconnay, E. Raymundo-Pinero, F. Béguin, *Energy Environ. Sci.* **2012**, *5*, 9611–9617.
- [33] V. Khomenko, E. Raymundo-Pinero, E. Frackowiak, F. Béguin, *Appl. Phys. A* **2006**, *82*, 567–573.
- [34] D. Weingarth, H. Noh, A. Foelske-Schmitz, A. Wokaun, R. Kötz, *Electrochim. Acta* **2013**, *103*, 119–124.
- [35] D. Weingarth, A. Foelske-Schmitz, R. Kötz, *J. Power Sources* **2013**, *225*, 84–88.
- [36] M. Aslan, D. Weingarth, P. Herbeck-Engel, I. Grobelsek, V. Presser, *J. Power Sources* **2015**, *279*, 323–333.
- [37] A. Lewandowski, P. Jakobczyk, M. Galinski, M. Biegun, *Phys. Chem. Chem. Phys.* **2013**, *15*, 8692–8699.
- [38] J. Kowal, E. Avaroglu, F. Chamekh, A. Šenfelds, T. Thien, D. Wijaya, D. U. Sauer, *J. Power Sources* **2011**, *196*, 573–579.
- [39] M. Kaus, J. Kowal, D. U. Sauer, *Electrochim. Acta* **2010**, *55*, 7516–7523.
- [40] D. Weingarth, M. Zeiger, N. Jäckel, M. Aslan, G. Feng, V. Presser, *Adv. Energy Mater.* **2014**, *4*, 1400316.

Received: July 21, 2015

Revised: August 9, 2015

Published online on October 13, 2015

Energy Technology

Supporting Information

Use of Surfactants for Continuous Operation of Aqueous Electrochemical Flow Capacitors

Juhan Lee,^[a, b] Daniel Weingarh,^[b] Ingrid Grobelsek,^[b] and Volker Presser^{*[a, b]}

ente_201500243_sm_miscellaneous_information.pdf

Cell design

The electrochemical flow used for the characterization of the film electrodes is schematically described in **Figure S1A**. The cell consists of two titanium pistons, cell body (polyether ether ketone), and two stainless steel caps. As illustrated in **Figure S1B**, two film electrodes were located between an upper and a bottom titanium piston and separated by an electrically insulating separator. To enhance the electrical contact resistance between titanium pistons and carbon based film electrodes, thin platinum sheets (200 nm) were placed between the electrode and the titanium pistons. As the spring with a specific spring constant was loaded in the cell, a constant force ($50 \text{ N}\cdot\text{cm}^{-2}$) was applied to the current collector-electrode-separator assembly.

For the electrochemical flow capacitor system, a custom-built cell (**Figure S1C**) was employed. The cell consists of two graphite current collectors with 1 cm thickness, silicone gaskets (0.59 mm), an outer housing (polyvinyl chloride), a separator and other mechanical parts such as O-rings made of ethylene propylene diene monomer.

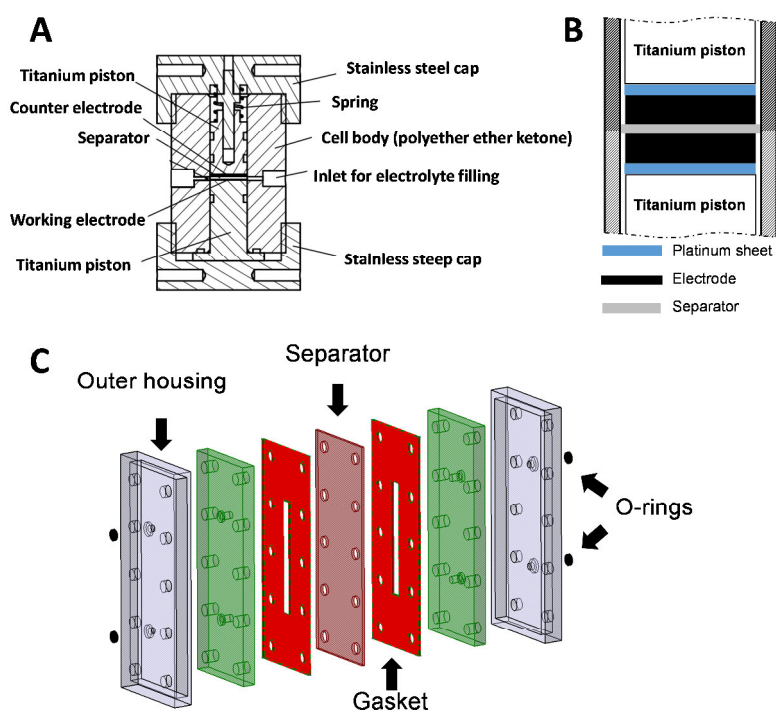


Figure S1. The geometry and the mechanical components of the electrochemical cells used for A) film electrode configuration and B) electrochemical flow capacitor system.

Viscosity of the suspensions and micelle formation

Figure S2A shows the apparent viscosity of the investigated carbon-electrolyte suspension (20 mass% carbon concentrated) at the shear rate of 100 s^{-1} as plotted vs. surfactant concentration. Almost identical trend can be seen as compared to **Figure 3B** except the absolute scale of the viscosity values. At the molar concentration of 5 mM, the carbon suspension with FDAB showed visible size micelle formation (**Figure S2B**).

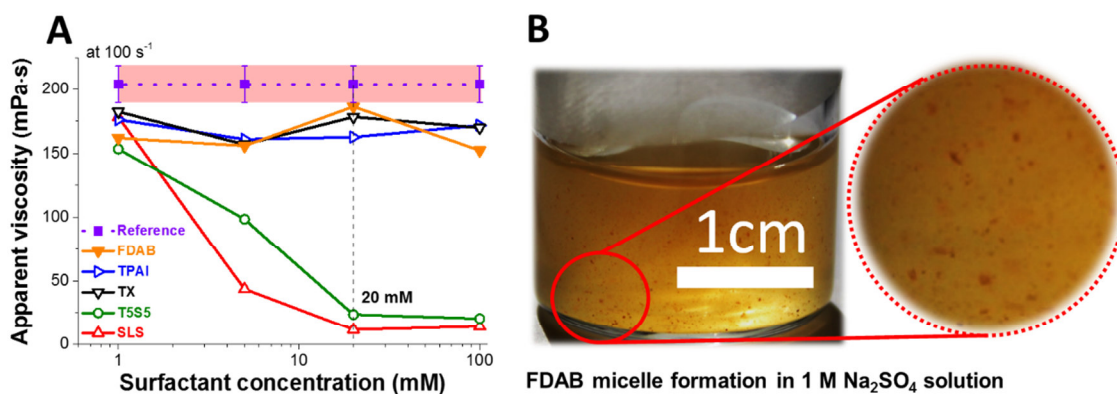


Figure S2. A) Apparent viscosity of 20 mass% carbon suspension as a function of surfactant concentration at shear rate 100 s^{-1} . B) Visible size of FDAB micelles were formed as 20 mass% carbon suspension (1 M Na_2SO_4) was modified by adding 5 mM FDAB.

Iodide/iodine redox reaction by TPAI

Figure S3A shows cyclic voltammograms obtained from a full cell (two symmetric electrode configuration) using 5 mass% polytetrafluoroethylene-bound (PTFE) film electrodes in 1 M Na₂SO₄ with and without surfactant at 5 mM concentration. Compared to a relatively rectangular shape of the cyclic voltammograms (CV) of the reference without any surfactant, the shape changes slightly for 5 mM TPAI. This effect was limited to TPAI while all other surfactants showed no significant deviation from the CV shape of the reference cell without surfactant. The difference in CV shape can be related to the highly reversible redox reaction with a Coulombic efficiency of ca. 99 % for 5 mM TPAI. An additional investigation of a half-cell (i.e., three-electrode configuration) revealed several distinct redox peaks (**Figure S3B**) at positive potential which can be identified as iodide/iodine redox couples with standard electrode potential at ca. 0.54 V vs. SHE (Eq. 1-3).^[1-2]



Capitalizing charge storage via this redox process has been reported for 6 mM KOH aqueous solution modified with 5 mM TPAI; this system showed a 20 % increase in capacitance for a full cell configuration.^[3] However, no such significant enhancement was found in our study in 1 M Na₂SO₄ except about 4 % increase in capacitance value (determined from a galvanostatic charging curve, **Figure S3C**) compared to that of the reference cells most probably due to difference in pH values.

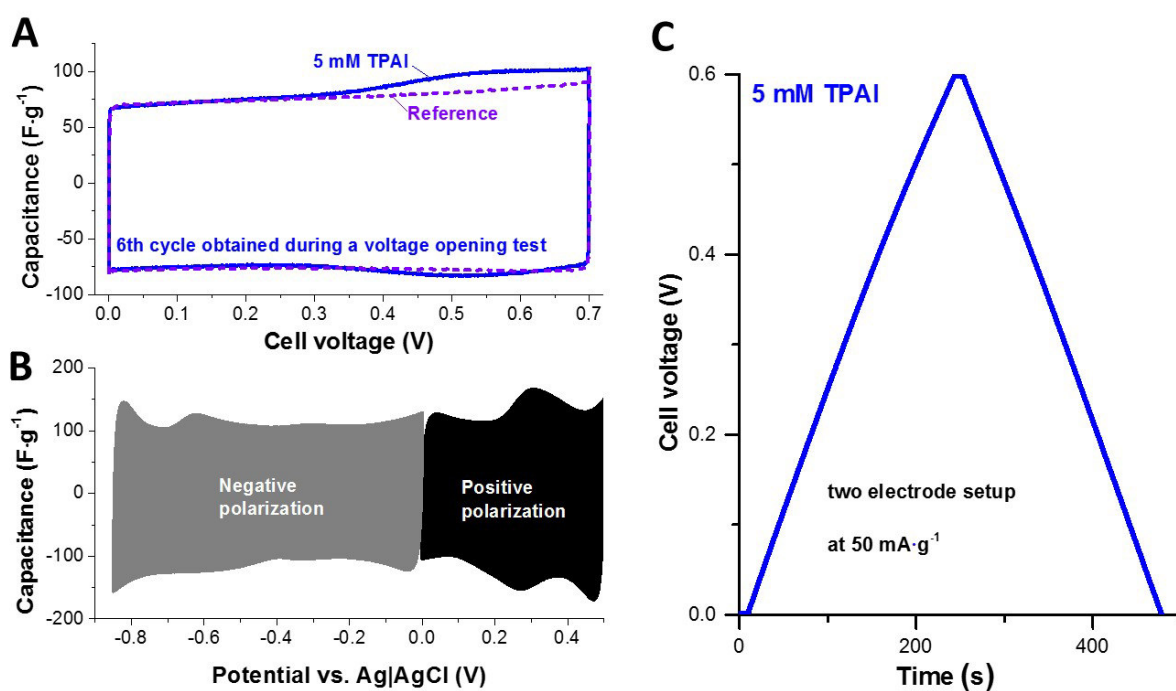


Figure S3. A) Voltammograms obtained at scan rate $1 \text{ mV}\cdot\text{s}^{-1}$ with symmetric two electrodes configuration for 5 mM tetrapropylammonium iodide and the reference without introducing surfactant. B) Voltammogram obtained at scan rate $10 \text{ mV}\cdot\text{s}^{-1}$ for 5 mM tetrapropylammonium iodide as the cell was assembled with two symmetric counter and working electrodes, and Ag|AgCl reference electrode. C) A galvanostatic charge/discharge curve obtained for 5 mM TPAI at a current density of $50 \text{ mA}\cdot\text{g}^{-1}$ in a cell voltage range from 0 to 0.6 V with 10 s resting time.

Data analysis for the EFC system performance

Figure S4A shows the current (red line) obtained from chronoamperometry mode at Cell 1 (see **Figure 1B**) while constant charging (0.6 V) and discharging voltage (0 V) was applied. At the same time, the open cell voltage of the system was measured (green line) at Cell 2. As shown in **Figure 1B**, the two cells are electrically separated from each other through drip chambers. As presented in **Figure S4B**, the system resistance was calculated from Ohm's law from the discharge current measured with Cell 1 and the cell voltage in Cell 2.

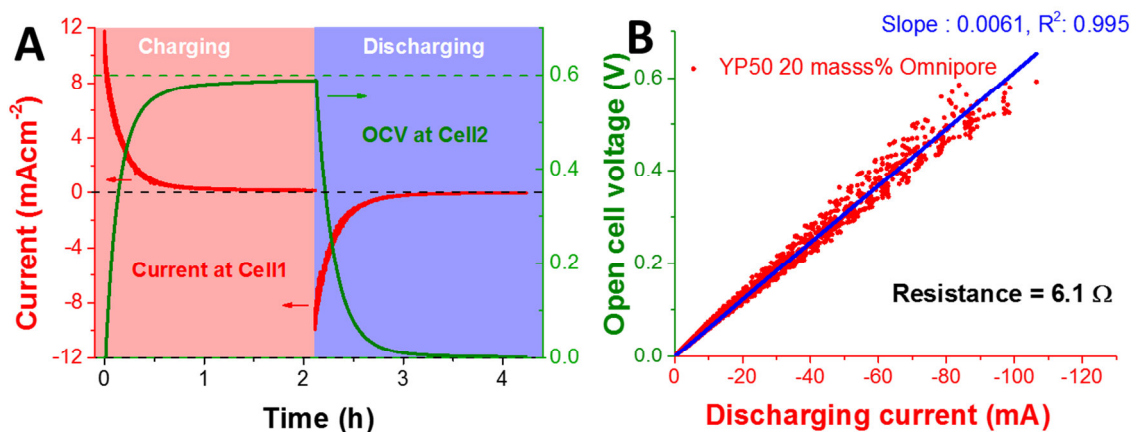


Figure S4. As illustrated in Figure 1, a particular measuring technique was performed for the characterization of the EFC system, employing two cells and probes together with drip chambers for the electrical separation between the cells. A) Current response (red line) from chronoamperometry at Cell 1 and the open cell voltage (green line) measured at Cell 2. B) I-V plot according to the discharging current and the corresponding open cell voltage.

Membrane fouling

As presented with the cross sectional SEM image (**Figure S5A**), a thin layer of carbon can be seen on the surface of the ONP separator with several tens of nanometer thickness. No significant difference can be seen between the SEM images obtained from the ONP separator operated without modification with surfactant in the EFC system (**Figure S5B**) and in the presence of 5 mM SLS (**Figure S5C**).

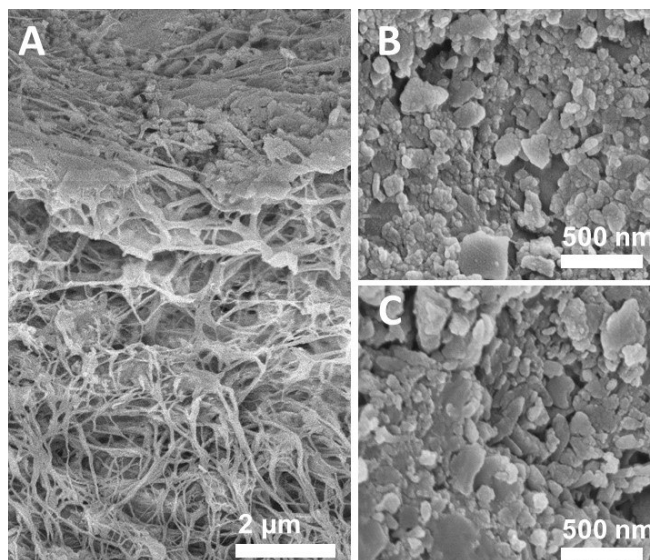


Figure S5. SEM images of the ONP separators were taken after they were operated in the EFC system for 200 h and cleaned by water prior to SEM measurement. A) Cross sectional view of the ONP separator as operated in the EFC system without surfactant and B) the top view. C) Top view image of the ONP separator as operated by the presence of 5 mM SLS.

References

- [1] L. Pataki, E. Zapp, R. Belcher, D. Betteridge, L. Meites, *Basic Analytical Chemistry*, Elsevier Science, **2013**.
- [2] A. L. Partners, H. K. Publishers, *First Steps: Your Healthy Living Journal*, Human Kinetics, **2006**.
- [3] K. Fic, G. Lota, E. Frackowiak, *Electrochim Acta* **2012**, *60*, 206-212.

3.2. High performance hybrid energy storage with potassium ferricyanide redox electrolyte

Juhan Lee,^{1,2} Soumyadip Choudhury,¹ Daniel Weingarth,¹ Daekyu Kim,^{1,3} and Volker Presser^{1,2}

¹ INM - Leibniz Institute for New Materials, Campus D2 2, 66123 Saarbrücken, Germany

² Saarland University, Campus D2 2, 66123 Saarbrücken, Germany

³ School of Energy, Materials and Chemical Engineering, Korea University of Technology and Education, Chungjeol-ro 1600, 31253, Cheonan, Republic of Korea

Citation:

Lee, J.; Choudhury, S.; Weingarth, D.; Kim, D.; Presser, V., High Performance hybrid energy storage with potassium ferricyanide redox electrolyte. *ACS Applied Materials & Interfaces* **2016**, 8 (36), 23676-23687.

Own contributions:

Design, planning, writing, cell design, experimental plan, and electrochemical analyses

Abstract

We demonstrate stable hybrid electrochemical energy storage performance of a redox-active electrolyte, namely potassium ferricyanide in aqueous media in a supercapacitor-like setup. Challenging issues associated with such a system are a large leakage current and high self-discharge, both stemming from ion redox shuttling through the separator. The latter is effectively eliminated when using an ion selective membrane instead of a porous separator. Other critical factors toward the optimization of a redox-active electrolyte system, especially electrolyte concentration and volume of electrolyte, have been studied by electrochemical methods. Finally, excellent long-term stability is demonstrated up to 10,000 charge/discharge cycles at 1.2 V and 1.8 V, with a broad maximum stability window of up to 1.8 V cell voltage as determined via cyclic voltammetry. An energy capacity of 28.3 Wh/kg or 11.4 Wh/L has been obtained from such cells, taking the nonlinearity of the charging/discharging profile into account. The power performance of our cell has been determined to be 7.1 kW/kg (ca. 2.9 kW/L or 1.2 kW/m²). These ratings are higher compared to the same cell operated in aqueous sodium sulfate. This hybrid electrochemical energy storage system is believed to find a strong foothold in future advanced energy storage applications.

High Performance Hybrid Energy Storage with Potassium Ferricyanide Redox Electrolyte

Juhan Lee,^{†,‡} Soumyadip Choudhury,[†] Daniel Weingarth,[†] Daekyu Kim,^{†,§} and Volker Presser^{*,†,‡}

[†]INM – Leibniz Institute for New Materials, Campus D2 2, 66123 Saarbrücken, Germany

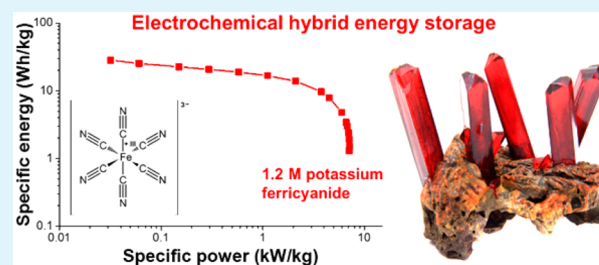
[‡]Department of Materials Science and Engineering, Saarland University, Campus D2 2, 66123 Saarbrücken, Germany

[§]School of Energy, Materials and Chemical Engineering, Korea University of Technology and Education, Chungjeol-ro 1600, 31253 Cheonan, Republic of Korea

S Supporting Information

ABSTRACT: We demonstrate stable hybrid electrochemical energy storage performance of a redox-active electrolyte, namely potassium ferricyanide in aqueous media in a supercapacitor-like setup. Challenging issues associated with such a system are a large leakage current and high self-discharge, both stemming from ion redox shuttling through the separator. The latter is effectively eliminated when using an ion exchange membrane instead of a porous separator. Other critical factors toward the optimization of a redox-active electrolyte system, especially electrolyte concentration and volume of electrolyte, have been studied by electrochemical methods. Finally, excellent long-term stability is demonstrated up to 10 000 charge/discharge cycles at 1.2 and 1.8 V, with a broad maximum stability window of up to 1.8 V cell voltage as determined via cyclic voltammetry. An energy capacity of 28.3 Wh/kg or 11.4 Wh/L has been obtained from such cells, taking the nonlinearity of the charge–discharge profile into account. The power performance of our cell has been determined to be 7.1 kW/kg (ca. 2.9 kW/L or 1.2 kW/m²). These ratings are higher compared to the same cell operated in aqueous sodium sulfate. This hybrid electrochemical energy storage system is believed to find a strong foothold in future advanced energy storage applications.

KEYWORDS: energy storage, redox electrolyte, redox shuttling, supercapacitor, ion exchange membrane



1. INTRODUCTION

Electrochemical energy storage (EES) has emerged over the last few decades as a key enabling technology for transitioning our fleet of combustion engine cars to electric and hybrid vehicles and for the large scale implementation of renewable energy sources to the power grid.^{1,2} Within the spectrum of EES devices and technologies, batteries and supercapacitors are the most prominent ones, employing Faradaic and non-Faradaic energy storage mechanisms.^{3,4} Supercapacitors are characterized by a high specific power performance (ca. 10 kW/kg) and very long cycle stability as compared to batteries; however, their low specific energy (ca. 5 Wh/kg) is a major drawback for the large scale application and prohibitive to many mobile technologies.⁵ The last years have seen enormous efforts in improving power handling and cycle lifetime of batteries on the one hand, and enhancing the energy storage capacity of supercapacitors on the other hand. The ultimate goal is the fabrication of energy storage devices possessing battery-like specific energy (>100 Wh/kg) and high specific power handling (>10 kW/kg) with more than 10 000 duty cycles of stable cell performance.⁶

A promising strategy to achieve this goal is to enable redox-activity in supercapacitors. The latter are a group of EES devices that range from charge storage via ion electrosorption

(electrical double-layer capacitors, EDLC) to pseudocapacitors consisting of Faradaic materials that electrically behave like capacitors (i.e., realizing a linear and monotonic dependency of the accumulated charge and the applied electric potential).^{6,7} In case of pseudocapacitors, the charge storage occurs through reversible and fast Faradaic reactions at electrode surfaces, which differentiates them from batteries, where the bulk material of the electrode contributes to the charge storage in combination with the electrolyte. The main advantage of pseudocapacitors is 5–10 times higher capacitance (up to 1000 F/g), as demonstrated for transition metal oxides, such as RuO₂ and MnO₂, as compared to that of EDLCs (ca. 200 F/g), whereas poor cycle life and high equivalent series resistance (ESR) are the main drawbacks.⁸

Battery–supercapacitor-hybrids have been actively explored with various degree of capacitor- or battery-like behavior. To capture this range, the group of G. Z. Chen has recently proposed to use new terms, “supercapattery” and “super-cabattery”,^{9,10} but the more general term “hybrid” has so far manifested as a commonly used term.¹¹ Advanced hybrid

Received: May 25, 2016

Accepted: August 19, 2016

Published: August 19, 2016

devices also require the implementation of hybrid materials, such as redox-active metal oxides, surface functional groups, or electroactive polymers on nanoporous carbons. Especially nanohybrid materials of lithium intercalation materials and nanocarbons^{12,13} and carbon surfaces decorated with quinone functional groups^{14,15} have demonstrated the large potential of this approach.

In general, most work on redox systems relates to redox materials like quinones,^{16–19} transition metal ions,^{20,21} and *p*-phenylenediamine (*p*-PD).^{22–24} The majority of literature on hybrid devices investigates design strategies to optimize the electrical, chemical, and morphological structure of the electrode materials to introduce high intrinsic energy storage capacity, as well as fast ion diffusion and charge carrier pathways maximizing the power handling. For these efforts, redox-enabling protic electrolytes (water or protic ionic liquids)²⁵ or lithium shuttling organic electrolytes have been used.²⁶

With the majority of research activities focused on electrode materials, redox-active electrolytes have been discovered as a facile way to improve significantly the energy storage capacity only very recently.⁸ Pioneering works include the use of quinone molecules added to an aqueous electrolyte¹⁴ or the utilization of the iodine/iodide redox couple.²⁷ In the case of redox electrolyte systems, the reversible redox species are dissolved in the electrolyte, rather than as a solid addition to the electrode, enabling a particularly practical approach for designing cells: the exact same nanoporous carbon electrodes, which are broadly applied to supercapacitor applications, can still be used for redox electrolyte systems, whereas only the liquid phase (electrolyte) is being changed.

For redox electrolytes, we can differentiate between redox-additive electrolytes, which add the redox-active species to a carrier electrolyte (which, itself, can provide double-layer charge storage), or the direct (and exclusive) use of a redox-active electrolyte.⁹ For instance, the quinone/hydroquinone redox couple can be used as a redox additive to H₂SO₄ aqueous electrolyte contributing remarkable enhancement to energy storage capacity (equivalent to up to 900 F/g).¹⁴ A promising, intrinsically redox-active electrolyte would be, for example, the iodine/iodide system with potassium iodide electrolyte (261 F/g).²⁷

However, the use of redox-additive or redox-active electrolytes brings along another issue: the need for carefully selecting an appropriate separator. The ability of the redox-active species to freely travel between the electrodes poses a severe limitation to the amount of effectively storable energy and a vast increase in self-discharge. As illustrated by recent works, this issue can be addressed by employing ion exchange membranes instead of porous separators.²⁸ Although this is a paradigm change in the cell design from the point of view of batteries and supercapacitors, it is only the consequent adaptation of the state-of-the-art for redox-flow batteries, where ion exchange membranes have been used for decades.^{29,30} Yet, the redox-active electrolyte system could provide not only a high specific energy, but in addition a high specific power (>2 kW/kg), which can be further improved by thorough understanding of the ion mobility in the macro- and nanopores of carbon, as well as in the separator.³¹

Redox-active electrolytes have emerged as a promising technology, but stable performance, exceeding common supercapacitors in terms of both specific power and energy, has not yet been established. In particular, the issue of cell self-

discharge in redox-systems has often been overlooked despite of its importance on practical energy storage applications.

In this work, we demonstrate the excellent performance and stability of potassium ferricyanide (K₃[Fe(CN)]₆), also known as Prussian Red, as an advanced aqueous redox-active electrolyte. The intriguing aspect is that the system both exhibits electrical double-layer and redox-active contributions to the total charge storage capacity. Self-discharge can be reduced to the common level known for aqueous supercapacitors by using a thin cation exchange membrane instead of a porous membrane. The factors which control the capacitive performance, such as electrolyte concentration, electrolyte volume, and membrane thickness, were studied systematically to achieve stable cell performance with prolonged charging–discharging cycles.

2. MATERIALS AND METHODS

2.1. Materials. Free standing carbon film electrodes were prepared using activated carbon type YP80F (Kuraray Chemicals) as active material. As characterized by nitrogen gas sorption,^{32,33} YP80F has a BET surface area of 2347 m²/g (calculated using the Brunauer–Emmett–Teller equation) or DFT surface area of 1756 m²/g (quenched-solid density functional theory). Via quenched-solid density functional theory with a hybrid model for slit and cylindrical pores and pore size between 0.56 and 37.5 nm, a total pore volume of 1.15 cm³/g and an average pore size of 1.6 nm were calculated. Hot-rolled film electrodes were produced by blending 95 mass % YP80F with 5 mass % polytetrafluoroethylene (PTFE). Following the procedure outlined in ref 34, free-standing film electrodes with 200 ± 6 μm and 600 ± 8 μm were created.

FKS-type cation exchange membranes (FKS) were provided by FuMA-Tech. They are produced ideally for applications, where high physicochemical stabilities are required. As reported elsewhere,^{35,36} FKS membranes provide high permselectivity and a low degree of membrane swelling, which are of high importance for the physicochemical stability. The influence of the ion exchange membranes was tested in case of EDLCs as well as for the redox-active electrolyte system. As determined with a digital micrometer caliper, the membranes had the following thicknesses: FKS10 = 17 ± 1 μm, FKS20 = 23 ± 2 μm, FKS30 = 34 ± 1 μm, and FKS50 = 60 ± 2 μm, FAS10 = 14 ± 1 μm, FAS20 = 25 ± 5 μm, FAS30 = 32 ± 1 μm, and FAS50 = 56 ± 14 μm (anion exchange membranes were used for data presented in the Supporting Information). Prior to use, the membranes were soaked in pure water for 8 h, then, in 0.5 M NaCl solution for 74 h, rinsed with deionized water, and then stored in aqueous 1 M Na₂SO₄. Afterward, the membranes were soaked for at least 12 h in the electrolyte before cell assembly. We also used a porous hydrophilic polytetrafluoroethylene, PTFE, separator (Merck Millipore, dry thickness: 25 μm); this separator is referred to as ONP. Both the separator and the membranes were characterized by scanning electron microscopy (SEM) with a JSM-7500F field-emission system at an accelerating voltage of up to 4 kV (see the Supporting Information). A thin platinum layer was sputtered on the sample surface to reduce the surface charging.

The electrolytes were prepared by adding potassium ferricyanide (PFC, Sigma-Aldrich) and Na₂SO₄ (Sigma-Aldrich) to water with various molar concentration: 1 M Na₂SO₄, 1 M Na₂SO₄ + 0.1 M PFC, 0.1, 0.6, 1.0, and 1.2 M PFC.

2.2. Cell Design and Assembly. For the hybrid system with redox electrolyte in a full cell configuration without a reference electrode, a particular cell is designed as described in Figure S1 in the Supporting Information. The cell consists of two graphite current collectors (10 mm thickness) being separated by the membranes, and two polymer gasket layers. Through the circular inner cut with an area of 1.33 cm² in the gasket, the film electrodes were placed between the graphite current collector and the membrane. Besides, the gasket worked as a seal for the membrane surrounding which is necessary to prevent the physical mixing of the electrolyte through unsealed edge of

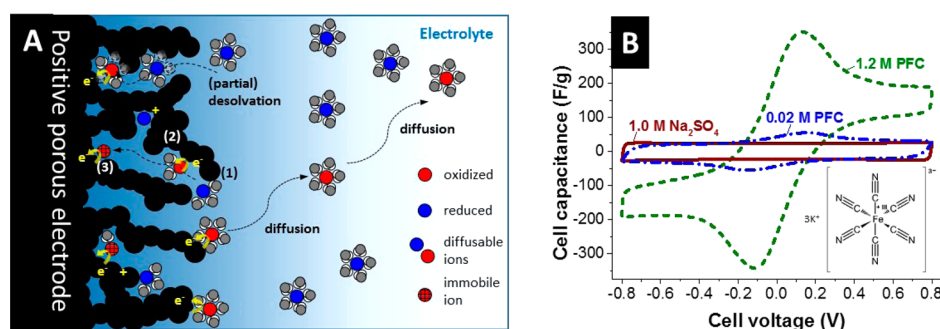


Figure 1. (A) Schematic illustration of hybrid energy storage with a redox electrolyte. (B) Cyclic voltammograms (CV) of an ideal electrical double-layer electrolyte (1 M Na₂SO₄) in comparison to 0.02 and 1.2 M potassium ferricyanide (PFC). The data were obtained at 10 mV/s when using a porous separator (ONP).

the membrane. The electrolyte is either injected by syringe after assembly or directly dropped to the gasket channel during assembly and sealed afterward. For the latter case, the electrodes were previously soaked in the electrolyte and degassed by applying vacuum for 5 min in order to prevent the electrolyte shortage that can happen as the electrode adsorbs the electrolyte after the cell assembly.

For the investigation of full cells with a reference electrode, we applied a spring-loaded two-piston cell whose detailed design can be found in ref 34. The symmetric electrodes with the diameter of 10 mm were placed between two graphite pistons while being separated by the membrane. For the reference electrode, we applied an Ag/AgCl electrode (saturated in 3 M NaCl, Bioanalytical Systems).

2.3. Electrochemical Characterization. A VMP300 potentiostat/galvanostat (Bio-Logic) was utilized to characterize the electrochemical performance of the cells while the temperature was kept to 25 °C. Cyclic voltammetry (CV) was carried out at various scan rate from 1 mV/s to 0.25 V/s at the cell voltage from -0.8 V to +0.8 V. For the characterization with potentiostatic electrochemical impedance spectroscopy (PEIS), a frequency range of 10⁻² to 10⁶ Hz with an alternating voltage amplitude of 5 or 50 mV was applied at the cell voltage of 0–0.8 V. Galvanostatic charge/discharge with potential limitation (GCPL) was applied with the voltage range from 0 to max. 1.8 V at 10 mA/g to 30 A/g with a resting time of 10 s. To investigate the time-dependent voltage loss at resting condition, the cells were charged with constant current at 37 mA/g to 0.8 V; then, the voltage was held at 0.8 V for 0, 2, or 10 h, and the open circuit voltage was measured for 10 h. To determine the voltage stability window, S-value analysis³⁷ was carried out by cyclic voltammetry at 1 mV/s while the cell voltage window was extending from 0.7 to 2.35 V with the potential interval of either 0.5 or 1 V.

For long-term cyclic stability test, we employed galvanostatic cycling test applying 10 000 cycles of charge/discharge at constant current of 0.4 A/g at the voltage window of 1.2 V; for every after 100 cycles, the voltage was swept from -1.2 to +1.2 V at 0.1 A/g for 2 cycles with subsequent resting time for 2 h in order to prevent the influence of incompletely charged or discharged ferricyanide/ferrocyanide ions in the electrolyte. We also tested a cell applying 1 A/g for 15 000 cycles at the voltage window of 1.8 V; for every after 100 cycles, the cell was discharged down to 0 V at 10 A/g with 30 min holding time and 1 h resting time.

To investigate the potential of the individual electrodes in a full cell configuration, a potential was controlled between the positive and the negative electrode by applying a constant current while measuring the potential between the negative and the reference electrode.

Cell capacitance values are provided in this work in order to emphasize more on the device performance than individual performance of a single electrode. The specific capacitance (C_{sp}) is four-times higher value of a cell capacitance when both electrodes have an equal capacitance. All cell capacitance and cell capacity values were derived from discharging curves via GCPL and normalized to the total mass of the two carbon electrodes while the Coulombic efficiency was calculated as the ratio of the recovered charge during discharging and the charge invested during charging. In case for the calculation of

cell capacitance at GCPL mode, the voltage was corrected by the iR drop determined after 0.2 ms of the application of the discharge current. To calculate the specific energy in CV mode, eq 1 was applied:

$$E = \frac{1}{m_{\text{total}}} \cdot \int U i dt \quad (1)$$

where i is the discharging current response, U is the cell potential (i.e., not corrected for iR drop), and m_{total} is the total mass of the active electrode materials.

For the normalization of the values, only the dry mass of the carbon was considered which means excluding the mass of the binder material and the electrolyte.

For the Ragone plot, the specific power was calculated by the following equation:

$$P = \frac{3600}{\Delta t_{\text{dis}}} \cdot E \quad (2)$$

where Δt_{dis} is the discharging time in seconds.

3. RESULTS AND DISCUSSION

3.1. Redox-Activity of Potassium Ferricyanide. Redox-active electrolytes exhibit a dual role: not only by virtue of their charge, they may act as ions accomplishing the formation of electrical double-layers, but also by virtue of their redox-activity, they enable reversible Faradaic charge transfer (Figure 1A). In our case, the ferricyanide anion [Fe(CN)₆]³⁻ can undergo a reversible redox reaction to ferrocyanide ion [Fe(CN)₆]⁴⁻ by transforming iron from +III to +II oxidation state while receiving one electron per ion. This redox process is clearly seen by comparing to a typical aqueous electrolyte, only exhibiting electrical double-layer capacitance, namely 1 M Na₂SO₄, with aqueous 1.2 M potassium ferricyanide (PFC). For this first comparison, we used a porous separator (ONP) and electrodes made from nanoporous carbon (YP80F). As seen from the cyclic voltammogram (CV) in Figure 1B, 1 M Na₂SO₄ shows a constant cell capacitance of roughly 25 F/g over the entire sweep range from -0.8 to +0.8 V cell voltage. When transitioning to the redox electrolyte, the CV shows the emergence of redox peaks at low PFC concentration (20 mM) and a significant contribution of electrical double-layer capacitance (in the range of 25 F/g), but also more resistive, as evidenced by the pronounced resistive knee at the vertex potentials. Still, capacitive energy storage clearly dominates the CV at low molar concentrations. The redox peaks at around -0.15 and +0.15 V become more pronounced for high PFC concentrations; the latter also pronouncedly decrease the resistive response of the cell because of the higher ion mobility at high molarities. Also, we see a strongly distorted CV for 1.2

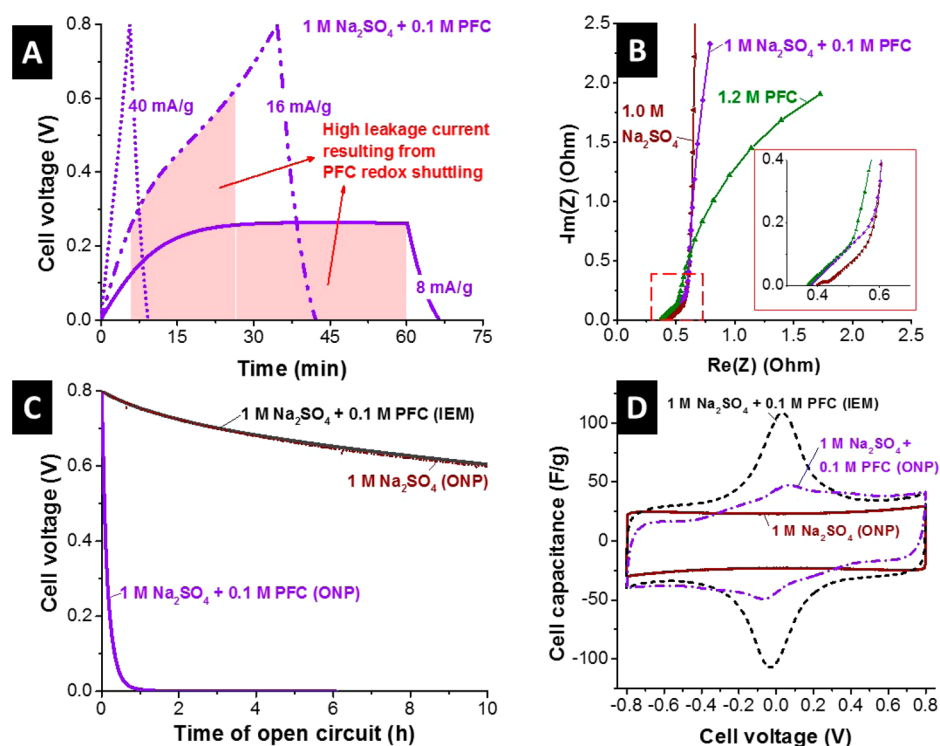


Figure 2. (A) Galvanostatic charge/discharge profiles when using 1 M Na_2SO_4 with an addition of 0.1 M PFC at different currents. (B) Electrochemical impedance spectra of 1 M Na_2SO_4 without and with 0.1 M PFC in comparison with 1.2 M. The voltage amplitude of 5 mV was applied at the cell voltage of 0 V. (C) Time dependence of the open circuit voltage for 1 M Na_2SO_4 without and with 0.1 M PFC. Data are provided for the use of a porous separator (ONP) and an ion exchange membrane (IEM; type FKS20 = cation exchange membrane). (D) Cyclic voltammograms at 2.5 mV/s of 1 M Na_2SO_4 without and with 0.1 M PFC when using a porous separator (ONP) compared to 1 M Na_2SO_4 with 0.1 M PFC for use of an ion exchange membrane (IEM; type FKS20).

M PFC, which makes a clear distinction between Faradaic and non-Faradaic charge storage capacity. This characteristic CV shape associated with very high currents have also been reported in other hybrid systems with redox electrolytes, such as vanadyl sulfate,^{31,38} Cu^{2+} ,³⁹ Fe^{2+} ,^{20,40} N,N' -diphenyl-*p*-phenylenediamine,⁴¹ and $[\text{Fe}(\text{CN})_6]^{4-}$.⁴² We note that “capacitance” is an inadequate unit to describe the charge storage ability of Faradaic systems.^{9,43} It is here only used to enable a qualitative comparison of the storage capacity of an electric double-layer electrolyte with a redox-active electrolyte.

3.2. Preventing Shuttling of Redox-Active Ions by Using a Cation Exchange Membrane. The CV data evidence the redox-activity of PFC, which is related to the Faradaic charge transfer associated with the ferrocyanide to ferricyanide transformation, but the extreme distortion with pronounced plateaus at positive and negative current indicates a severe issue when used for reversible electrochemical energy storage. Effectively, we see with lowered specific current a very high leakage current emerging in galvanostatic charge/discharge curves. As exemplified in Figure 2A, it becomes impossible for the system to be fully charged to the preset value of 0.8 V at very low current (in our case: 8 mA/g). These data were collected when adding 0.1 M PFC to 1 M Na_2SO_4 to enable a high ion mobility, while keeping the amount of the redox species small. The system could only be fully charged to the cell voltage of 0.8 V when exceeding a specific current of 40 mA/g, but even then, only a very low Coulombic efficiency (21%) was encountered. For comparison: when only using PFC (1.2 M), charging of the cell up to 0.8 V was only possible at a high specific current of 1.3 A/g with an extremely low Coulombic

efficiency of just 6%. The mechanism behind this phenomenon is the random transport of ferricyanide/ferrocyanide ions between the two electrodes through the bulk electrolyte. This process is known as the (ion) shuttle effect and is enabled by the use of a porous separator between the two carbon electrodes.

The shuttling of redox-active ions can also be seen in potentiostatic electrochemical impedance spectra (PEIS; Figure 2B). As seen from the Nyquist plot, adding 0.1 M PFC to 1 M Na_2SO_4 causes a distinct bending at low frequencies region; this effect becomes more pronounced in absence of Na_2SO_4 (exemplified for 1.2 M PFC). The bending of the curves in the Nyquist plot implies a diffusion-controlled chemical leakage current through the porous separator. Another important observation is that the PFC hybrid system does not exhibit a semicircle shape in the Nyquist plot, which is characteristic for charge transfer resistance (CTR) due to Faradaic activity of the redox species in the electrolyte;^{44,45} even at a larger voltage amplitude (50 mV) at the cell voltage of up to 0.8 V, no semicircle shape was observed via PEIS.

Dissolved PFC molecules, once electrochemically reduced at the negatively charged electrode, are oxidized at the opposite electrode (and vice versa for oxidized PFC molecules). This way, charge is effectively transported between the two carbon electrodes, leading to a drastic drop of the cell voltage when monitoring the open circuit voltage (OCV). As exemplified for an initial cell voltage of 0.8 V after charging with a constant current of 37 mA/g with a subsequent voltage holding for 2 h, basically full cell discharge occurs within less than 1 h (Figure 2C). For comparison, a fully charged cell using 1 M Na_2SO_4

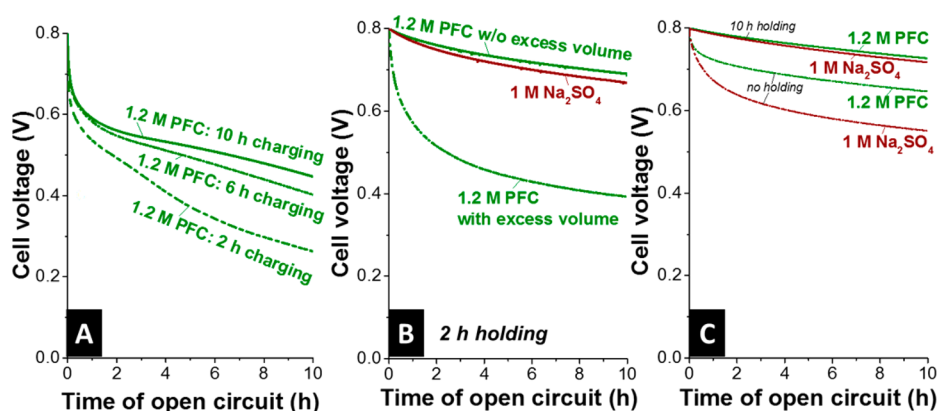


Figure 3. (A) Open circuit voltage (OCV) decay behavior (self-discharge) showing the influence of different charging times for the empty cell, that is, a cell with 0.18 mL of redox electrolyte (1.2 M PFC) but no activated carbon electrode (only graphite current collectors; 600 μm of the channel depth). (B) Influence of excess electrolyte volume (4 mL) on the OCV decay over time for 1.2 M PFC and comparative data for the 1 M Na_2SO_4 system. (C) OCV decay data with 10 h of voltage holding and without voltage holding measured in the cells without (w/o) excess electrolyte volume.

loses around 0.2 V (i.e., ca. 25% for an initial voltage of 0.8 V) after an OCV period of 10 h, as it is typical for an aqueous supercapacitor.⁴⁶ The redox-related OCV drop can be drastically reduced and a behavior virtually identical to a conventional electrical-double layer capacitor can be obtained when simply replacing the porous separator with an ion exchange membrane (IEM), more precisely, with a cation exchange membrane. In our case, we used FKS20 with a thickness of 20 μm and by doing so, a much less distorted CV (Figure 2D) can be seen. By this way, we can identify for 1 M Na_2SO_4 + 0.1 M PFC electrolyte a clear contribution of electrical double-layer capacitance and a pair of well-pronounced redox-peaks. Direct comparison to the 0.1 M PFC system with a porous separator shows much larger charges in the case of the system with FKS20; as the larger total area of the CV curve indicates, the cation exchange membrane enables a much more effective charge recovery caused by the suppression of the redox shuttling. Our results align with a recent study of Chen et al. demonstrating the ability of an IEM to avoid shuttling of redox-active species, as exemplified for a proton exchange membrane (sulfonated tetrafluoroethylene based fluoropolymer-copolymer, Nafion).²⁸

By now, suppression of the redox shuttling has been reported with various types of ion selective membranes for various redox-active electrolytes: *N,N'*-diphenyl-*p*-phenylenediamine,⁴¹ hydroquinone,²⁸ and acetylferrocene.⁴⁰ To avoid redox ion shuttling, the use of ion exchange membranes is highly promising. Depending on the nature of the ions responsible for redox activity, a different membrane must be selected, for example cation exchange membrane for redox active anions. For the quinone-hydroquinone (HQ/Q) system, there is a need for proton exchange membrane such as sulfonated tetrafluoroethylene fluoropolymer copolymer (e.g., Nafion). Thus, the choice and design of the ion exchange membrane is crucial for redox active energy storage systems and has to be selected according to the nature of the charged species. The necessity of a proton exchange membrane, however, significantly increases the cell costs as compared to general ion exchange membranes (cationic and anionic); the costs of popular Nafion membranes are several times higher than general cation exchange membranes, as used in this study.⁴⁷ Therefore, our PFC system can be more cost-effective in terms

of membrane price than any other redox electrolyte system, where a proton exchange membrane is required.

With a restricted transport of anions, the use of a cation exchange membrane (see Supporting Information, Figure S2), as done in our study, is effective to stop any reduced or oxidized PFC anions from being transferred between the two electrodes. We also note that the use of an IEM does not alter the electrochemical performance of an electrical-double layer using, for example, 1 M Na_2SO_4 , but just provides lower power handling due to the intrinsically lower ion transport rates, when compared to a porous separator (see Supporting Information, Figure S3). For the use of IEMs, while still achieving charge neutrality, we have to consider a slightly different charge compensation mechanism (see Supporting Information, Figure S4). In the case of a cation exchange membrane, only cations can pass through the barrier between the two electrodes. Thus, to accomplish charge neutrality of the bulk electrolyte, an excess of cations has to travel to the compartment near the negatively polarized electrode, while cations are depleted on the opposite side. In the case of a conventional porous separator system, cations and anions both move freely between the two electrode compartments and an equal ion concentration is maintained in the bulk electrolyte on both sides.

3.3. Effect of an Excess Volume of Redox Electrolyte.

The amount of excess volume of the redox electrolyte plays an important role for the electrochemical performance. Because not all ferricyanide/ferrocyanide ions are confined in carbon nanopores, the electrolyte in the carbon macropores, in the space between carbon particles, and in the residual parts of the device volume, serves as a reservoir.⁹ Using a redox electrolyte, charge is not only stored via electrostatically immobilized ions at the fluid–solid interface or by using redox-active materials (e.g., metal oxides), but via reduced/oxidized species of redox-active molecules throughout the bulk electrolyte. In this sense, a redox electrolyte hybrid energy storage system can be seen as a redox flow battery operated in a nonflow mode with a very small reservoir volume.

Lacking forced mechanical convection, ion transport can only be accomplished by diffusion. When operating our cell without carbon electrodes but only with the graphite current collectors (i.e., “empty” cell with a total redox electrolyte volume of 0.18 cm^3), a very small energy storage capacity was seen. In particular, a device capacity of 0.016 mAh was obtained after 2

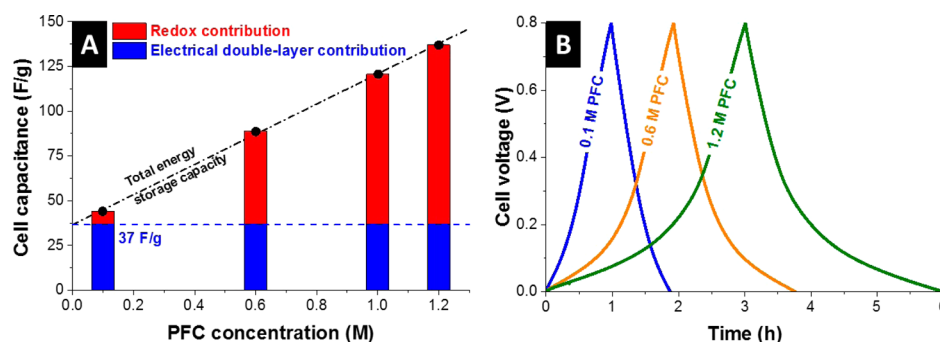


Figure 4. (A) Calculated cell capacitance measured with galvanostatic cycling at 10 mA/g when using an ion exchange membrane (IEM; type FKS30) for different PFC concentrations. (B) Galvanostatic charge–discharge profiles obtained at different PFC concentrations (10 mA/g).

h charging, which is about 3% of the maximum capacity obtained for the full PFC hybrid cell. Further charging did not significantly improve the capacity, which saturated at ca. 0.019 mAh after 6 h of charging. Possibly, the formation of the electrical double-layer on the flat graphite surface may limit the further access of the PFC ions for Faradaic charge transfer. The presence of an electrical double-layer at the flat electrode/electrolyte interface may also relate to the very fast voltage drop over time when monitoring the OCV over time (Figure 3A). Longer charging times reduce the voltage drop over time to some extent, but the performance is still inferior to the 1 M Na₂SO₄ system (Figure 2C). A probable explanation is that electroadsorbed PFC ions on the graphite current collector rearrange as soon as the external potential is removed, and through this rearrangement, the charged PFC ions diffuse away to the bulk electrolyte. The electrolyte charge balance through solvated potassium ions may also influence the electrochemical performance of the system by introducing issues like osmotic pressure and electrolyte volume changes via water transfer through selective ion diffusions (Figure S4).^{48,49}

These data illustrate that a significant amount of an electrolyte excess volume may contribute to the self-discharge. Excess, in this context, refers to any extra volume of redox electrolyte not limited to the fluid–solid interface; in context of porous carbons, excess would be any extra volume beyond the pore volume and the space between the carbon particles. This can be validated for the PFC cell with carbon electrodes, where an excess electrolyte volume of 4 mL was added (i.e., 80 times larger than the total electrode volume). Introduction of this extra volume did increase the energy ratings by 15%, but led to a very significant voltage drop over time, as exemplified for 1.2 M PFC (Figure 3B). After around 5 h, the data of 1.2 M PFC show an OCV drop over time comparably low as an electrical double-layer capacitor using a cation exchange membrane (the so far discussed data were obtained after 2 h of charging via voltage holding at 0.8 V).

Without excess volume, 1.2 M PFC shows noticeably less OCV decay than 1 M Na₂SO₄ when no voltage holding time is applied, particularly at the initial state (Figure 3C). This implies that the majority of the OCV decay of the double-layer capacitor system (1 M Na₂SO₄) originates from charge redistribution at the interface between porous electrode and the electrolyte. In contrast, the PFC hybrid system (1.2 M PFC) suffers less from charge redistribution, because the main governing charge storage mechanism of the PFC system is not just double-layer formation, but largely the reversible Faradaic reaction of redox electrolyte.^{46,50} Compared to no holding time, a long holding time of 10 h led to a severely suppressed OCV

decay, possibly due to a longer equalization time introduced for the charge distribution.^{51,52} In comparison to the often overlooked self-discharge issue of the redox electrolyte system,^{28,40} our system's performance is a significant step forward toward the practical energy storage applications, where energy is often required to be stored up to several hours.

3.4. Effect of PFC Concentration. Based on the fact that the ferricyanide/ferrocyanide ions have a reversible redox contribution, the capacity of the PFC hybrid system is expected to scale with the concentration of the PFC ions in the electrolyte. This is also accomplished by the very large fluid–solid interface between nanoporous carbon and the electrolyte to overcome the issues illustrated for the empty cell (Figure 3A). We varied the PFC concentration in water between 0.1 and 1.2 M, with the latter representing a value reaching the maximum solubility. The maximum solubility of potassium ferricyanide in water is 385.5 g/L at 25 °C, which corresponds to 1.2 M and is almost 2 times as high as the solubility of hydroquinone (0.65 M at 25 °C). In the latter case, there is a fundamental concentration limit posed by acidic media, such as H₂SO₄, which are needed due to the requirement of protons in the quinone/hydroquinone reaction.⁵³ Where the system behaves like an ideal capacitor, eqs 3 and 4 are employed to calculate the specific energy, E_{sp} (Wh/kg), and the specific power, P_{sp} (W/kg):

$$E_{sp} = \frac{C \cdot U^2}{2 \cdot 3600} \quad (3)$$

$$P_{sp} = \frac{U^2}{4 \cdot ESR \cdot m_{total}} \quad (4)$$

In these equations, U is the applied voltage, C is the cell capacitance, and the factor 3600 comes from the unit conversion from Joule to Watt-hour. A linear correlation was found between the energy storage capacitance and the PFC concentration (Figure 4A). The cell capacitance values were determined by galvanostatic cycling with potential limitation (GCPL) at the low specific current of 10 mA/g through eq 5:

$$C = \frac{i \cdot t}{m_{total} \cdot U} \quad (5)$$

where i is the constant discharging current, t is the discharging time, and U is the applied voltage window.

At a low specific current (such as 10 mA/g) we can assume the measured capacitance to be near the equilibrium (maximum) of the electrical double-layer capacitance and as a first approximation, this value can be considered to be the same

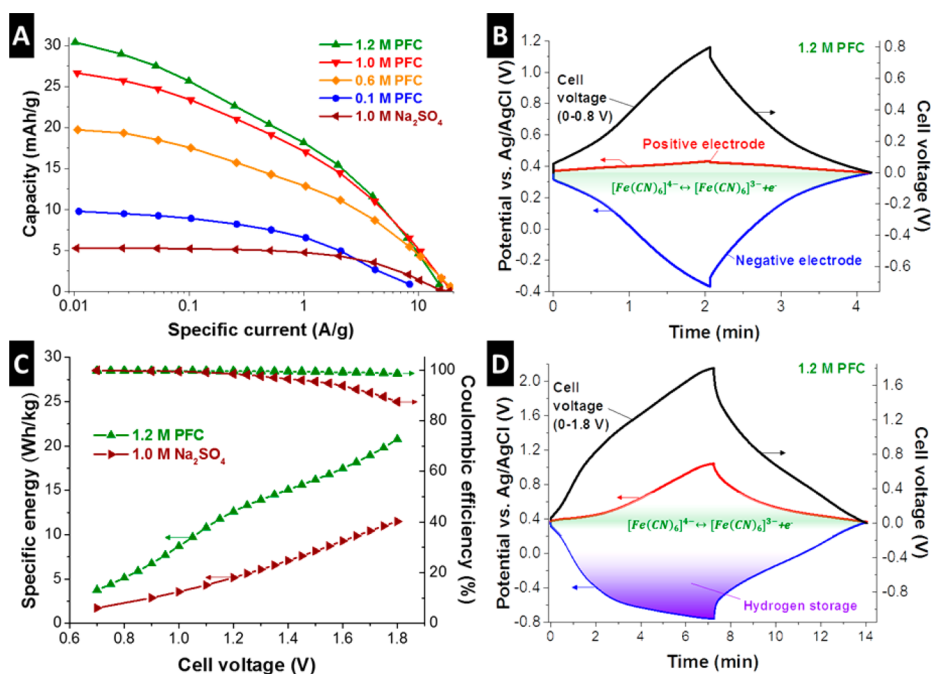


Figure 5. Electrochemical properties of the PFC hybrid system with various concentrations and 1 M Na₂SO₄ in a full cell configuration without a reference electrode (A, C) and the potential profile of the negative and the positive electrodes for 1.2 M PFC system in a full cell configuration with Ag/AgCl reference electrode (B, D); a full cell was charged and discharged in different voltage ranges at 0.5 A/g while measuring individual potential at each electrode. (A) Galvanostatic power handling behavior of the PFC hybrid systems with different PFC concentration and 1 M Na₂SO₄ as comparison. (B) A full cell in 1.2 M PFC was charged and discharged in the voltage range of 0–0.8 V at 0.5 A/g while measuring the individual potential at each electrode. (C) The specific energy of the cells was measured by cyclic voltammetry at the scan rate of 1 mV/s with various voltage window from 0.7 to 1.8 V via eq 1. Coulombic efficiency on the right y-axis indicates the chemical stability of each system.

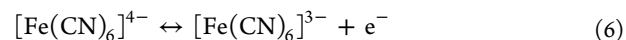
for all PFC concentrations. Therefore, the value of the electrical double-layer capacitance of the PFC electrolyte and the activated carbon electrode may be determined at the intersection of the fitted line with the *y*-axis in Figure 4A. The determined equilibrium double-layer capacitance of 37 F/g corresponds with the data seen from CV analysis (Figure S5B).

At a low PFC concentration (0.1 M PFC), a capacitor-like GCPL curve was observed with a characteristic triangular shape; however, the transition from a capacitor-like to a redox-dominated system occurred when increasing the PFC concentration (Figure 4B). Following the recommendations in recent review articles,^{54–56} one should abstain from calling the redox-enabled PFC system supercapacitor or pseudocapacitor, because the electrochemical response of our PFC redox electrolyte system has both capacitive and battery-like elements. For that reason, the term “hybrid system” is preferably used in this work. For comparison, a cell capacitance value of 597 F/g can be derived for our system when the voltage window is taken from 0 to 0.1 V through eq 5, whereas the value drops to 137 F/g considering the voltage window up to 0.8 V. Hence, we will use the concept of cell capacity (unit: mAh/g) instead of cell capacitance (unit: F/g) to quantify the performance of the PFC hybrid system.

3.5. Power Handling and Performance Stability. As shown in Figure 5A, the charge storage capacity of the 1.2 M PFC system (30.4 mAh/g) is more than 6 times higher than for the supercapacitor system (1 M Na₂SO₄: 5 mAh/g). One remarkable feature of the PFC hybrid system is its excellent energy storage capacity retention. Even at a high specific current of 10 A/g, capacity values of ca. 4.8 mAh/g can be found for the PFC system, which is comparable to the equilibrium capacity (ca. 5 mAh/g) of the electrical double-

layer capacitor. Also, at 10 A/g, the capacity of the 1 M Na₂SO₄ system has already dropped below 1 mAh/g, which is less than one-fifth of the capacity of 1.2 M PFC at the same specific current. Obviously, not only the charge storage capacity can be significantly improved for the hybrid system, but it is also possible to obtain a power handling superior to a conventional supercapacitor system.

The excellent power handling of the PFC system may surprise when considering that redox-systems, especially battery-like systems, commonly show a very limited capacity retention, when transitioning from moderate to high charge/discharge rates of ca. 1–10 W/g, which is in our case in the specific current range from 1 to 10 A/g.⁵ As pointed out by Tian et al.,⁴² the high power handling performance of the PFC system is believed to be due to its charge storage mechanism. As schematically depicted in Figure 1A, reduced ferrocyanide ions will be attracted to the positive porous carbon electrode when an external potential is applied. Charge transfer can occur for ferrocyanide ions at the fluid–solid interface through the following chemical reaction (eq 6):



This electron transfer mechanism is much faster than the mere diffusion of the redox-active molecules at the fluid–solid interface as we have observed earlier with Nyquist plots (Figure 2B) exhibiting no semicircle, which implies a charge transfer resistance. The redox peak currents follow a $v^{0.7}$ relation (v : scan rate; Figure S5A) instead of a classical diffusion controlled $v^{0.5}$ relation, which also supports the electrosorption accelerated electron transfer mechanism for the PFC hybrid system in well confined nanopores.^{57,58} This synergetic charge storage mechanism was also proven by the much faster redox kinetics

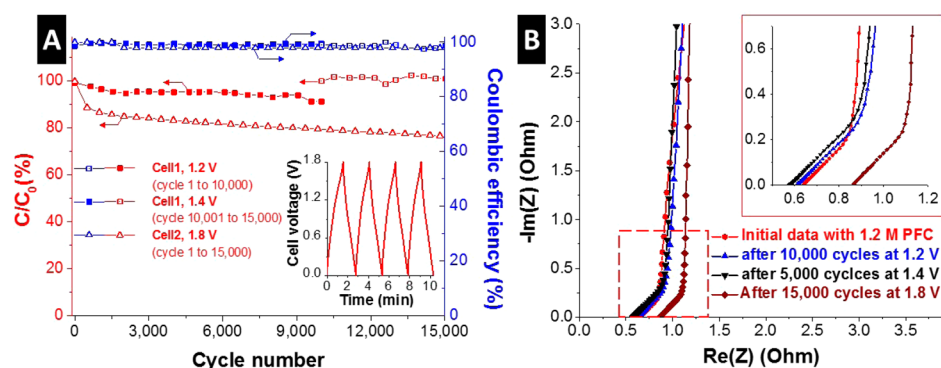


Figure 6. (A) Galvanostatic charge/discharge cycling stability was obtained for Cell1 at 400 mA/g from 0 to 1.2 V and for Cell2 at 1 A/g from 0 to 1.8 V with 1.2 M PFC; the inset shows the galvanostatic charge/discharge profiles for 4 cycles from Cell2. Subsequently, Cell1 was tested at 1.4 V for additional 5000 cycles. The Coulombic efficiency was higher than 0.98 for all cycles. (B) Electrochemical impedance spectra of 1.2 M PFC system measured before and after 10 000 galvanostatic cycles at 1.2 V and the subsequent 5000 cycles at 1.4 V from Cell1, and 15 000 cycles at 1.8 V from Cell2. The voltage amplitude of 5 mV was applied at the cell voltage of 0 V; the inset shows the magnified EIS spectra.

Table 1. Summary of the Electrochemical Performances from Other Redox Electrolyte Systems

electrode	redox electrolyte	E_{sp} (Wh/kg)	C_{sp} (F/g)	capacity retention after cycling (%)	ref.
CuS nanotubes	KOH + Na ₂ S + S	592.0 (eq 3)	2175	80 (1000 cycles)	60
nitrogen doped AC	H ₂ SO ₄ + Na ₂ MoO ₄	378.5 (eq 3)	841	88.2 (1000 cycles)	61
porous carbon	HNO ₃ + CuCl ₂	73.0 (eq 8)	4700	99.1 (1000 cycles)	39
reduced graphene oxide	KOH + KI	44.0 (eq 3)	500	81 (5000 cycles)	62
AC	Na ₂ SO ₄ + KI	33 (eq 8)	493	100 (10 000 cycles)	63
AC	KOH + HQ	31.3 (eq 3)	901	35 (4000 cycles)	14
AC	K ₃ Fe(CN) ₆	28.3 (eq 8)		80 (9000 cycles)	this work
polyaniline	H ₂ SO ₄ + K ₄ Fe(CN) ₆	20.0 (eq 8)	342	100 (100 cycles)	64
AC	KOH + <i>p</i> -PD	19.9 (eq 3)	605	94.5 (4000 cycles)	65
AC	H ₂ SO ₄ + KI	19.0 (eq 8)	912	100 (4000 cycles)	66
AC/graphite felt (GF)	H ₂ SO ₄ + Ce	13.8 (eq 8)	232 (AC), 408 (GF)	94 (3000 cycles)	67
AC	H ₂ SO ₄ + KBr	11.6 (eq 8)	572	100 (4000 cycles)	66
AC	KOH + <i>m</i> -PD	10.0 (eq 3)	78	90.7 (10 000 cycles)	68
Co–Al layered double hydroxide	KOH + K ₃ Fe(CN) ₆	not reported	477	not reported	69
AC	K ₄ Fe(CN) ₆	not reported	272	not reported	42

^aThe data are arranged by descending specific energy (E_{sp}). ^bThe specific capacitance (C_{sp}) values can be equivalent of 4 times higher value of the cell capacitance.

at the positive electrode than that of at the negative electrode (Figure 5B). Potential was controlled between the negative and the positive electrode from 0 to 0.8 V at 0.5 A/g in a full cell configuration while measuring simultaneously the potential difference between a reference electrode (Ag/AgCl) and the negative electrode. The green colored area represents the ferricyanide/ferrocyanide redox reactions in a potential range from 0.2 to 0.4 V vs Ag/AgCl as characterized by the plateau of the curve. Interestingly, this redox reaction occurs at both electrodes, while the majority of the reaction takes place at the positive electrode indicating much active redox reactions through the improved kinetic.

The high power handling ability is complemented with an excellent performance stability in terms of voltage stability window and cyclic lifetime. To determine the voltage stability window, S -value analysis can be effectively applied introducing S -value as³⁷

$$S = \frac{Q_{\text{char}}}{Q_{\text{dis}}} - 1 \quad (7)$$

where Q_{char} is the accumulated charge during charging and Q_{dis} is the charge restored during discharging. When the applied voltage exceeds the chemical decomposition potential of the

electrolyte, the Faradaic leakage currents ($d^2S/dV^2 \neq 0$) greatly contribute to the increase in S -value and can be distinguished from the linear contribution of the non-Faradaic leakage current ($dS/dV \neq 0$, but $d^2S/dV^2 = 0$). In case of 1.0 M Na₂SO₄, the stable voltage window can be considered to extend to around 1.4–1.55 V as the sudden slope change in the S -value vs cell voltage plot (Supporting Information, Figure S5C) indicates the onset of the chemical decomposition. A similar result has been reported from a similar condition as the actual stability was further confirmed by additional floating test.³⁷ By contrast, a cyclic voltammogram indicating very high stability (Supporting Information, Figure S5D) can be seen for the PFC hybrid system even at 1.8 V, which translates to an almost flat slope in the S -value plot (in contrast to 1.0 M Na₂SO₄). At a cell voltage of 1.8 V, the specific energy of the system exceeds 20 Wh/kg, as determined from cyclic voltammetry at the scan rate of 1 mV/s (Figure 5C). The reason for this high stability up to 1.8 V is a biased potential increase at the negative electrode (Figure 5D). We see that the potential at the positive electrode is suppressed by the broad voltage plateau due to ferricyanide/ferrocyanide redox reaction, which leads to a biased potential development at the negative electrode. This positive influence on the extension of the potential window

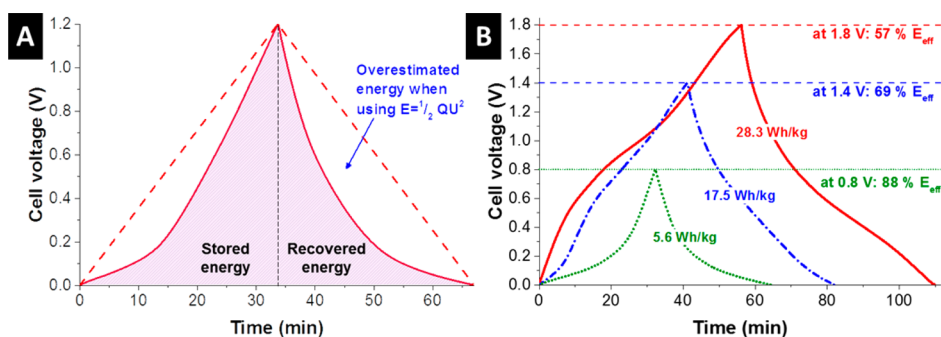


Figure 7. (a) Galvanostatic data for 1.2 M PFC (cation exchange membrane) obtained at 50 mA/g with a Coulombic efficiency of 99% showing the actually stored energy versus the amount of energy incorrectly obtained when assuming $E = \frac{1}{2}QU^2$ (Q , charge; U , voltage). (b) Galvanostatic charging/discharging curve obtained at 50 mA/g with the potential limitation to 0.8, 1.4, and 1.8 V. The values for the specific energy were calculated by eq 8.

may enable hydrogen storage in the micropores at the negative electrode.⁵⁶ As shown in Supporting Information Figure S5D, the peaks in the cyclic voltammogram (cell voltage range from 0 to 1.8 V) indicate the evolution of hydrogen and its reversible chemi-physorption into carbon micropores, as well as possible enhancement related to oxygen-based functionalities.⁵⁹

As neither chemical bonding nor intercalation of PFC ions occurs at the electrode, the PFC hybrid system showed an excellent electrochemical stability as illustrated over 10 000 galvanostatic charge/discharge cycles (Figure 6A) at the cell voltage range from 0 to 1.2 V (Cell1) at a specific current of 400 mA/g (1.2 M PFC, electrode thickness: 200 μm) and over 15 000 cycles from 0 to 1.8 V at a specific current of 1 A/g (Cell2). Cell1 showed a small initial decrease in system capacity over the first 2000 cycles, the performance stabilized at 94–96% with a Coulombic efficiency close to 99% during the remaining 8000 cycles. After applying initial 10 000 cycles at 1.2 V, Cell1 was further tested for 5000 cycles at 1.4 V. During these additional 5000 cycles, no noticeable degradation was observed, which is in agreement with the Nyquist plot (Figure 6B), where essentially no difference could be found from the curves obtained before and after the cycle test at 1.2 and 1.4 V. This indicates a very high electrochemical stability of the entire system including the membrane, electrode, and the electrolyte. A high performance stability over ca. 9,000 cycles was observed for Cell2 even at 1.8 V, as the stability can be evaluated to be the point where the capacity of the cell decreases about 20%, compared to the initial performance. After a rapid performance degradation of ca. 11% in the first 500 cycles, Cell2 showed a rather slow continuous degradation during the remaining 14 500 cycles. The capacity degradation of Cell2 at 1.8 V might have been caused by the oxidation of the electrode through slow irreversible chemical reactions, as the Nyquist plot (Figure 6B) obtained after the stability test exhibits higher resistance, compared to the initial performance. In comparison to the cycling stability of other redox electrolyte systems (Table 1), our system provides a capacity retention of 80% up to 9000 cycles at a high cell potential of 1.8 V. This aligns with reports of other redox electrolyte systems with activated carbon (80% capacity retention >10 000 cycles), but not for all, for example a capacity loss >5% per 1000 cycles was documented for CuS nanotubes⁶⁰ or heteroatom containing carbon based electrodes, such as reduced graphene oxides and nitrogen doped activated carbon.^{61,62} In the case of redox electrolytes with quinone functionalities, in-depth understanding of interfacial electro-

chemistry in the carbon micropores is considered to be crucial for the further improvement of the cycling stability.¹⁹

3.6. Specific Energy Evaluation. Up to the present, various redox-active electrolytes have been studied (Table 1), yielding in general a specific energy of 5–20 Wh/kg.⁸ These values are significantly higher compared to many supercapacitor systems, especially when operating nonredox materials in aqueous media at limited voltage ranges up to 1.2 V. Noticeably, a few studies have reported even higher values: 592 Wh/kg for polysulfide electrolyte,⁶⁰ 73 Wh/kg for Cu^{2+} electrolyte,³⁹ and 31.3 Wh/kg for a quinone/hydroquinone redox couple.¹⁴ However, the specific energy of the redox electrolyte systems strongly depends on how the values have been calculated and normalized. A particularly problematic issue is the adaption of battery- or supercapacitor-related calculation methods. With the linear correlation between charge and voltage, the use of eq 3 and eq 5 is a facile way to calculate the energy for a supercapacitor device (including actual pseudocapacitors).

However, if these supercapacitor equations are used to calculate the energy ratings of a noncapacitive (i.e., Faradaic) system, the actual device performance may be severely overestimated.⁵⁴ This is illustrated for a typical galvanostatic charge/discharge profile of 1.2 M PFC at 50 mA/g when using a FKS10 type cation exchange membrane (Figure 7A). As seen from Figure 7A, the blue colored area under the dashed triangle is significantly larger than the area representing the actually stored energy (dashed area). Thus, a more realistic value for the specific energy can be obtained through eq 8 from the GCPL discharging data of a full cell by integrating the as-measured cell voltage with respect to the discharging time while applying any other corrections:

$$E = \frac{i}{m_{\text{total}}} \int U dt \quad (8)$$

The specific energy values can also greatly vary depending on how the values are normalized. In general, the specific energy of a laboratory-scale supercapacitor is normalized to the mass of the electrode, without considering the mass of the electrolyte and the separator materials. However, the energy values should not be normalized to just the mass of the dry carbon electrodes when the system has capacity to store energy in the volume of the reserved electrolyte; particularly, gel electrolyte containing conductive polymers, and redox additives.^{9,45} This discussion is in analogy to the disputed normalization of charge storage

capacity to just the amount of a solid redox-active species, such as polyaniline on nanoporous carbons.⁷⁰

For our hybrid system employing a concentration of 1.2 M PFC and a cell voltage of 1.2 V, we calculated a specific energy of 10.5 Wh/kg by means of eq 8. This would correspond to a specific energy of 27 Wh/kg if one would be using eq 3. Another important aspect regarding the calculation is the energy efficiency of the system: it is a common misconception that even a Coulombic efficiency of nearly 100% would imply an energy efficiency of also almost 100%, even in supercapacitors.⁵⁴ In most cases of reported redox electrolyte based supercapacitors, energy efficiency less than 50% can be seen when the practical energy efficiency is calculated based on eq 8.⁵⁴ The energy efficiency of the redox electrolyte-based system is expected to be lower as the cell is charged up to a higher voltage, because the redox reactions at higher potentials contribute to the overpotential, as well as the more significant influence of ion redistribution. At the low voltage of 0.8 V, the energy efficiency, E_{eff} of the PFC hybrid system is 88% (Figure 7B), as determined from GCPL at a specific current of 50 mA/g. The energy efficiency drops to 57% at a higher voltage (1.8 V), whereas the Coulombic efficiency was measured to be still 96%. This illustrates the high need to differentiate more closely between the concepts of charge storage and energy storage. Interestingly, for the purely capacitive system 1 M Na_2SO_4 , the energy efficiency at 1.4 V was found to be only 77.2%, which is far lower than the typical values of >95% expected for supercapacitors at a low specific current. Therefore, it seems that the low energy efficiency should be considered as the supercapacitor research in aqueous system is aiming for high voltage applications (>1.2 V). When our redox active energy storage system was charged at higher voltage, for instance at 1.8 V, the energy efficiency dropped to 57%, which is still at a considerably close value of some of the rechargeable battery systems.⁷¹ Depending on the application, lower energy efficiency at higher applied voltage may still be accepted considering the high power performance over 10 A/g and the maximum specific energy up to 28.3 Wh/kg (Figure 7B); the volumetric energy storage capacity is about 11.4 Wh/L, when the energy storage capacity is normalized to the volume of the both electrodes and the membrane.

For a facile performance comparison of our system's performance, we have mapped the data in a Ragone plot (Figure 8) by applying eq 2. In the graph, the data of the PFC

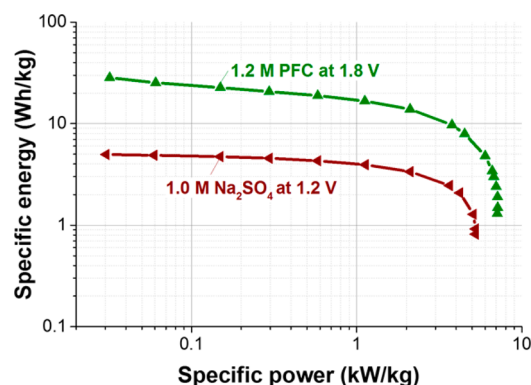


Figure 8. Best optimized performance of the PFC system is presented in form of a Ragone plot and compared to the performance of aqueous 1 M Na_2SO_4 when using the same electrode material/size/configuration.

system are complemented by a measurement of 1 M Na_2SO_4 measured in the same cell with a porous separator instead of a cation exchange membrane. The performance of the PFC cell is superior to the electrical double-layer capacitor not only in terms of energy but also in terms of power ratings. By virtue of the fast charge transfer and storage mechanism, the PFC hybrid system showed a maximum specific power of 7.14 kW/kg, still retaining the specific energy of 1.9 Wh/kg. The system with 1 M Na_2SO_4 , for comparison, yielded a maximum specific energy of 5.0 Wh/kg; at an energy rating of 1.5 Wh/kg, the power rating of the PFC system was 7.1 kW/kg, whereas the supercapacitor system showed 4.7 kW/kg. Thus, we can conclude that PFC in combination with an IEM does not only enable to double the energy storage ability but also to enhance the power handling ability.

4. CONCLUSIONS

Potassium ferricyanide is a promising electrolyte that can capitalize on both the formation of an electrical double-layer and fast redox reactions by the virtue of it being a redox electrolyte. As a benefit for implementation, we have shown that standard activated carbon electrodes, as commonly used for supercapacitors, can be employed in conjunction with an aqueous electrolyte. The electrochemical performance largely depends on PFC concentration in the electrolyte and also the presence of an excess amount of electrolyte has to be considered. The beneficial performance of PFC can only be fully exploited when replacing a porous separator (as used for supercapacitors) with a cation exchange membrane (as used for redox-flow batteries or fuel cells) to suppress the shuttle effect of ferricyanide/ferrocyanide ions, which leads to a high leakage current. The cost of cation exchange membranes is still a concern for cost-effective energy storage applications; however, the cost of the cation exchange membrane is expected to be further reduced through low cost materials such as non-fluorinated hydrocarbon membrane or the direct coating of the ion-exchange resin on the electrode material.⁴⁷ We benchmarked the performance up to 1.2 M PFC concentration, which is the limit to avoid precipitation.⁵³ The stability test with optimized cell at 1.2 M PFC demonstrates very high longevity up to 10 000 cycles at 1.2 and 1.8 V, and a possible stability voltage window up to 1.8 V. Our system showed a specific energy of 28.3 Wh/kg (11.4 Wh/L) and specific power of 7.14 kW/kg, which can be converted to 2.9 kW/L or 1.2 kW/m², when normalized to the volume of the two electrodes and the membrane, or to the membrane area, respectively. The specific energy of our PFC system is calculated by integrating the voltage with respect to the discharging time from the GCPL curves as the PFC system showed a slightly battery-like feature at high concentration of PFC; for comparison, an over-estimated specific energy of 39.5 Wh/kg and specific capacitance of 597 F/g can be derived by assuming the system as a capacitor. Further improvements may be possible by employing advanced carbon nanomaterials as electrodes whose pore volume is large to reserve electrolyte but limited to nanopores to minimize diffusion kinetics of redox ions and to prevent the voltage drop via the ion diffusion to the bulk electrolyte.

■ ASSOCIATED CONTENT

Supporting Information

The Supporting Information is available free of charge on the ACS Publications website at DOI: 10.1021/acsami.6b06264.

Schematic setup of the electrochemical cell, scanning electron micrographs of the membranes, supplementary electrochemical data (PDF).

AUTHOR INFORMATION

Corresponding Author

*V. Presser. E-mail: volker.presser@leibniz-inm.de.

Notes

The authors declare no competing financial interest.

ACKNOWLEDGMENTS

We acknowledge funding from the German Federal Ministry for Research and Education (BMBF) in support of the nanoEES^{3D} project (award number 03EK3013) as part of the strategic funding initiative energy storage framework. The authors thank Prof. Eduard Arzt (INM) for his continuing support and FuMA-Tech for kindly providing membranes and helpful discussions. We also thank Simon Fleischmann, Jeongwook Jeon, Anna Schreiber, and Dr. Ingrid Grobelsek (all INM) for discussions and technical support.

REFERENCES

- (1) Miller, J. R. Valuing Reversible Energy Storage. *Science* **2012**, *335* (6074), 1312–1313.
- (2) Yang, Z.; Zhang, J.; Kintner-Meyer, M. C. W.; Lu, X.; Choi, D.; Lemmon, J. P.; Liu, J. Electrochemical Energy Storage for Green Grid. *Chem. Rev.* **2011**, *111* (5), 3577–3613.
- (3) Goodenough, J. B. Energy Storage Materials: A Perspective. *Energy Stor. Mater.* **2015**, *1*, 158–161.
- (4) Simon, P.; Gogotsi, Y.; Dunn, B. Where Do Batteries End and Supercapacitors Begin? *Science* **2014**, *343* (6176), 1210–1211.
- (5) Simon, P.; Gogotsi, Y. Materials for Electrochemical Capacitors. *Nat. Mater.* **2008**, *7*, 845–854.
- (6) Béguin, F.; Presser, V.; Balducci, A.; Frackowiak, E. Carbons and Electrolytes for Advanced Supercapacitors. *Adv. Mater.* **2014**, *26* (14), 2219–2251.
- (7) Péan, C.; Merlet, C.; Rotenberg, B.; Madden, P. A.; Taberna, P.-L.; Daffos, B.; Salanne, M.; Simon, P. On the Dynamics of Charging in Nanoporous Carbon-Based Supercapacitors. *ACS Nano* **2014**, *8* (2), 1576–1583.
- (8) Senthilkumar, S. T.; Selvan, R. K.; Melo, J. S. Redox Additive/Active Electrolytes: A Novel Approach to Enhance the Performance of Supercapacitors. *J. Mater. Chem. A* **2013**, *1* (40), 12386–12394.
- (9) Akinwolemiwa, B.; Peng, C.; Chen, G. Z. Redox Electrolytes in Supercapacitors. *J. Electrochem. Soc.* **2015**, *162* (5), A5054–A5059.
- (10) Yu, L.; Chen, G. Z. Redox Electrode Materials for Supercapacitors. *J. Power Sources* **2016**, *326*, 604.
- (11) Naoi, K.; Naoi, W.; Aoyagi, S.; Miyamoto, J.-I.; Kamino, T. New Generation “Nanohybrid Supercapacitor”. *Acc. Chem. Res.* **2013**, *46* (5), 1075–1083.
- (12) Naoi, K.; Ishimoto, S.; Miyamoto, J.-I.; Naoi, W. Second Generation “Nanohybrid Supercapacitor”: Evolution of capacitive energy storage devices. *Energy Environ. Sci.* **2012**, *5* (11), 9363–9373.
- (13) Fleischmann, S.; Jäckel, N.; Zeiger, M.; Krüner, B.; Grobelsek, I.; Formanek, P.; Choudhury, S.; Weingarh, D.; Presser, V. Enhanced Electrochemical Energy Storage by Nanoscopic Decoration of Endohedral and Exohedral Carbon with Vanadium Oxide via Atomic Layer Deposition. *Chem. Mater.* **2016**, *28* (8), 2802–2813.
- (14) Roldán, S.; Blanco, C.; Granda, M.; Menéndez, R.; Santamaría, R. Towards a Further Generation of High-Energy Carbon-Based Capacitors by Using Redox-Active Electrolytes. *Angew. Chem., Int. Ed.* **2011**, *50* (7), 1699–1701.
- (15) Anjos, D. M.; McDonough, J. K.; Perre, E.; Brown, G. M.; Overbury, S. H.; Gogotsi, Y.; Presser, V. Pseudocapacitance and Performance Stability of Quinone-Coated Carbon Onions. *Nano Energy* **2013**, *2* (5), 702–712.
- (16) Roldán, S.; Granda, M.; Menéndez, R.; Santamaría, R.; Blanco, C. Mechanisms of Energy Storage in Carbon-Based Supercapacitors Modified with a Quinoid Redox-Active Electrolyte. *J. Phys. Chem. C* **2011**, *115* (35), 17606–17611.
- (17) Tian, Y.; Xue, R.; Zhou, X.; Liu, Z.; Huang, L. Double Layer Capacitor Based on Active Carbon and Its Improved Capacitive Properties Using Redox Additive Electrolyte of Anthraquinonedisulphonate. *Electrochim. Acta* **2015**, *152*, 135–139.
- (18) Gastol, D.; Walkowiak, J.; Fic, K.; Frackowiak, E. Enhancement of the Carbon Electrode Capacitance by Brominated Hydroquinones. *J. Power Sources* **2016**, *326*, 587.
- (19) Le Comte, A.; Chhin, D.; Gagnon, A.; Retoux, R.; Brousse, T.; Belanger, D. Spontaneous Grafting of 9, 10-Phenanthrenequinone on Porous Carbon as an Active Electrode Material in an Electrochemical Capacitor in an Alkaline Electrolyte. *J. Mater. Chem. A* **2015**, *3* (11), 6146–6156.
- (20) Li, Q.; Li, K.; Sun, C.; Li, Y. An investigation of Cu²⁺ and Fe²⁺ Ions as Active Materials for Electrochemical Redox Supercapacitors. *J. Electroanal. Chem.* **2007**, *611* (1), 43–50.
- (21) Sun, G.; Li, K.; Sun, C. Electrochemical Performance of Electrochemical Capacitors Using Cu(II)-Containing Ionic Liquid as the Electrolyte. *Microporous Mesoporous Mater.* **2010**, *128* (1–3), 56–61.
- (22) Su, L. H.; Gong, L. Y.; Lu, H. T.; Xu, Q. Enhanced Low-Temperature Capacitance of MnO₂ Nanorods in a Redox-Active Electrolyte. *J. Power Sources* **2014**, *248*, 212–217.
- (23) Yu, H.; Wu, J.; Fan, L.; Lin, Y.; Chen, S.; Chen, Y.; Wang, J.; Huang, M.; Lin, J.; Lan, Z.; Huang, Y. Application of a Novel Redox-Active Electrolyte in MnO₂-Based Supercapacitors. *Sci. China: Chem.* **2012**, *55* (7), 1319–1324.
- (24) Zhang, Z. J.; Zhu, Y. Q.; Chen, X. Y.; Cao, Y. Pronounced Improvement of Supercapacitor Capacitance by Using Redox Active Electrolyte of p-Phenylenediamine. *Electrochim. Acta* **2015**, *176*, 941–948.
- (25) Conway, B. E. *Electrochemical Supercapacitors*, 1st ed.; Springer: Berlin, Germany, 1999; p 736.
- (26) Augustyn, V.; Come, J.; Lowe, M. A.; Kim, J. W.; Taberna, P.-L.; Tolbert, S. H.; Abruña, H. D.; Simon, P.; Dunn, B. High-Rate Electrochemical Energy Storage Through Li⁺ Intercalation Pseudocapacitance. *Nat. Mater.* **2013**, *12* (6), 518–522.
- (27) Lota, G.; Frackowiak, E. Striking Capacitance of Carbon/Iodide Interface. *Electrochem. Commun.* **2009**, *11* (1), 87–90.
- (28) Chen, L.; Bai, H.; Huang, Z.; Li, L. Mechanism Investigation and Suppression of Self-Discharge in Active Electrolyte Enhanced Supercapacitors. *Energy Environ. Sci.* **2014**, *7* (5), 1750–1759.
- (29) Li, L.; Kim, S.; Wang, W.; Vijayakumar, M.; Nie, Z.; Chen, B.; Zhang, J.; Xia, G.; Hu, J.; Graff, G.; Liu, J.; Yang, Z. A Stable Vanadium Redox-Flow Battery with High Energy Density for Large-Scale Energy Storage. *Adv. Energy Mater.* **2011**, *1* (3), 394–400.
- (30) Weber, A. Z.; Mench, M. M.; Meyers, J. P.; Ross, P. N.; Gostick, J. T.; Liu, Q. Redox Flow Batteries: A Review. *J. Appl. Electrochem.* **2011**, *41* (10), 1137–1164.
- (31) Frackowiak, E.; Fic, K.; Meller, M.; Lota, G. Electrochemistry Serving People and Nature: High-Energy Ecocapacitors based on Redox-Active Electrolytes. *ChemSusChem* **2012**, *5* (7), 1181–1185.
- (32) Jäckel, N.; Rodner, M.; Schreiber, A.; Jeongwook, J.; Zeiger, M.; Aslan, M.; Weingarh, D.; Presser, V. Anomalous or Regular Capacitance? The Influence of Pore Size Dispersion on Double-Layer Formation. *J. Power Sources* **2016**, *326*, 660.
- (33) Jäckel, N.; Weingarh, D.; Zeiger, M.; Aslan, M.; Grobelsek, I.; Presser, V. Comparison of Carbon Onions and Carbon Blacks as Conductive Additives for Carbon Supercapacitors in Organic Electrolytes. *J. Power Sources* **2014**, *272*, 1122–1133.
- (34) Weingarh, D.; Zeiger, M.; Jäckel, N.; Aslan, M.; Feng, G.; Presser, V. Graphitization as a Universal Tool to Tailor the Potential-Dependent Capacitance of Carbon Supercapacitors. *Adv. Energy Mater.* **2014**, *4* (13), 1400316.
- (35) Gi Hong, J.; Glabman, S.; Chen, Y. Effect of Inorganic Filler Size on Electrochemical Performance of Nanocomposite Cation Exchange

Membranes for Salinity Gradient Power Generation. *J. Membr. Sci.* **2015**, *482*, 33–41.

(36) Güler, E.; Elizen, R.; Vermaas, D. A.; Saakes, M.; Nijmeijer, K. Performance-Determining Membrane Properties in Reverse Electrodialysis. *J. Membr. Sci.* **2013**, *446*, 266–276.

(37) Weingarth, D.; Noh, H.; Foelske-Schmitz, A.; Wokaun, A.; Kötz, R. A Reliable Determination Method of Stability Limits for Electrochemical Double Layer Capacitors. *Electrochim. Acta* **2013**, *103*, 119–124.

(38) Lee, J.; Kruner, B.; Tolosa, A.; Sathyamoorthi, S.; Kim, D.; Choudhury, S.; Seo, K.-H.; Presser, V. Tin/Vanadium Redox Electrolyte for Battery-Like Energy Storage Capacity Combined with Supercapacitor-Like Power Handling. *Energy Environ. Sci.* **2016**, DOI: 10.1039/C6EE00712K.

(39) Mai, L. Q.; Minhas-Khan, A.; Tian, X. C.; Hercule, K. M.; Zhao, Y. L.; Lin, X.; Xu, X. Synergistic Interaction Between Redox-Active Electrolyte and Binder-Free Functionalized Carbon for Ultrahigh Supercapacitor Performance. *Nat. Commun.* **2013**, *4*, 2923.

(40) Tachibana, M.; Ohishi, T.; Tsukada, Y.; Kitajima, A.; Yamagishi, H.; Murakami, M. Supercapacitor Using an Electrolyte Charge Storage System. *Electrochemistry* **2011**, *79* (11), 882–886.

(41) Tachibana, M.; Tsukada, Y.; Ohishi, T.; Yamagishi, H.; Murakami, M. New High Capacity Electric Energy Storage Device with an Electrolyte that Contains a Conducting Polymer. *Kobunshi Ronbunshu* **2009**, *66* (7), 259–265.

(42) Tian, Y.; Yan, J.; Xue, R.; Yi, B. Capacitive Properties of Activated Carbon in $K_4Fe(CN)_6$. *J. Electrochem. Soc.* **2011**, *158* (7), A818–A821.

(43) Brousse, T.; Bélanger, D.; Long, J. W. To Be Or Not To Be Pseudocapacitive? *J. Electrochem. Soc.* **2015**, *162* (5), A5185–A5189.

(44) Fic, K.; Meller, M.; Frackowiak, E. Interfacial Redox Phenomena for Enhanced Aqueous Supercapacitors. *J. Electrochem. Soc.* **2015**, *162* (5), A5140–A5147.

(45) Senthilkumar, S. T.; Selvan, R. K.; Ponpandian, N.; Melo, J. S. Redox Additive Aqueous Polymer Gel Electrolyte for an Electric Double Layer Capacitor. *RSC Adv.* **2012**, *2* (24), 8937–8940.

(46) Andreas, H. A. Self-Discharge in Electrochemical Capacitors: A Perspective Article. *J. Electrochem. Soc.* **2015**, *162* (5), A5047–A5053.

(47) Yee, R.; Rozendal, R.; Zhang, K.; Ladewig, B. Cost Effective Cation Exchange Membranes: A Review. *Chem. Eng. Res. Des.* **2012**, *90* (7), 950–959.

(48) Sukkar, T.; Skyllas-Kazacos, M. Water Transfer Behaviour Across Cation Exchange Membranes in the Vanadium Redox Battery. *J. Membr. Sci.* **2003**, *222* (1–2), 235–247.

(49) Mohammadi, T.; Chieng, S. C.; Skyllas Kazacos, M. Water Transport Study Across Commercial Ion Exchange Membranes in the Vanadium Redox Flow Battery. *J. Membr. Sci.* **1997**, *133* (2), 151–159.

(50) Black, J.; Andreas, H. A. Effects of Charge Redistribution on Self-Discharge of Electrochemical Capacitors. *Electrochim. Acta* **2009**, *54* (13), 3568–3574.

(51) Kowal, J.; Avaroglu, E.; Chamekh, F.; Šenfelds, A.; Thien, T.; Wijaya, D.; Sauer, D. U. Detailed Analysis of the Self-Discharge of Supercapacitors. *J. Power Sources* **2011**, *196* (1), 573–579.

(52) Kaus, M.; Kowal, J.; Sauer, D. U. Modelling the Effects of Charge Redistribution During Self-Discharge of Supercapacitors. *Electrochim. Acta* **2010**, *55* (25), 7516–7523.

(53) Friend, J. A. N.; Smirles, W. N. The Solubility of Potassium Ferricyanide in Water Between 0° and 100°C. *J. Chem. Soc.* **1928**, *0*, 2242–2245.

(54) Laheäär, A.; Przygocki, P.; Abbas, Q.; Béguin, F. Appropriate Methods for Evaluating the Efficiency and Capacitive Behavior of Different Types of Supercapacitors. *Electrochem. Commun.* **2015**, *60*, 21–25.

(55) Stoller, M. D.; Ruoff, R. S. Best Practice Methods for Determining an Electrode Material's Performance for Ultracapacitors. *Energy Environ. Sci.* **2010**, *3* (9), 1294–1301.

(56) Zhang, S.; Pan, N. Supercapacitors Performance Evaluation. *Adv. Energy Mater.* **2015**, *5* (6), 1401401.

(57) Ardizzone, S.; Fregonara, G.; Trasatti, S. Inner and “outer” active surface of RuO_2 electrodes. *Electrochim. Acta* **1990**, *35* (1), 263–267.

(58) Narayanan, R.; Bandaru, P. R. High Rate Capacity through Redox Electrolytes Confined in Macroporous Electrodes. *J. Electrochem. Soc.* **2015**, *162* (1), A86–A91.

(59) Fic, K.; Meller, M.; Menzel, J.; Frackowiak, E. Around the Thermodynamic Limitations of Supercapacitors Operating in Aqueous Electrolytes. *Electrochim. Acta* **2016**, *206*, 496–503.

(60) Qian, L.; Tian, X.; Yang, L.; Mao, J.; Yuan, H.; Xiao, D. High Specific Capacitance of CuS Nanotubes in Redox Active Polysulfide Electrolyte. *RSC Adv.* **2013**, *3* (6), 1703–1708.

(61) Sun, K.; Feng, E.; Peng, H.; Ma, G.; Wu, Y.; Wang, H.; Lei, Z. A Simple and High-Performance Supercapacitor Based on Nitrogen-Doped Porous Carbon in Redox-Mediated Sodium Molybdate Electrolyte. *Electrochim. Acta* **2015**, *158*, 361–367.

(62) Sankar, K. V.; Kalai Selvan, R. Improved Electrochemical Performances of Reduced Graphene Oxide Based Supercapacitor Using Redox Additive Electrolyte. *Carbon* **2015**, *90*, 260–273.

(63) Krüner, B.; Lee, J.; Jäckel, N.; Tolosa, A.; Presser, V. Sub-Micrometer Novolac-Derived Carbon Beads for High Performance Supercapacitors and Redox Electrolyte Energy Storage. *ACS Appl. Mater. Interfaces* **2016**, *8* (14), 9104–9115.

(64) Shanmugavani, A.; Kaviselvi, S.; Sankar, K. V.; Selvan, R. K. Enhanced Electrochemical Performances of PANI Using Redox Additive of $K_4[Fe(CN)_6]$ in Aqueous Electrolyte for Symmetric Supercapacitors. *Mater. Res. Bull.* **2015**, *62*, 161–167.

(65) Wu, J.; Yu, H.; Fan, L.; Luo, G.; Lin, J.; Huang, M. A Simple and High-Effective Electrolyte Mediated with p-Phenylenediamine for Supercapacitor. *J. Mater. Chem.* **2012**, *22* (36), 19025–19030.

(66) Senthilkumar, S.; Selvan, R. K.; Lee, Y.; Melo, J. Electric Double Layer Capacitor and its Improved Specific Capacitance Using Redox Additive Electrolyte. *J. Mater. Chem. A* **2013**, *1* (4), 1086–1095.

(67) Díaz, P.; González, Z.; Santamaría, R.; Granda, M.; Menéndez, R.; Blanco, C. Enhanced Energy Density of Carbon-Based Supercapacitors Using Cerium (III) Sulphate as Inorganic Redox Electrolyte. *Electrochim. Acta* **2015**, *168*, 277–284.

(68) Yu, H.; Fan, L.; Wu, J.; Lin, Y.; Huang, M.; Lin, J.; Lan, Z. Redox-Active Alkaline Electrolyte for Carbon-Based Supercapacitor with Pseudocapacitive Performance and Excellent Cyclability. *RSC Adv.* **2012**, *2* (17), 6736–6740.

(69) Su, L. H.; Zhang, X. G.; Mi, C. H.; Gao, B.; Liu, Y. Improvement of the Capacitive Performances for Co-Al Layered Double Hydroxide by Adding Hexacyanoferrate into the Electrolyte. *Phys. Chem. Chem. Phys.* **2009**, *11* (13), 2195–2202.

(70) Benson, J.; Kovalenko, I.; Boukhalfa, S.; Lashmore, D.; Sanghadasa, M.; Yushin, G. Multifunctional CNT-Polymer Composites for Ultra-Tough Structural Supercapacitors and Desalination Devices. *Adv. Mater.* **2013**, *25* (45), 6625–6632.

(71) Rydh, C. J.; Sandén, B. A. Energy analysis of batteries in photovoltaic systems. Part I: Performance and Energy Requirements. *Energy Convers. Manage.* **2005**, *46* (11–12), 1957–1979.

Supporting Information

HIGH PERFORMANCE HYBRID ENERGY STORAGE WITH POTASSIUM FERRICYANIDE REDOX ELECTROLYTE

Juhan Lee^{1,2}, Soumyadip Choudhury¹, Daniel Weingarh¹, Daekyu Kim,^{1,3} and Volker Presser^{1,2,}*

¹ INM – Leibniz Institute for New Materials, Campus D2 2, 66123 Saarbrücken, Germany

² Department of Materials Science and Engineering, Saarland University, Campus D2 2, 66123 Saarbrücken, Germany

³ School of Energy, Materials and Chemical Engineering, Korea University of Technology and Education, Chungjeol-ro 1600, 31253 Cheonan, Republic of Korea

* Corresponding author's eMail: volker.presser@leibniz-inm.de

Schematic setup of the used electrochemical cell

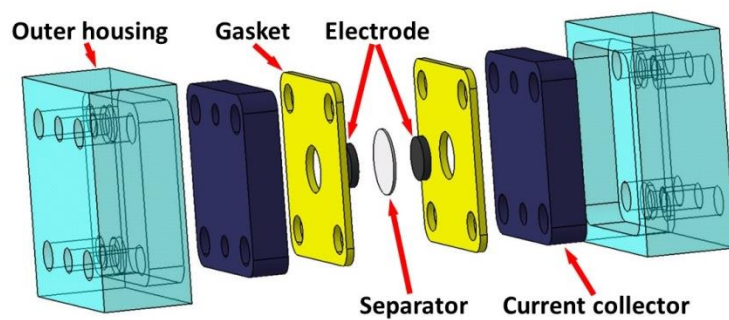


Figure S1: Exploded-view drawing of the used electrochemical cell. Graph adapted from Ref. ¹ published by the Royal Society of Chemistry; reproduced with permission.

A supercapacitor cell operating either with a porous separator or a non-porous ion exchange membrane

An important aspect, poorly evidenced by data in the literature, is the side-by-side benchmarking of a supercapacitor cell with either a porous separator or a non-porous ion-exchange membrane. Thus, we here provide data to illustrate two key aspects: (1) at low rates, the electrochemical performance of an aqueous supercapacitor with an ion exchange membrane (IEM) can be just as good as when using a porous separator, and (2) the long-term stability and self-discharge behavior of an aqueous supercapacitor with an ion exchange membrane are virtually indistinguishable from cells employing a porous separator (called in our study ONP; hydrophilic polytetrafluoroethylene, PTFE, separator Omnipore, Merck Millipore, thickness = 25 μm).

The SEM images of FKS10 and FAS10 (**Figure S2A**) are characteristic examples for all used IEMs, and they show a very smooth and non-porous surface morphology. In contrast, the porous separator shows an open pore network with mesh openings up to ca. 500 nm (**Figure S2B**). We note that this value is still considerably smaller than the particle size of AC (i.e., 2-5 μm), but larger than the size of common conductive additives, like carbon black (typically below 50 nm; not used in this study).

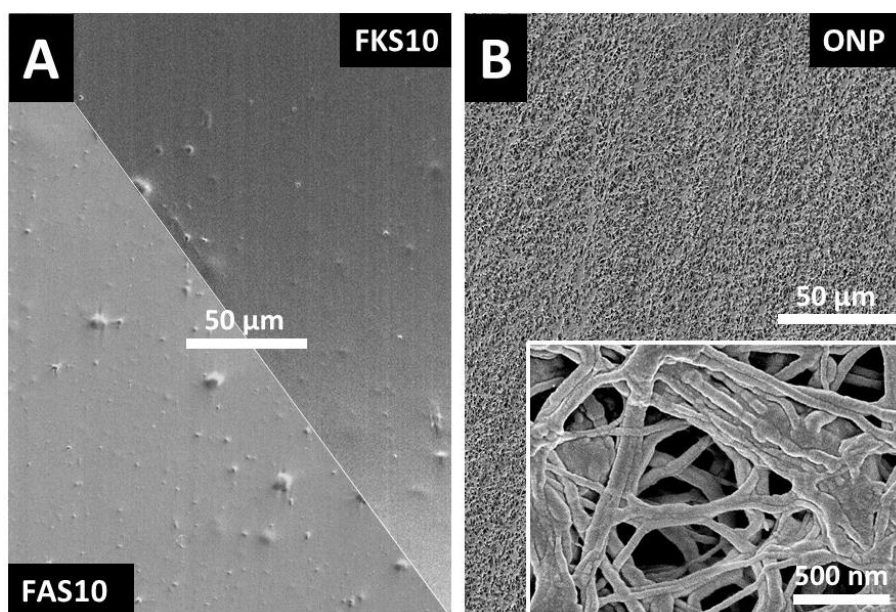


Figure S2: Scanning electron micrographs of (A) cation (FKS10) and anion (FAS10) exchange membranes, and (B) porous polymer separator at two different magnification illustrating the dense and porous morphology of membrane and separator, respectively.

At a slow scan rate of 5 mV/s, the cyclic voltammograms for ONP, FAS10, and FKS10 in 1 M Na₂SO₄ overlap up to 1.2 V cell voltage (**Figure S3A**) and show the characteristic rectangular shape expected for double-layer charge storage. In all cases, based on the discharging currents, the cell capacitance shows a typical value for YP80F, namely 26±1 F/g, and Coulombic efficiencies of around 99%. Evidently, the capacitive performance is not affected by the choice of separator and virtually identical values are obtained when using a thin IEM or a porous separator. Also, it is important to note that no indication for the emergence of electrochemical reactions related with degradation of the membrane can be seen in the CVs for the two IEMs.

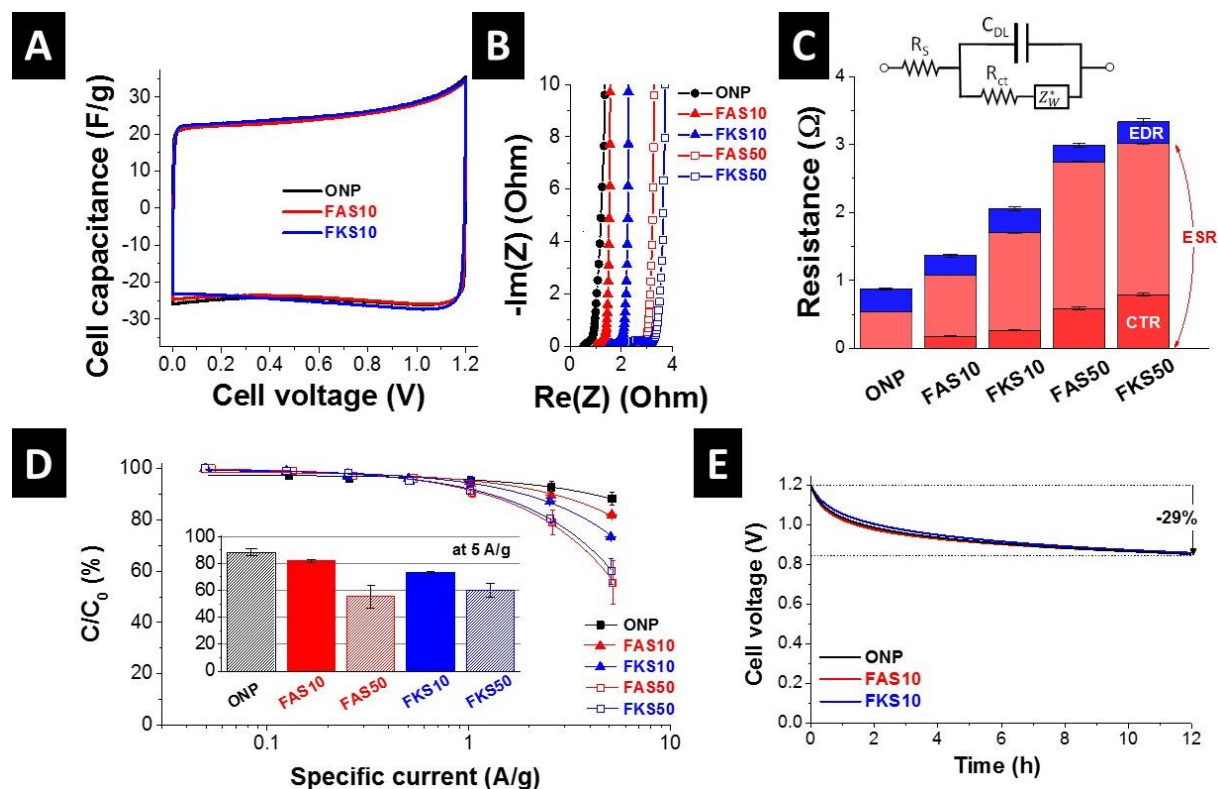


Figure S3: (A) Cyclic voltammograms at 5 mV/s shows the characteristic rectangular shape almost identical in all cases, (B) Nyquist plot obtained in frequency range of 10⁻² to 10⁶ Hz, (C) System resistance derived from Nyquist plot employing a Randles circuit; equivalent distributed resistance, equivalent series resistance, and charge transfer resistance, (D) Capacitance retention derived from galvanostatic charge/discharge at different values of specific current. Even at 5 A/g, the FAS10 membrane retained more than 80 % of its initial capacitance. (E) Cell voltage decay after charging the cells with 500 mA/g up to 1.2 V, and holding at 1.2 V for 15 min.

As can be seen in Nyquist plots (**Figure S3B**), the lowest system resistance was obtained with a porous separator (ONP) while higher resistance can be seen for IEM especially with increasing thickness. Different to ONP, a flat semi-circle appeared for all investigated IEMs as the charge transfer resistance (CTR) grows (**Figure S3C**). The higher CTR values were derived for thicker membranes while all measured EDR values remained almost constant. This indicates that the main contribution to the CTR is related not only to the contact resistance between electrode and current collector or carbon particles, but also to ion mobility. In other words, the high CTR values obtained for the thicker membranes can be interpreted as the results of a low ion transport rate. A similar shape of semi-circles was reported in Ref. ² as the number of separator layers was increased. As the latter study also reported the bigger semi-circle size with the increased number of separator stacks, it further supports the impact of ion transport to CTR.

The increase in resistance for thicker membranes also limits the power handling ability, as seen from the plot of capacitance retention over specific current obtained from galvanostatic charge/discharge in **Figure S3D**. At a very low specific current (50 mA/g), the cell capacitance for all setups was $26 \pm 1 \text{ F/g}$. It is important to note that all types of separators yielded a capacitance within $\pm 10 \%$ of scatter up to a specific current of 1 A/g, including the very thick IEMs with 50 μm thickness. The best performing IEM was FAS10 with a loss of 18 % in capacitance, compared to 12 % for the conventional separator ONP at 1 A/g. The higher performance of FAS over FKS also aligns with the higher ion conductivity as specified by the membrane manufacturer.

Additionally, we investigated the influence of voltage decay over time. As seen in **Figure S3E**, after being charged to 1.2 V and held for 15 min, IEMs and ONP show an identical behavior and the cell voltage drops by 29 % over a duration of 12 h. Since the initial large voltage drop is mostly carried by local ion redistribution inside the carbon electrodes,³ there is obviously no statistically relevant influence of the type of separator. The almost linear voltage decay over time is related with the actual self-discharge of the system, but also no significant difference is seen when comparing FAS10, FKS10, and ONP.

Schematic illustration of charge compensation for porous and non-porous separators

The concentration at each compartment is expected to be changed as the state of the charge changes during charging and discharging in the presence of an ion exchange membrane. The concentration fluctuation in a bulk electrolyte solution, however, is expected to be negligible when we considered the mass of the carbon (total mass: ca. 19 mg) applied to our hybrid system. The influence of this concentration change is not expected to be significant on the general electrochemical properties of our hybrid system.

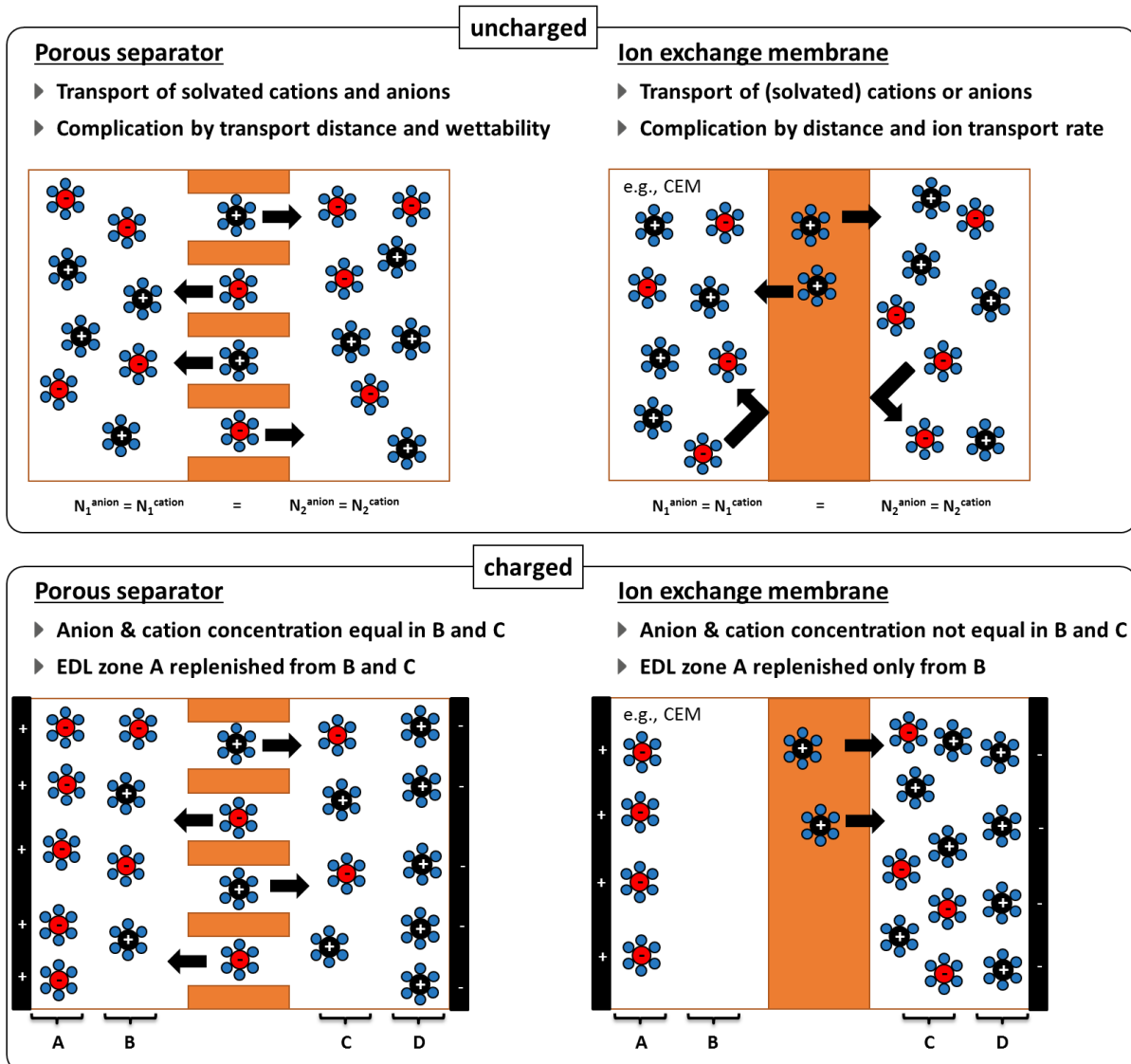


Figure S4: When using an ion exchange membrane, the charge compensation mechanism is slightly different from when using a porous separator (especially relevant for low concentrations). When balancing the bulk electrolyte's charge by transporting cations and ions from side to side via a porous separator, the total number of ions remains constant at both electrodes. However, when using an ion exchange membrane, only one ion species can pass the membrane. As exemplified for a cation exchange membrane, this means that to achieve charge neutrality in the bulk electrolyte, more anions have to move from the compartment near the positively polarized electrode to the opposite side when compared to the case for porous separators.

Electrochemical performance of the PFC redox electrolyte system

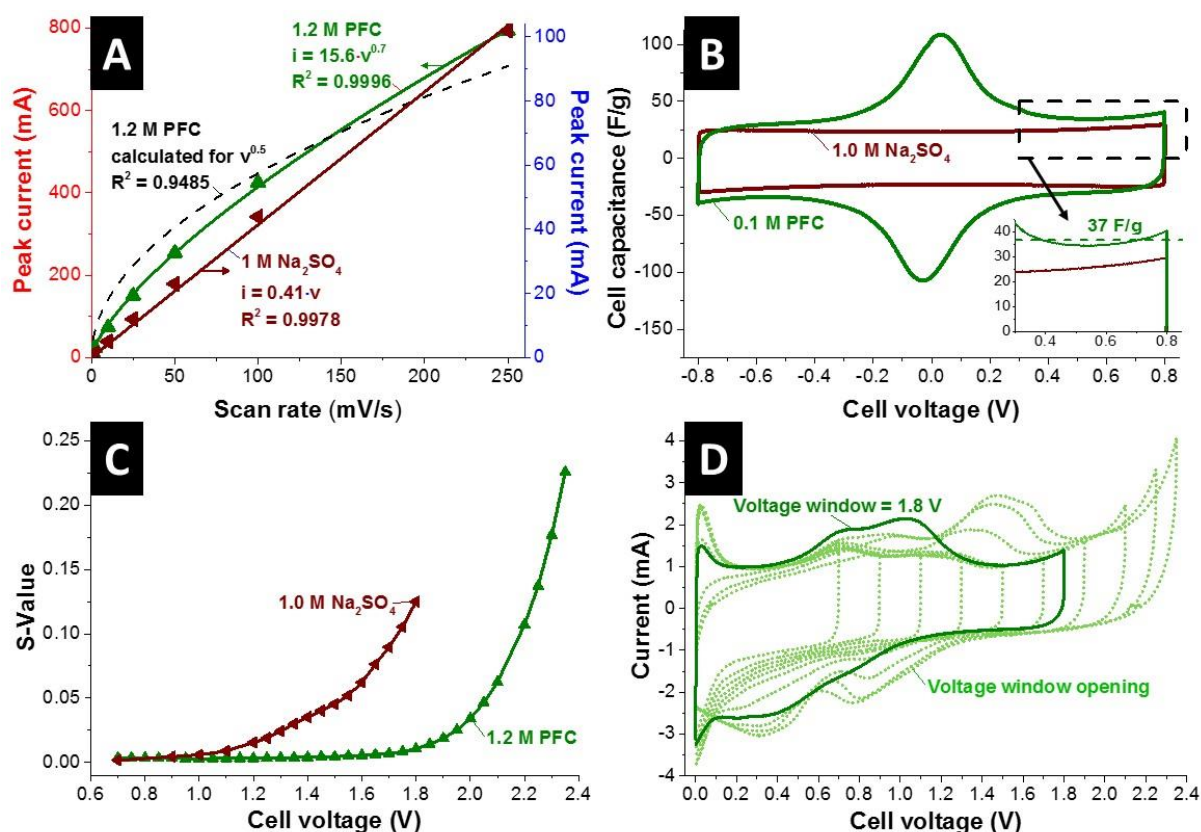


Figure S5: (A) Trend of peak current with varying scan rate for 1 M Na₂SO₄ and 1.2 M PFC. (B) Cyclic voltammograms at a scan rate of 1 mV/s for 1 M Na₂SO₄ and 0.1 M PFC. Assuming that the rectangular shape current response corresponds mainly to the double layer contribution and the majority of the redox contribution represents by the currents peak near to 0 V, the approximate capacitance value of 37 F/g can be considered to originate from electrical double-layer formation of potassium and ferricyanide/ferrocyanide ions. The inset in (B) has the same units on the axes as the main graph. (C) S-values were calculated by Eq. (5) in the main text as the voltage window was increased from 0.7 V to 1.8 V for 1 M Na₂SO₄ and 0.7 V to 2.35 V for 1.2 M PFC. (D) Cyclic voltammograms measured for 1.2 M PFC at a scan rate of 1 mV/s while increasing the voltage window to 2.35 V.

Supporting references

1. Lee, J.; Krüner, B.; Tolosa, A.; Sathyamoorthi, S.; Kim, D.; Choudhury, S.; Seo, K.-H.; Presser, V., Tin/Vanadium Redox Electrolyte for Battery-Like Energy Storage Capacity Combined with Supercapacitor-Like Power Handling. *Energy Environ. Sci.* **2016**, DOI:10.1039/C6EE00712K.
2. Tönurist, K.; Thomberg, T.; Jänes, A.; Romann, T.; Sammelselg, V.; Lust, E., Influence of Separator Properties on Electrochemical Performance of Electrical Double-Layer Capacitors. *J. Electroanal. Chem.* **2013**, 689, 8-20.
3. Kaus, M.; Kowal, J.; Sauer, D. U., Modelling the Effects of Charge Redistribution During Self-Discharge of Supercapacitors. *Electrochim. Acta* **2010**, 55 (25), 7516-7523.

3.3. Sub-micrometer novolac-derived carbon beads for high performance supercapacitors and redox electrolyte energy storage

Benjamin Krüner,^{1,2} Juhan Lee,^{1,2} Nicolas Jäckel,^{1,2} Aura Tolosa,^{1,2} and Volker Presser^{1,2}

¹ INM - Leibniz Institute for New Materials, Campus D2 2, 66123 Saarbrücken, Germany

² Saarland University, Campus D2 2, 66123 Saarbrücken, Germany

Citation:

Krüner, B.; Lee, J.; Jäckel, N.; Tolosa, A.; Presser, V., Sub-micrometer Novolac-derived carbon beads for high performance supercapacitors and redox electrolyte energy storage. *ACS Applied Materials & Interfaces* **2016**, 8 (14), 9104-9115.

Own contributions:

Design and planning for redox electrolyte system, writing, and discussions

Abstract

Carbon beads with sub-micrometer diameter were produced with a self-emulsifying novolac–ethanol–water system. A physical activation with CO₂ was carried out to create a high micro-porosity with a specific surface area varying from 771 m²/g (DFT) to 2237 m²/g (DFT) and a total pore volume from 0.28 cm³/g to 1.7 cm³/g. The carbon particles conserve their spherical shape after the thermal treatments. The controllable porosity of the carbon spheres is attractive for the application in electrochemical double layer capacitors. The electrochemical characterization was carried out in aqueous 1 M Na₂SO₄ (127 F/g) and organic 1 M tetraethylammonium tetrafluoroborate in propylene carbonate (123 F/g). Furthermore, an aqueous redox electrolyte (6 M KI) was tested with the highly porous carbon and a specific energy of 33 Wh/kg (equivalent to 493 F/g) was obtained. In addition to a high specific capacitance, the carbon beads also provide an excellent rate performance at high current and potential in all tested electrolytes, which leads to a high specific power (>11 kW/kg) with an electrode thickness of ca. 200 μm.

Sub-micrometer Novolac-Derived Carbon Beads for High Performance Supercapacitors and Redox Electrolyte Energy Storage

Benjamin Krüner,^{†,‡} Juhan Lee,^{†,‡} Nicolas Jäckel,^{†,‡} Aura Tolosa,^{†,‡} and Volker Presser^{*,†,‡}

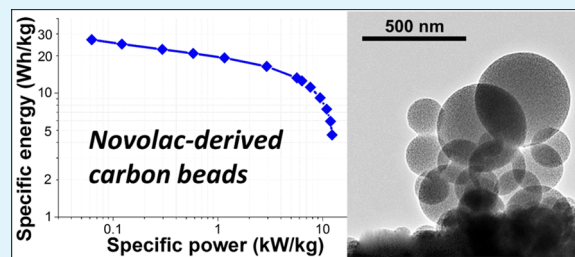
[†]INM—Leibniz Institute for New Materials, 66123 Saarbrücken, Germany

[‡]Department of Materials Science and Engineering, Saarland University, 66123 Saarbrücken, Germany

S Supporting Information

ABSTRACT: Carbon beads with sub-micrometer diameter were produced with a self-emulsifying novolac–ethanol–water system. A physical activation with CO₂ was carried out to create a high microporosity with a specific surface area varying from 771 (DFT) to 2237 m²/g (DFT) and a total pore volume from 0.28 to 1.71 cm³/g. The carbon particles conserve their spherical shape after the thermal treatments. The controllable porosity of the carbon spheres is attractive for the application in electrochemical double layer capacitors. The electrochemical characterization was carried out in aqueous 1 M Na₂SO₄ (127 F/g) and organic 1 M tetraethylammonium tetrafluoroborate in propylene carbonate (123 F/g). Furthermore, an aqueous redox electrolyte (6 M KI) was tested with the highly porous carbon and a specific energy of 33 W·h/kg (equivalent to 493 F/g) was obtained. In addition to a high specific capacitance, the carbon beads also provide an excellent rate performance at high current and potential in all tested electrolytes, which leads to a high specific power (>11 kW/kg) with an electrode thickness of ca. 200 μm.

KEYWORDS: supercapacitors, porous carbon, energy storage, redox electrolyte, self-emulsifying



1. INTRODUCTION

Electrical double layer capacitors, also known as supercapacitors or ultracapacitors, store electrical energy via fast ion electro-sorption processes at the fluid–solid interface between a charged electrode and electrolyte.¹ Due to the nonfaradaic and interfacial nature of this process, a supercapacitor typically shows a power handling ability superior to lithium ion batteries where the ions intercalate into a solid material with a suitable (often layered) structure.² In consequence, supercapacitors have higher specific power (800–2000 W/kg) than lithium ion batteries (typical specific power, 100 W/kg).³ Another advantage of supercapacitors is their long cycling performance stability and high Coulombic efficiency. However, this comes at the price of a comparably low specific energy of 5–15 W·h/kg for supercapacitor cells (lithium ion batteries, ca. 100 W·h/kg).³

Commonly, electrodes for supercapacitor applications employ micrometer-sized particles of nanoporous carbon consolidated by the use of polymer binder.^{4,5} To further enhance the power performance via fast ion transport, sub-micrometer particles are of high interest.^{6–9} For example, using an emulsion synthesis process, we have recently shown the superior rate handling ability of sub-micrometer carbide-derived carbon (CDC) beads with diameters ranging from 20 to 200 nm.¹⁰ This aligns with the enhanced performance of nanometer-sized TiC powders, which demonstrate an enhanced power rating compared to their micrometer-sized counterparts.⁸ Yet, the necessity of chlorine gas to etch all noncarbon atoms makes the production of CDCs less attractive to large scale industrial processing. Also alternative synthesis methods

for sub-micrometer-sized carbon particles (especially spherical ones) have been reported, such as camphoric carbon nanobeads (ca. 80 m²/g specific surface area (SSA))¹¹ or spongy carbon nanobeads (16 m²/g SSA),¹² but commonly high porosity values cannot be achieved without postsynthesis activation.

A well-established method to synthesize spherical particles (including sub-micrometer diameter) is emulsion polymerization.¹³ The advantages of particle synthesis from emulsions are (i) the simplicity of the setup and scalability, (ii) the possibility to prepare a great variety of materials with a broad range in particle sizes, and (iii) a flexibility on adjusting the composition.¹⁴ The diameters of the emulsion's liquid droplets may range from 10 nm to 100 μm, and phenolic resins can be used as carbon precursor for emulsion polymerization.^{15–19} Phenolic resin systems are formed with a base or acid catalyst to obtain resoles or novolacs.²⁰ Resoles can cross-link without the help of cross-linking agents in contrast to novolacs which can only cross-link by adding a hardener (e.g., hexamethylenetetramine).²⁰ As reported in the literature so far, as-pyrolyzed beads from phenolic resin may exhibit a specific BET surface area (SSA_{BET}) up to 1131 m²/g which can be further increased by physical or chemical activation.^{17,21} Typical SSA_{BET}, which can be obtained with physical or chemical activations of carbon materials, are between 500 and 3100 m²/g.^{16,22,23} For example, the physical activation of carbon microspheres (200–1000 μm)

Received: January 18, 2016

Accepted: March 21, 2016

Published: March 21, 2016

with CO₂ gas has been investigated by Singh and Lal, varying the CO₂ flow rate, the gasification temperature, and the activation time.¹⁶ An increased flow rate decreased the porosity because of a shorter dwell time, while increasing the temperature from 850 to 1150 °C led to an enhanced SSA_{BET} of up to 1031 m²/g while sacrificing the total yield of the final product.¹⁶ A prolonged activation time from 5 to 15 h at 950 °C was the most effective step to increase the porosity: the burnoff increased from 32 to 88 mass% while the SSA_{BET} increased from 574 to 3101 m²/g.¹⁶

To establish industrial production, Tennison (MAST Carbon) developed the synthesis of nonspherical phenolic-resin-derived carbon particles with a particle size of 1–50 μm.²⁴ By using physical activation with carbon dioxide, it was possible to achieve SSA_{BET} from 800 to 1500 m²/g.²⁴ Later, Tennison et al. improved the synthesis procedure to obtain phenolic-resin-derived carbon with adjusted particle sizes between 5 and 2000 μm by using a water-in-oil emulsion.²⁵ Using this approach, they reached a SSA_{BET} of up to 750 m²/g with total pore volume of ca. 1 cm³/g. The unique feature of their synthesis is the use of pore formers, such as diols, diol-ethers, cyclic esters, cyclic and linear amides, or aminoalcohols. These pore formers do not react with the polymer but remain within the cross-linked resin and can be removed in a later stage. An initial study of the electrochemical properties of such novolac-derived carbon microbeads was provided by Fernández et al.²⁶ These beads were pyrolyzed at 800 °C and activated with carbon dioxide at 900 °C to obtain a SSA_{BET} up to 1773 m²/g and up to 124 F/g capacitance in 1 M TEA-BF₄ in acetonitrile (ACN).

To overcome the inherently limited specific energy of electrical double layer capacitor, the use of redox-active electrolytes has emerged as a facile and powerful approach.^{27–29} Unlike supercapacitors, redox electrolytes do not limit the energy storage capacity of the system to ion electrosorption at the fluid/solid interface at the electrode. Instead, the electrolyte volume actively participates in the energy storage mechanisms through soluble redox couples, for instance, quinone/hydroquinone, iodine/iodide/triiodide, ferricyanide/ferricyanide, or vanadium oxide.^{30,31} Redox electrolyte systems provide not only a very high specific energy (10–50 W·h/kg) but also high specific power almost close to that of supercapacitors.³² The latter can be explained by the enhanced diffusion kinetic of the redox ions in the carbon nanopores where the pore size is smaller than the equivalent diffusion layer thickness.³² Thus, an electrode should exhibit a synergistic combination of larger transport pores for the transport of redox ions and a total high pore volume to provide a large reservoir of redox-active species. This requirement can be met with nanoporous carbon spheres with sub-micrometer size, where the large intraparticle pore volume serves as reservoir, short diffusion path lengths are provided via the small particle size, and an additional reservoir for ions is provided by large interparticle porosity.

Our work presents the synthesis of sub-micrometer novolac-derived carbon (abbreviated as NovoCarb or PNC) beads by a simple emulsion polymerization, followed by carbonization and physical activation. The self-emulsifying characteristic of the emulsion (novolac–ethanol–water) makes this synthesis method particularly practical because no high shear mixer or ultrasonic device is needed. This and the small particle size set our synthesis apart from established approaches, such as that developed by Tennison.²⁵ For the highly nanoporous NovoCarb spheres, we first establish the performance as a

conventional supercapacitor electrode in aqueous (1 M Na₂SO₄) and organic media (1 M TEA-BF₄ in propylene carbonate, PC). Finally, the very high energy storage capacity of the material is demonstrated for aqueous 6 M KI (potassium iodide). Such a high molar concentration of potassium iodide has not been studied before, and we benchmark all data vs conventional activated carbon (AC, YP-80F from Kuraray).

2. EXPERIMENTAL DESCRIPTION

2.1. Synthesis of Ultrasmall Novolac-Derived Carbon Beads.

A 25 g amount of novolac (ALNOVOL PN320, Allnex Germany GmbH) was dissolved in 100 mL of ethanol. The cross-linker, 2.5 g of hexamethylenetetramine (TCI Deutschland GmbH), was dissolved in 500 mL of Milli-Q water. The novolac–ethanol solution was added to the aqueous phase in a 1 L autoclave. The transparent solutions became milky directly after the addition of the second phase, and the self-emulsifying effect of the system eliminated the need for additional stirring of the emulsion. A pressure of approximately 3 × 10⁶ Pa of nitrogen was applied to the autoclave before heating. The autoclave was heated to 150 °C (measured inside the autoclave) with a heating rate of 5 °C/min and held at this temperature for 8 h. The pressure increased from 3 × 10⁶ Pa to approximately 4.3 × 10⁶ Pa during the reaction. After synthesis, the suspension was freeze-dried using liquid nitrogen to minimize agglomeration so that a dry powder was obtained.

The novolac beads were pyrolyzed at 700 °C with a heating rate of 20 °C/min in argon (purity, 4.6) and held at this temperature for 2 h. Subsequently, physical activation via CO₂ treatment (purity of CO₂, 4.5) was carried out by heating to 1000 °C with a heating rate of 20 °C/min while CO₂ flow rate was controlled to 100 cm³/min at 1000 °C. The process time (denoted as X; see Supporting Information Figure S1) was varied between 0 and 3 h to adjust the porosity of the carbon beads. In this work, the activation time is reflected by the subscript in the sample's name; for example, PNC_{2h} refers to phenol novolac carbon (PNC = NovoCarb) that has been exposed to 2 h of CO₂ activation.

2.2. Materials Characterization. The carbon beads were imaged by a field emission scanning electron microscope (SEM; JEOL-JSM-7500F from JEOL Ltd.) and a transmission electron microscope (TEM; JEOL JEM-2100F operating at 200 kV). The bead diameter was measured on the basis of the SEM images with ImageJ 1.47t for a number of 150 beads.³³ Chemical characterization via CHNS analysis was carried out with the Vario Micro Cube of Elementar GmbH with a temperature of the reduction tube of 850 and 1150 °C of the combustion tube. The device was calibrated with sulfanilamide.

Raman spectra were measured with a Renishaw inVia Raman Microscope, equipped with a grating of 2400 lines/mm and a 50× objective (numeric aperture, 0.9), reaching a spectral resolution of ~1.2 cm⁻¹. An Nd:YAG laser with an excitation wavelength of 532 nm was used. The acquisition time was 20–30 s, and 3–10 accumulations were used to enhance the signal-to-noise ratio. After the background noise was subtracted from the obtained Raman spectra, the D- and G-peaks were fitted with a Voigt function, as was the background contribution.

The nitrogen and carbon dioxide gas sorption analyses were carried out with a Quantachrome Autosorb iQ system. The pyrolyzed and activated samples were degassed at 150 °C for 1 h and subsequently heated to 300 °C and kept at this temperature for up to 20 h at a relative pressure of 0.1 Pa to remove volatile molecules from the surface. The nitrogen sorption analysis was performed in liquid nitrogen at –196 °C and the carbon dioxide sorption analysis at 0 °C using ethylene glycol as cooling agent. The relative pressure with nitrogen was 5 × 10⁻⁷ to 1.0 in 76 steps and 4.5 × 10⁻⁴ to 1 × 10⁻² in 55 steps for the CO₂ measurements. The pore size distribution (PSD) was derived using the quenched-solid density functional theory (QSDFT), assuming slit-like pores, for the nitrogen measurements and the nonlocal density functional theory (NLDFT) for the carbon dioxide measurements.^{34–36} The specific surface area (SSA) was also calculated using the Brunauer–Emmett–Teller equation (BET) in the

linear regime of the measured isotherms, typically 3×10^{-2} to 2×10^{-1} (relative pressure), with a Quantachrome Autosorb 6B.³⁷ All calculations were performed with the ASIQwin-software 3.0, and the average pore size was calculated by volume weighing (i.e., d_{50} value = cumulative pore size corresponding with half of the total pore volume).³⁸

The novolac beads were pyrolyzed in an Ar atmosphere (purity, 4.6) in a thermogravimetric analysis (TGA; TG209F1 Libra from Netzsch) with a heating rate of 10 °C/min to 1100 °C. A similar experiment was performed in a CO₂ atmosphere (purity, 4.5) with the pyrolyzed sample. The pyrolysis in Ar (purity, 5.0) was also investigated in a TGA with mass spectrometer (TGA-MS; STA449F3 Jupiter and QMS 403C Aëolos from Netzsch). The density of the NovoCarb particles was measured by helium pycnometry (AccuPyc 1330 pycnometer from Micromeritics; purity, 5.0).

2.3. Electrochemical Measurements. Freestanding carbon electrodes were prepared either with NovoCarb beads or commercially available activated carbon (AC, YP-80F from Kuraray) by applying polytetrafluoroethylene (PTFE; 60 mass % in H₂O) as binder. After dispersing the carbon material in ethanol, the PTFE solution was added. Then, the mixture was crushed in a mortar during the evaporation of the ethanol. The doughy carbon paste was then rolled out via a rolling machine (HR01 hot rolling machine from MTI Corp.). Finally, 120–220 μm thick freestanding electrodes were produced with 5–10 mass % PTFE for the AC based electrode and 9–12 mass % for the NovoCarb beads. Afterward, the electrodes were dried in a vacuum oven at 120 °C for 48 h at 2×10^3 Pa. For the cell assembly, an electrode disc was punched out of the rolled blank with a diameter of 12 mm. The active electrode mass varied between 2 and 15 mg depending on the activation time (Supporting Information Table S1) since the particle packing and electrode thickness were kept constant.

For the organic electrolyte (1 M TEA-BF₄ in PC; BASF, battery grade) and the aqueous system (1 M Na₂SO₄ in Milli-Q water; Sigma-Aldrich), custom-built cells were assembled employing a symmetrical two-electrode setup.³⁹ In order to minimize the contact resistance between the cell piston made of titanium and the electrode, a carbon-coated aluminum current collector (type Zflo 2653, Coveris Advanced Coatings, Matthews, NC, USA) was placed between the electrode and the cell piston made of titanium for measurements in organic media. In aqueous media, we used a platinum current collector instead. The electrodes were separated with a glass-fiber separator with a diameter of 13 mm (GF/A, Whatman, GE Healthcare Life Science). Before the cells were filled with the organic electrolyte in an argon-filled glovebox (MBraun Labmaster 130; O₂, H₂O < 1 ppm), they were dried at 120 °C and at 2×10^3 Pa for 24 h.

For the redox electrolyte system, a custom-made cell with graphite current collectors (10 mm thickness) was used with two-electrode configuration using two symmetric electrodes with a diameter of 12 mm. A schematic drawing is provided in Supporting Information Figure S2. To prevent the possible redox shuttling of the redox ions between anode and cathode,⁴⁰ a cation exchange membrane (FKS15, FuMA-Tech; thickness, ca. 15 μm) was used as a separator. In order to provide an effective seal for the membrane, polymer gasket layers were placed between graphite current collectors and the membrane. Through the circular inner cut (1.33 cm²) of the gaskets, the electrodes were placed between the membrane and the current collector. Before the cell assembly, the electrodes were soaked in the redox electrolyte (1 or 6 M KI) with application of vacuum (10⁴ Pa) for 5 min for degassing. During the cell assembly, the electrolyte was dropped on the electrode and the empty space in the gasket inner cut was completely filled with the electrolyte as the cell was sealed afterward.

All of the electrochemical measurements were conducted with a VMP300 potentiostat/galvanostat from BioLogic. From the obtained data, the specific capacitance was calculated with eq 1 from cyclic voltammograms (CVs) and with eq 2 for data from galvanostatic cycling with potential limitation (GCPL). The calculated capacitance values in this work are always the average of two measurements with a

standard deviation below 10%. To compare the capacitance of different materials, it is common to normalize the capacitance to the active mass of the electrode material.⁴¹

$$C_s = \frac{I(t)}{(dU(t)/dt)m} \quad (1)$$

where C_s is the specific capacitance per electrode; $I(t)$, the discharge current; $dU(t)/dt$, the scan rate; and m , the mass of carbon in the electrode.

$$C_s = \frac{4Q_{\text{dis}}}{Um} \quad (2)$$

where C_s is the specific capacitance per electrode; Q_{dis} , the charge of the discharging cycle; U , the IR-drop corrected cell voltage; and m , the mass of carbon in the electrode.

For the calculation of the specific energy (W-h/kg) of the cells with the redox electrolyte, eq 3 was applied by integrating the cell voltage with respect to the discharging time measured in GCPL mode.

$$E = \frac{i}{m_{\text{total}}} \int U dt \quad (3)$$

where E is the specific energy of the cell; i , the constant current applied during the measurement; and m_{total} , the total mass of the two carbon electrodes of equal weight.

To determine the electrochemical stability window of KI aqueous solution with AC activated carbon and NovoCarb beads, a voltage opening test with cyclic voltammetry was initially applied to the cells at the scan rate of 1 mV/s from 0.6 to 1.4 V in intervals of 0.05 V. In order to characterize rate handling performance, CV, and GCPL were carried out in a full cell (symmetric two-electrode setup) with 1 M TEA-BF₄ in PC, 1 M Na₂SO₄, or 1 or 6 M KI.

For long-term stability testing, voltage floating was performed with a battery cycler (BAT-SMALL battery cycler from Astrol Electronic AG) with a symmetric two-electrode cell configuration. The voltage was kept at 1.2 V in aqueous and at 2.7 V in organic electrolyte for 100 h, and the specific capacity was measured every 10 h by galvanostatic cycling (aqueous, 1.2 V; organic, 2.5 V). In the case of the redox electrolyte system, a galvanostatic cycling test was carried out at 1 A/g from 0 to 1.4 V in a symmetric two-electrode configuration.

2.4. Electrochemical Dilatometry. The height change (strain) of the carbon electrodes during charging and discharging was measured with a ECD-nano dilatometer from EL-CELL. The dilatometer cell is based on a two-electrode design using an oversized PTFE-bound AC as counter and quasi-reference electrode. The investigated electrodes were compressed between the separator and a movable titanium plunger with a constant weight load of 10 N. Prior to the experiments, the cell was dried for 12 h at 120 °C under vacuum (2 kPa). A DP15 displacement transducer (Solartron Metrology), with an accuracy of 15 nm, was used. The experiments were performed at constant temperature of 25.0 ± 0.1 °C using a climate chamber (Binder). Prior to the electrochemical characterization, the cell was conditioned with a holding period at 0 V vs carbon for 10 h followed by five charge/discharge cycles between 0 and 2.5 V vs carbon, and only data of the fifth cycle are shown.

3. RESULTS AND DISCUSSION

3.1. Morphology and Porosity. Electron microscopy confirmed conservation of the spherical droplets structure generated in the emulsion after polymerization and pyrolysis (Figure 1A,B). Image analysis yielded an average number-dependent sphere diameter of 302 ± 142 nm for PNC_{0h}. Transmission electron microscopy (TEM) also showed the highly homogeneous character of the beads with no differentiation, for example, between core and shell. The overall nonordered character of the carbon is also evident from the absence of lattice fringes or visible crystalline domains (Figure 1B, inset). As seen from Figure 1C,D, the size of the particles

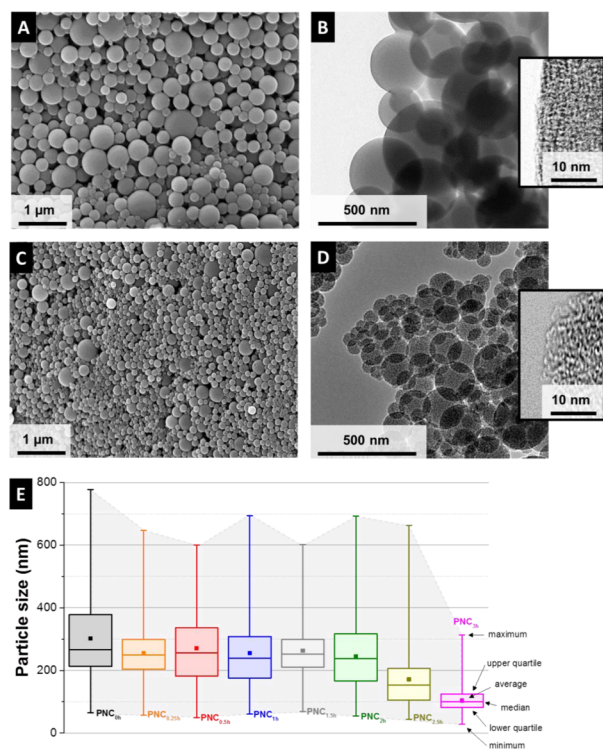


Figure 1. SEM images (A, C) and TEM images (B, D) of PNC_{0h} (A, B) and PNC_{3h} (C, D). Box-whisker plot (E) with maximum and minimum, upper and lower quartile, and number-dependent average and median of the carbon beads after the pyrolysis PNC_{0h} and after CO₂ activation (PNC_{0.25h}, PNC_{0.5h}, PNC_{1h}, PNC_{1.5h}, PNC_{2h}, PNC_{2.5h}, and PNC_{3h}).

after 3 h of CO₂ activation was significantly reduced to 104 ± 40 nm as was the spread of minimum and maximum diameters (Figure 1E and Supporting Information Figures S3 and S4). No significant change in bead diameter was encountered for CO₂ activation up to 2.5 h. The noncrystalline character of the carbon beads can be seen well from high resolution TEM micrographs (Figure 1D, inset) and the increased transparency of CO₂-treated beads indicates that the particles became less dense through removal of carbon by the physical activation (see also Supporting Information Figure S5).

To further investigate the pyrolysis process and CO₂ activation as a facile way to enhance the porosity of NovoCarb beads, we carried out thermogravimetric analysis. The TGA data presented in Figure 2A show the mass loss of the carbon beads during the pyrolysis and the CO₂ treatment. The pyrolysis of phenolic resins can be classified in three phases.⁴² The small mass loss at approximately 100 °C was not part of the three stages of the pyrolysis and was caused by desorption of water and other light molecules (e.g., ethanol and ammonia; Supporting Information Figure S5). The first stage is identified by the formation of cross-links and the evolution of water and other condensates between 200 and 500 °C. The second stage is dominated by breaking cross-linking bonds between 400 and 800 °C (i.e., amino, methylene, and oxygen groups). This leads to the evolution of water, carbon monoxide, nitrogen, and amino groups among others (Supporting Information Figure S5). The oxygen signal is dropping at approximately 350 and 630 °C because of the evolution of carbon dioxide. The residual oxygen of the Ar flow is also reacting with the sample during the pyrolysis, and the final stage (560–900 °C) is dominated by

the production of hydrogen by the splitting of hydrogen atoms directly bonded to benzene nuclei.⁴² Pyrolyzed carbon is formed in this temperature range via the coalescence of aromatic rings, and the yield is 48 mass % at 700 °C and 43 mass % at 1100 °C of the initial sample mass. During the CO₂ treatment, we observed a massive oxidation-induced mass loss above 950 °C and adjusted the activation parameters to 1000 °C for this study.

As seen from electron micrographs, the beads became smaller and rougher with progressed activation (Figure 1C–E). With an additional decrease in contrast, TEM images indicate an increase in particle porosity, while the small nanopores themselves cannot be resolved by the imaging method directly. A more detailed characterization of the porosity of the beads prior to and after thermal activation with CO₂ for different durations can be gained by gas sorption analysis (GSA), as shown in Figure 2B–D.³⁸ Values for the mass loss, SSA_{BET} and SSA_{DFT}, total pore volume, and average pore size are provided in Table 1. The pyrolyzed carbon beads showed exclusively micropores with pores only smaller than 0.8 nm and a SSA_{DFT} of 771 m²/g. The average pore size was 0.5 nm which is similar to the calculated molecular diameter of ethanol (0.52 nm),⁴³ indicating the role of ethanol as a pore former. The CO₂ activation and the increase in activation time led to a higher total mass loss. The SSA_{DFT} also increased to reach a maximum of 2237 m²/g (SSA_{BET}, 3104 m²/g) with a total pore volume of 1.71 cm³/g at a mass loss of 90 mass %. These values are similar to the highest SSA_{BET} reported in literature for activated carbon materials.^{16,22,23} Progressing activation caused a coalescence of the pores and a progressing increase of the average pore size. Finally, the enhanced pore coalescence at an activation of more than 2 h led to an ultimate decrease of the SSA and total pore volume while the average pore size constantly increased (Figure 2B). Additionally, the width of the pore size dispersity increased from 0.3 to 1.1 nm (PNC_{0h}) to 0.4–2.0 nm (PNC_{1h}) and to 0.5–3.4 nm (PNC_{3h}).

3.2. Structure, Density, and Chemical Composition. TEM micrographs (Figure 1) evidenced the amorphous nature of NovoCarb beads and the lack of crystalline ordering after pyrolysis and CO₂ activation. Further insights into the carbon structure can be gained by means of Raman spectroscopy (Table 2). The Raman spectrum of PNC_{0h} is shown in Figure S6A (Supporting Information) with the fitted peaks for D-mode (at 1345 cm⁻¹) and G-mode (at 1602 cm⁻¹). The I_D/I_G ratio can be used to calculate the average in-plane domain size (L_a),⁴⁴ for example with the Tuinstra–Koenig⁴⁵ or the Ferrari–Robertson equation.⁴⁶ To understand the data, we need to consider that the two equations are only valid for different domain sizes: the Tuinstra–Koenig (TK) equation can be used for $L_a < 2$ nm and the Ferrari–Robertson (FR) equation for $L_a > 2$ nm.⁴⁷ We have to assume a transition in the values from the TK to the FR model, as shown in Figure S6C. Starting from an amorphous polymeric precursor, the pyrolyzed carbon showed a relatively small L_a of 1.4 nm. This value slightly increased after activation due to the longer holding time at higher temperatures and the removal of nongraphitic carbon for PNC_{0.25h} (1.5 nm) and PNC_{0.5h} (1.7 nm). For longer activation durations and L_a close to the critical domain size of 2 nm, we have to transition to the use of the FR model. Accordingly, the L_a values for PNC_{1h} to PNC_{3h} showed a small level of variation between 2.3 and 2.5 nm.

The two competing effects of graphitic domain size growth at high temperatures and the removal of carbon atoms by the

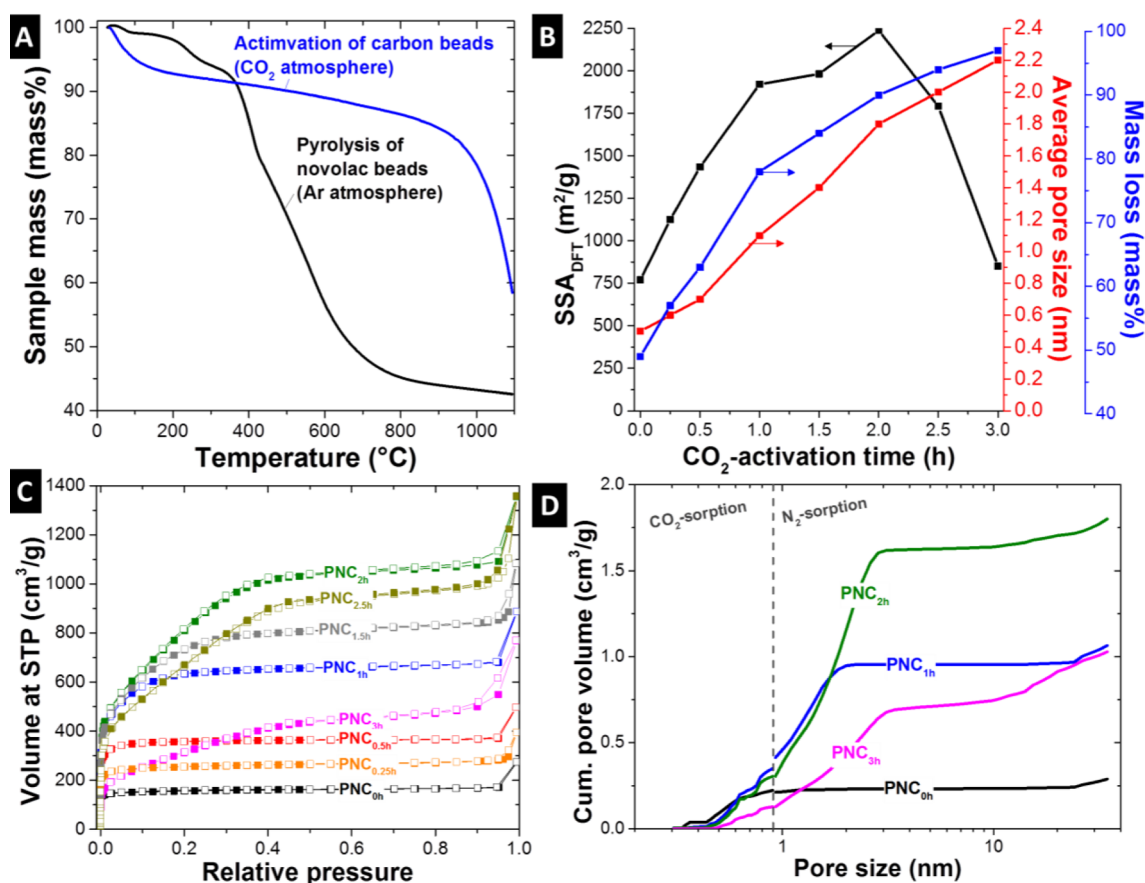


Figure 2. TGA of the pyrolysis of novolac beads in Ar atmosphere and of the CO₂ treatment of the pyrolyzed beads recorded with a heating rate of 10 °C/min (A). Correlation of SSA_{DFT}, average pore size, and mass loss on the CO₂-activation time (B). Nitrogen sorption isotherms at -196 °C on carbon beads (C). Cumulative pore size distributions of the CO₂ (at 0 °C) and N₂ (at -196 °C) gas adsorption measurement of the samples PNC_{0h}, PNC_{1h}, PNC_{2h}, and PNC_{3h} (D).

Table 1. Mass Loss of the Beads Introduced by the Pyrolysis and CO₂-Activation and Surface Characteristics of the Carbon Beads^a

	mass loss (mass %)	SSA _{DFT} (m ² /g)	SSA _{BET} (m ² /g)	total pore vol (cm ³ /g)	av pore size (nm)
PNC _{0h}	49	771	624	0.28	0.5
PNC _{0.25h}	57	1125	998	0.44	0.6
PNC _{0.5h}	63	1434	1433	0.57	0.7
PNC _{1h}	78	1921	2383	1.05	1.1
PNC _{1.5h}	84	1982	2633	1.32	1.4
PNC _{2h}	90	2237	3104	1.71	1.8
PNC _{2.5h}	94	1792	2571	1.58	2.0
PNC _{3h}	97	851	1189	0.88	2.2
AC		1756	2347	1.15	1.6

^aFor data on AC, see also ref 61.

physical activation influence the domain size of the carbon materials, as also seen from Raman spectroscopy (Supporting Information Figure S6c). The position of the D-mode shifted from 1345 to 1335 cm⁻¹ when increasing the activation time. For comparison, the G-mode of all samples was located at approximately 1600 cm⁻¹, which indicates partially graphitic carbon, as also supported by a range of I_D/I_G ratio between 2.02 and 2.49.⁴⁸ For the physical activation, we have to consider the preferential etching of less-ordered carbon in addition to structural ordering caused by the thermal treatment.

Table 2. Peak Fitting Results of the Raman Spectra, with Position of the D- and G-Mode, the FWHM, I_D/I_G Ratio and L_a

	mode	position (cm ⁻¹)	FWHM (cm ⁻¹)	I _D /I _G	L _a (nm)
PNC _{0h}	D	1345.0	165.9	2.49	1.43
	G	1601.9	66.7		
PNC _{0.25h}	D	1346.2	173.5	2.32	1.55
	G	1600.8	74.7		
PNC _{0.5h}	D	1345.7	164.5	2.02	1.71
	G	1597.8	81.5		
PNC _{1h}	D	1339.6	132.9	2.17	2.49
	G	1601.2	61.2		
PNC _{1.5h}	D	1339.4	126.7	2.03	2.31
	G	1601.8	62.4		
PNC _{2h}	D	1336.2	122.9	2.07	2.39
	G	1600.9	59.4		
PNC _{2.5h}	D	1335.1	122.2	2.08	2.37
	G	1599.8	58.7		
PNC _{3h}	D	1335.1	122.0	2.11	2.41
	G	1599.7	57.9		

The analysis of the skeletal density supports the transition toward a higher degree of carbon ordering. Initially, the density of the pyrolyzed carbon beads was 1.99 ± 0.01 g/cm³. For comparison, glassy carbon has a density of 1.48 g/cm³ and graphite of 2.25 g/cm³.⁴⁹ Activation led to an initial increase of the skeletal density after 1 h (2.33 ± 0.08 g/cm³), as shown in

Table 3. Results of the CHNS Analysis^a

	C (mass %)	H (mass %)	N (mass %)	S (mass %)	ΔO (mass %)
ALNOVOL PN 320	73.4 ± 1.7	5.83 ± 0.27	≤0.2	b.d.	20.8 ± 1.7
polymer beads	70.8 ± 1.3	6.32 ± 2.22	2.3 ± 0.1	b.d.	20.5 ± 2.6
PNC _{0h}	92.6 ± 1.5	1.34 ± 0.02	≤0.4	b.d.	5.7 ± 1.5
PNC _{0.25h}	90.7 ± 2.2	1.04 ± 0.03	≤0.5	b.d.	7.8 ± 2.3
PNC _{0.5h}	90.4 ± 1.6	1.13 ± 0.02	≤0.4	b.d.	8.1 ± 1.6
PNC _{1h}	90.1 ± 2.8	0.82 ± 0.05	≤0.5	b.d.	8.6 ± 2.8
PNC _{1.5h}	90.4 ± 8.7	0.77 ± 0.04	≤0.5	b.d.	8.3 ± 8.7
PNC _{2h}	89.3 ± 2.5	0.90 ± 0.13	≤0.8	b.d.	9.0 ± 2.6
PNC _{2.5h}	82.1 ± 4.5	0.66 ± 0.40	≤0.7	b.d.	16.6 ± 4.6

^aThe difference to 100% is attributed to oxygen and listed as ΔO; as no other elements were seen by elemental analysis with energy-dispersive X-ray analysis (EDX), the value for ΔO is an approximation for the actual oxygen content (b.d.: below limit of detection).

Figure S7 (Supporting Information). This value is relatively high compared to other CO₂-activated resol-derived carbons in the literature (2.2 g/cm³; see ref 24), and this can be explained with the removal of less-dense material by the CO₂ activation and enhanced structural ordering of disordered carbon at high temperature. Continued CO₂ activation decreased the density to 1.95 ± 0.07 g/cm³ after 1.5 h and to 1.51 ± 0.05 g/cm³ after 2 h (the latter is the sample with the highest SSA and pore volume). The measured skeletal density after 2.5 h of CO₂ treatment was the lowest, namely, 1.44 ± 0.05 g/cm³ (sample showing an onset of decreasing SSA).

Chemically, as shown by EDX analysis exemplified for PNC_{0h}, the beads predominantly consisted of carbon with some amounts of oxygen (Supporting Information Figure S8). These data were characteristic for all samples. The much higher sensitivity and accuracy of CHNS analysis allow a more precise quantitative analysis. Since EDX did not detect other elements outside the CHNS system except oxygen, we used the latter method to also assess the oxygen content (referred to as ΔO; Table 3). Initially, the novolac beads showed a carbon content of 70.8 mass %, which increased after pyrolysis to 92.6 mass % and decreased after CO₂ activation to 90.7 to 82.1 mass % (with a major decrease of the carbon content PNC_{2.5h}). While, after pyrolysis, ΔO was decreased from 20.5 to 5.7 mass %, CO₂ activation led to a slight increase to 7.8–9.0 mass % (for PNC_{0.25h} to PNC_{2h}). The hydrogen content decreased from 6.3 mass % of the polymer beads to a nondetectable level after pyrolysis. The nitrogen content was lowered after the pyrolysis from 2.3 mass % to only ≤0.4 mass %, yet the nitrogen content increased after the CO₂ activation to ≤0.8 mass %, which can be explained by the preferred removal of carbon (i.e., the nitrogen content only increased relatively).

3.3. Supercapacitor Performance in Aqueous and Organic Electrolytes. Electrochemical characterization (Table 4) of NovoCarb beads as supercapacitor electrodes was carried out for aqueous (1 M Na₂SO₄) and organic electrolyte media (1 M TEA-BF₄ in PC). Aqueous media are highly attractive because of the reduced energy required during supercapacitor manufacturing invested for thorough drying of the electrode materials and the low electrolyte costs.⁵⁰ Especially pH-neutral electrolytes are very promising because of their high electrochemical performance stability and beneficial voltage window.⁵¹ Organic electrolytes are currently in widespread use for commercial supercapacitors because of their extended voltage window up to 2.7 V, although ion mobility is lower than in aqueous media.⁵⁰ The cyclic voltammograms of the carbon beads (Figure 3A,B) show that even a short physical activation (e.g., PNC_{0.25h}) was sufficient to

Table 4. Specific Capacitance of the Carbon Beads in Aqueous 1 M Na₂SO₄ and 1 M TEA-BF₄ in PC (n.d., Not Determined; for Comparison, Data for AC Given As Well)

	specific capacitance in aqueous 1 M Na ₂ SO ₄ (F/g)	specific capacitance in 1 M TEA-BF ₄ in PC (F/g)
AC	140	103
PNC _{0h}	n.d.	1
PNC _{0.25h}	84	44
PNC _{0.5h}	89	84
PNC _{1h}	117	112
PNC _{1.5h}	127	123
PNC _{2h}	123	123

enable enhanced double layer capacitance. As the only exception, the nonactivated pyrolyzed material (PNC_{0h}) did not yield stable electrochemical performance in aqueous media and was deselected for further characterization. In general, longer activation enhanced the SSA and a higher specific capacitance can be seen. The highest capacitance of 127 F/g at 1.2 V was achieved after 1.5 h of CO₂ activation, even though the highest SSA was achieved after 2 h. Obviously, limitations to the achievable specific capacitance of highly porous carbons with high surface area are encountered,⁵² such as limited interfacial capacitance in carbon nanopores with very thin walls and incomplete charge screening.⁵³

Like in aqueous media, the CVs showed also the behavior of a near-ideal capacitor in 1 M TEA-BF₄ in PC (Figure 3B) for an activation duration of 0.5 h or longer. A maximum of 123 F/g was measured for PNC_{1.5h} and PNC_{2h} at 2.5 V. All CV were pronouncedly rectangular with a continuous increase in capacitance for higher cell voltages (known as butterfly shaped CV) stemming from electrochemical doping.^{39,54} As an exception, the CV of PNC_{0.25h} showed a continuous narrowing and reduced capacitance at higher voltages which was not observed in aqueous media (Figure 3A). This effect can be explained by steric (volumetric) effects as shown by Segalini et al. for nanoporous carbon with a very narrow pore size distribution and an average size of 0.68 nm (TiC-CDC) for 1 M TEA-BF₄ in ACN as electrolyte.⁵⁵ For comparison, the ionic diameters of ACN-solvated TEA⁺ and BF₄⁻ are 1.30 and 1.16 nm, respectively, and similar values are expected for PC (1.35 nm for TEA⁺ in PC and 1.40 nm for BF₄⁻ in PC).⁵⁶ Ion electroadsorption in pores smaller than this value is accomplished by (partial)⁵⁷ desolvation (ionic diameter, 0.67 nm for TEA⁺ and 0.45 nm for BF₄⁻).⁵⁸ Smaller ion diameters are expected for the aqueous media, and, thus, no such effects were seen for PNC_{0.25h} in 1 M Na₂SO₄.⁵⁹ In our case, PNC_{0.25h} had an average pore size of 0.6 nm which poses severe accessibility

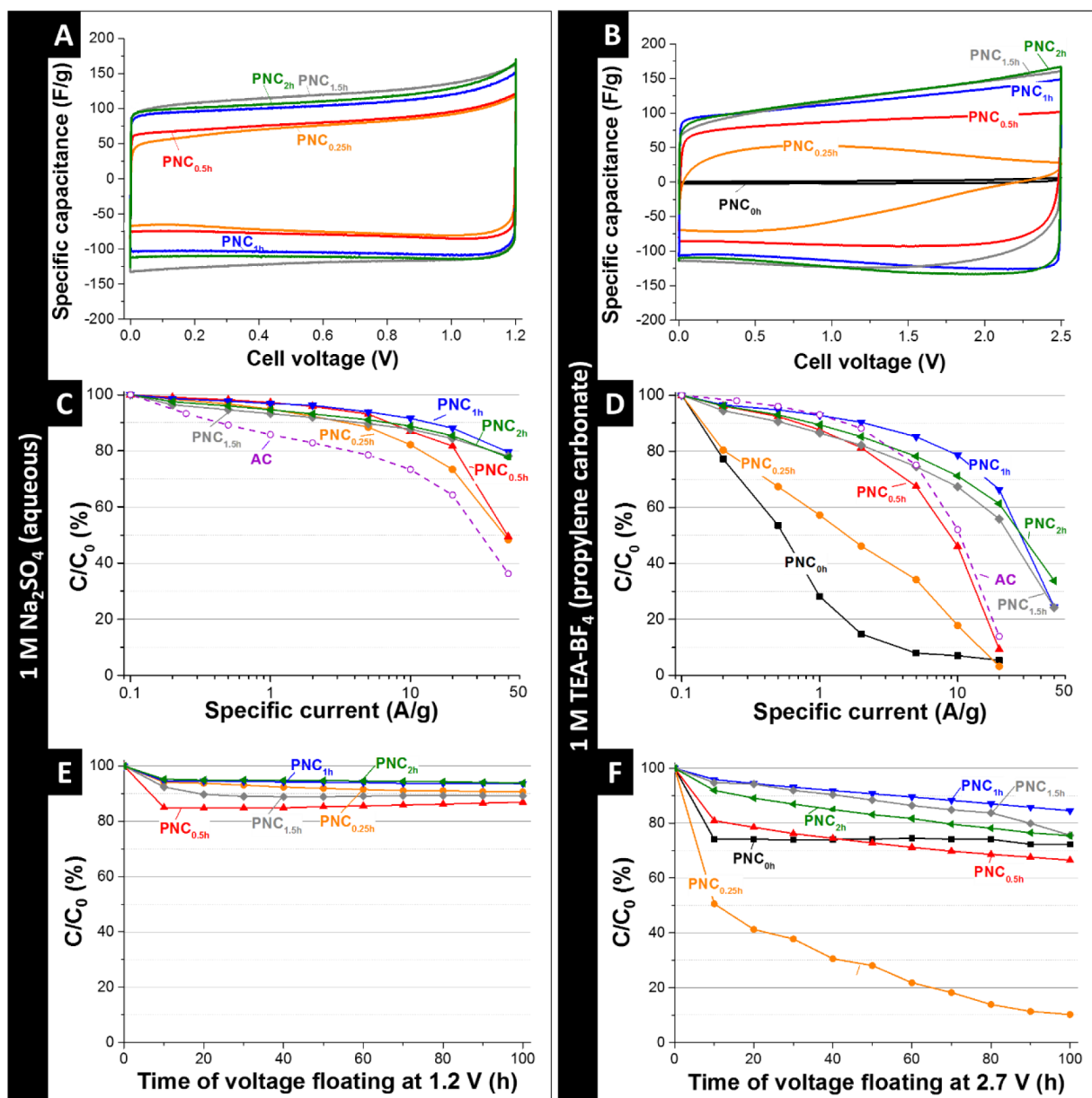


Figure 3. CVs of the carbon bead film electrodes in aqueous 1 M Na₂SO₄ (A) and in 1 M TEA-BF₄ in PC (B) with a scan rate of 5 mV/s. Rate handling of the film electrodes in aqueous 1 M Na₂SO₄ (C) and in 1 M TEA-BF₄ in PC (D) from a range of specific current of 0.1–50 A/g. For comparison, the rate handling ability of a conventional activated carbon (AC) is added as well to panels C and D. Long-time floating stability testing in aqueous 1 M Na₂SO₄ at 1.2 V (E) and in 1 M TEA-BF₄ in PC at 2.7 V (F).

limitations to the electrolyte ions in organic media (Table 1). CO₂ activation for at least 0.5 h was sufficient to yield an average pore size of 0.7 nm or more and no steric hindrance, and resulting CV deformation is observed.

In situ electrochemical dilatometry supports that PNC_{0.5h} suffered from volumetric restrictions to ion electrosorption in sub-nanometer carbon micropores (Supporting Information Figure S9). In particular, we see an increased strain of PNC_{0.25h} when compared to PNC_{0.5h}. At 75 C/g, PNC_{0.25h} shows a small expansion of 0.07%, compared to 0.05% of PNC_{0.5h} and the values divert at 175 C/g, namely, 0.29% and 0.22%, respectively. The ion sieving effect leads to a higher desolvation of ions to fit into the pores of PNC_{0.25h} and a higher total strain of the electrode. PNC_{0h} with even smaller pores (average pore size = 0.5 nm) and moderate specific surface area (SSA_{DFT} = 771 m²/g) yielded a negligible specific capacitance of around 1

F/g (since the ion radius of bare BF₄ is 0.45 nm) and, in comparison, a severely enhanced strain of 0.28% at 75 C/g.⁵⁸ These data align well with the increased pore swelling caused by steric effects when the pore size rivals the ion size shown by Hantel et al. for TiC-CDC in 1 M TEA-BF₄ in ACN with in situ electrochemical dilatometry.⁶⁰

All NovoCarb samples showed an excellent rate handling ability in aqueous media with a loss of capacitance of less than 7% at 1 A/g (Figure 3C). Activation for 1 h or longer enabled one to maintain more than 77% of the initial low rate capacitance at a high specific current of 50 A/g. This high power handling ability is also reflected by the very small distortion of CVs at very high scan rates of 1 V/s, as exemplified for PNC_{2h} (Supporting Information Figure S10A). For all activation conditions in aqueous Na₂SO₄, the measured power performance was also superior compared to a conven-

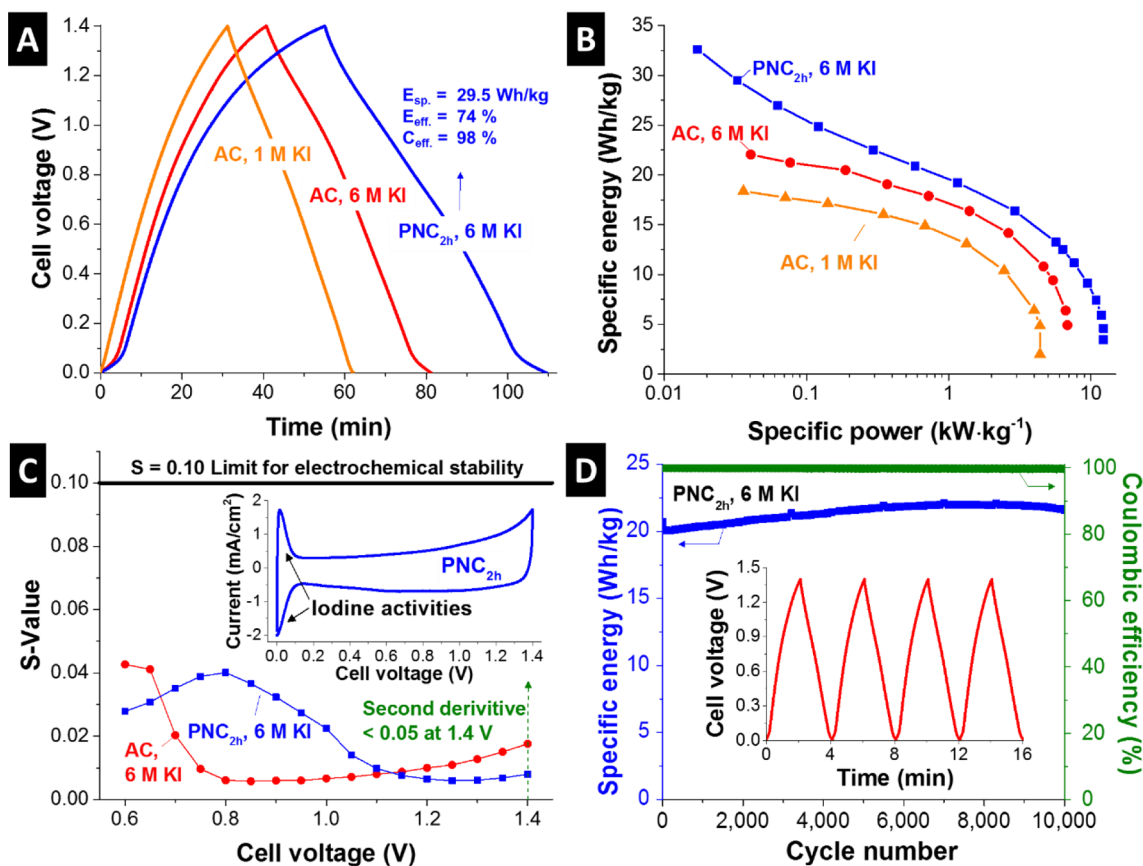


Figure 4. Galvanostatic charge/discharge curve at 50 mA/g (A) and the rate characteristics (B) obtained at various specific power in the cell voltage range from 0 to 1.4 V for different redox electrolyte systems. AC is a standard activated carbon used for the comparison of the performance for 1 and 6 M KI (aqueous). The electrochemical stability window was evaluated by the S-value method for 6 M KI with AC or PNC_{2h}. The inset shows the cyclic voltammogram of the cell with PNC_{2h} in 6 M KI at 1 mV/s for the cell stability window of 1.4 V. (C). Cyclic stability testing of PNC_{2h} in 6 M KI in the cell voltage range from 0 to 1.4 V at 1 A/g for 10,000 cycles and galvanostatic charge/discharge curve of the first few cycles (D).

tional nanoporous AC, for which the specific capacitance dropped to 86% at 1 A/g of the initial capacitance and to 73% at 10 A/g. In PC, a much lower overall rate handling is observed in agreement with the much lower ion mobility.⁶¹ Perfectly aligning with the accessibility issues seen from CV and dilatometry, we see a very poor rate handling for PNC_{0h} and PNC_{0.25h} (Figure 3D). On-setting for an activation time of 0.5 h (corresponding to an average pore size of 0.7 nm), we see an enhanced power performance and PNC_{1h} already significantly surpasses the values seen for the activated carbon reference. In detail, PNC_{1h} provided 78% of the initial capacitance at a very high specific current of 10 A/g compared to 52% for AC. The beneficial power handling ability of NovoCarb is also exemplified for PNC_{2h} when sweeping the scan rate in CV up to 1 V/s.

The enhanced power handling ability may relate to the sub-micrometer size of the NovoCarb beads used in this study. This aligns with the conclusions drawn by Perez et al. that nanosizing is an effective tool to enhance the rate handling ability even when comparing materials with virtually identical pore size distribution.⁸ Consequently, the improved power performance of NovoCarb beads over micrometer-sized activated carbon is well-explained. When compared to spherical carbide-derived carbon with an average particle diameter of ca. 150 nm, we still see an enhanced performance of NovoCarb. In particular, the mentioned CDC beads material maintained at 20 A/g 80% of the initial low rate capacitance of 110 F/g (in

relation to one electrode) in 1 M Na₂SO₄, which is lower than what we obtained for the best-performing NovoCarb beads (i.e., 88% PNC_{1h} with an average bead diameter of 255 nm).¹⁰

The stability of the NovoCarb is shown in Figure 3E,F for the aqueous and organic electrolytes. Voltage floating is a more demanding benchmarking to survey the electrochemical performance stability compared to voltage cycling.⁶² For the aqueous system, a very high electrochemical performance stability was observed with a decrease in capacitance between 6 and 13% after floating at 1.2 V for 100 h. As such, the values stayed above the industry-relevant level of 80% of the initial capacitance.⁶² Yet, a significantly higher loss of capacitive energy storage is observed in organic media. Albeit having a vanishing small capacitance of 1 F/g, the nonactivated material PNC_{0h} showed a fair performance stability with a reduction of 27% after 100 h at 2.7 V. Interestingly, PNC_{0.25h} exhibited a drastic performance drop of 90% after 100 h at 2.7 V, while the PNC_{0.5h} maintained 67% of the initial capacitance. The introduction of carbon heteroatoms and active surface sites may have severely reduced the energy storage stability by an enhanced electrolyte degeneration.⁶³ Longer activation times led to a significantly improved performance stability with capacitive retention between 75 and 85% after 100 h at 2.7 V. Seemingly, the enhanced structural ordering of the carbon and removal of more disordered material as seen from Raman analysis (Supporting Information Figure S6) leads to an improved energy storage capacity retention.

3.4. Electrochemical Performance in an Aqueous Redox Electrolyte. Since the NovoCarb beads exhibit a very high total pore volume with a large fraction of micropores and the potential for facile ion transport, the material is highly attractive for use with redox electrolytes. Besides the pore volume, a highly concentrated redox electrolyte is expected to be advantageous for maximizing redox activity and accomplishing high ion conductivities.^{64,65} So far, potassium iodide (KI) had only been explored up to 1 M concentration, yet the low concentrated KI systems have shown already promising performances such as high cyclic lifetime, high energy density, and power density via the variety of halide oxidation states and possibly no need of ion selective membrane through the specific adsorption of the oxidized halide into carbon micropores.²⁸ The solubility of the KI aqueous solution is very high as compared to other redox electrolyte solutions such as vanadyl sulfate (<3.5 M), potassium ferricyanide (<1.2 M), or hydroquinone solutions (<1 M) at room temperature.⁶⁶ For that reason, we provide first data for the potassium iodide system at 6 M concentration and benchmark the performance of PNC_{2h} (i.e., the sample with the largest pore volume) in comparison with conventional AC.

In our experiments, we were able to charge the cells using aqueous KI safely up to 1.4 V cell voltage. Extended S-value testing surveyed the entire range of cell voltages up to 1.4 V for the 6 M KI system in AC and PNC_{2h} (Figure 4C). S-value testing indicates the onset of enhanced charge transfer related to nonreversible reactions, and values below 0.1 are deemed indicative of stable cell performance.⁶² Within the studied range for both molar concentrations of potassium iodide, the second derivative of S-values remained below 0.05.

The increase in energy storage capacity at higher concentration can be seen from the galvanostatic charge/discharge profiles in Figure 4A for AC when transitioning from 1 M potassium iodide to 6 M KI. By deriving the specific energy by adequately considering the noncapacitive energy storage mechanism and noncapacitive GCPL shape following the procedure outlined in ref 67 and using eq 3, we calculate for the 1 M KI system in AC a maximum value of 18.4 W·h/kg at a low specific power of 36 W/kg. Note that due to the noncapacitive and nonpseudocapacitive response of the system, values for the specific capacitance (i.e., F/g) are disfavored to avoid misleading data and values are just given for the specific energy. For comparison, 6 M KI yielded at 40 W/kg a maximum specific energy of 22.0 W·h/kg in AC. This performance was severely surpassed when using PNC_{2h} and a specific energy of 29.5 W·h/kg was obtained at 33 W/kg for 6 M KI. This corresponds with a Coulombic efficiency of 98% and an energy efficiency of 74%. For comparison, Laheäär et al. recently reported for a system employing 0.5 M KI and operating at 1.6 V an energy efficiency of 52% and a Coulombic efficiency of 91% (86% and 97%, respectively, at 1.2 V).⁶⁷ At even lower specific power (i.e., 17 W/kg), a value of 32.6 W·h/kg was calculated for PNC_{2h} in 6 M KI at 1.4 V, and at a high specific power of 5.7 kW/kg, the system still provided a performance of 13.3 W·h/kg. The PNC_{2h} electrode with 6 M KI maintained about 4.6 W·h/kg at a very high specific power of 12.3 kW/kg. It seems that the system does not show a complete diffusion limited feature of the iodine redox reactions. The high power performance of PNC_{2h} electrode with 6 M KI can be explained by the confinement of redox ions in the micropores which overcome the diffusion limitation through micropores exhibiting pore size smaller than the equivalent

diffusion layer.³² Cyclic stability testing (Figure 4D) showed an excellent stability after 10,000 cycles (virtually no loss in energy storage capacity). The specific energy increased slightly by 4% after 10,000 cycles, due to improved wettability of carbon in aqueous electrolytes after an initial run-in period (conditioning).⁴

3.5. Ragone Plot for Novolac-Derived Carbon Electrodes. The energy vs power performance of the two high energy electrolytes, namely, 1 M TEA-BF₄ in PC (high energy by virtue of the high cell voltage) and aqueous 6 M KI (high energy by virtue of the redox energy storage) is shown for PNC_{2h} and AC (Figure 5). The resulting Ragone chart shows

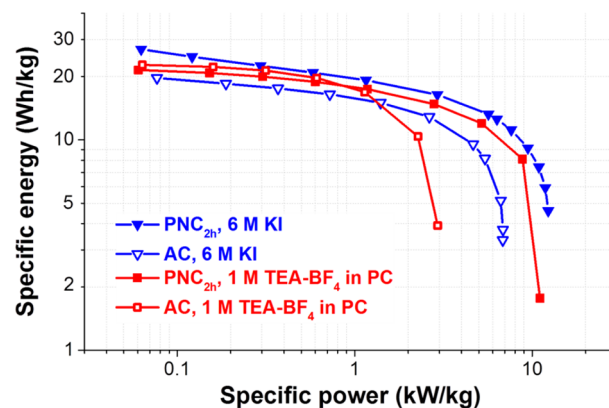


Figure 5. Ragone plot of PNC_{2h} and standard AC with an organic (1 M TEA-BF₄ in PC) and a redox electrolyte (aqueous 6 M KI).

the high potential of novolac-derived carbon beads for electrochemical energy storage, constantly yielding higher power handling and, at the same specific power, higher specific energy when compared to a common activated carbon (Table 5). The zeolite-templated carbons (ZTC) have a SSA similar to that of NovoCarb but have a higher specific capacitance, due to ordered structure and narrow PSD of the ZTCs which makes the pores well-accessible.⁶⁸ The main disadvantage of ZTC is the complex synthesis which requires toxic reactants (furfuryl alcohol or acetonitrile) and hydrofluoric acid. The AC, BP2000, activated carbon aerogel, biowaste-derived carbon, and onion-like carbon (OLC) show a lower capacitance than PNC_{2h} due to their lower SSAs. The rate handling behavior of the PNC_{2h} is quite similar to OLC, which is known for its good conductivity which makes it a promising material as a conductive additive.⁶¹ The high rate performance of NovoCarb makes the use of conductive additives redundant. The relative performance of BP2000 at high rates is best, but the specific capacitance of the NovoCarb is still higher. The beneficial performance is particularly attractive when considering the very low raw material costs of the novolac precursor of currently around 3 €/kg (as specified by the manufacturer) and the simple synthesis procedure.

4. CONCLUSIONS

Our work presents a facile synthesis method to obtain ultrasmall spherical carbon particles with a high specific surface and pore volume. A key advantage of our synthesis route is the facile self-emulsifying feature of the novolac–ethanol–water mixture. Therefore, no high shearing forces are needed to produce particles with an average diameter of 300 nm, setting this process apart from the established MAST carbon process.

Table 5. Overview of the Electrochemical Performance of NovoCarb-Material Compared to Other Carbon Materials for Supercapacitor Applications in Organic Media^a

material	ref	SSA _{BET} (m ² /g)	electrolyte	specific capacitance at 0.1 A/g (F/g)	capacitance loss at 10 A/g (%)
PNC _{2h}	this work	3104	1 M TEA-BF ₄ in PC	123	29
zeolite-templated carbon	68	3040	1 M TEA-BF ₄ in PC	168	not reported
activated carbon (YP-80, Kuraray)	this work	2347	1 M TEA-BF ₄ in PC	103	48
biowaste-derived carbon	69	1635	1 M TEA-BF ₄ in PC	75	not reported
activated carbon aerogel	70	1408	1 M TEA-BF ₄ in PC	101	not reported
activated carbon black (BP2000)	61	1389	1 M TEA-BF ₄ in PC	90	18
activated carbon black (BP2000)	61	1389	1 M TEA-BF ₄ in ACN	86	9
carbon onions	61	398	1 M TEA-BF ₄ in PC	18	28
carbon onions	61	398	1 M TEA-BF ₄ in ACN	18	10

^aThe data are arranged by descending BET surface area.

Pyrolyzed material already exhibits a SSA_{DFT} of 771 m²/g with a total pore volume of 0.26 cm³/g due to ethanol acting as a pore former. The sub-micrometer spheres are ideal for a physical activation which can further increase the SSA_{DFT} to 2237 m²/g (total pore volume, 1.71 cm³/g).

The specific capacitance of the novolac-derived carbon beads can reach approximately 125 F/g in an aqueous or organic electrolyte. The materials showed excellent performance at high scan rates and current densities with capacitance retention of approximately 80% at 50 A/g in aqueous and approximately 30% at 50 A/g in (highly viscous) organic electrolyte. For the redox electrolyte system, the combination of high molar concentration of potassium iodide (i.e., 6 M) and the large pore volume of PNC_{2h} enabled a very high specific energy exceeding 30 W·h/kg. Thereby, it is possible with an aqueous redox electrolyte to reach energy densities similar to that of an organic electrolyte. Due to the adjustability of the porosity via physical activation, novolac-derived carbon beads are highly promising for not only electrochemical energy storage but also for capacitive deionization as well as flow capacitor applications where spherical particles are preferable for the low viscosity.

■ ASSOCIATED CONTENT

📄 Supporting Information

The Supporting Information is available free of charge on the ACS Publications website at DOI: 10.1021/acsami.6b00669.

Electrode properties, reaction scheme, cell setup, scanning and transmission electron micrographs, combined thermogravimetry with mass spectroscopy data, Raman spectra, skeletal density, elemental analysis, and supplementary electrochemical data (PDF)

■ AUTHOR INFORMATION

Corresponding Author

*E-mail: volker.presser@leibniz-inm.de.

Notes

The authors declare no competing financial interest.

■ ACKNOWLEDGMENTS

We acknowledge funding from the German Federal Ministry for research and Education (BMBF) in support of the nanoEES^{3D} project (Award No. 03EK3013) as part of the strategic funding initiative energy storage framework. We kindly acknowledge the continuing support of Prof. Eduard Arzt (INM). Furthermore, we thank Ralph Schäfer from Allnex Germany GmbH for his help and supply of ALVONOL PN

320. We thank Karl-Peter Schmitt for his support with the hydrothermal process, Robert Drumm for the TGA-MS measurements, Andrea Jung for the CHNS analysis, and Daekyu Kim for the cell assembly (all at INM). This work was supported by the CREATE-Network Project, Horizon 2020 of the European Commission (RISE Project No. 644013). We also thank Dr. Daniel Weingarth, Anna Schreiber, and Marco Zeiger (all at the INM) for helpful discussions and their kind support.

■ REFERENCES

- (1) Beguin, F.; Frackowiak, E., Eds. *Supercapacitors: Materials, Systems and Applications*. Wiley-VCH Verlag: Weinheim, Germany, 2013; 568 pp.
- (2) Simon, P.; Gogotsi, Y. *Materials for Electrochemical Capacitors*. *Nat. Mater.* **2008**, *7*, 845–854.
- (3) Ibrahim, H.; Ilinca, A.; Perron, J. *Energy Storage Systems—Characteristics and Comparisons*. *Renewable Sustainable Energy Rev.* **2008**, *12* (5), 1221–1250.
- (4) Aslan, M.; Weingarth, D.; Jäckel, N.; Atchison, J. S.; Grobelsek, I.; Presser, V. Polyvinylpyrrolidone as Binder for Castable Supercapacitor Electrodes with High Electrochemical Performance in Organic Electrolytes. *J. Power Sources* **2014**, *266*, 374–383.
- (5) Inagaki, M.; Konno, H.; Tanaiki, O. Carbon Materials for Electrochemical Capacitors. *J. Power Sources* **2010**, *195* (24), 7880–7903.
- (6) Zang, L.; Cao, X.; Zhang, Y.; Sun, L.; Qin, C.; Wang, C. Microfluidic Generation of Graphene Beads for Supercapacitor Electrode Materials. *J. Mater. Chem. A* **2015**, *3*, 22088–22093.
- (7) Tang, K.; Fu, L.; White, R. J.; Yu, L.; Titirici, M.-M.; Antonietti, M.; Maier, J. Hollow Carbon Nanospheres with Superior Rate Capability for Sodium-Based Batteries. *Adv. Energy Mater.* **2012**, *2* (7), 873–877.
- (8) Pérez, C. R.; Yeon, S.-H.; Ségalini, J.; Presser, V.; Taberna, P.-L.; Simon, P.; Gogotsi, Y. Structure and Electrochemical Performance of Carbide-Derived Carbon Nanopowders. *Adv. Funct. Mater.* **2013**, *23* (8), 1081–1089.
- (9) Rose, M.; Korenblit, Y.; Kockrick, E.; Borchardt, L.; Oschatz, M.; Kaskel, S.; Yushin, G. Hierarchical Micro- and Mesoporous Carbide-Derived Carbon as a High-Performance Electrode Material in Supercapacitors. *Small* **2011**, *7* (8), 1108–1117.
- (10) Oschatz, M.; Zeiger, M.; Jäckel, N.; Strubel, P.; Borchardt, L.; Reinhold, R.; Nickel, W.; Eckert, J.; Presser, V.; Kaskel, S. Emulsion Soft Templating of Carbide-Derived Carbon Nanospheres with Controllable Porosity for Capacitive Electrochemical Energy Storage. *J. Mater. Chem. A* **2015**, *3*, 17983–17990.
- (11) Kalpana, D.; Karthikeyan, K.; Renganathan, N. G.; Lee, Y. S. Camphoric Carbon Nanobeads – A New Electrode Material for Supercapacitors. *Electrochem. Commun.* **2008**, *10* (7), 977–979.

- (12) Sharon, M.; Mukhopadhyay, K.; Yase, K.; Iijima, S.; Ando, Y.; Zhao, X. Spongy Carbon Nanobeads—A New Material. *Carbon* **1998**, *36* (5–6), 507–511.
- (13) Landfester, K. Miniemulsion Polymerization and the Structure of Polymer and Hybrid Nanoparticles. *Angew. Chem., Int. Ed.* **2009**, *48* (25), 4488–4507.
- (14) Sanchez-Dominguez, M.; Aubery, C.; Solans, C., New Trends on the Synthesis of Inorganic Nanoparticles Using Microemulsions as Confined Reaction Media. In *Smart Nanoparticles Technology*, Hashim, A., Ed.; InTech Europe: Rijeka, Croatia, 2012; Chapter 9, pp 195–220, DOI: [10.5772/33010](https://doi.org/10.5772/33010).
- (15) Yang, J.-B.; Ling, L.-C.; Liu, L.; Kang, F.-Y.; Huang, Z.-H.; Wu, H. Preparation and Properties of Phenolic Resin-Based Activated Carbon Spheres with Controlled Pore Size Distribution. *Carbon* **2002**, *40*, 911–916.
- (16) Singh, A.; Lal, D. Microporous Activated Carbon Spheres Prepared from Resole-Type Crosslinked Phenolic Beads by Physical Activation. *J. Appl. Polym. Sci.* **2008**, *110* (5), 3283–3291.
- (17) Fang, Y.; Gu, D.; Zou, Y.; Wu, Z.; Li, F.; Che, R.; Deng, Y.; Tu, B.; Zhao, D. A Low-Concentration Hydrothermal Synthesis of Biocompatible Ordered Mesoporous Carbon Nanospheres with Tunable and Uniform Size. *Angew. Chem., Int. Ed.* **2010**, *49* (43), 7987–7991.
- (18) Huang, Y.-P.; Hsi, H.-C.; Liu, S.-C. Preparation of Spherical Activated Phenol-Formaldehyde Beads from Bamboo Tar for Adsorption of Toluene. *J. Air Waste Manage. Assoc.* **2013**, *63* (8), 977–983.
- (19) Slomkowski, S.; Alemán, J. V.; Gilbert, R. G.; Hess, M.; Horie, K.; Jones, R. G.; Kubisa, P.; Meisel, I.; Mormann, W.; Penczek, S.; Stepto, R. F. T. Terminology of Polymers and Polymerization Processes in Dispersed Systems (IUPAC Recommendations 2011). *Pure Appl. Chem.* **2011**, *83* (12), 2229–2259.
- (20) Wan, J.; Wang, S.; Li, C.; Zhou, D.; Chen, J.; Liu, Z.; Yu, L.; Fan, H.; Li, B.-G. Effect of Molecular Weight and Molecular Weight Distribution on Cure Reaction of Novolac with Hexamethylenetetramine and Properties of Related Composites. *Thermochim. Acta* **2012**, *530*, 32–41.
- (21) Ahmadpour, A.; Do, D. D. The Preparation of Active Carbons from Coal by Chemical and Physical Activation. *Carbon* **1996**, *34* (4), 471–479.
- (22) Bleda-Martínez, M. J.; Maciá-Agulló, J. A.; Lozano-Castelló, D.; Morallón, E.; Cazorla-Amorós, D.; Linares-Solano, A. Role of Surface Chemistry on Electric Double Layer Capacitance of Carbon Materials. *Carbon* **2005**, *43* (13), 2677–2684.
- (23) Maciá-Agulló, J. A.; Moore, B. C.; Cazorla-Amorós, D.; Linares-Solano, A. Activation of Coal Tar Pitch Carbon Fibres: Physical Activation vs. Chemical Activation. *Carbon* **2004**, *42* (7), 1367–1370.
- (24) Tennison, S. R. Phenolic-Resin-Derived Activated Carbons. *Appl. Catal., A* **1998**, *173* (2), 289–311.
- (25) Tennison, S. R.; Kozynchenko, O. P.; Strelko, V. V.; Blackburn, A. J. Porous Carbons. U.S. Patent US 20040024074 A1, 2008
- (26) Fernández, J. A.; Tennison, S.; Kozynchenko, O.; Rubiera, F.; Stoeckli, F.; Centeno, T. A. Effect of Mesoporosity on Specific Capacitance of Carbons. *Carbon* **2009**, *47* (6), 1598–1604.
- (27) Frackowiak, E.; Meller, M.; Menzel, J.; Gastol, D.; Fic, K. Redox-Active Electrolyte for Supercapacitor Application. *Faraday Discuss.* **2014**, *172*, 179–198.
- (28) Frackowiak, E.; Fic, K.; Meller, M.; Lota, G. Electrochemistry Serving People and Nature: High-Energy Ecocapacitors based on Redox-Active Electrolytes. *ChemSusChem* **2012**, *5* (7), 1181–1185.
- (29) Akinwolemiwa, B.; Peng, C.; Chen, G. Z. Redox Electrolytes in Supercapacitors. *J. Electrochem. Soc.* **2015**, *162* (5), A5054–A5059.
- (30) Roldán, S.; Granda, M.; Menéndez, R.; Santamaría, R.; Blanco, C. Mechanisms of Energy Storage in Carbon-Based Supercapacitors Modified with a Quinoid Redox-Active Electrolyte. *J. Phys. Chem. C* **2011**, *115* (35), 17606–17611.
- (31) Roldán, S.; Blanco, C.; Granda, M.; Menéndez, R.; Santamaría, R. Towards a Further Generation of High-Energy Carbon-Based Capacitors by Using Redox-Active Electrolytes. *Angew. Chem.* **2011**, *123* (7), 1737–1739.
- (32) Narayanan, R.; Bandaru, P. R. High Rate Capacity through Redox Electrolytes Confined in Macroporous Electrodes. *J. Electrochem. Soc.* **2015**, *162* (1), A86–A91.
- (33) Schneider, C. A.; Rasband, W. S.; Eliceiri, K. W. NIH Image to ImageJ: 25 years of Image Analysis. *Nat. Methods* **2012**, *9* (7), 671–675.
- (34) Presser, V.; McDonough, J.; Yeon, S.-H.; Gogotsi, Y. Effect of Pore Size on Carbon Dioxide Sorption by Carbide Derived Carbon. *Energy Environ. Sci.* **2011**, *4* (8), 3059.
- (35) Vishnyakov, A.; Ravikovitch, P. I.; Neimark, A. V. Molecular Level Models for CO₂ Sorption in Nanopores. *Langmuir* **1999**, *15* (25), 8736–8742.
- (36) Gor, G. Y.; Thommes, M.; Cychosz, K. A.; Neimark, A. V. Quenched Solid Density Functional Theory Method for Characterization of Mesoporous Carbons by Nitrogen Adsorption. *Carbon* **2012**, *50* (4), 1583–1590.
- (37) Brunauer, S.; Emmett, P. H.; Teller, E. Adsorption of Gases in Multimolecular Layers. *J. Am. Chem. Soc.* **1938**, *60* (2), 309–319.
- (38) Presser, V.; McDonough, J.; Yeon, S. H.; Gogotsi, Y. Effect of Pore Size on Carbon Dioxide Sorption by Carbide Derived Carbon. *Energy Environ. Sci.* **2011**, *4* (8), 3059–3066.
- (39) Weingarth, D.; Zeiger, M.; Jäckel, N.; Aslan, M.; Feng, G.; Presser, V. Graphitization as a Universal Tool to Tailor the Potential-Dependent Capacitance of Carbon Supercapacitors. *Adv. Energy Mater.* **2014**, *4* (13), 1400316.
- (40) Chen, L.; Bai, H.; Huang, Z.; Li, L. Mechanism Investigation and Suppression of Self-Discharge in Active Electrolyte Enhanced Supercapacitors. *Energy Environ. Sci.* **2014**, *7* (5), 1750–1759.
- (41) Stoller, M. D.; Ruoff, R. S. Best Practice Methods for Determining an Electrode Material's Performance for Ultracapacitors. *Energy Environ. Sci.* **2010**, *3* (9), 1294–1301.
- (42) Trick, K. A.; Saliba, T. E. Mechanisms of the Pyrolysis of Phenolic Resin in a Carbon/Phenolic Composite. *Carbon* **1995**, *33* (11), 1509–1515.
- (43) Van der Bruggen, B.; Schaep, J.; Wilms, D.; Vandecasteele, C. Influence of Molecular Size, Polarity and Charge on the Retention of Organic Molecules by Nanofiltration. *J. Membr. Sci.* **1999**, *156* (1), 29.
- (44) Zickler, G. A.; Smarsly, B.; Gierlinger, N.; Peterlik, H.; Paris, O. A Reconsideration of the Relationship between the Crystallite Size La of Carbons Determined by X-ray Diffraction and Raman Spectroscopy. *Carbon* **2006**, *44* (15), 3239–3246.
- (45) Tuinstra, F.; Koenig, J. L. Raman Spectrum of Graphite. *J. Chem. Phys.* **1970**, *53* (3), 1126–1130.
- (46) Ferrari, A. C.; Robertson, J. Interpretation of Raman Spectra of Disordered and Amorphous Carbon. *Phys. Rev. B: Condens. Matter Mater. Phys.* **2000**, *61* (20), 14095.
- (47) Faber, K.; Badaczewski, F.; Oschatz, M.; Mondin, G.; Nickel, W.; Kaskel, S.; Smarsly, B. M. In-Depth Investigation of the Carbon Microstructure of Silicon Carbide-Derived Carbons by Wide-Angle X-ray Scattering. *J. Phys. Chem. C* **2014**, *118* (29), 15705–15715.
- (48) Ferrari, A. C. A Model To Interpret the Raman Spectry of Disordered Amorphous and Nanostructured Carbons. *MRS Online Proc. Libr.* **2001**, *675*, W11.5.1.
- (49) Findeisen, E.; Feidenhans'l, R.; Vigild, M. E.; Clausen, K. N.; Hansen, J. B.; Bentzon, M. D.; Goff, J. P. Hydrogen Concentration and Mass Density of Diamondlike Carbon Films Obtained by X-ray and Neutron Reflectivity. *J. Appl. Phys.* **1994**, *76* (8), 4636.
- (50) Béguin, F.; Presser, V.; Balducci, A.; Frackowiak, E. Carbons and Electrolytes for Advanced Supercapacitors. *Adv. Mater.* **2014**, *26* (14), 2219–2251.
- (51) Fic, K.; Lota, G.; Meller, M.; Frackowiak, E. Novel Insight into Neutral Medium as Electrolyte for High-Voltage Supercapacitors. *Energy Environ. Sci.* **2012**, *5* (2), 5842–5850.
- (52) Barbieri, O.; Hahn, M.; Herzog, A.; Kötz, R. Capacitance Limits of High Surface Area Activated Carbons for Double Layer Capacitors. *Carbon* **2005**, *43* (6), 1303–1310.

- (53) Stoller, M. D.; Magnuson, C. W.; Zhu, Y.; Murali, S.; Suk, J. W.; Piner, R.; Ruoff, R. S. Interfacial Capacitance of Single Layer Graphene. *Energy Environ. Sci.* **2011**, *4* (11), 4685–4689.
- (54) Gerischer, H.; McIntyre, R.; Scherson, D.; Storck, W. Density of the Electronic States of Graphite: Derivation from Differential Capacitance Measurements. *J. Phys. Chem.* **1987**, *91* (7), 1930–1935.
- (55) Segalini, J.; Iwama, E.; Taberna, P.-L.; Gogotsi, Y.; Simon, P. Steric Effects in Adsorption of Ions from Mixed Electrolytes into Microporous Carbon. *Electrochem. Commun.* **2012**, *15* (1), 63–65.
- (56) Yang, C.-M.; Kim, Y.-J.; Endo, M.; Kanoh, H.; Yudasaka, M.; Iijima, S.; Kaneko, K. Nanowindow-Regulated Specific Capacitance of Supercapacitor Electrodes of Single-Wall Carbon Nanohorns. *J. Am. Chem. Soc.* **2007**, *129* (1), 20–21.
- (57) Chmiola, J.; Yushin, G.; Gogotsi, Y.; Portet, C.; Simon, P.; Taberna, P. L. Anomalous Increase in Carbon Capacitance at Pore Sizes Less than 1 nm. *Science* **2006**, *313* (5794), 1760–1763.
- (58) Chmiola, J.; Largeot, C.; Taberna, P.-L.; Simon, P.; Gogotsi, Y. Desolvation of Ions in Subnanometer Pores and Its Effect on Capacitance and Double-Layer Theory. *Angew. Chem., Int. Ed.* **2008**, *47* (18), 3392–3395.
- (59) Raymundo-Piñero, E.; Kierzek, K.; Machnikowski, J.; Béguin, F. Relationship between the Nanoporous Texture of Activated Carbons and Their Capacitance Properties in Different Electrolytes. *Carbon* **2006**, *44* (12), 2498–2507.
- (60) Hantel, M. M.; Presser, V.; Kötz, R.; Gogotsi, Y. In Situ Electrochemical Dilatometry of Carbide-Derived Carbons. *Electrochem. Commun.* **2011**, *13* (11), 1221–1224.
- (61) Jäckel, N.; Weingarh, D.; Zeiger, M.; Aslan, M.; Grobelsek, I.; Presser, V. Comparison of Carbon Onions and Carbon Blacks As Conductive Additives for Carbon Supercapacitors in Organic Electrolytes. *J. Power Sources* **2014**, *272* (1), 1122–1133.
- (62) Weingarh, D.; Noh, H.; Foelske-Schmitz, A.; Wokaun, A.; Kötz, R. A Reliable Determination Method of Stability Limits for Electrochemical Double Layer Capacitors. *Electrochim. Acta* **2013**, *103*, 119–124.
- (63) Cericola, D.; Ruch, P. W.; Foelske-Schmitz, A.; Weingarh, D.; Kötz, R. Effect of Water on the Aging of Activated Carbon Based Electrochemical Double Layer Capacitors during Constant Voltage Load Tests. *Int. J. Electrochem. Sci.* **2011**, *6* (4), 988–996.
- (64) Wang, W.; Luo, Q.; Li, B.; Wei, X.; Li, L.; Yang, Z. Recent Progress in Redox Flow Battery Research and Development. *Adv. Funct. Mater.* **2013**, *23* (8), 970–986.
- (65) Weber, A. Z.; Mench, M. M.; Meyers, J. P.; Ross, P. N.; Gostick, J. T.; Liu, Q. Redox Flow Batteries: A Review. *J. Appl. Electrochem.* **2011**, *41* (10), 1137–1164.
- (66) Rahman, F.; Skyllas-Kazacos, M. Solubility of Vanadyl Sulfate in Concentrated Sulfuric Acid Solutions. *J. Power Sources* **1998**, *72* (2), 105–110.
- (67) Laheäär, A.; Przygocki, P.; Abbas, Q.; Béguin, F. Appropriate Methods for Evaluating the Efficiency and Capacitive Behavior of Different Types of Supercapacitors. *Electrochem. Commun.* **2015**, *60*, 21–25.
- (68) Nishihara, H.; Itoi, H.; Kogure, T.; Hou, P.-X.; Touhara, H.; Okino, F.; Kyotani, F. Investigation of the Ion Storage/Transfer Behavior in an Electrical Double-Layer Capacitor by Using Ordered Microporous Carbons as Model Materials. *Chem. - Eur. J.* **2009**, *15* (21), 5355–5363.
- (69) Ramirez-Castro, C.; Schütter, C.; Passerini, S.; Balducci, A. Microporous Carbonaceous Materials Prepared from Biowaste for Supercapacitor Application. *Electrochim. Acta* **2016**, DOI: [10.1016/j.electacta.2015.12.126](https://doi.org/10.1016/j.electacta.2015.12.126).
- (70) Fang, B.; Wei, Y. Z.; Maruyama, K.; Kumagai, M. High Capacity Supercapacitors Based on Modified Activated Carbon Aerogel. *J. Appl. Electrochem.* **2005**, *35* (3), 229–233.

Sub-micrometer Novolac-Derived Carbon Beads for High Performance Supercapacitors and Redox Electrolyte Energy Storage

Benjamin Krüner,^{1,2} Juhan Lee,^{1,2} Nicolas Jäckel,^{1,2} Aura Tolosa,^{1,2} and Volker Presser^{1,2,*}

¹ *INM - Leibniz Institute for New Materials, 66123 Saarbrücken, Germany*

² *Department of Materials Science and Engineering, Saarland University, 66123 Saarbrücken, Germany*

* *Corresponding author's eMail: volker.presser@leibniz-inm.de*

Table S1: Electrode properties. Note the reduced active mass per electrode as a result of the increased porosity at comparable electrode thickness.

	Electrode density (mg/cm³)	Active mass (mg)	Electrode diameter (mm)	Electrode thickness (mm)
PNC _{0h}	611	15.2	12	0.22
PNC _{0.25h}	442	8.5	12	0.17
PNC _{0.5h}	385	8.7	12	0.20
PNC _{1h}	230	3.9	12	0.15
PNC _{1.5h}	169	2.3	12	0.12
PNC _{2h}	161	3.1	12	0.17

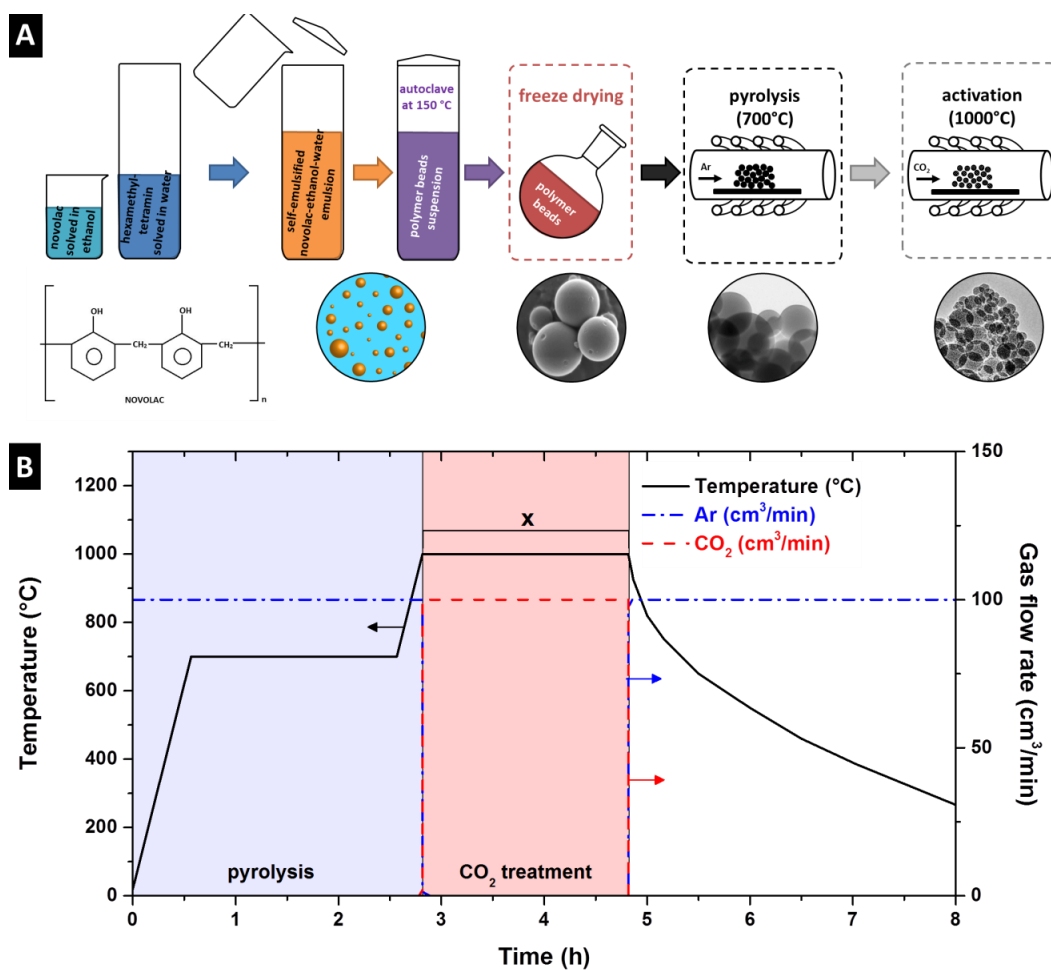


Figure S1: Schematic illustration of the synthesis route (A) and processing conditions of the pyrolysis and CO₂-treatment (B). The parameter X denotes the duration of the CO₂-treatment (physical activation), which was varied for the different experiments.

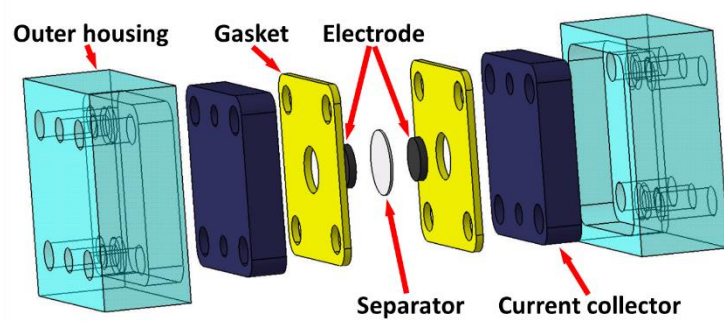


Figure S2: Schematic setup of the redox-electrolyte cell.

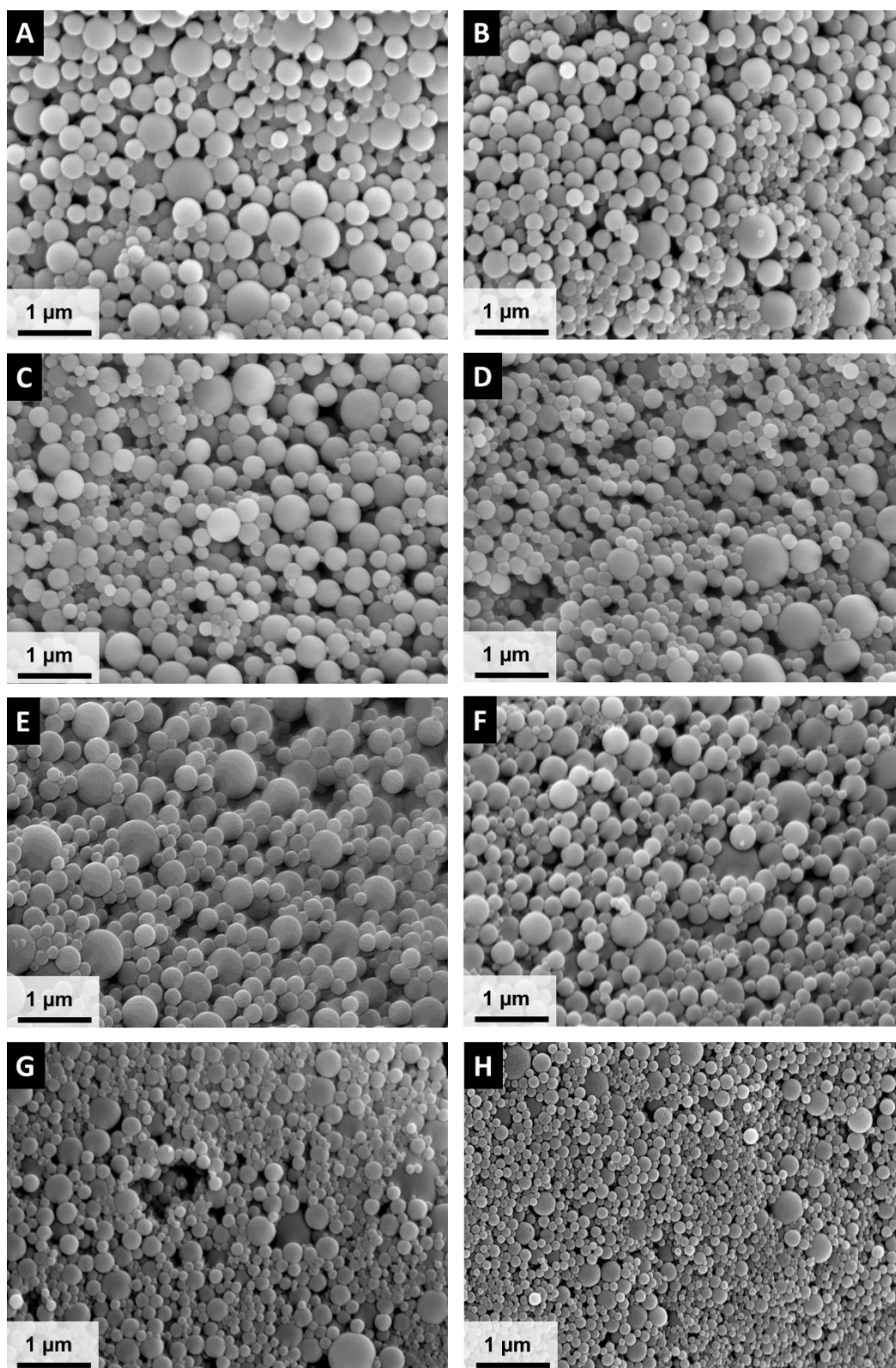


Figure S3: SEM images of PNC_{0h} (A), PNC_{0.25h} (B), PNC_{0.5h} (C), PNC_{1h} (D), PNC_{1.5h} (E), PNC_{2h} (F), PNC_{2.5h} (G), and PNC_{3h} (H).

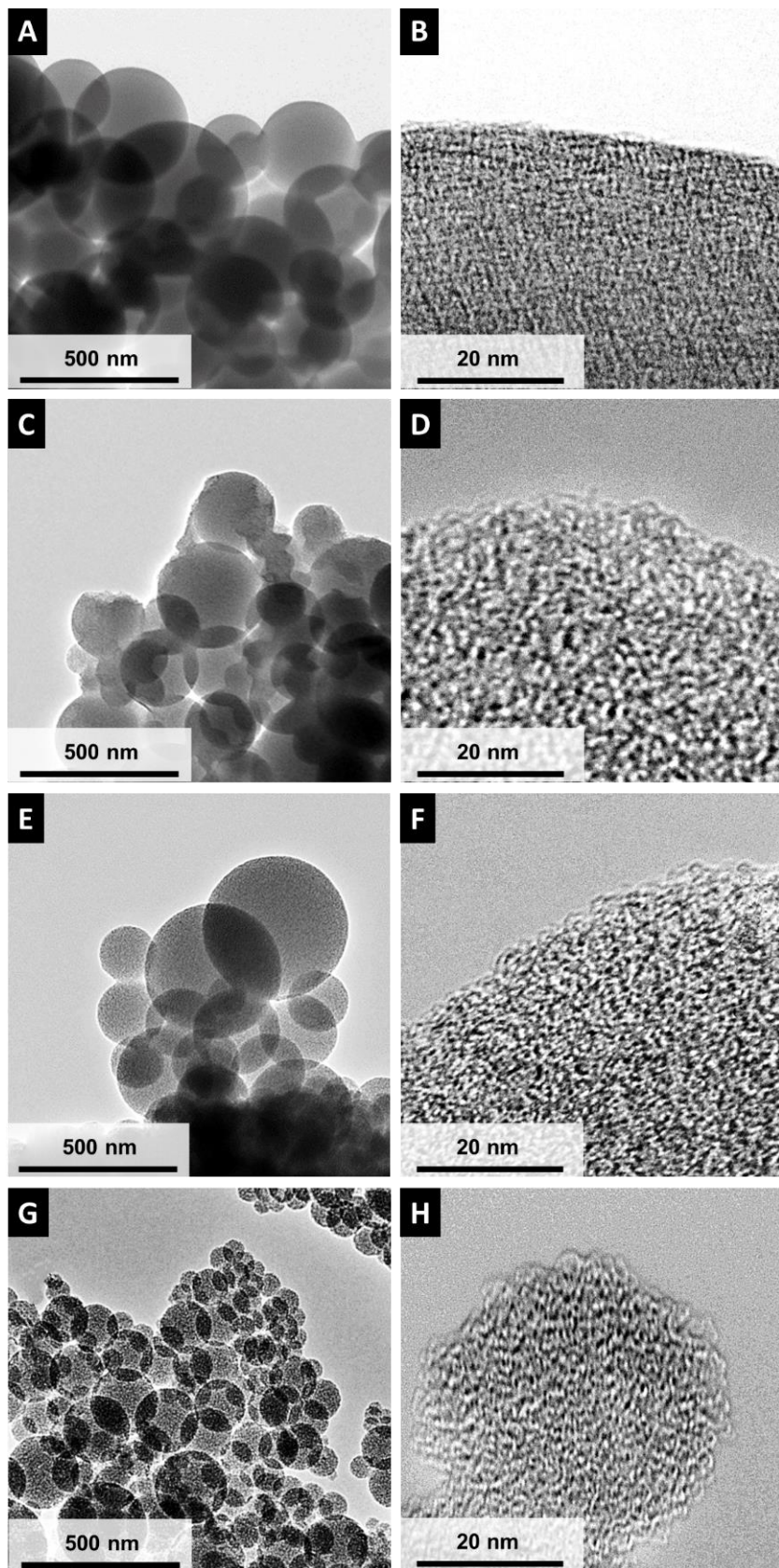


Figure S4: TEM images of the pyrolyzed PNC_{0h} (a, b) and the CO₂ activated PNC_{1h} (c, d), PNC_{2h} (e, f) and PNC_{3h} (g, h).

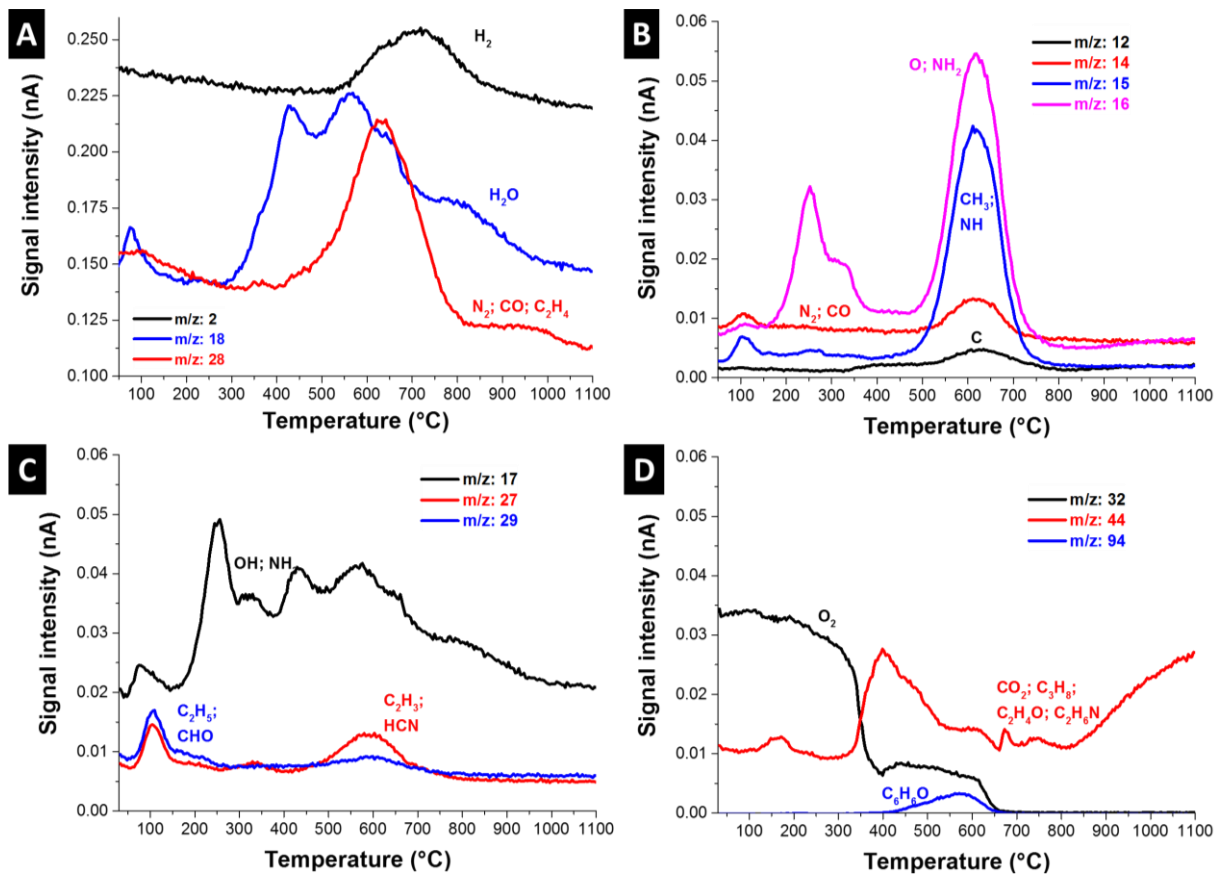


Figure S5: TGA-MS graphs (ionic current vs. temperature) of the pyrolysis of the polymeric beads for the m/z: 2, 18, and 28 (a), m/z: 12, 14, 15, and 16 (b), m/z: 17, 27, and 29 (c), m/z: 32, 44, and 94 (d).

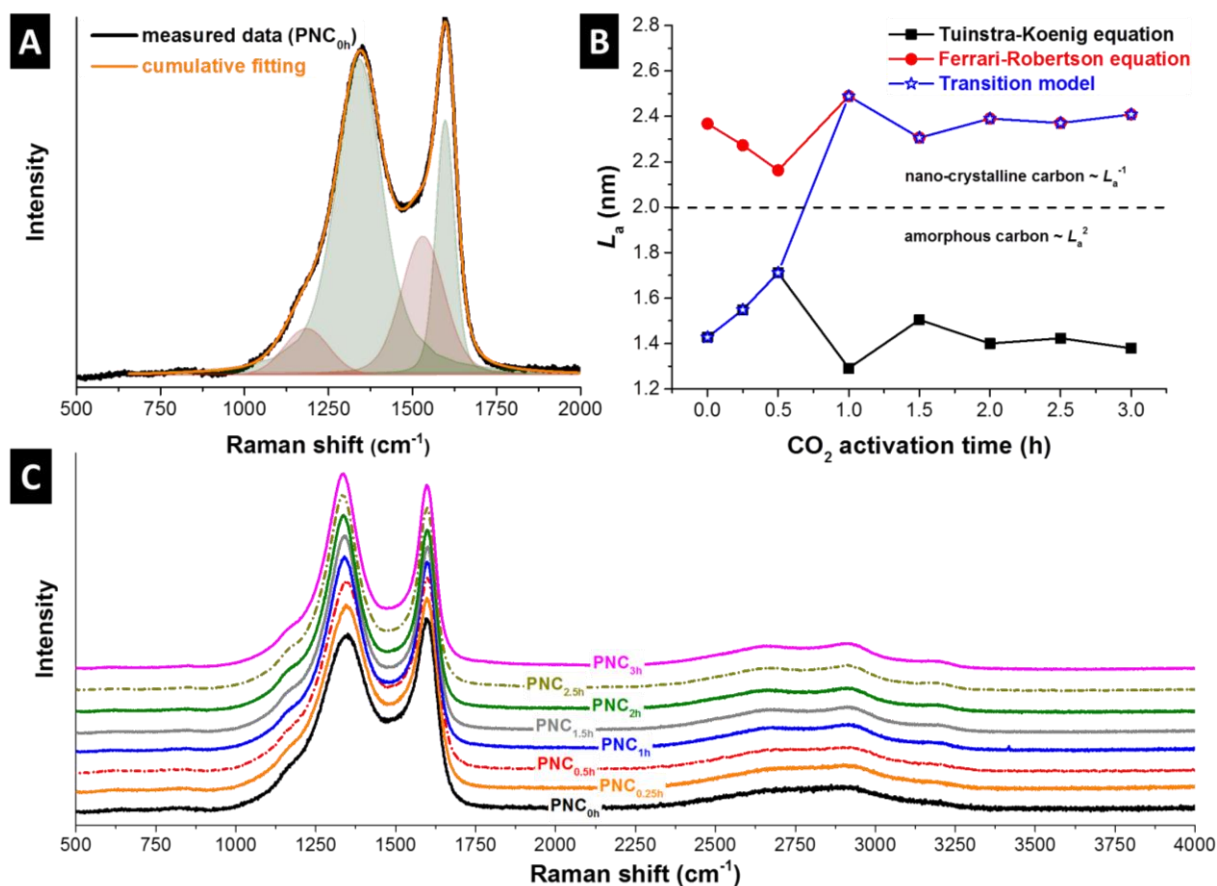


Figure S6: Raman spectra of $\text{PN}_{0\text{h}}$ showing the two-peak fitting for the D- and G-mode (A) and the average in-plane domain size (L_a) calculated with the Tuinstra-Koenig (black) and Ferrari-Robertson equation (red) and assuming a transition between the two models regarding the L_a values (blue) (B). Raman spectra of the pyrolyzed and activated carbon beads (C). The spectra were off-set by 10% along the y-axis for improved visibility.

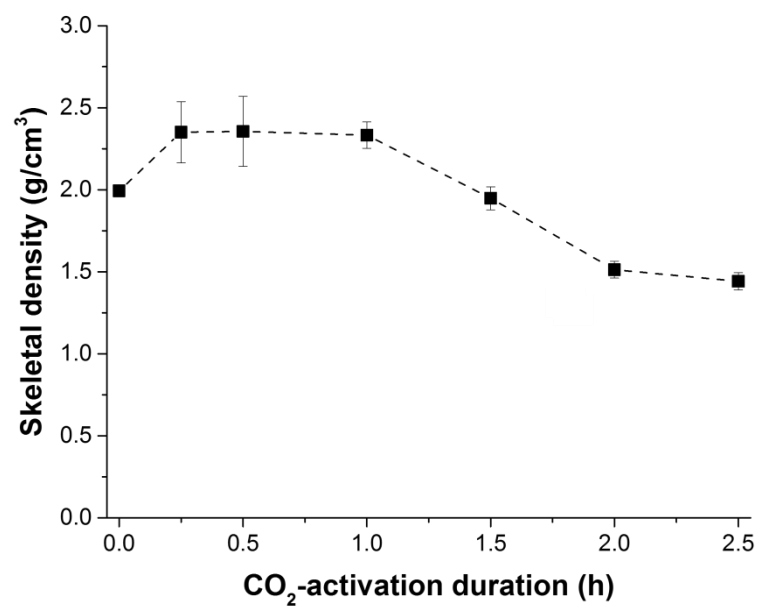


Figure S7: Skeletal density of the carbon beads vs. the CO₂-activation duration measured by pycnometry.

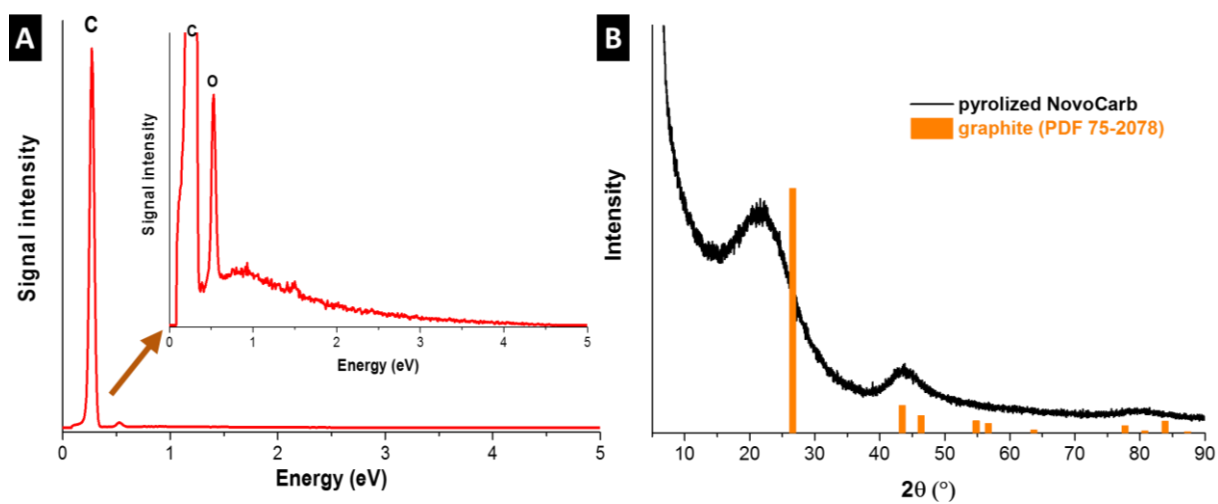


Figure S8: EDX spectra of the pyrolyzed carbon beads (PN_{0h}) by an accelerating voltage of 5 keV (A). Only carbon and oxygen can be clearly identified. XRD pattern of the pyrolyzed NovoCarb (at 1000 °C), which is mainly amorphous (B).

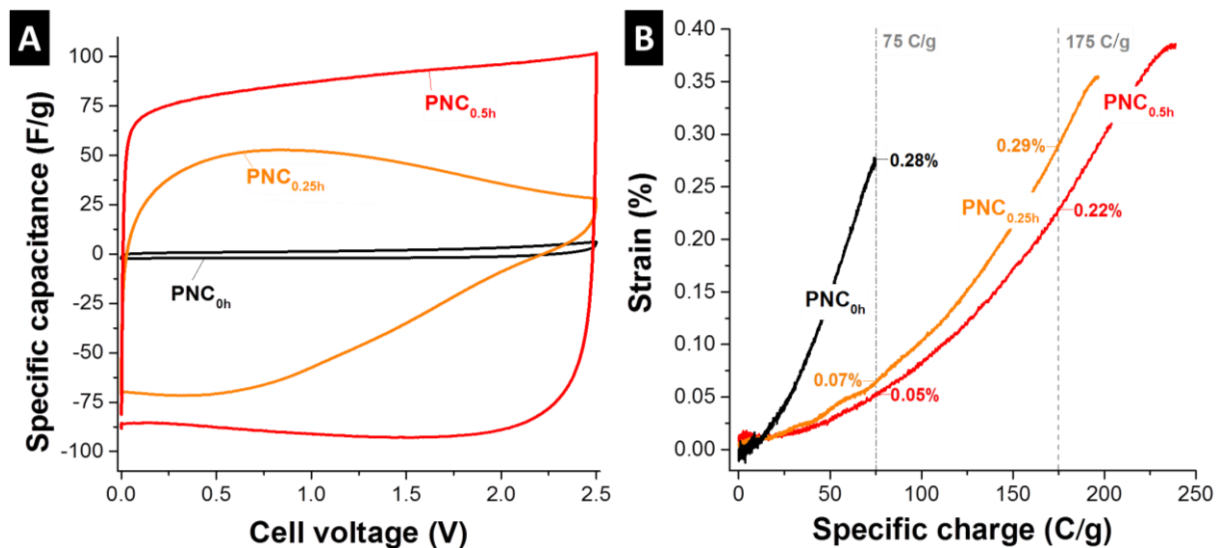


Figure S9: Cyclic voltammograms at 5 mV/s (A) and in-situ dilatometry data (B) of non-activated PNC_{0h} and two activated novolac-derived carbons (PNC_{0.25h} and PNC_{0.5h}) in 1 M TEA-BF₄ in PC. The strain data were recorded with a scan rate of 1 mV/s and only data during charging (not discharging) are shown. For a relative comparison, the strain values at 75 C/g and 175 C/g are denoted.

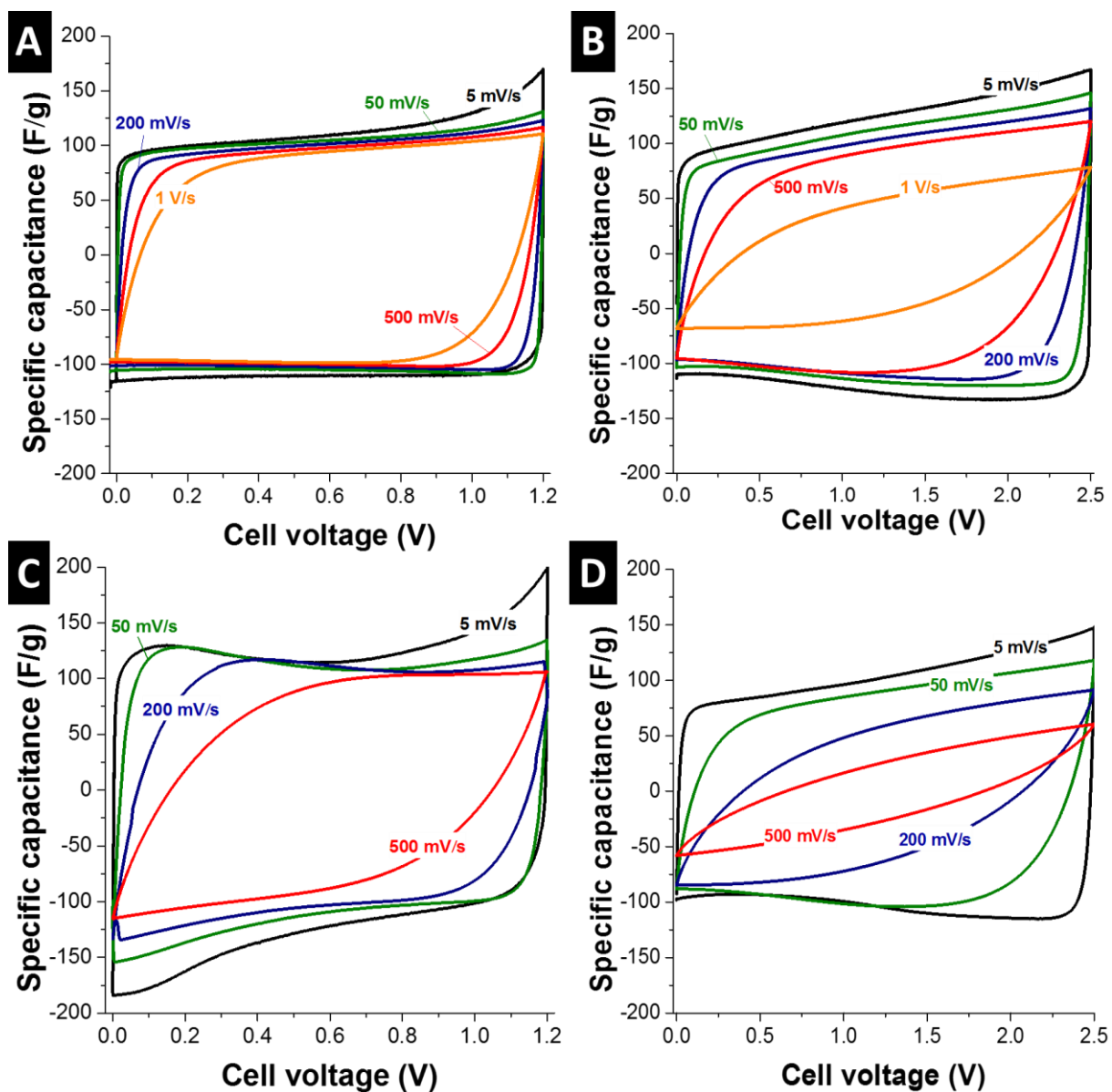


Figure S10: CVs of PNC_{2h} in aqueous 1 M Na₂SO₄ (a) and in 1 M TEA-BF₄ in PC (b) with a scan rate varying from 5 mV/s to 1 V/s and CVs of AC in aqueous 1 M Na₂SO₄ (c) and in 1 M TEA-BF₄ in PC (d) with a scan rate varying from 5 mV/s to 500 mV/s.

3.4. Tin/vanadium redox electrolyte for battery-like energy storage capacity combined with supercapacitor-like power handling

Juhan Lee,^{1,2} Benjamin Krüner,^{1,2} Aura Tolosa,^{1,2} Sethuraman Sathyamoorthi,^{1,4} Daekyu Kim,^{1,3} Soumyadip Choudhury,¹ Kum-Hee Seo,³ and Volker Presser^{1,2}

¹ INM - Leibniz Institute for New Materials, Campus D2 2, 66123 Saarbrücken, Germany

² Saarland University, Campus D2 2, 66123 Saarbrücken, Germany

³ School of Energy, Materials and Chemical Engineering, Korea University of Technology and Education, Chungjeol-ro 1600, 31253, Cheonan, Republic of Korea

⁴ Electrochemical Process Engineering Division, CSIR-Central Electrochemical Research Institute, Karaikudi, 630 006, India

Citation:

Lee, J.; Krüner, B.; Tolosa, A.; Sathyamoorthi, S.; Kim, D.; Choudhury, S.; Seo, K.-H.; Presser, V., Tin/vanadium redox electrolyte for battery-like energy storage capacity combined with supercapacitor-like power handling. *Energy & Environmental Science* **2016**, 9 (11), 3392-3398. *Cover story*

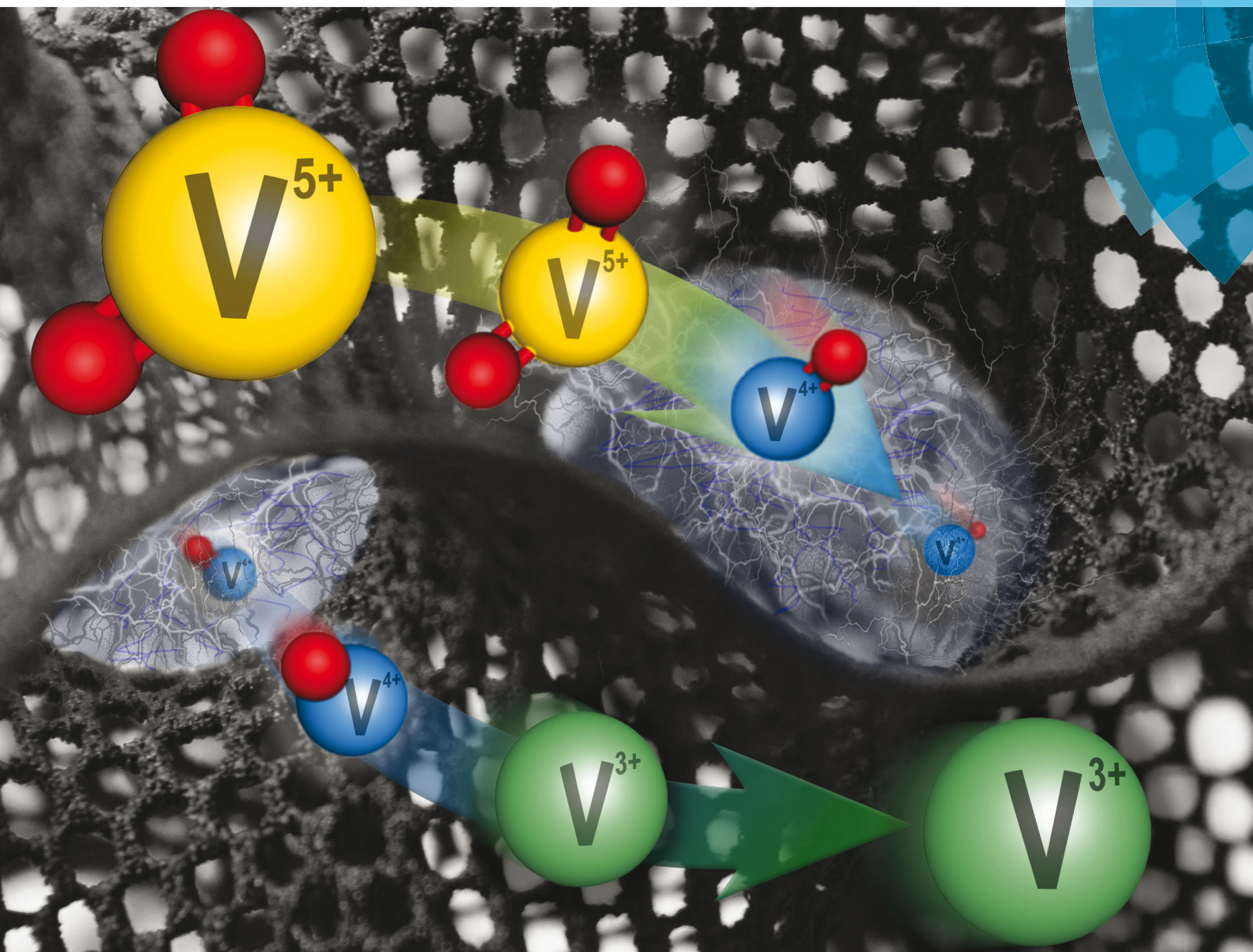
Own contributions: Design, planning, writing, cell design, experimental plan, electrochemical analyses

Abstract

We introduce a high performance hybrid electrochemical energy storage system based on an aqueous electrolyte containing tin sulfate (SnSO_4) and vanadyl sulfate (VOSO_4) with nanoporous activated carbon. The energy storage mechanism of this system benefits from the unique synergy of concurrent electric double-layer formation, reversible tin redox reactions, and three-step redox reactions of vanadium. The hybrid system showed excellent electrochemical properties such as a promising energy capacity (ca. 75 Wh/kg, 30Wh/L) and a maximum power of up to 1.5 kW/kg (600 W/L, 250 W/m²), exhibiting capacitor-like galvanostatic cyclic stability and a low level of self-discharging rate.

Energy & Environmental Science

www.rsc.org/ees



ISSN 1754-5692



ROYAL SOCIETY
OF CHEMISTRY

COMMUNICATION

Volker Presser *et al.*

Tin/vanadium redox electrolyte for battery-like energy storage capacity combined with supercapacitor-like power handling

175
YEARS



Cite this: *Energy Environ. Sci.*, 2016, 9, 3392

Received 8th March 2016,
Accepted 9th June 2016

DOI: 10.1039/c6ee00712k

www.rsc.org/ees

Tin/vanadium redox electrolyte for battery-like energy storage capacity combined with supercapacitor-like power handling†

Juhan Lee,^{ab} Benjamin Krüner,^{ab} Aura Tolosa,^{ab} Sethuraman Sathyamoorthi,^{ac} Daekyu Kim,^{ad} Soumyadip Choudhury,^a Kum-Hee Seo^d and Volker Presser^{*ab}

We introduce a high performance hybrid electrochemical energy storage system based on an aqueous electrolyte containing tin sulfate (SnSO₄) and vanadyl sulfate (VOSO₄) with nanoporous activated carbon. The energy storage mechanism of this system benefits from the unique synergy of concurrent electric double-layer formation, reversible tin redox reactions, and three-step redox reactions of vanadium. The hybrid system showed excellent electrochemical properties such as a promising energy capacity (ca. 75 W h kg⁻¹, 30 W h L⁻¹) and a maximum power of up to 1.5 kW kg⁻¹ (600 W L⁻¹, 250 W m⁻²), exhibiting capacitor-like galvanostatic cycling stability and a low level of self-discharging rate.

Electrochemical energy storage (EES) systems such as batteries and supercapacitors are key enabling technologies for a sustainable and efficient use of energy.^{1–3} With a growth in the demand for a reliable supply for renewable energy sources, EES systems have drawn more and more attention since the grid scale application of EES systems could resolve the intermittent power generation features of the renewable energy sources.⁴ In general, common batteries can provide high energy storage capacity (30–300 W h kg⁻¹) while suffering from low power performance (<1 kW kg⁻¹) and limited cycle lifetime (<5000 cycles). Supercapacitors are characterized by a high power performance (5–10 kW kg⁻¹) and extremely high stability (>100 000 cycles), but exhibit low energy storage capacity (<8 W h kg⁻¹).⁵ These differences originate from different charge storage mechanisms.⁶ In principle, the charge storage mechanisms for EES devices can be classified into four categories (Fig. 1A): (1) electrical double-layer formation at the electrode/electrolyte

Broader context

Redox electrolytes have received particular attention in supercapacitor research studies in the last decade as they could replace the conventional ‘electrochemically inert’ electrolyte, still contribute to the double layer formation, and significantly enhance the intrinsically low energy density of the supercapacitors. *Via* the redox reactions in a liquid state, there is no intrinsic stress/strain degradation as known from intercalation-type battery materials. So far, redox electrolyte systems have been investigated mostly using redox couples which do not have solid phase transition throughout the reactions since the solid phase transition is believed to bring negative effects such as low power performance and short cyclic lifetime. In this communication, we report that the redox activities of tin sulfate can be effectively coupled with the redox activities of vanadyl sulfate. Even with the partial solid phase transition of the tin redox ions, the tin/vanadium hybrid system can show capacitor-like high power performance and cycling stability when such complex redox phase transitions occur in the well-confined nanopores of the carbon based electrode material. Such advanced hybrid energy storage systems are envisioned to play an important role to exceed the current performance range of both supercapacitors and batteries.

interface (electrical double-layer capacitors), (2) redox intercalation through a layered structure *via* bulk reaction of the electrode (typical batteries), (3) solid phase redox reaction at the near surface of the electrode but not through the bulk material which can be pseudocapacitive,⁷ and (4) electrochemical reactions of soluble redox couples (redox electrolytes).⁸ Electric double-layer formation is accomplished by fast ion electrosorption and this purely physical charge separation process at the electrode/electrolyte interface enables rapid charge storage and recovery.⁹ Redox intercalation provides much higher charge storage capacity through the intercalation of ions (such as lithium, sodium, or potassium) into the layered structure of the electrode *via* a charge transfer process.^{10–12} The intercalation process, however, is severely limited by the diffusion kinetics of the ions and may degrade the layered structure of the electrode with increasing cycle numbers, particularly at a high rate.¹³ Nanoscale design and optimization of the electrode materials,¹⁴ or the use of novel nanotextured materials, like MXene,¹⁵ may provide unique

^a INM – Leibniz Institute for New Materials, Campus D2 2, 66123 Saarbrücken, Germany. E-mail: volker.presser@leibniz-inm.de

^b Department of Materials Science and Engineering, Saarland University, Campus D2 2, 66123 Saarbrücken, Germany

^c Electrochemical Process Engineering Division, CSIR-Central Electrochemical Research Institute, Karaikudi, 630 006, India

^d School of Energy, Materials and Chemical Engineering, Korea University of Technology and Education, Chungjeol-ro 1600, 31253 Cheonan, Republic of Korea

† Electronic supplementary information (ESI) available. See DOI: 10.1039/c6ee00712k



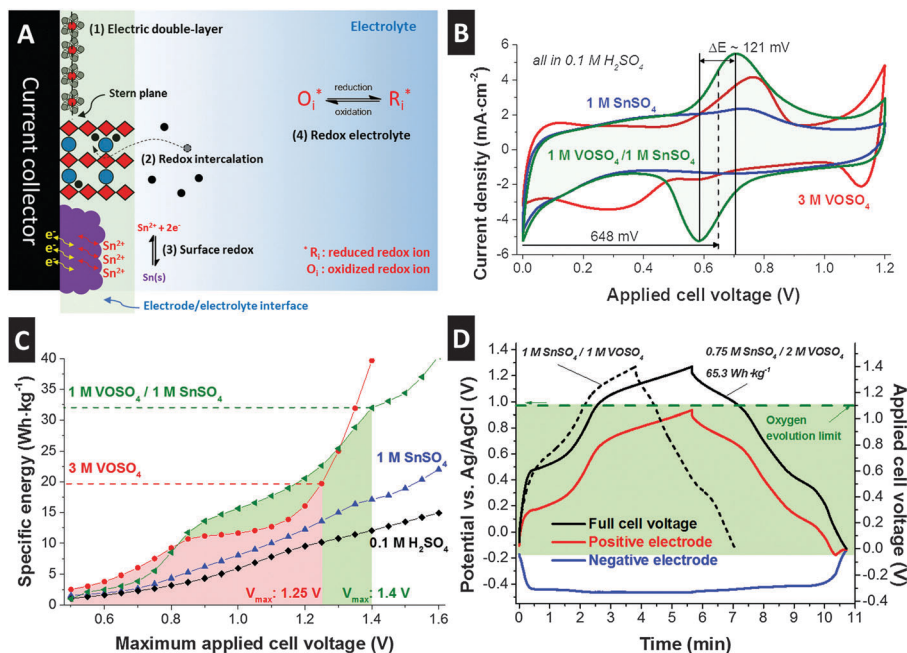


Fig. 1 Schematic illustration of various electrochemical energy storage mechanisms (A). Electrochemical analysis with a full-cell configuration without a reference electrode (B and C) and with the Ag/AgCl reference electrode (D). (B) Cyclic voltammograms were obtained for various redox electrolytes at 1 mV s^{-1} . (C) Specific energies were calculated from the cyclic voltammograms at 1 mV s^{-1} via voltage range extension with the interval of 50 mV . The colored area indicates the maximum stability windows of each system, which are determined by a thorough investigation of the irreversible portion of the reaction or known as S-value analysis. The highest specific energy was obtained for the $1 \text{ M VOSO}_4 / 1 \text{ M SnSO}_4$ system in a stable cell potential window. (D) A full-cell is charged up to 1.4 V while observing the potential of the negative electrode through an Ag/AgCl reference electrode. The $0.75 \text{ M SnSO}_4 / 2 \text{ M VOSO}_4$ system shows the best optimized performance in terms of specific energy.

possibilities to improve on this limitation, but alternative concepts are still in high demand. In particular, the non-ideal reversibility of chemical and/or structural changes in redox-active electrode materials complicates the achievement of longevity and stable performance.¹⁶

While the use of redox-active electrode materials has attracted tremendous research interest, the field of redox-active electrolytes remains largely uncharted at present.^{17,18} Unlike the other mentioned charge storage mechanisms, energy storage *via* redox electrolytes is not exclusively confined to the electrode/electrolyte interface and encompasses the entire fluid volume. For instance, vanadyl sulfate (VOSO_4) will not only provide charge storage *via* double-layer formation at the electrode/electrolyte interface, but additional charge transfer is accomplished through a series of vanadium redox states.^{19,20} This dual (hybrid) energy storage mechanism brings along the need for the implementation of ion exchange membranes to avoid ion shuttling and rapid self-discharge.²¹ When no solid phase transition occurs and there are no electrolyte cross-contamination issues,²² a redox electrolyte based energy storage system can offer a cycling lifetime of over 10 000 cycles.^{23,24}

To maximize the volumetric and gravimetric energy storage capacity, an intriguing approach has been used to employ a synergistic combination of ultrafast ion electrosorption, fast redox-electrolyte charge transfer, and high-energy interfacial redox reactions. For that purpose, we introduce in this work, for the first time, the effective and stable coupling of tin and

vanadium redox activities. Our work employs conventional nanoporous carbon to illustrate the facile implementation of the approach to already existing electrode technologies. A large energy capacity is expected based on the large standard potential difference between $\text{V}^{3+}/\text{V}^{2+}$ and $\text{VO}^{2+}/\text{VO}_2^+$ reactions (ESI†, Fig. S1) in combination with the reversible Sn^{2+}/Sn phase transition inside carbon nanopores. The latter provides a large charge storage capacity involving the transfer of two electrons and the possibility of further oxidation to $\text{Sn}[\text{IV}]$.²⁵

We prepared free-standing carbon film electrodes made from YP80F activated carbon (Kuraray Chemicals) with a specific surface area of $1756 \text{ m}^2 \text{ g}^{-1}$ and an average pore size of 1.6 nm as characterized by nitrogen gas adsorption analysis (ESI†).²⁶ The final hot-rolled films were produced with $200 \pm 6 \mu\text{m}$ thickness containing 5 mass% polytetrafluoroethylene (PTFE) as the binder (see ref. 27). For the redox electrolyte, vanadyl sulfate (VOSO_4) with 97% purity, tin sulfate (SnSO_4) with 95% purity, sodium sulfate (Na_2SO_4) with 99% purity, and H_2SO_4 with 99.99% purity were purchased from Sigma Aldrich and mixed with deionized water. For the stability of the electrolyte and enhanced redox activity, all redox electrolytes were prepared by addition of $0.1 \text{ M H}_2\text{SO}_4$. We used a type FAS15 anion exchange membrane (FuMa-Tech) to effectively prevent redox shuttling of vanadium and vanadium oxide ions between the two electrodes. As the reference electrode, we applied an Ag/AgCl electrode (Bioanalytical Systems, saturated, 3 M NaCl). For more information on electrochemical testing using a VMP300 potentiostat/galvanostat (Bio-Logic),



see the ESI† (esp. Fig. S2). For post-mortem analysis, electrode samples were collected after charging the working electrode to -0.2 V and -0.57 V vs. Ag/AgCl in chronoamperometry mode for 30 min. After cell disassembly, the samples were soaked in 0.1 M H₂SO₄ aqueous solution for a day, then subsequently soaked in deionized water for a day, and dried at room temperature in a desiccator in order to remove the dissolved ions. The possible contribution of the graphite current collector to the energy storage capacity (e.g., via intercalation^{28,29}) was excluded by comparative experiments with platinum current collectors (Fig. S4D, ESI†).

As seen from the cyclic voltammogram for a full cell presented in Fig. 1B, the aqueous VOSO₄/SnSO₄ redox electrolyte system with added 0.1 M H₂SO₄ is ideally suited to maximize the energy storage capacity over the entire range of accessible cell voltage (exemplified for up to 1.2 V). A large area under the discharging curve is indicative of a high-energy storage (recovery) capacity which can be quantified by integrating the discharging current. We obtained 42 mA h g⁻¹ (16.8 mA h mL⁻¹) for a mixture of 1 M VOSO₄/1 M SnSO₄, 38 mA h g⁻¹ (15.2 mA h mL⁻¹) for 3 M VOSO₄, and 29 mA h g⁻¹ (11.6 mA h mL⁻¹) for 1 M SnSO₄ at a slow rate of 1 mV s⁻¹. For a comparison, only 9.1 mA h g⁻¹ (3.6 mA h mL⁻¹) was achieved when using the same carbon material in 1 M Na₂SO₄ or 17 mA h g⁻¹ (6.8 mA h mL⁻¹) for 1 H₂SO₄ in the same voltage range. A clearly visible and broad redox peak pair at around 648 mV with small ΔE for 1 M VOSO₄/1 M SnSO₄ is additionally beneficial to achieve a high specific energy. The maximum specific energy (W h kg⁻¹) of a hybrid energy storage system greatly depends on the charge/voltage profile (voltage plateau) and the voltage stability window. Accordingly, a thorough assessment of the voltage stability window needs to predate further performance evaluation. Quantitative data analysis of cyclic voltammograms *via* *S*-value testing (Fig. S4A, ESI†) is a powerful tool providing (i) the onset potential window of the chemical decomposition potential by thorough investigation of the irreversible portion of the charge,^{30,31} (ii) specific energies at the applied voltage window, and (iii) cyclic voltammograms containing information about the redox reactions. The comprehensive data from the *S*-value testing can directly be converted to a plot of specific energy vs. maximum applied cell voltage, as can be seen from Fig. 1C. The limit for the stable cell voltage (marked green and red) is determined by an *S*-value of 0.1, which corresponds to a maximum deviation between the transferred charge during charging and the recovered charge during discharging of max. 10%. For the 1 M VOSO₄/1 M SnSO₄ system, we see that a stable cell performance is maintained (by definition of $S < 0.1$ and its second derivative < 0.05) up to 1.4 V applied cell voltage (Fig. S4A, ESI†). These values for the cell voltage in acidic media are much higher than the theoretical thermodynamic limit of 1.23 V. Voltage floating confirmed good electrochemical performance stability for pure 0.1 M H₂SO₄ aqueous solution at 1.3 V and 1.4 V cell voltage (Fig. S4E, ESI†). This behavior may be associated with the cathodic limit extension *via* hydrogen adsorption and/or overpotential influence depending on the type and pore structure of the carbon.^{32–36}

A high amount of Faradaic charge transfer associated with redox reactions contributes to an enhanced specific energy and occurs at a fixed cell voltage. For instance, 3 M VOSO₄ exhibits two increases in specific energy at 0.5–0.8 V and > 1.1 V (Fig. 1C), which correspond to the two large redox peaks observed in the cyclic voltammogram (Fig. 1B). As a result, a maximum specific energy rating of 19.8 W h kg⁻¹ can be reached. For 3 M VOSO₄, however, no further increase in specific energy is possible because of the voltage stability window being limited to ~ 1.25 V, most probably due to water splitting. An even higher specific energy of 32 W h kg⁻¹ was achieved by the 1 M VOSO₄/1 M SnSO₄ system, having a much larger voltage stability window of up to 1.4 V. This clearly implies a synergetic influence of the VOSO₄/SnSO₄ combination in terms of high specific energy. The individual application of VOSO₄ and SnSO₄ could not provide such high specific energy (Fig. 1C) due to their solubility limits (SnSO₄: 1.6 M in water at 20 °C in absence of vanadyl sulfate, VOSO₄: 3.3 M in water at 20 °C).^{37,38} Initially, we see an *S*-value (Fig. S4A, ESI†) above 0.1 from 0.5 V to 0.8 V. However, this value drops below 0.1 as the tin sulfate system becomes conditioned. This indicates that *S*-value analysis is to be carefully employed when adapting to redox systems.

The data so far relate to two-electrode cells. To gain a more detailed insight into the electrochemistry of the VOSO₄/SnSO₄ system, a three-electrode configuration was applied with an Ag/AgCl reference electrode (Fig. S2B, ESI†) to study the voltage development at each individual electrode. This particular configuration allows us to not only operate the cell voltage in a full-cell-like manner, but also access the potential information of the positive and negative electrode at the same time. Fig. S4B (ESI†) shows the potential profile of the positive and negative electrode while the voltage applied between the negative and positive electrodes was ranged from 0 V to 1.4 V. In the case of the 1 M VOSO₄/1 M SnSO₄ system, the potential at the positive electrode increases much faster than the potential at the negative electrode due to the strong redox activities at the negative potential at around -0.45 V vs. Ag/AgCl.

Since the asymmetric potential development of the negative and positive electrode implies an inefficient utilization of the total charge storage capacity of a system, charge balancing is required.³⁹ The performance can be severely improved by balancing the charge storage capacity of both electrodes while keeping the potential of each electrode below their respective stability limits. One unique advantage of the redox electrolyte system is the highly facile charge balancing through concentration adjustment. In this way, charge balancing is much simpler as compared to the mass balancing commonly employed for super-capacitor devices, which brings complexity through imbalance in the geometrical shape of the electrodes.⁴⁰ In order to maximize the specific energy of the system, the voltage imbalance of the negative and positive electrode can be adjusted by enhancing the charge storage capacity at the positive electrode. The 1 M VOSO₄/1 M SnSO₄ system already represented its maximum possible electrolytic concentration due to the low solubility of SnSO₄ (ca. 1.6 M) as compared to that of VOSO₄ (ca. 3.3 M). Further optimization of the electrochemical performance can be obtained



by carefully increasing the VOSO_4 -to- SnSO_4 ratio in order to balance the strong redox activity at the negative electrode *via* the enhancement of vanadium redox activities at the positive electrode. An array of different molar ratios is presented in the ESI,† Fig. S4C. The best performance was obtained for 0.75 M SnSO_4 /2 M VOSO_4 in terms of high energy density as the potential increase at the positive electrode was suppressed by the redox activity of VOSO_4 at around +0.75 V and +0.14 V *vs.* Ag/AgCl and remained below the oxygen evolution potential (Fig. 1D). The specific energy of this system was 65.3 Wh kg^{-1} as calculated from the discharging potential profile shown in Fig. 1D, as compared to 37 Wh kg^{-1} for the 1 M SnSO_4 /1 M VOSO_4 cell.

For a comprehensive understanding of the redox activities of the negative and positive electrode, we employed a three-electrode configuration with an oversized counter electrode (oversized by *ca.* 35 times compared to the working electrode; Fig. S2B, ESI†). In the case of the 0.75 M SnSO_4 /2 M VOSO_4 system, the $\text{VO}_2^+/\text{VO}^{2+}$ redox reaction was investigated at the working electrode while keeping the potential of the counter electrode outside the range of the other redox activities (Fig. S3, ESI†). As a first step, 1 M SnSO_4 and 1 M VOSO_4 redox electrolytes were individually studied at the potential range from around -0.6 V to +0.8 V (Fig. 2A). The vanadium system shows three distinguishable redox peaks, which can be identified as $\text{V}^{3+}/\text{V}^{2+}$, $\text{VO}^{2+}/\text{V}^{3+}$, and $\text{VO}_2^+/\text{VO}^{2+}$ at around -0.5 V, +0.1 V, and +0.75 V *vs.* Ag/AgCl.⁴

In the case of the tin system, a very sharp and large peak appears at around -0.47 V, which aligns with the reduction of Sn^{2+} to metallic tin (tin electroplating). As the scanning

direction changes to the anodic scan, the metallic tin is expected to be oxidized to Sn^{2+} . A slightly broader anodic peak (-0.43 V) might indicate a series of tin oxidation reactions towards $\text{Sn}[\text{IV}]$ (Fig. S1, ESI†). As a next step, two cells were prepared with 0.75 M SnSO_4 /0.2 M VOSO_4 in order to study the electrochemical behavior of the positive and negative electrodes (Fig. 2B). Reversible reactions of the $\text{VO}_2^+/\text{VO}^{2+}$ and $\text{VO}_2^+/\text{VO}^{2+}$ couples can be seen at the positive electrode. During the reduction of the negative electrode, a steep increase in cathodic current was observed at -0.43 V, which aligns with the reduction of Sn^{2+} to tin metal. The results of the post-mortem nitrogen gas adsorption test (Table S2, ESI†) are in excellent agreement with the results of the formation of metallic tin, possibly in the carbon nanopores with pore sizes below 3 nm (Fig. S5, ESI†). The formation of the metal is believed to block the carbon nanopores as supported by the lower specific surface area (minus 41%) and the total pore volume (minus 48%) of the reduced negative electrode as compared to the pristine electrode. A high cathodic peak at -0.5 V (Fig. 2B) indicates the contribution of the V^{3+} to V^{2+} reaction. During reverse polarization (Fig. 2B), a broad anodic peak arises at around -0.41 V, which aligns with the oxidation of V^{2+} to V^{3+} and tin metal to Sn^{2+} . The dissolution of the tin metal to Sn^{2+} is also evidenced by the higher specific surface area and the total pore volume of the oxidized negative electrode (Table S2, ESI†) from the post-mortem nitrogen gas adsorption analysis (Fig. S5, ESI†). During further oxidation from -0.36 V to -0.27 V, we still see a high anodic current, perhaps implying further oxidation of tin to $\text{Sn}[\text{IV}]$,

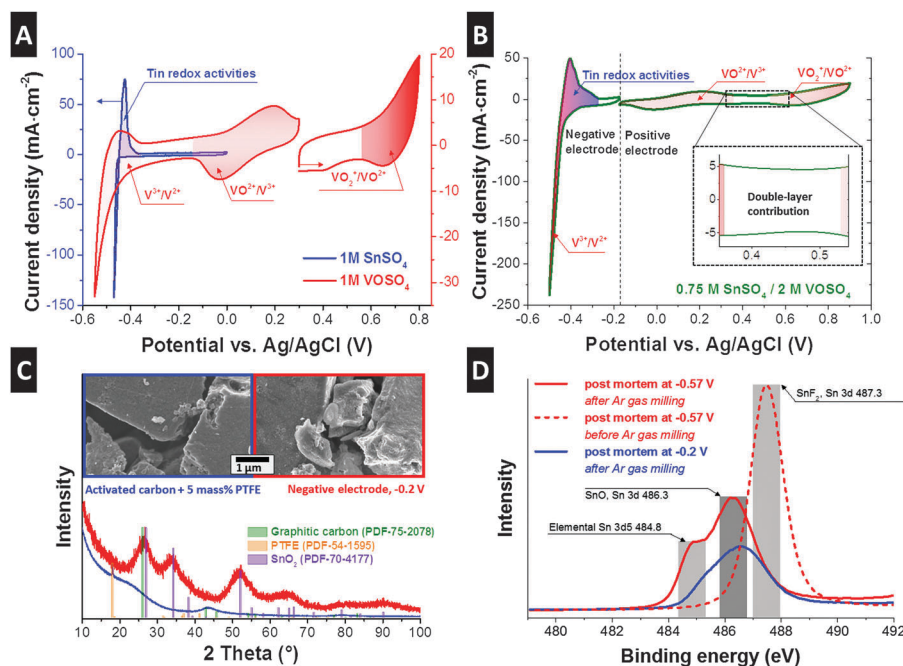


Fig. 2 Cyclic voltammograms of various redox electrolyte systems with three-electrode configuration with an overbalanced counter electrode (A and B). (A) Cyclic voltammograms from individual 1 M SnSO_4 system and 1 M VOSO_4 system. (B) Cyclic voltammograms from the best optimized redox electrolytes containing 0.75 M SnSO_4 and 2 M VOSO_4 . The inset shows a close-up on the part of the current response indicating double-layer formation. (C) SEM images and XRD data are obtained from the negative electrode. XRD peak positions indicate the formation of SnO_2 with the domain size of around 2 nm. (D) XPS results, providing evidence for the formation of tin oxides, metallic tin, and superficial SnF_2 at the negative electrode.



which aligns with the lower specific surface area and total pore volume from the post-mortem analysis of the oxidized negative electrode. We see a capacitive behavior of the electrode in the range where no specific redox reactions are expected (Fig. 2B, inset) as characterized by a rectangular shape in the cyclic voltammogram. This capacitive contribution aligns with the formation of the electric double-layer by vanadium (V^{3+} , V^{2+}), vanadium oxides (VO^{2+} , VO_2^+), and tin cations (Sn^{2+}) as well as sulfates (SO_4^{2-}), or by the pseudocapacitive mechanism of the redox species; the capacitive contribution can be also seen in the cyclic voltammogram obtained from a full-cell configuration (Fig. S4D, ESI[†]).

To confirm the oxidation states of the tin system, we carried out post-mortem characterization of the negative electrode. For that, the electrodes were charged to -0.2 V and -0.57 V vs. Ag/AgCl, washed with 0.1 M H_2SO_4 aqueous solution and deionized water, and dried in vacuum. The electron micrographs (Fig. 2C) show that the surface of the carbon particles became roughened after the electrode was exposed to -0.2 V vs. Ag/AgCl as compared to the pristine electrode (activated carbon with 5 mass% PTFE). The Raman spectra support the fact that no change in the carbon structure occurred, maintaining the same ID/IG ratio (1.08 ± 0.05) before and after electrochemical testing (Fig. S6A, ESI[†]). The XRD pattern of the pristine electrode shows the presence of amorphous carbon and PTFE binder (Fig. 2C). The negative electrode exhibits amorphous SnO_2 peaks, meaning that the metallic tin could have been further oxidized to Sn^{IV} through electrochemical operation. The formation of tin oxides is also supported by the increase in oxygen and tin content measured from EDX (ESI[†]). The calculated domain size (coherence length; measured *via* XRD) of SnO_2 is approximately 2 nm, which is in the range of pore sizes of the activated carbon and supports the assumption that the Sn^{IV} transition took place within the pores. Post-mortem nitrogen gas sorption analyses (Fig. S5, ESI[†]) support the formation of tin metal in nanopores with the possible size of below 3 nm. In order to confirm the oxidation state of tin present in the electrodes, XPS analysis was carried out (Fig. 2D). The samples were measured before and after ion milling with argon gas with the depth of approximately 1–2 μ m to

differentiate the signal information coming from the outer activated carbon particle surface and from inside. Samples before ion milling showed the peak with the binding energy of around 487.3 eV, which can be identified as the Sn 3d signal of tin fluoride (SnF_2). The existence of SnF_2 can also be supported by the F 1s electron binding energy (Fig. S6B, ESI[†]). After ion milling with argon gas (Fig. 2D), two distinctive peaks arise at around 484.8 eV and 486.3 eV, which are considered to stem from the electron binding energy of SnO or SnO_2 (Sn 3d) and tin metal (Sn 3d5). Therefore, SnF_2 formation as a result of the reaction between tin and fluoride from the PTFE-binder is possibly limited to the outer surface of the activated carbon. Inside the large volume of carbon nanopores, however, exclusively tin oxides and metallic tin are formed. We assume that the PTFE was partially decomposed to fluorine and carbon.

As investigated so far, the $SnSO_4/VOSO_4$ electrolyte system provides battery-like specific energy (>60 W h kg^{-1}) through a complex charge storage mechanism of tin and vanadium redox activities and electric double-layer formation. For broader applications of this promising energy storage system, a high power performance is required. For the characterization of rate handling, galvanostatic charge/discharge was applied to the 0.75 M $SnSO_4/2$ M $VOSO_4$ cells with a full-cell configuration (Fig. S2A, ESI[†]) up to 1.4 V (Fig. 3A). For comparison, we added the data for the performance of a double-layer capacitor in 1 M Na_2SO_4 aqueous solution with the same type of activated carbon electrode. At a low specific current of around 55 mA g^{-1} , the 0.75 M $SnSO_4/2$ M $VOSO_4$ system exhibited a battery-like energy specific energy of up to 75 W h kg^{-1} , which can be converted to *ca.* 30 W h L^{-1} when normalized to the volume of the two electrodes, the membrane, and the electrolyte. At a low specific current, the double-layer capacitor employing 1 M Na_2SO_4 only provides a maximum of 5 W h kg^{-1} (2 W h L^{-1}). At a specific current of 4 A g^{-1} , the 0.75 M $SnSO_4/2$ M $VOSO_4$ system shows much higher specific energy (8.2 W h kg^{-1}) than the 1 M Na_2SO_4 supercapacitor (3.1 W h kg^{-1}). The poor energy rating at higher specific currents (>6 A g^{-1}) is possibly due to the solid phase transition of Sn^{2+} ions to solid tin as also supported by the increase in ohmic resistance (see the ESI[†] for the calculation) at the specific current regime over 1 A g^{-1} , which indicates the

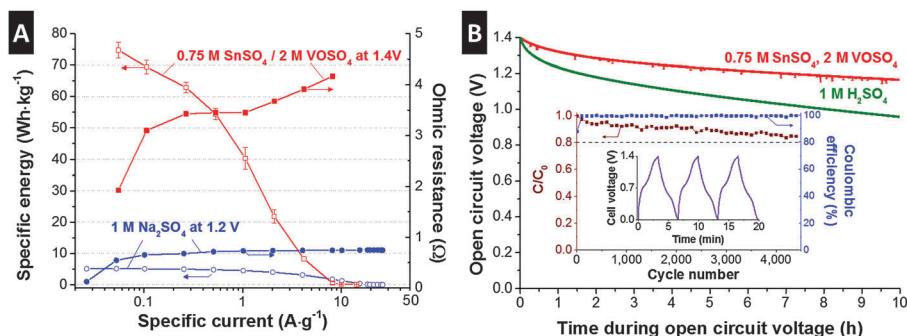


Fig. 3 (A) The rate performance of the $SnSO_4/VOSO_4$ system is plotted, as well as the ohmic resistance of the cell measured at each applied specific current in comparison to the 1 M Na_2SO_4 system. (B) Open circuit voltage for 10 h after charging the cells up to 1.4 V. The $SnSO_4/VOSO_4$ system shows also a stable cyclic performance over 4000 cycles with a Coulombic efficiency close to 100%. The inset shows a profile of the galvanostatic charge/discharge for several cycles.



overpotential due to mass transfer. When the specific current is converted to specific power (Fig. S7, ESI[†]), the 0.75 M SnSO₄/2 M VOSO₄ system provides a maximum performance of up to ca. 1.5 kW kg⁻¹, which can be converted to ca. 600 W L⁻¹ or 250 W m⁻² when normalized to the volume of the two electrodes, the membrane, and the electrolyte, or to the membrane area, respectively.

An important but often not discussed property of energy storage systems is the self-discharge, or more specifically, the time-dependent loss of the open circuit voltage after charging up to a specific cell voltage. As reported in several studies,^{21,41,42} redox electrolyte based systems are expected to suffer from a large self-discharging rate due to redox shuttling when ions are not selectively separated, for instance, by application of an ion exchange membrane. To prevent the ion shuttling of the vanadium ions, we employed a type FAS15 ion exchange membrane and achieved a very stable behavior (Fig. 3B). After 10 h of OCV measurement, the initial voltage dropped to about 17%, which is only half the self-discharge of an aqueous supercapacitor operated in 1 M H₂SO₄. Interestingly, the redox electrolyte system yields a self-discharge superior to supercapacitors, possibly due to less effect of ion-redistribution on the potential loss as the system has a hybrid charge storage principle.^{43–45}

The high performance stability (Fig. 3B, inset) is particularly remarkable when we consider that battery-like electrochemical energy storage systems commonly feature poor cycling stability. However, our redox electrolyte system presents very stable performance and after 4500 cycles (ca. 400 h of continuous testing), the specific capacity of the 0.75 M SnSO₄/2 M VOSO₄ cell degraded only by ca. 15% compared to the initial capacity of the system. The comparably high cycling stability is complemented by a high Coulombic efficiency of almost 100%, which is in excellent agreement with the electrochemical stability determined by the *S*-value analysis (Fig. S4C, ESI[†]).

In summary, we demonstrated a new type of hybrid energy storage system by applying an aqueous redox electrolyte with SnSO₄ and VOSO₄ into a nanoporous carbon based electrode. Through a simple charge balancing by adjusting the relative molar concentration of SnSO₄ and VOSO₄, the best optimized cell exhibited a broad voltage stability window of up to 1.4 V in a full-cell configuration, a promising specific energy of 75.4 ± 2.3 W h kg⁻¹, a maximum specific power of ca. 1.5 kW kg⁻¹ as well as a high cycling stability over 4500 cycles, and a low level of self-discharging rate. The origin of the high specific energy is the three-step redox activities of vanadium by changing the oxidation state from 2+ to 5+ and the large redox activities of tin at the negative electrode. From the XPS analysis, these tin redox activities are believed to be due to the formation of the metallic tin in the carbon micropores, further oxidation of metallic tin to Sn[IV], or a further reduction of metallic tin to tin fluoride on the outside of the carbon particles, where PTFE is accessible. As the solid phase transition through the redox activities of tin can narrow or block carbon micropores, studies regarding the detailed solid phase formation mechanism in the micropores are necessary which will allow the estimation of the best pore structure of the electrode material, thus, further improvement of the power performance is expected.

Acknowledgements

We acknowledge the funding from the German Federal Ministry for Research and Education (BMBF) in support of the nanoEES3D project (award number 03EK3013) as part of the strategic funding initiative energy storage framework. The authors thank Prof. Eduard Arzt (INM) for his continuing support, FuMA-Tech (esp. Dr Bauer and Dr Klicpera) for kindly providing membranes and helpful discussions, Dr Ingrid Grobelsek for the EDX and SEM measurements, Dr Mesut Aslan, Srimuk Pattarachai, Nicolas Jäckel, Simon Fleischmann, Friedrich Kaasik, and Anna Schreiber (all at INM) for useful discussions and technical support.

References

- 1 P. Simon and Y. Gogotsi, *Nat. Mater.*, 2008, 7, 845–854.
- 2 F. Béguin, V. Presser, A. Balducci and E. Frackowiak, *Adv. Mater.*, 2014, 26, 2219–2251.
- 3 M. Barghamadi, A. S. Best, A. I. Bhatt, A. F. Hollenkamp, M. Musameh, R. J. Rees and T. Ruther, *Energy Environ. Sci.*, 2014, 7, 3902–3920.
- 4 Z. Yang, J. Zhang, M. C. Kintner-Meyer, X. Lu, D. Choi, J. P. Lemmon and J. Liu, *Chem. Rev.*, 2011, 111, 3577–3613.
- 5 J. R. Miller and A. F. Burke, *Electrochem. Soc. Interface*, 2008, 17, 53.
- 6 P. Simon, Y. Gogotsi and B. Dunn, *Science*, 2014, 343, 1210–1211.
- 7 V. Augustyn, P. Simon and B. Dunn, *Energy Environ. Sci.*, 2014, 7, 1597–1614.
- 8 P. Bandaru, H. Yamada, R. Narayanan and M. Hofer, *Mater. Sci. Eng., R*, 2015, 96, 1–69.
- 9 D. Pech, M. Brunet, H. Durou, P. Huang, V. Mochalin, Y. Gogotsi, P.-L. Taberna and P. Simon, *Nat. Nanotechnol.*, 2010, 5, 651–654.
- 10 V. Etacheri, R. Marom, R. Elazari, G. Salitra and D. Aurbach, *Energy Environ. Sci.*, 2011, 4, 3243–3262.
- 11 W. Luo, J. Wan, B. Ozdemir, W. Bao, Y. Chen, J. Dai, H. Lin, Y. Xu, F. Gu, V. Barone and L. Hu, *Nano Lett.*, 2015, 15, 7671–7677.
- 12 M. Shirpour, J. Cabana and M. Doeff, *Energy Environ. Sci.*, 2013, 6, 2538–2547.
- 13 A. Mukhopadhyay and B. W. Sheldon, *Prog. Mater. Sci.*, 2014, 63, 58–116.
- 14 V. Augustyn, J. Come, M. A. Lowe, J. W. Kim, P.-L. Taberna, S. H. Tolbert, H. D. Abruña, P. Simon and B. Dunn, *Nat. Mater.*, 2013, 12, 518–522.
- 15 M. D. Levi, M. R. Lukatskaya, S. Sigalov, M. Beidaghi, N. Shpigel, L. Daikhin, D. Aurbach, M. W. Barsoum and Y. Gogotsi, *Adv. Energy Mater.*, 2015, 5, 1400815.
- 16 S. T. Senthilkumar, R. K. Selvan and J. S. Melo, *J. Mater. Chem. A*, 2013, 1, 12386–12394.
- 17 B. Akinwolemiwa, C. Peng and G. Z. Chen, *J. Electrochem. Soc.*, 2015, 162, A5054–A5059.
- 18 L. Guan, L. Yu and G. Z. Chen, *Electrochim. Acta*, 2016, 206, 464–478.
- 19 E. Frackowiak, K. Fic, M. Meller and G. Lota, *ChemSusChem*, 2012, 5, 1181–1185.



- 20 S. Senthilkumar, R. K. Selvan, N. Ponpandian, J. Melo and Y. Lee, *J. Mater. Chem. A*, 2013, **1**, 7913–7919.
- 21 L. Chen, H. Bai, Z. Huang and L. Li, *Energy Environ. Sci.*, 2014, **7**, 1750–1759.
- 22 D. Reed, E. Thomsen, W. Wang, Z. Nie, B. Li, X. Wei, B. Koeppl and V. Sprenkle, *J. Power Sources*, 2015, **285**, 425–430.
- 23 K. Fic, M. Meller and E. Frackowiak, *J. Electrochem. Soc.*, 2015, **162**, A5140–A5147.
- 24 B. Krüner, J. Lee, N. Jäckel, A. Tolosa and V. Presser, *ACS Appl. Mater. Interfaces*, 2016, **8**, 9104–9115.
- 25 R. Narayanan and P. R. Bandaru, *J. Electrochem. Soc.*, 2014, **162**, A86–A91.
- 26 G. Y. Gor, M. Thommes, K. A. Cychosz and A. V. Neimark, *Carbon*, 2012, **50**, 1583–1590.
- 27 N. Jäckel, D. Weingarh, M. Zeiger, M. Aslan, I. Grobelsek and V. Presser, *J. Power Sources*, 2014, **272**, 1122–1133.
- 28 N. E. Sorokina, M. A. Khaskov, V. V. Avdeev and I. V. Nikol'skaya, *Russ. J. Gen. Chem.*, 2005, **75**, 162–168.
- 29 M. D. Levi, E. Levi, Y. Gofer, D. Aurbach, E. Vieil and J. Serose, *J. Phys. Chem. B*, 1999, **103**, 1499–1508.
- 30 D. Weingarh, H. Noh, A. Foelske-Schmitz, A. Wokaun and R. Kötz, *Electrochim. Acta*, 2013, **103**, 119–124.
- 31 J. Lee, D. Weingarh, I. Grobelsek and V. Presser, *Energy Technol.*, 2016, **4**, 75–84.
- 32 C. Vix-Guterl, E. Frackowiak, K. Jurewicz, M. Friebe, J. Parmentier and F. Béguin, *Carbon*, 2005, **43**, 1293–1302.
- 33 E. Frackowiak and F. Béguin, *Carbon*, 2002, **40**, 1775–1787.
- 34 Q. Gao, L. Demarconnay, E. Raymundo-Pinero and F. Béguin, *Energy Environ. Sci.*, 2012, **5**, 9611–9617.
- 35 K. Fic, M. Meller, J. Menzel and E. Frackowiak, *Electrochim. Acta*, 2016, **206**, 496–503.
- 36 K. Fic, G. Lota, M. Meller and E. Frackowiak, *Energy Environ. Sci.*, 2012, **5**, 5842–5850.
- 37 F. Rahman and M. Skyllas-Kazacos, *J. Power Sources*, 1998, **72**, 105–110.
- 38 J. Donaldson and W. Moser, *J. Chem. Soc.*, 1960, 4000–4003.
- 39 M. Lazzari, F. Soavi and M. Mastragostino, *J. Power Sources*, 2008, **178**, 490–496.
- 40 A. Brandt, P. Isken, A. Lex-Balducci and A. Balducci, *J. Power Sources*, 2012, **204**, 213–219.
- 41 M. Tachibana, Y. Tsukada, T. Ohishi, H. Yamagishi and M. Murakami, *Kobunshi Ronbunshu*, 2009, **66**, 259–265.
- 42 M. Tachibana, T. Ohishi, Y. Tsukada, A. Kitajima, H. Yamagishi and M. Murakami, *Electrochemistry*, 2011, **79**, 882–886.
- 43 J. Kowal, E. Avaroglu, F. Chamekh, A. Šenfělds, T. Thien, D. Wijaya and D. U. Sauer, *J. Power Sources*, 2011, **196**, 573–579.
- 44 M. Kaus, J. Kowal and D. U. Sauer, *Electrochim. Acta*, 2010, **55**, 7516–7523.
- 45 H. A. Andreas, *J. Electrochem. Soc.*, 2015, **162**, A5047–A5053.



Supporting Information

TIN/VANADIUM REDOX ELECTROLYTE COMBINING BATTERY-LIKE ENERGY STORAGE CAPACITY WITH SUPERCAPACITOR-LIKE POWER HANDLING

Juhan Lee,^{a,b} Benjamin Krüner,^{a,b} Aura Tolosa,^{a,b} Sethuraman Sathyamoorthi,^{a,c} Daekyu Kim,^{a,d}
Soumyadip Choudhury,^a Kum-Hee Seo,^d and Volker Presser^{a,b,*}

^a INM – Leibniz Institute for New Materials, Campus D2 2, 66123 Saarbrücken, Germany

^b Department of Materials Science and Engineering, Saarland University, Campus D2 2, 66123 Saarbrücken, Germany

^c Electrochemical Process Engineering Division, CSIR-Central Electrochemical Research Institute, Karaikudi, 630 006, India

^d School of Energy, Materials and Chemical Engineering, Korea University of Technology and Education, Chungjeol-ro 1600, 31253 Cheonan, Republic of Korea

* Corresponding author's eMail: volker.presser@leibniz-inm.de

Standard redox potential of various elements

Standard redox potential of various redox couples are shown in **Figure S1**: the potential values are taken from Ref [1]. The oxygen evolution potential described in **Figure 1D** is determined according to the pH value of the 0.75 M SnSO₄ / 2 M VOSO₄ aqueous solution (pH = 0.63) obtained by SG2-SevenGo pH-Meter (Mettler Toledo).

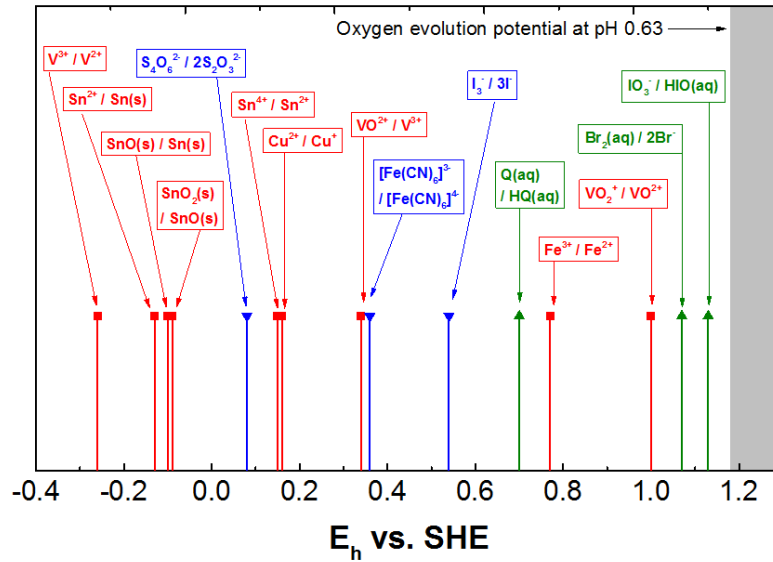


Figure S1: Standard redox potentials of various redox couples which can be applied to redox electrolyte hybrid system.

Membrane treatment, cell assembly and cell configurations for the electrochemical analysis

Anion exchange membranes (FAS15) were provided by FuMA-Tech with the dry thickness of $14 \pm 1 \mu\text{m}$ as measured by a digital micrometer caliper. In order to activate the as-received FAS15 membranes, the membranes were soaked in deionized water for 8 h, then for at least 72 h in 0.5 M H_2SO_4 solution while changing the electrolyte with fresh electrolyte more than three times. We also applied a porous separator (Merck Milipore) made of PTFE with dry thickness of $25 \mu\text{m}$ in order to characterize the electrochemical performance of the double-layer capacitors in 1 M H_2SO_4 and 1 M Na_2SO_4 aqueous solution for comparison.

In case of a full-cell without employing a reference electrode, a particular cell was designed (**Figure S2A**) which allowed the complete sealing of the ion exchange membrane and to limit the excess volume of the redox electrolyte; here, excessive volume means the volume of the electrolyte in the cell except the geometrical volume of the film electrode. For the cell assembly, the redox electrolyte was dropped to the gasket channel having a size of 1.33 cm^2 where the circular film electrode with the same size (1.13 cm^2) was placed, and the cell was tightly sealed afterward.

For the utilization of the Ag/AgCl reference electrode, a spring-loaded two-piston cell (**Figure S2B**) was applied. Even though this cell design does not allow the complete sealing of the ion exchange membrane, the redox shuttling kinetic was reduced into a significantly low level allowing the short term measurement ($<1 \text{ h}$) with the negligible influence of redox shuttling.

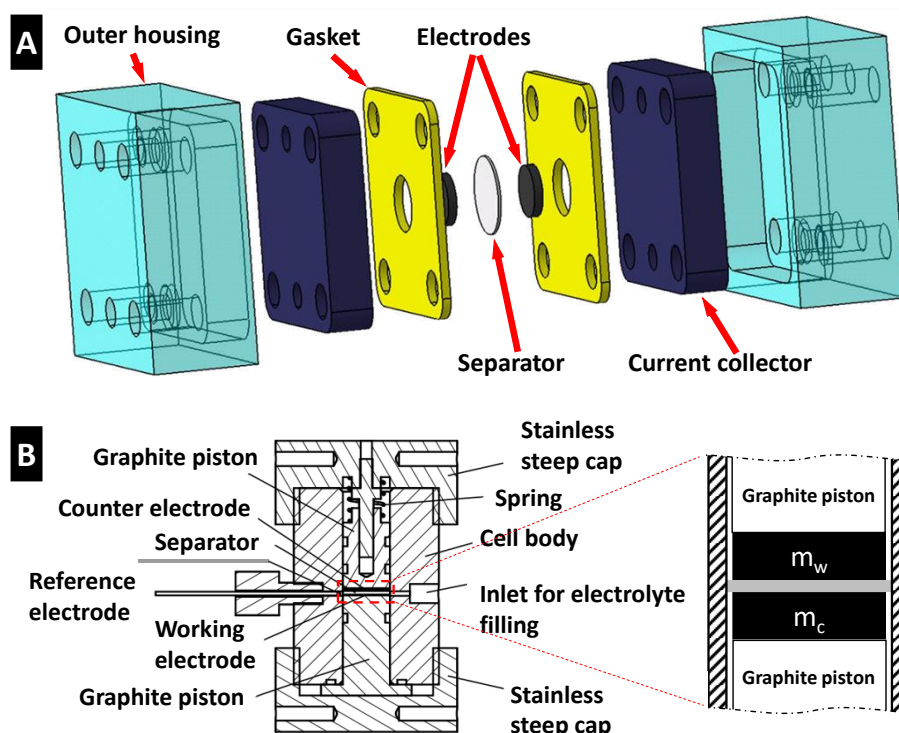


Figure S2: Design of the cells applied for the electrochemical analysis (A-B). (A) Exploded-view drawing of the full-cell without excess volume of electrolyte via gasket sealing for the limited amount of the electrolyte. (B) Schematic illustration of the cell with excess volume of electrolyte. Inset shows the mass of the working electrode (m_w) and the counter electrode (m_c).

In case of measuring the individual potential profile of the positive and negative electrodes in the full-cell (**Figure 1SB**) with a galvanostatic charge and discharge mode, symmetric film electrodes with a diameter of 10 mm were placed between graphite current collectors while being separated by FAS15 membrane. With the aid of the reference electrode, the potential of the counter electrode was measured vs. Ag/AgCl while the potential of the cell was controlled through the potential difference between the positive and the negative electrode (**Table S1**). In case of a half-cell configuration, an electrode with a diameter of 4 mm was applied as working electrode while placing a counter electrode with ca. 38 mg that is more than 30 times larger mass than that of working electrode. Through this mass overbalance, the potential range at the counter electrode was relatively smaller than the applied potential range at the working electrode which allowed to investigate the redox activity at the working electrode without the influence of the redox reactions at the counter electrode (**Figure S3**).

Table S1: Different wire configurations for the potentiostat /galvanostat were applied for the cell in redox electrolytes with a reference electrode. Working electrode potential (U_w) and counter electrode potential (U_c) were controlled or measured either by GCPL or cyclic voltammetry.

Type	U_w	U_c	m_w	m_c
Full-cell	working vs. counter	counter vs. reference	7 mg	7 mg
Half-cell	working vs. reference	counter vs. reference	1.1 mg	38 mg

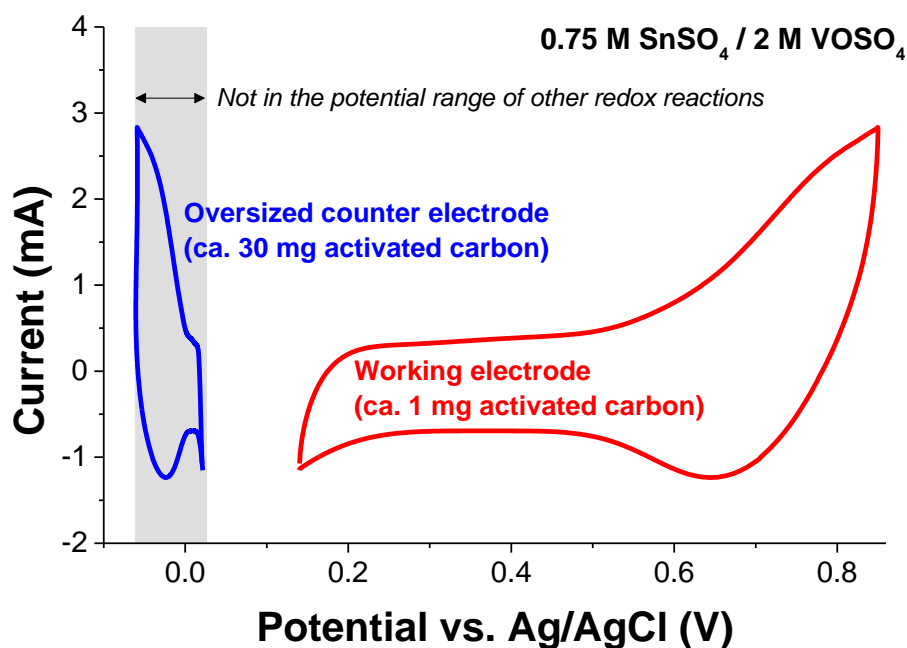


Figure S3: Cyclic voltammogram of a half-cell was obtained for the investigation of the redox activities at the working electrode by minimizing the potential range of the counter electrode via mass overbalance. In case of 0.75 M SnSO₄ / 2 M VOSO₄ system, the potential range of the counter electrode was not in the range of the other possible redox reactions.

Electrochemical characterization

For the electrochemical characterizations, a VMP300 potentiostat/galvanostat (Bio-Logic) was used while keeping the temperature at 25 °C. For the normalization of the specific energy (E), specific power (P), and specific current, the total mass of activated carbon material is considered to provide a comparative data basis with battery and supercapacitor materials in the literature. Specific energy was calculated by Eq. S1 and Eq. S2.

$$E_{CV} = \frac{1}{m_{total}} \cdot \int U i_{CV} dt \quad (S1)$$

$$E_{GC} = \frac{i}{m_{total}} \cdot \int U dt \quad (S2)$$

where E_{CV} is the energy density calculated from cyclic voltammetry, U is the applied voltage, i_{CV} is the measured current, m_{total} is the total mass of the active carbon material in a full-cell, E_{GC} is the energy density calculated from galvanostatic charge and discharge mode, and i is the applied current. The specific power of the full-cell was derived by dividing the specific energy from galvanostatic discharge (E_{GC}) by discharging time (Δt_{dis}) at each specific current step via Eq. S3.

$$P = \frac{E_{GC}}{\Delta t_{dis}} \quad (S3)$$

To determine the voltage stability window, S-value test (see Ref. [2]) was performed by cyclic voltammetry (CV) extending the voltage range of the full-cell (**Figure S2A**) from 0.5 V to 1.6 V with the potential interval of 0.5 V at $1 \text{ mV}\cdot\text{s}^{-1}$. From the cyclic voltammograms, the S-value were calculated according to the following Eq. S4:

$$S = \frac{Q_{char}}{Q_{dis}} - 1 \quad (S4)$$

where Q_{char} is the charge accumulated during charging, Q_{dis} is the recovered charge during discharging.

To condition the cell before the rate handling characterization of the full-cell (**Figure S2A**), a cyclic voltammetry was initially carried out at $1 \text{ mV}\cdot\text{s}^{-1}$ for 10 cycles at the voltage from 0 V to 1.4 V before further characterization was done. In case of cyclic voltammetry, scan rates from $1 \text{ mV}\cdot\text{s}^{-1}$ to $2.5 \text{ V}\cdot\text{s}^{-1}$ were applied for 3 cycles at each scan rate at the voltage from 0 V to 1.4 V. Subsequently, galvanostatic charge/discharge with potential limitation (GCPL) was performed at 50 mA g^{-1} to 30 A g^{-1} with the voltage range from 0 V to 1.2 V or 1.4 V. Afterwards, open circuit voltage measurements over 10 h were carried out after the cell had been discharged to 0 V for 30 min, then, a constant specific current of 400 mA g^{-1} was applied to the cell up to 1.4 V and held at that voltage for 5 h. For the long term cyclic stability test, a galvanostatic cyclic test was applied to the full-cell at 1 A g^{-1} at the voltage window of 1.4 V. For the floating test, symmetric full-cells were charged at 500 mA g^{-1} up to 1.4 V; after that the potential was kept to 1.4 V for 250 h while measuring capacitance for every 10 h by applying 3 cycles in GCPL mode at 500 mA g^{-1} at the voltage window of 1.2 V.

In case of the full-cell with the reference electrode (**Table S1**), the cell was charged by applying a potential from 0 V to 1.4 V between the negative and the positive electrode at 1 A g^{-1} while measuring the potential difference between the negative and the reference electrode. Initially, the cell was stabilized over 20 cycles at 1 A g^{-1} .

In case of the half-cell with the reference electrode (**Table S1**), the cyclic voltammograms of working electrode were measured at a scan rate of $1 \text{ mV}\cdot\text{s}^{-1}$.

Electrochemical performance of the SnSO₄ / VOSO₄ system

For the conditioning of the cell before the S-value characterization, a cyclic voltammetry was initially carried out at 1 mV·s⁻¹ for 20 cycles at the voltage from 0 V to 1.4 V. In case of 0.75 M SnSO₄ / 2 M VOSO₄ system, a very high stability of the electrolyte was observed from the S-value results (Figure S4C) which perhaps originate from the high overpotential of metallic tin against hydrogen evolution.

While most of the studies on the SnSO₄ / VOSO₄ system were carried out with a graphite current collector, we also carried out control experiments with a 100 μm thick platinum current collector (Figure S4D) in order to investigate the possible contribution of graphite current collector for the additional energy storage. As characterized at a low scan rate (1 mV·s⁻¹), no noticeable difference could be found in the cyclic voltammograms obtained from platinum and graphite current collectors.

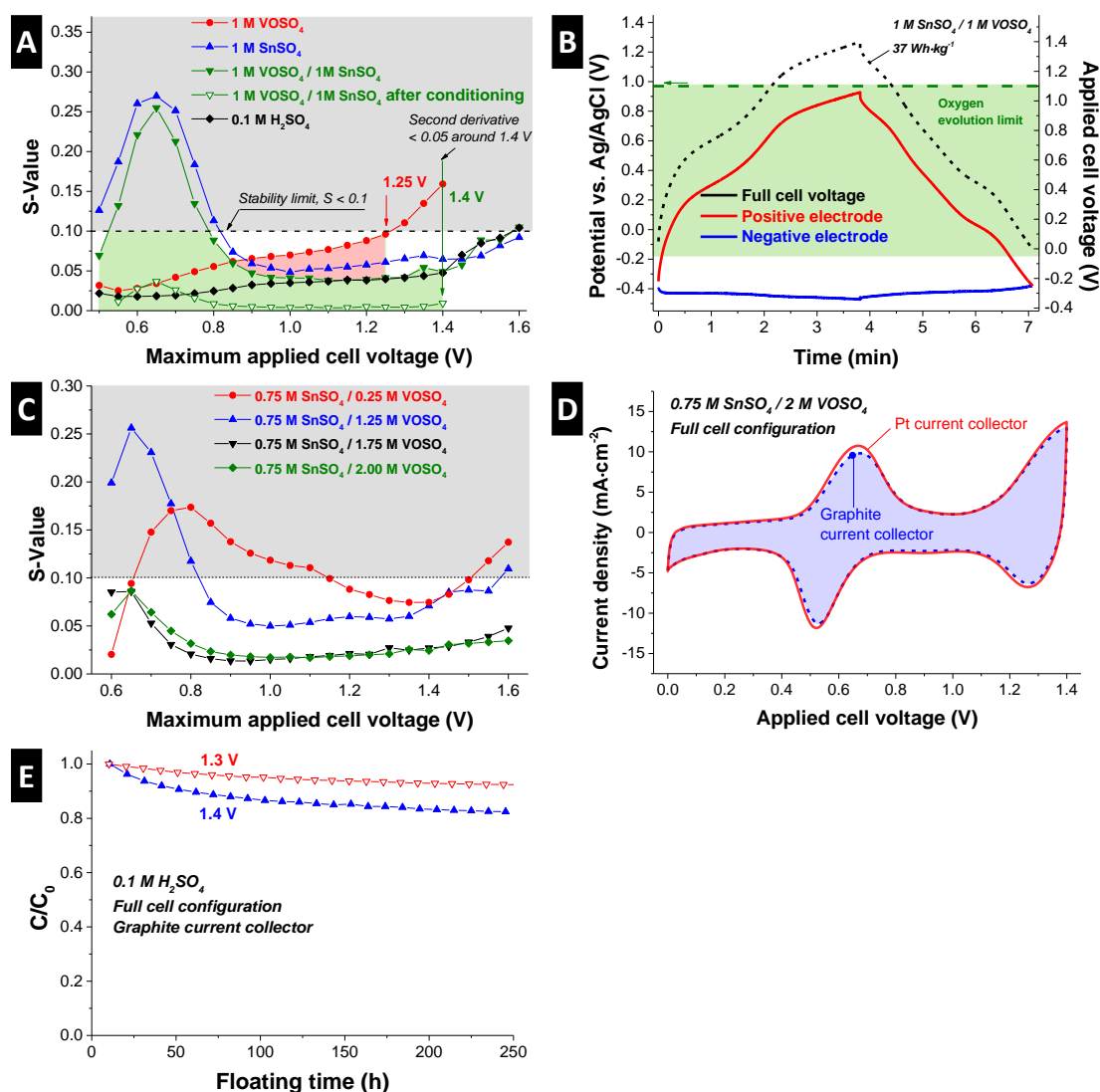


Figure S4: S-Value analysis with various redox electrolytes (A, C). (A) For the conditioning of the 1 M VOSO₄ / 1 M SnSO₄ cell, initial cyclic voltammograms were applied before the S-Value analysis. (B) Potential profile of the full-cell, the positive, and negative electrode from 1 M SnSO₄ / 1 M VOSO₄ system by applying a galvanostatic charge and discharge at 1 A·g⁻¹. (D) Cyclic voltammogram obtained from a full-cell with 0.75 M SnSO₄ / 2 M VOSO₄ aqueous solution at 1 mV·s⁻¹ by applying graphite current collectors or platinum current collectors. (E) The stability of 0.1 M H₂SO₄ aqueous solution is evaluated by floating test via potential holding at 1.3 V and 1.4 V with symmetric full-cell configuration. The measured capacitance values were normalized to the initial capacitance (C₀).

Structural and chemical analysis

Changes in the morphology of the electrodes were examined by a JEOL JSM 7500F field emission scanning microscope (FE-SEM). The electrodes were fixed with sticky carbon tape on steel sample holder. The composition of the electrodes before and after electrochemical characterization was measured by energy dispersive X-ray spectroscopy (EDX) using a X-Max-150 detector from Oxford Instruments attached to the SEM chamber. Using an accelerating voltage of 10 kV and an emission current of 10 μ A, the spectra of 10 different particles was measured. According to the EDX results, the electrode before electrochemical testing contained 0.021 ± 0.004 mole of oxygen per mole of carbon. The electrode with post mortem analysis at -0.2 V showed the increased oxygen and tin content to 0.14 ± 0.03 mole and 0.061 ± 0.004 mole per mole of carbon, respectively.

XPS measurements of the electrode samples were carried out using a K-Alpha+ spectrometer (Thermo Scientific) by applying an Al- K_{α} mono-source (power: 30 W; spot diameter: 200 μ m). For the mounting, the samples were attached to the carbon tape and stayed in the chamber until the vacuum was reached below 10^{-8} mbar before the measurements. The spectra of the samples were obtained in constant analyzer energy mode with a pass energy of 50 eV. The device was calibrated through Au $4f_{7/2}$, Cu $2p_{3/2}$, and Ag $3d_{5/2}$ lines from copper, gold, and silver. For the ion milling, Ar ion beam (4000 eV, 180 s) was applied for etching with the depth of approximately 1-2 μ m.

Raman spectra were recorded with a Renishaw InVia Raman system using a laser with a 532 nm excitation wavelength and 0.5 mW power on the sample with a spectral resolution of ca. 1.2 cm^{-1} , using a 50x objective (numeric aperture: 0.9). Raman spectra were recorded with 10 seconds acquisition time using 10 accumulations. The spectra of 15 different points were measured for each side of electrode, the side in contact with the current collector and the side in contact with the ionic exchange membrane. Peak analysis and peak fitting were performed assuming four Voigt peak fitting between 500 and 2000 cm^{-1} .

X-ray diffractograms were collected with a Bruker D8 Discover diffractometer with a LYNXEYE detector using Cu- K_{α} radiation (0.154 nm) with a step size of 0.02° . The electrodes were placed on a sapphire single crystal to avoid reflexes of the substrate. The system was calibrated with an alumina standard.

The nitrogen gas sorption analyses were carried out with a Quantachrome Autosorb iQ system. For the post mortem analysis, electrode samples were collected after charging the full-cell (**Figure S2A**) to 1.4 V or discharging to 0 V in chronoamperometry mode for 30 min. Afterwards, the negative electrode samples were soaked in 0.1 M H_2SO_4 aqueous solution for a day after the cell disassembly, subsequently soaked into deionized water for a day, and dried in a desiccator in order to remove the dissolved ions. Next, the samples were degassed at 150°C for up to 20 h at a relative pressure of 0.1 Pa to remove volatile molecules from the surface. The nitrogen sorption analysis was performed in liquid nitrogen at -196°C . The relative pressure with nitrogen was $5 \cdot 10^{-7}$ to 1.0 in 76 steps. The pore size distribution (PSD) was derived using the quenched-solid density functional theory (QSDFT), assuming slit-like pores.[3-5] The specific surface area (SSA) was also calculated using the Brunauer-Emmett-Teller equation (BET) in the linear regime of the measured isotherms, typically $3 \cdot 10^{-2}$ to $2 \cdot 10^{-1}$ (relative pressure),[6] with a Quantachrome Autosorb 6B. All calculations were performed with the ASiQwin-software 3.0. The evaluated values are summarized in **Table S2**.

The pore size distribution shown in **Figure S5C** shows that the pore size distribution in the range of 0.5-1 nm was not much influenced after the electrochemical conditions of the electrodes. In order to see the clear trend, the dV/dd values were normalized to peak value around 0.9 nm assuming that the pores in that range were not influenced by the electrochemical treatment (**Figure S5D**). The normalized values indicate that the reduced negative electrode at the cell voltage of 1.4 V might have less pore volumes particularly in the pore size range from 1.2 nm to 3 nm as compared to the pristine electrode made of activated carbon.

Table S2: Summary of the nitrogen gas sorption analysis from the negative electrodes and the pristine electrode made of YP80 type activated carbon and PTFE binder. The post mortem analysis was applied to full-cells exposed to a cell voltage of 1.4 V or 0 V.

Type	SSA _{BET} (m ² ·g ⁻¹)	SSA _{DFT} (m ² ·g ⁻¹)	Total pore volume (cm ³ ·g ⁻¹)
YP80 + 5 mass% PTFE	2094	1662	1.05
Post mortem, 1.4 V (full-cell)	1130	981	0.55
Post mortem, 0 V (full-cell)	1783	1520	0.90

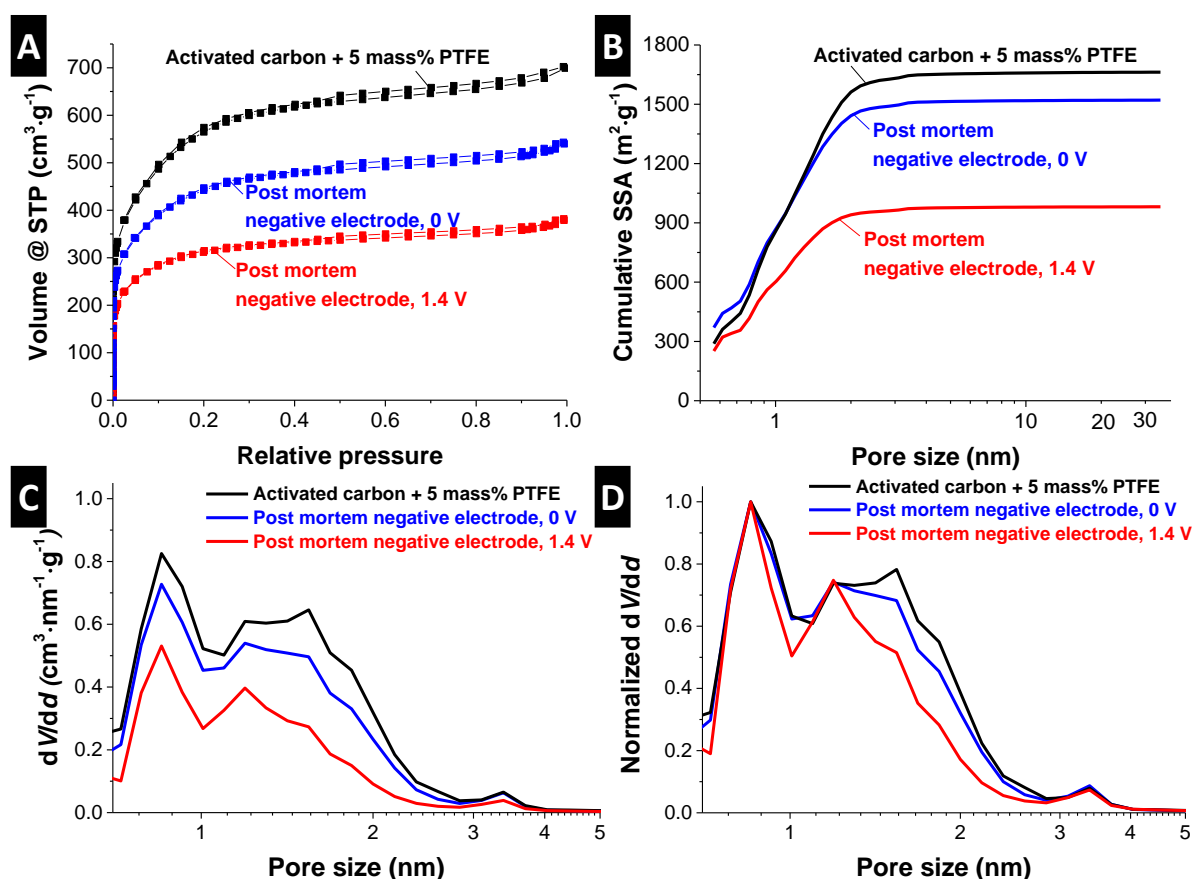


Figure S5: (A-B) Results from post mortem nitrogen gas adsorption analysis. (A) Nitrogen gas sorption isotherms obtained at -196 °C normalized to the total electrode mass and the volume calculated at standard temperature and pressure (STP). (B) Cumulative specific surface area. (C) Pore size distribution calculated by applying the quenched solid density functional theory with slit shape pore model. (D) dV/dd values are normalized to the peak value obtained in the pore size range 0.5-1 nm.

Tin fluoride formation

The as-prepared activated carbon electrode bound with 5 mass% PTFE, presents a clear F 1s peak of the polytetrafluoroethylene (PTFE) compared to the electrode sample with post mortem analysis at -0.57 V (Figure S6B), which shows an extremely small peak for PTFE and a huge peak for metal fluoride. The metal fluorine peak can be identified as SnF₂.

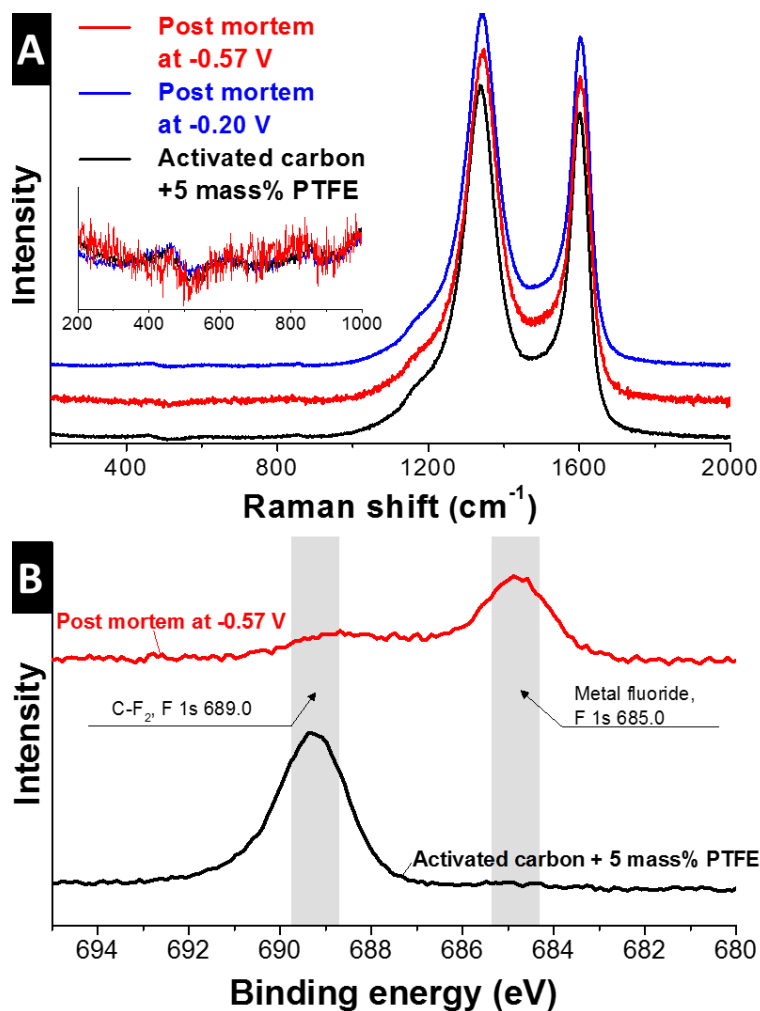


Figure S6: (A) Raman spectra of electrodes before and after electrochemical testing, the inset shows the Raman spectra between 100 cm⁻¹ and 1000 cm⁻¹, wavelength range at which crystalline SnO₂ presents active modes [7]. However due to the amorphous character, this peaks cannot be distinguished from the background. (B) XPS spectra show metal fluoride formation and the weakening of the C-F₂ binding signal for the negative electrode with post mortem analysis at -0.57 V.

Rate handling performance of the $\text{SnSO}_4 / \text{VOSO}_4$ system plotted as a Ragone diagram

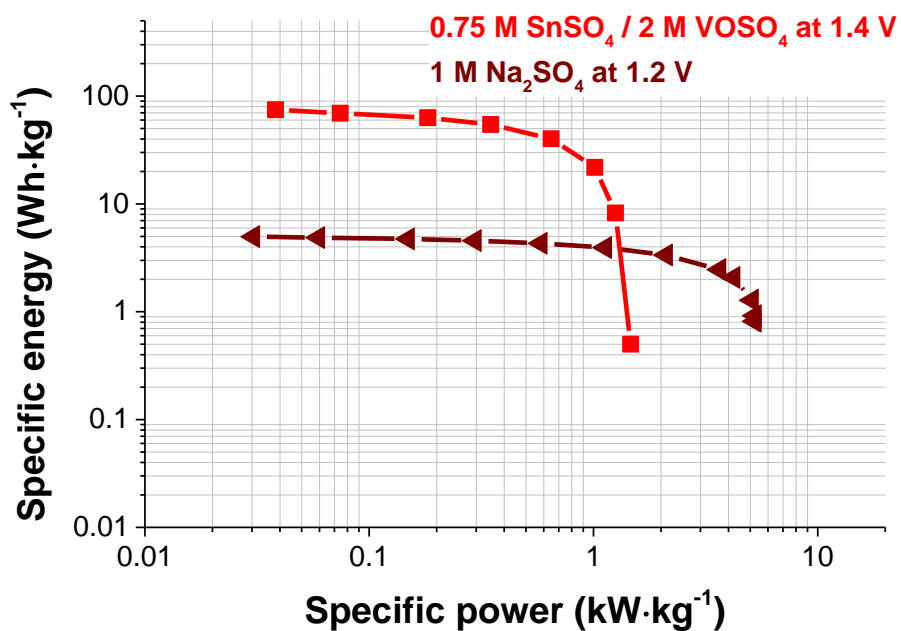


Figure S7: The rate performance of 1 M Na_2SO_4 at 1.2 V and 0.75 M $\text{SnSO}_4 / 2$ M VOSO_4 at 1.4 V are plotted in a Ragone chart.

Supporting references

- [1] B. Averill, P. Eldredge, General chemistry: principles, patterns, and applications, 2011.
- [2] D. Weingarh, H. Noh, A. Foelske-Schmitz, A. Wokaun, R. Kötz, *Electrochim Acta*, 103 (2013) 119-124.
- [3] V. Presser, J. McDonough, S.-H. Yeon, Y. Gogotsi, *Energ Environ Sci*, 4 (2011) 3059.
- [4] G.Y. Gor, M. Thommes, K.A. Cychosz, A.V. Neimark, *Carbon*, 50 (2012) 1583-1590.
- [5] A. Vishnyakov, P.I. Ravikovitch, A.V. Neimark, *Langmuir*, 15 (1999) 8736 - 8742.
- [6] S. Brunauer, P.H. Emmett, E. Teller, *Journal of the American Chemical Society*, 60 (1938) 11.
- [7] J. Zuo, C. Xu, X. Liu, C. Wang, C. Wang, Y. Hu, Y. Qian, *Journal of applied physics*, 75 (1994) 1835-1836.

3.5. Asymmetric tin-vanadium redox electrolyte for hybrid energy storage with nanoporous carbon electrodes

Juhan Lee,^{1,2} Aura Tolosa,^{1,2} Benjamin Krüner,^{1,2} Nicolas Jäckel,^{1,2} Simon Fleischmann,² Marco Zeiger,^{1,2} Daekyu Kim,^{1,3} and Volker Presser^{1,2}

¹ INM - Leibniz Institute for New Materials, Campus D2 2, 66123 Saarbrücken, Germany

² Saarland University, Campus D2 2, 66123 Saarbrücken, Germany

³ School of Energy, Materials and Chemical Engineering, Korea University of Technology and Education, Chungjeol-ro 1600, 31253, Cheonan, Republic of Korea

Citation:

Lee, J.; Tolosa, A.; Krüner, B.; Jäckel, N.; Fleischmann, S.; Zeiger, M.; Kim, D.; Presser, V., Asymmetric tin-vanadium redox electrolyte for hybrid energy storage with nanoporous carbon electrodes. *Sustainable Energy & Fuels* 2017, 1 (2), 299-307.

Own contributions:

Design, planning, writing, cell design, experimental plan, electrochemical analyses, and thermogravimetric analysis

Abstract

In recent decades, redox-active electrolytes have been applied in stationary energy storage systems, benefitting from Faradaic reactions of the electrolyte instead of the electrode material. One of the challenging tasks is to balance the redox activities between the negative and positive electrode. As a possible solution, a mixed electrolyte with vanadyl and tin sulfate was previously suggested; however, a low power performance is a great challenge to be overcome. Here, we found that the origin of the poor power performance in the mixture electrolyte system (vanadium complex and tin solution) is the reduction of the pore volume at the positive electrode via irreversible tin dioxide formation. To prevent the latter, we introduce a hybrid energy storage system exhibiting both battery-like and supercapacitor-like features via asymmetric redox electrolytes at the microporous activated carbon electrodes; SnF₂ solution as anolyte and VOSO₄ as catholyte. By employing an anion exchange membrane, the irreversible SnO₂ formation at the positive electrode is effectively suppressed; thus, an asymmetric 1 M SnF₂|3 M VOSO₄ system provides a high maximum specific power (3.8 kW/kg or 1.5 kW/L), while still exhibiting a high maximum specific energy up to 58.4 Wh/kg (23.4 Wh/L) and a high cycling stability over 6,500 cycles.

CrossMark
click for updatesCite this: *Sustainable Energy Fuels*,
2017, 1, 299

Asymmetric tin–vanadium redox electrolyte for hybrid energy storage with nanoporous carbon electrodes†

Juhan Lee,^{ab} Aura Tolosa,^{ab} Benjamin Krüner,^{ab} Nicolas Jäckel,^{ab}
Simon Fleischmann,^b Marco Zeiger,^{ab} Daekyu Kim^{ac} and Volker Presser^{*ab}

In recent decades, redox-active electrolytes have been applied in stationary energy storage systems, benefitting from Faradaic reactions of the electrolyte instead of the electrode material. One of the challenging tasks is to balance the redox activities between the negative and positive electrode. As a possible solution, a mixed electrolyte with vanadyl and tin sulfate was previously suggested; however, a low power performance is a great challenge to be overcome. Here, we found that the origin of the poor power performance in the mixture electrolyte system (vanadium complex and tin solution) is the reduction of the pore volume at the positive electrode via irreversible tin dioxide formation. To prevent the latter, we introduce a hybrid energy storage system exhibiting both battery-like and supercapacitor-like features via asymmetric redox electrolytes at the microporous activated carbon electrodes; SnF₂ solution as anolyte and VOSO₄ as catholyte. By employing an anion exchange membrane, the irreversible SnO₂ formation at the positive electrode is effectively suppressed; thus, an asymmetric 1 M SnF₂/3 M VOSO₄ system provides a high maximum specific power (3.8 kW kg⁻¹ or 1.5 kW L⁻¹), while still exhibiting a high maximum specific energy up to 58.4 W h kg⁻¹ (23.4 W h L⁻¹) and a high cycling stability over 6500 cycles.

Received 19th November 2016
Accepted 4th January 2017

DOI: 10.1039/c6se00062b

rsc.li/sustainable-energy

Introduction

Ranging from intercalation batteries and redox flow systems to supercapacitors and hybrid devices: electrochemical energy storage is getting more and more integrated in our daily lives.^{1,2} Achieving high storage capacities combined with rapid charge/discharge rates and performance longevity remains a particular challenge. For example, batteries demonstrate very high energy storage capacities with a rather limited power and cycling longevity. In contrast, supercapacitors, especially double-layer capacitors, are characterized by particularly high power and performance stability owing to the physical mechanism of ion electrosorption at the interface between high surface area of carbons and the electrolyte. Enhancing the energy storage capacity by adding redox active electrolytes to porous carbon has emerged as a promising strategy for hybrid energy storage systems combining the principles of supercapacitors and batteries.^{3–5} Unlike other hybrid approaches, redox electrolytes

can be directly used in combination with conventional nanoporous carbons as they benefit from Faradaic reactions of the electrolyte instead of the electrode material.

After the pioneering work, for example, by Li *et al.* (2007),⁶ Lota *et al.* (2009),⁷ and Roldán (2011),⁸ redox-active electrolyte aided hybrid energy storage (REHES) systems have quickly evolved to high performance devices.^{3–5} The specific energy of REHES systems is close to that of lead acid batteries, reaching values of *ca.* 10–20 W h kg⁻¹, while keeping the power performance as high as that of supercapacitors (>5 kW kg⁻¹) with a high cycling stability over 5000 cycles.⁴ The most frequently studied REHES systems rely on soluble redox couples like quinone/hydroquinone (H/HQ)^{9–11} ferricyanide/ferrocyanide,^{12–16} *p*-phenylenediamine,^{17–19} vanadium complexes,^{20,21} and halides.^{22–24} Advanced systems approach energy storage capacities nearing lithium ion batteries (~100 W h kg⁻¹), such as the mixture electrolytes of vanadyl and tin sulfate (75 W h kg⁻¹)²¹ or solutions of cupric chloride (73 W h kg⁻¹).²⁵ As most REHES systems are based on aqueous solutions, they also have strong advantages regarding cost, safety, and environmental issues.⁴

The reason of the high performance of REHES systems is the synergetic charge storage enhancement by the redox activities of the soluble ions and the rapid charge transfer across short distances within the confinement of carbon nanopores.^{12,26} In addition to the redox-activity (*i.e.*, Faradaic charge transfer), fast electrostatic physisorption of the ions on the electrode occurs (*i.e.*, electric double-layer (EDL) formation).²⁶ The aspect of

^aINM – Leibniz Institute for New Materials, Campus D2 2, 66123 Saarbrücken, Germany. E-mail: volker.presser@leibniz-inm.de

^bDepartment of Materials Science and Technology, Saarland University, Campus D2 2, 66123 Saarbrücken, Germany

^cSchool of Energy, Materials and Chemical Engineering, Korea University of Technology and Education, Chungjeol-ro 1600, 31253 Cheonan, Republic of Korea

† Electronic supplementary information (ESI) available: Electrochemical measurements, selected area electron diffraction pattern. See DOI: 10.1039/c6se00062b

rapid charge transfer in nanopores distinguishes REHES systems from flow battery technologies, where confinement of redox electrolytes in the micropores causes a pressure drop for the circulation of the electrolyte in flow mode.²⁷

A key challenge for REHES is to balance the redox activities occurring at the negative and positive electrode. For instance, iodide is a promising redox ion at the positive electrode;⁷ however, so far, only the vanadyl sulfate system has been introduced at the negative electrode to balance the iodide's enormous redox capacity at the positive electrode.²⁰ This system could also work without introducing a redox electrolyte at the negative electrode because reversible hydrogen storage at the negative electrode can be utilized as a balance to the iodine redox activities.²² However, since the electrochemical hydrogen storage shows a huge separation potential between anodic and cathodic reactions, the energy efficiency of the system is observed to be rather low (<80%).²⁸ Furthermore, the hydrogen redox activity cannot fully compensate for the huge redox capacity of the iodine at the positive electrode.²⁹ Pioneering works can be found regarding the balance of the redox activities from viologen/bromide^{23,24} and vanadyl sulfate/potassium iodide²⁰ systems reaching specific energies up to 50 W h kg⁻¹. Even higher energy storage capacities exceeding 70 W h kg⁻¹ can be obtained for a well-balanced REHES employing SnSO₄·VOSO₄, as recently demonstrated by us.²¹ Though the latter redox electrolyte system exhibited a highly promising energy storage capacity (~75 W h kg⁻¹), the limited power performance (1.5 kW kg⁻¹ or 0.6 kW L⁻¹) must be overcome to achieve high energy storage capacity and high power handling.

In this work, as a starting point for designing a power-enhanced system, we will first explore the origin of the low power performance for the mixture electrolyte system (SnSO₄·VOSO₄) by post mortem analysis of positive and negative electrodes *via* scanning electron microscopy (SEM), nitrogen gas sorption analysis (GSA), and X-ray diffraction (XRD). As a solution to the pore volume reduction at the positive electrode *via* tin oxide formation, we then introduce an asymmetric electrolyte design by applying SnF₂ solution as electrolyte at the negative electrode (anolyte) and VOSO₄ solution as electrolyte at the positive electrode (catholyte). The electrochemical performance of the asymmetric electrolyte system (SnF₂|VOSO₄) will be discussed as well as the post mortem analysis with electron micrographs, GSA, and XRD to understand the morphological and electrochemical state change of the positive and negative electrode after electrochemical operation.

Experimental section

Materials

For the free-standing film electrodes, we applied a mechanical rolling process to mixture paste of YP-80F type activated carbon (Kuraray Chemicals) as active electrode material, ethanol as solvent, and polytetrafluoroethylene (PTFE) as binder material. Finally, 200 ± 6 μm thick electrodes were obtained with 5 mass% PTFE after being dried in a vacuum oven (120 °C, 2 × 10³ Pa) for 48 h.

The commercially available activated carbon electrode exhibits a specific surface area of 2105 m² g⁻¹ by applying the Brunauer–Emmett–Teller (BET)³⁰ equation or density-functional theory (DFT) surface area of 1672 m² g⁻¹ using quenched-solid density functional theory.³¹ *Via* quenched-solid density functional theory with a slit model and pore size in the range of 0.56–37.5 nm, a total pore volume of 1.01 cm³ g⁻¹ and an average pore size of 1.6 nm were calculated.

Type FAS15 (FuMA-TECH) anion exchange membranes (dry thickness of 14 ± 1 μm) were activated by being soaked in deionized water for 8 h, then, in 0.5 M H₂SO₄ for at least 72 h while changing the electrolyte more than three times. The selectivity of the FAS15 membrane was determined to be higher than 95% by the manufacturer. In case of half-cell investigation, glassy fiber filter (GF/A, Whatman) was applied.

For the electrolyte, vanadyl sulfate (VOSO₄, 97% purity), tin sulfate (SnSO₄, 95% purity), tin fluoride (SnF₂, 99% purity), sodium sulfate (Na₂SO₄) with 99% purity, and sulfuric acid (H₂SO₄, 99.99% purity based on trace metal analysis) were purchased from Sigma Aldrich and mixed with deionized water.

Cell design and assembly

For the half-cell experiments, a spring-loaded two-piston cell was applied with the Ag/AgCl reference electrode (saturated, 3 M NaCl); the scheme of our cell design can be found elsewhere.^{32,33} While two graphite pistons served as current collectors, the working (4 mm diameter, 200 μm thickness) and counter electrode (12 mm diameter, 500 μm thickness) were separated by GF/A glassy fiber filter (Whatman). We used two cell designs for full-cell operation: (i) spring-loaded two-piston cells (see ref. 33), and (ii) cells which allow the complete sealing of the ion exchange membrane and to limit the excess volume of the redox electrolyte; here, excessive volume means the volume of the electrolyte in the cell except the geometrical volume of the film electrode. The drawing of the latter cell can be found in our previous reports.^{12,21,22} For the latter cell, the electrolyte was dropped to the gasket channel having a size of 1.33 cm² where the circular film electrode (12 mm diameter, 200 μm thickness) was placed above the glassy carbon current collectors, and the cell was tightly sealed afterward. To prevent the electrolyte shortage *via* the electrolyte adsorption during the electrochemical operation, the electrodes were previously soaked in the electrolyte and degassed by applying vacuum for 5 min. For the cells with reference electrode, thin string of FKS15 membrane was additionally mounted at the negative electrode as an ion bridge to the reference electrode (Ag/AgCl). Through the tight gap between the gaskets this porous membrane string was extended to the glass container with H₂SO₄ (1 M) aqueous solution where Ag/AgCl reference electrode was mounted. In case of spring-loaded cells, electrolyte is injected by syringe after assembly.

Electrochemical characterization

For the electrochemical characterizations, a VMP300 potentiostat/galvanostat (Bio-Logic) was used. The cells were stored at 25 °C in a climate chamber.

For the normalization of the specific energy (E), specific power (P), and specific current, the total mass of activated carbon material is considered to provide a comparative data basis with battery and supercapacitor materials in the literature. Values for the specific energy were calculated by eqn (1):

$$E_{GC} = \frac{i}{m_{\text{total}}} \int U dt \quad (1)$$

where E_{GC} is the specific energy calculated from galvanostatic charge and discharge mode, U is the cell voltage, and i is the discharge current. The specific power of the full-cell was derived by dividing the specific energy from galvanostatic discharge (E_{GC}) by discharging time (Δt_{dis}) at each specific current step via eqn (2):

$$P = \frac{E_{GC}}{\Delta t_{\text{dis}}} \quad (2)$$

To condition the cell, cyclic voltage sweeping was carried out at 1 mV s^{-1} for 10 cycles at the voltage from 0–1.4 V cell voltage prior to further characterization. Subsequently, cyclic voltammetry was carried out at the scan rates from 1 mV s^{-1} to 2.5 V s^{-1} for 3 cycles at each scan rate at the cell voltage from 0 V to 1.4 V. Afterwards, galvanostatic charge/discharge with potential limitation (GCPL) was performed at 100 mA g^{-1} to 30 A g^{-1} with the voltage range from 0–1.4 V. Next, open circuit voltage measurements over 10 h were carried out after the cell had been discharged to 0 V for 30 min, then, a constant specific current of 50 mA g^{-1} was applied to reach a cell voltage of 1.4 V. For the cyclic stability test, galvanostatic cycling was applied to the full-cell at 1 A g^{-1} at the voltage window of 1.4 V.

In case of the full-cell with the reference electrode, the cell was charged by applying a potential from 0 V to 1.4 V between the negative and the positive electrode at 0.5 A g^{-1} while measuring the potential difference between the negative and the reference electrode. Initially, the cell was conditioned over 20 cycles at 0.5 A g^{-1} .

Material characterization

The nitrogen gas sorption analyses were carried out with a Quantachrome Autosorb iQ system. The electrodes were degassed at $150 \text{ }^\circ\text{C}$ for up to 20 h at a relative pressure of 0.1 Pa. The analysis was performed in liquid nitrogen at $-196 \text{ }^\circ\text{C}$ by applying relative pressure of 1×10^{-6} to 1.0 in 56 steps. The pore size distribution (PSD) was derived using the quenched-solid density functional theory (QSDFT), assuming slit-like pores.^{31,34} Additionally, the specific surface area (SSA) was also calculated using the Brunauer–Emmett–Teller equation (BET) in the linear regime of the measured isotherms, typically 3×10^{-2} to 2×10^{-1} in relative pressure,³⁰ with a Quantachrome Autosorb 6B. All calculations were performed with the ASiQwin-software 3.0.

The X-ray diffraction measurements were carried out with a Bruker D8 Discover using Cu-K_α radiation with a Goebel mirror, a point focus (diameter: 0.5 mm), and a 2D-detector (Vantec-500). The device was calibrated with a corundum standard and the sample moved during the measurement to obtain

a better statistic (amplitude in x and y : 5 mm; speed in x : 0.5 mm s^{-1} ; speed in y : 0.2 mm s^{-1}). The diffraction pattern was fitted with TOPAS (version 5 from Bruker AXS).

Changes in the morphology of the electrodes were examined by a JEOL JSM 7500F field emission scanning microscope (FE-SEM) at 3 kV. The post mortem electrodes were fixed on steel sample holders with sticky carbon tape. The composition of the electrodes was determined by energy dispersive X-ray spectroscopy (EDX) using an X-Max-150 detector from Oxford Instruments attached to the SEM chamber. The spectra of 10 particles were measured using an accelerating voltage of 10 kV and averaged. For standardization, silicon crystal was used. For high resolution analysis, a JEOL JEM-2100F high resolution transmission electron microscope (TEM) was employed at 200 kV. TEM samples were prepared by mechanically dispersing the electrodes in isopropanol, and drop casting them on a carbon film on copper grid. Using TEM, we also carried out selected area electron diffraction (SAED).

Thermogravimetric analysis (TGA) was carried out with a TG 209 F1 Libra system (Netzsch) in oxygen containing synthetic air (80% N_2 , 20% O_2). The temperature was increased at a rate of $19 \text{ }^\circ\text{C min}^{-1}$ to $250 \text{ }^\circ\text{C}$ and held for 2 h to remove surface groups. Afterwards, the temperature was further increased up to $900 \text{ }^\circ\text{C}$ at a rate of $5 \text{ }^\circ\text{C min}^{-1}$ to burn off the carbon and to determine the mass of residual tin oxide.

For the post mortem analysis, full-cells were initially conditioned with 20 cycles in GCPL mode (0.5 A g^{-1} 0–1.4 V) and subsequently charged to 1.4 V or discharged to 0 V in chronoamperometry mode for 30 min. Afterwards, the negative and positive electrode samples were soaked in 1 M H_2SO_4 aqueous solution for a day after the cell disassembly, subsequently soaked into deionized water for a day, and dried in a desiccator to remove the dissolved ions.

Results and discussion

Issues and limitations of the $\text{SnSO}_4 \cdot \text{VOSO}_4$ redox electrolyte system

As we have recently demonstrated,²¹ the specific energy of a well-balanced redox-active electrolyte aided hybrid energy storage (REHES) can exceed 70 W h kg^{-1} by employing a semi-soluble redox system like $\text{Sn}^{2+}/\text{Sn}(\text{s})$ redox couple as a balance to the activities of vanadium complexes at the positive electrode (see ESI,† Fig. S1A). For the latter study, the mixture of 0.75 M SnSO_4 and 2 M VOSO_4 in 0.1 H_2SO_4 aqueous solution was applied as redox electrolyte. When a constant current is applied to a full-cell in the potential range from 0 V to 1.4 V, two distinctive voltage plateaus arise: one due to the redox activities of vanadyl sulfate, namely $\text{V}^{3+}/\text{VO}^{2+}$ and $\text{VO}^{2+}/\text{VO}_2^+$ redox couples at the positive electrode, and one related to tin redox activities and the $\text{V}^{2+}/\text{V}^{3+}$ redox couple (see ESI,† Fig. S1B) at the negative electrode. Chemical analyses with X-ray photoelectron spectroscopy (XPS) after electrochemical operation (post mortem) confirm the reversible $\text{Sn}(\text{s})/\text{Sn}^{2+}$ redox reaction for the negative electrode in charged state ($-0.57 \text{ V vs. Ag/AgCl}$).²¹ The strong redox activities of the $\text{Sn}^{2+}/\text{Sn}(\text{s})$ redox couple prevents

the irreversible hydrogen evolution reaction which would onset at a potential below -0.5 V vs. Ag/AgCl.

The starting point to design a redox electrolyte system with improved power handling ability was our previous work on the $\text{SnSO}_4 \cdot \text{VOSO}_4$ redox electrolyte system,²¹ where tin electroplating occurs at the negative electrode when a full-cell system is charged up to 1.4 V. As metallic tin is formed in the pore network of the activated carbon electrode, the pore volume of the electrode decreases when the negative electrode is in charged state since the metal tin is formed in the pores (see ESI,† Fig. S2A). When the negative electrode is in a discharged state, most of the pore volume is recovered as the metallic tin is dissolved in the solution again, indicating that the $\text{Sn}^{2+}/\text{Sn}(\text{s})$ redox reaction occurs reversibly in the pore network at the negative electrode. The pore volume of the charged and discharged positive electrodes are significantly lower compared to that of its initial value which implies that some of the pores are filled and possibly blocked at the positive electrode.

From the post mortem XRD results, there is clear evidence of stannic oxide (SnO_2) at both electrodes (see ESI,† Fig. S2B). Therefore, SnO_2 formation can be the origin of the irreversible pore volume reduction at the positive electrode, as also supported by the morphological changes seen on post mortem samples in scanning electron micrographs (ESI,† Fig. S2C–F). While the discharged negative electrode maintains the initial morphology with smooth activated carbon particles (Fig. S2E†), the positive electrode presents a non-uniform coating, which

implies the possibility of blocked micropores (Fig. S2D and F†). Given that the $\text{SnSO}_4 \cdot \text{VOSO}_4$ redox electrolyte system relies mostly on the reversible redox reaction of the vanadium complex at the positive electrode and the tin redox activities at the negative electrode, the stannous oxide formation at the positive electrode blocks the active surface area and energy storage mechanism is limited. Also, the transition between dissolved and solid state of tin is a key limiting factor which prevents this specific redox electrolyte system to achieve rapid charge and discharge rates.

Electrochemistry of the new $\text{SnF}_2|\text{VOSO}_4$ redox electrolyte system

To prevent the reduction of the pore volume at the positive electrode *via* tin oxide formation, we designed a new system based on separate electrolytes at the positive and negative electrode by using an anion ion exchange membrane (AEM): a tin containing solution as anolyte for the negative electrode and vanadium containing solution as catholyte for the positive electrode. Stannous fluoride (SnF_2) was selected as solute for the anolyte due to its even higher solubility compared to SnSO_4 which can be beneficial for the stability of the solution.³⁵ For the catholyte, VOSO_4 was selected as a solute.

First, the individual redox activities of VOSO_4 and SnF_2 can be identified in the cyclic voltammograms at 1 M concentration in 1 M H_2SO_4 solution (Fig. 1A). In the potential range from -0.17 V to $+0.9$ V vs. Ag/AgCl, two pairs of redox reactions can be

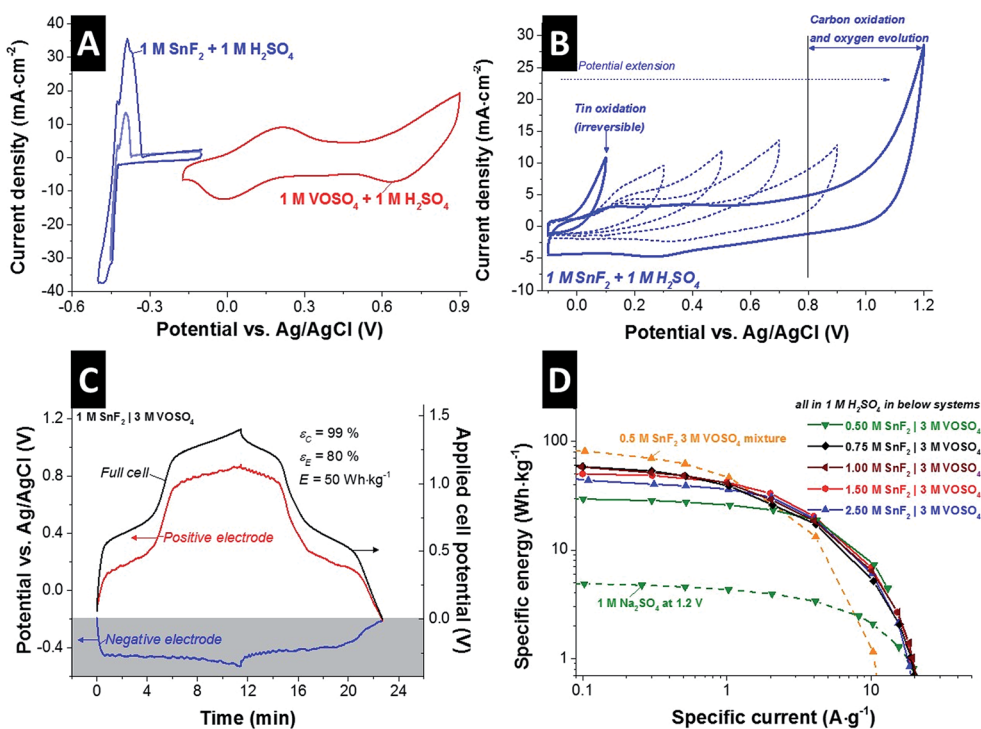
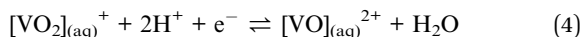
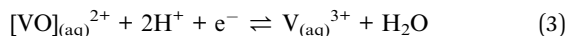
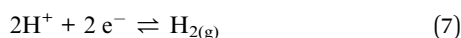
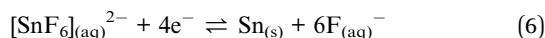
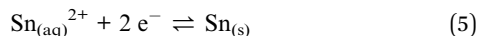


Fig. 1 (A) Cyclic voltammograms obtained for individual 1 M $\text{SnF}_2 + 1$ M H_2SO_4 and 1 M $\text{VOSO}_4 + 1$ M H_2SO_4 . (B) Electrochemical behavior of 1 M $\text{SnF}_2 + 1$ M H_2SO_4 was investigated by cyclic voltammetry in the positive potential range. (C) The potential developments of the positive and the negative electrode were measured for the 1 M $\text{SnF}_2|3$ M VOSO_4 system in 1 M H_2SO_4 . (D) Rate handling comparison with the separate electrolyte system ($\text{SnF}_2|\text{VOSO}_4$) by various SnF_2 concentration and the mixture electrolyte system ($\text{SnF}_2 \cdot \text{VOSO}_4$).

seen for 1 M VOSO₄ in 1 M H₂SO₄ solution which can be identified as the following redox reactions (eqn (3) and (4)):



For aqueous 1 M SnF₂, there is a significant, redox-related current emerging at -423 mV vs. Ag/AgCl, indicative of tin electroplating *via* eqn (5). Without having a clear peak, the reduction current shows a slight plateau and a subsequent second current increase at around -453 mV vs. Ag/AgCl (see also ESI,† Fig. S3A) which indicates the possibility of tin fluoride redox reaction *via* eqn (6)^{36,37} and/or hydrogen gas evolution *via* eqn (7).



In the anodic scan, two distinctive oxidations peaks (at -426 mV and -386 mV) and a small shoulder (at -371 mV) appear which are also indications for the possible redox reactions *via* eqn (5)–(7). For reversible energy storage, hydrogen evolution in such a low potential range (around -500 mV vs. Ag/AgCl) is not preferable. However, the cathodic stability limit for the solution can be slightly extended to -500 mV vs. Ag/AgCl *via* reversible hydrogen storage (Fig. S3B†) in the carbon micropores and the tin induced overpotential; which was demonstrated by our earlier work by rigorous stability test with voltage cycling and floating tests.²¹

The cyclic voltammograms (Fig. 1B) show the irreversible redox behavior of the tin fluoride solution in the potential range from -0.1 V to $+1.2$ V which is the possible potential range for the positive electrode. The onset potential of *ca.* -40 mV vs. Ag/AgCl for the increasing oxidation current implies a change of the tin oxidation state from 2⁺ to 4⁺ which does not seem to be reversible because no clear reduction current can be seen during backward scan. As the cycle number increases and the potential window is extended, we see that the oxidation potential is shifting to a higher potential until carbon oxidation and oxygen generation occur. However, as illustrated by our post mortem findings (Fig. S2†), this irreversible transition to Sn⁴⁺ seems to be the origin of the active surface area blocking in the carbon electrode *via* the formation of SnO₂ which can be the major reason for the low power performance of the mixture electrolyte system (SnSO₄·VOSO₄). Our results also indicate that SnO₂ is a much more favorable form than tin hydroxides in acidic solution which also line with previous reports.^{38–41}

To prevent the unfavorable SnO₂ formation at the positive electrode, an anion exchange membrane (AEM) was applied to effectively separate SnF₂ anolyte and VOSO₄ catholyte. The AEM prevents also the redox shutting *via* V³⁺, VO²⁺, and VO₂⁺ cations which causes a low energy efficiency of the system.^{11,12} Fig. 1C shows the full-cell performance of the separate electrolytes

system in acidic media (1 M H₂SO₄) as exemplified with 1 M SnF₂|3 M VOSO₄ during galvanostatic cycling, while also monitoring the potential of the negative electrode by a spectator Ag/AgCl reference electrode. As the cell is charged to 1.4 V, the potential of the positive electrode changes from -0.2 V to $+0.88$ V vs. Ag/AgCl having two clear potential plateaus corresponding to the redox reactions of the vanadium complex *via* eqn (3) and (4). At the negative electrode, the potential develops from -0.2 V to -0.53 V vs. Ag/AgCl showing a single potential plateau *via* the redox activities of SnF₂ (eqn (5) and (6)) and the reduction of protons. Capitalizing on tin and vanadium redox activities, a specific energy of 50 W h kg⁻¹ (20 W h L⁻¹) was achieved at 0.5 A g⁻¹ for 1 M SnF₂|3 M VOSO₄ system with high efficiencies (Coulombic efficiency: 99%; energy efficiency: 80%).

The improved rate behavior of the system with separated electrolytes (SnF₂|VOSO₄) can be seen in Fig. 1D as compared to the mixture electrolyte system (SnF₂·VOSO₄). The concentration of separated SnF₂ anolyte was varied from 0.5 M to 2.5 M, and 1 M SnF₂ was found to be the optimized system in terms of maximum specific energy as well as high Coulombic and energy efficiency (ESI,† Fig. S4A). At a high current density of 10 A g⁻¹, the optimized SnF₂|VOSO₄ system retains a high specific energy of 5–7 W h kg⁻¹. All investigated SnF₂|VOSO₄ systems, surveying different concentrations, exhibit a significantly higher power performance than the mixture electrolyte (exemplified for 0.5 M SnF₂ and 3 M VOSO₄ in Fig. 1D). Since the V³⁺/V²⁺ redox reaction does not occur in the separate electrolyte system, 0.5 M SnF₂|3 M VOSO₄ shows a lower maximum specific energy (29.5 W h kg⁻¹) compared to 0.5 M SnF₂·3 M VOSO₄ system (81.5 W h kg⁻¹) but still far more than the constituent double-layer capacitor (1 M Na₂SO₄: 2.1 W h kg⁻¹).

The highest specific energy (at 0.1 A g⁻¹) of 81.5 W h kg⁻¹ was achieved for mixed 0.5 M SnF₂·3 M VOSO₄, which is about 1.4 times higher than that the separated 1 M SnF₂|3 M VOSO₄ (58.4 W h kg⁻¹) and over one magnitude higher than the electric double-layer system (1 M Na₂SO₄: 5 W h kg⁻¹). Considering the maximum specific power of 1.6 kW kg⁻¹ (640 W L⁻¹) for mixed 0.5 M SnF₂·3 M VOSO₄ and 3.8 kW kg⁻¹ (1.5 kW L⁻¹) for separated 1 M SnF₂|VOSO₄, the power enhancement of *ca.* 138% by separating the catholyte and anolyte is promising as seen more clearly when using a Ragone plot applying various normalization methods (ESI,† Fig. S5).

Fig. 2A shows the long-term stability of the optimized SnF₂|VOSO₄ system in a full-cell configuration by GCPL mode; the cell was charged to 1.4 V and discharged to 0 V at 1 A g⁻¹. After a rapid performance degradation after 100 cycles, the system exhibited a stable performance over 6500 cycles (*ca.* 40 days) showing a 20% capacitance loss as compared to the stabilized value after 100 cycles (75.7 mA h g⁻¹ or 46 W h kg⁻¹) with almost 100% Coulombic efficiency throughout the test. The initial performance degradation might have been caused by the pore volume reduction *via* formation of irreversible solid phase since post mortem GSA (Fig. 3A and B) shows slightly lower pore volume from the positive and the negative electrodes as compared to the pristine electrode. The inset shows the GCPL curves obtained after the stabilization period. The small *iR* drop (*ca.* 42 mV; ESI† Fig. S4B) assures that the actual stability

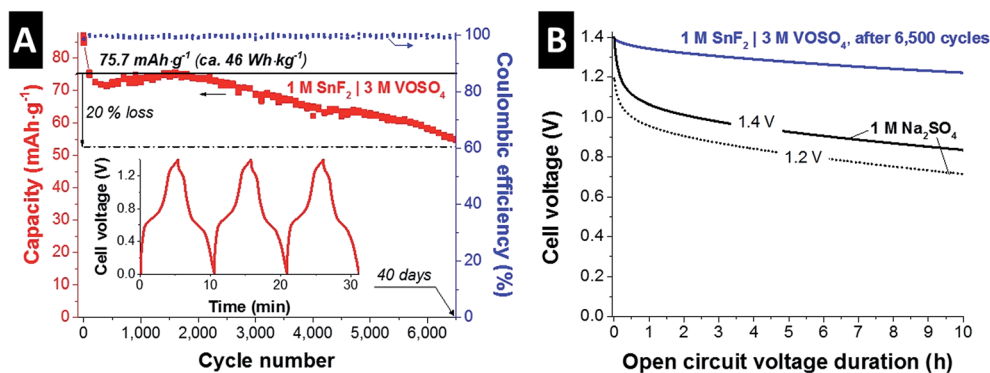


Fig. 2 (A) Cycling stability test for 1 M $\text{SnF}_2|3 \text{ M VOSO}_4$ system in 1 M H_2SO_4 . A full-cell was charged (1.4 V) and discharged (0 V) at 1 A g^{-1} . Inset shows the GCPL curves for three initial cycles. (B) Self-discharging performance obtained from 1 M $\text{SnF}_2|3 \text{ M VOSO}_4$ system in 1 M H_2SO_4 and a double-layer capacitor (1 M Na_2SO_4) which was charged up to 1.2 V and 1.4 V.

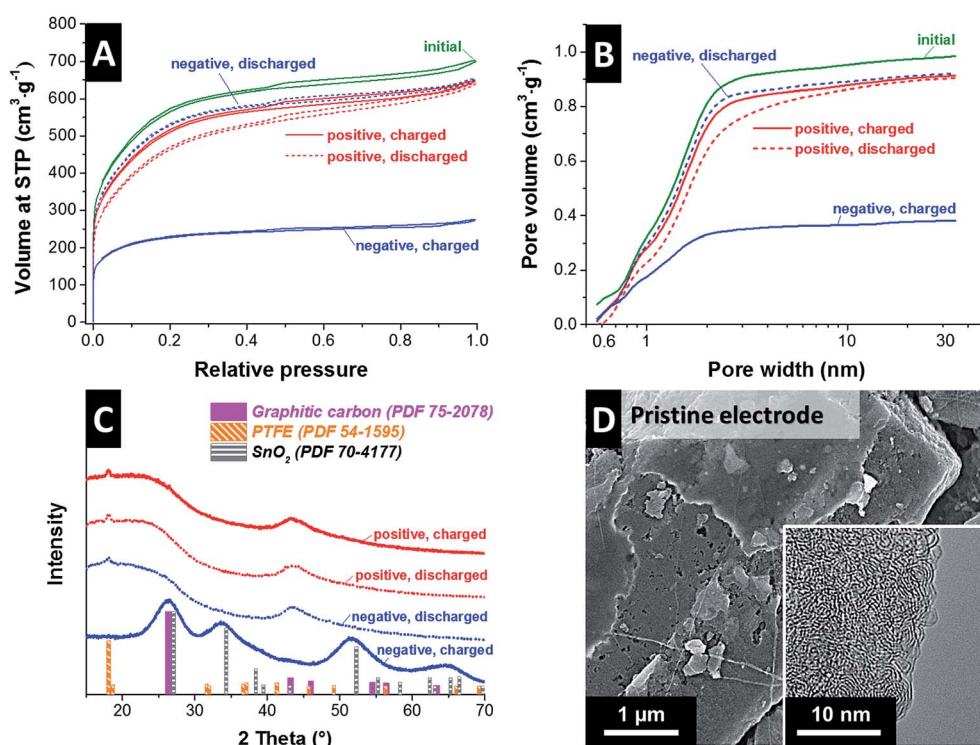


Fig. 3 Nitrogen gas sorption isotherms (A) and cumulative pore volume (B) as well as X-ray diffractograms obtained for the negative and positive electrodes for 1 M $\text{SnF}_2|3 \text{ M VOSO}_4$ system in 1 M H_2SO_4 after electrochemical operations (C). (D) Scanning electron micrograph and transmission electron micrograph (inset) of the carbon electrode before electrochemical testing.

window applied for the stability test was close to 1.4 V.⁴² As compared to the reported long-term stability of the other redox electrolyte hybrid energy storage systems,¹² capacity retention over 80% after 6500 cycles is promising.

Fig. 2B shows the self-discharging (voltage decay) performance of the $\text{SnF}_2|\text{VOSO}_4$ system compared to a conventional double-layer capacitor system (1 M Na_2SO_4). Aqueous electric double-layer capacitors suffer from high self-discharging rate; yet, not the entire voltage decay is caused by actual loss of charge, but is associated with ion redistribution and consequently there is a dependency of the charging duration prior to

open circuit operation.^{43–46} In case of aqueous 1 M Na_2SO_4 , we see a rapid, initial voltage decay after charging to 1.2 V or 1.4 V, most likely linked to ion redistribution. Over time, the slope decreases and a continued linear voltage decrease is caused by actual self-discharging (loss of charge rather than just loss of voltage). In case of 1 M $\text{SnF}_2|3 \text{ M VOSO}_4$, the potential loss is significantly lower than that of 1 M Na_2SO_4 ; 87% potential retention for 1 M $\text{SnF}_2|3 \text{ M VOSO}_4$ after 10 h and 60% (both 1.2 V and 1.4 V) for 1 M Na_2SO_4 as compared to the initial potential. The lower level of the potential loss can be since the hybrid system has more battery-like feature than that of

double-layer capacitors as also demonstrated in our earlier works.^{12,21}

Post mortem analysis of electrodes after using the SnF_2 /VOSO₄ redox electrolyte system

So far, we have shown the improved power handling performance by using a system with separated electrolytes (SnF_2 /VOSO₄) as compared to the mixed electrolyte system ($\text{SnF}_2 \cdot \text{VOSO}_4$). Yet, the mechanism triggering the power enhancement needs further clarification. For the first step, post mortem nitrogen gas sorption analysis was carried out for the positive and negative electrodes which were electrochemically operated in a full-cell to have different charge states (charged state: cell voltage of 1.4 V;

discharged state: cell voltage of 0 V). The activated carbon electrode before the electrochemical operation exhibits a type I(b) isotherm; the high amount of adsorbed nitrogen at very low pressures indicates a predominantly microporous system with pore sizes below 2 nm (Fig. 3A). The pore size distribution pattern calculated by DFT confirm that most pores of the pristine carbon electrode are below 3 nm (Fig. 3B).

All nitrogen gas sorption isotherms of the operated positive and negative electrode are of a similar shape as the pristine activated carbon electrode (Fig. 3A). The only main difference lies within changes in the total pore volume (*i.e.*, total amount of adsorbed nitrogen). Therefore, the pore structure of the operated electrodes does not seem to be significantly changed

Table 1 Summary of the nitrogen gas sorption analysis from the negative and positive electrodes, and the pristine electrode made of YP-80F type activated carbon and PTFE binder. The post mortem analysis was applied to full-cells exposed to a cell voltage of 1.4 V (charged state) or 0 V (discharged state) with separated electrolytes

Sample	SSA DFT (m ² g ⁻¹)	SSA BET (m ² g ⁻¹)	Average pore size (nm)	Total pore volume (cm ³ g ⁻¹)	Volume of micropores (cm ³ g ⁻¹)
Initial	1648	2094	1.4	1.05	0.81
Negative, charged	717	837	1.2	0.41	0.33
Negative, discharged	1449	1909	1.4	0.97	0.75
Positive, charged	1426	1864	1.4	0.97	0.73
Positive, discharged	1261	1703	1.5	0.96	0.64

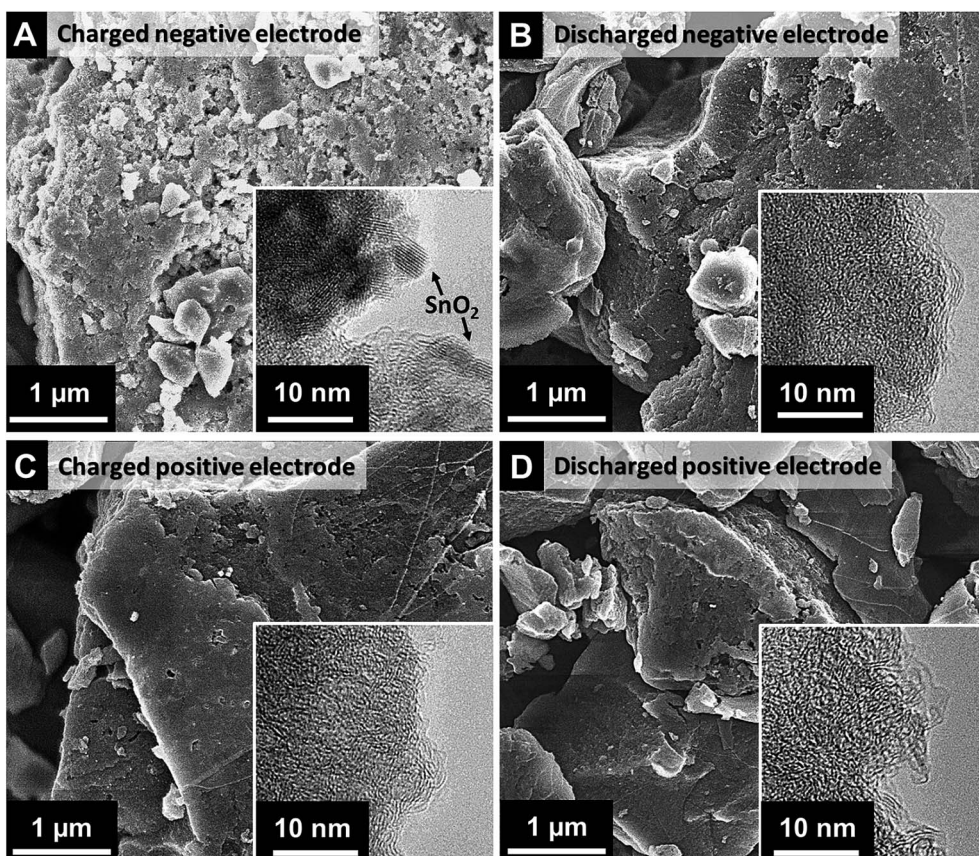


Fig. 4 Post mortem analysis by SEM and TEM (inset) for the positive and negative electrode in charged and discharged state in 1 M SnF_2 /3 M VOSO₄ in 1 M H_2SO_4 system.

Table 2 Atomic and mass fraction of the composition measured from the negative and positive electrodes obtained from EDX analysis

Sample	C (atom%)	C (mass%)	O (atom%)	O (mass%)	F (atom%)	F (mass%)	S (atom%)	S (mass%)	Sn (atom%)	Sn (mass%)
Initial	96.4 ± 0.5	95.1 ± 0.6	3.2 ± 0.3	4.2 ± 0.5	0.4 ± 0.2	0.7 ± 0.4	—	—	—	—
Negative, charged	78.4 ± 4.5	51.5 ± 8.4	13.0 ± 3.2	11.2 ± 2.2	2.6 ± 0.6	2.7 ± 0.8	0.5 ± 0.1	0.9 ± 0.2	5.4 ± 1.9	33.7 ± 7.9
Negative, discharged	95.6 ± 1.4	93.8 ± 1.9	3.5 ± 0.9	4.5 ± 1.2	0.8 ± 0.5	1.2 ± 0.8	0.2 ± 0.0	0.4 ± 0.1	—	—
Positive, charged	93.5 ± 0.8	91.2 ± 1.0	5.6 ± 0.7	7.6 ± 0.8	0.6 ± 0.3	±1.0 ± 0.5	0.1 ± 0.0	0.3 ± 0.1	—	—
Positive, discharged	94.3 ± 0.7	94.2 ± 0.9	5.0 ± 0.4	6.5 ± 0.6	0.6 ± 0.4	0.9 ± 0.6	0.1 ± 0.0	0.4 ± 0.1	—	—

with the only exception of the charged negative electrode. The latter exhibits the largest loss in pores of the size above 1 nm which implies the deposition of SnO₂ in the micro/mesopore space. This feature can be better seen when the pore volume is normalized and by assessing the different pore size distribution pattern (dV/dd) as shown in ESI,† Fig. S6A–C. In case of the charged negative electrode, the number of pores > 1 nm decreases compared to the pristine electrode (Table 1). This is in line with the growth of SnO₂, as previous studies have shown preferential oxide growth in pores above 1 nm.⁴⁷ The formation of a pore blocking, non-carbon phase (like SnO₂) also further supported by thermogravimetric analysis and the occurrence of a significant residual mass after heat treatment in synthetic air up to 900 °C (ESI,† Fig. S6D).

Post mortem XRD analysis reveals that loss in pore volume in the charged negative electrode was caused by rutile-type SnO₂ formation (Fig. 3C). All other samples showed no indication of SnO₂ and the corresponding XRD pattern only exhibited signals from amorphous carbon and PTFE binder. The very broad peak width SnO₂ is related to a very small domain size of *ca.* 2 nm which further supports that the tin dioxides are formed in the pores with the size over 1 nm.

For the detailed investigation on the SnO₂ formation, post mortem scanning and transmission electron micrographs were obtained. Apparently different morphologies of the electrode surface can be seen from SEM images for the negative electrode between charged and discharged state (Fig. 4A–B). As compared to the smooth morphology of the pristine electrode (Fig. 3D) and the discharged negative electrode (Fig. 4B), the charged negative electrode (Fig. 4A) exhibits relatively rough surface most probably due to SnO₂ formation. As obtained from the post mortem EDX analysis, the atomic percent of oxygen to tin ratio (*ca.* 2.4, Table 2) further confirms the stoichiometry of SnO₂ (excess oxygen correlates with oxygen-containing carbon functional groups). No tin was found by EDX analysis for the discharged negative electrode nor charged and discharged positive electrode. This indicates that metallic tin is reversibly dissolved and the electrolyte separation *via* the ion exchange membrane is effectively functioning. The electron micrograph from TEM (Fig. 3A, inset) shows the presence of distributed SnO₂ nanocrystals in the size range of 2–4 nm and rutile-type SnO₂ is further confirmed by the SAED pattern (see ESI,† Fig. S7). From the positive electrode in both charged and discharged state as well as the discharged negative electrode, no SnO₂ was found in TEM images or SAED patterns.⁴⁸ Thus, the results from the post mortem analyses show the presence of

SnO₂ (Sn[IV]) nanocrystals only at the charged negative electrode in intraparticle micro/mesopores and interparticle macropores.

Conclusion

We have demonstrated that the tin and vanadium complex mixture electrolyte shows limited power performance due to pore blocking of the positive electrode *via* tin oxide formation, as proven by post mortem gas sorption, XRD, and electron microscopy analyses. To prevent tin oxide formation at the positive electrode, a system with separated electrolytes was demonstrated, namely SnF₂ + H₂SO₄ solution as anolyte and VOSO₄ + H₂SO₄ solution as catholyte. As the anion exchange membrane effectively prevents the mixing of the electrolytes, no significant level of pore blocking occurred at the positive electrode during cycling. Therefore, a high specific power (3.8 kW kg⁻¹ or 1.5 kW L⁻¹) was achieved with the 1 M SnF₂|3 M VOSO₄ system while providing still a high specific energy up to 58.4 W h kg⁻¹ (23.4 W h L⁻¹). This system also showed a highly promising cycling stability over 6500 cycles with a capacity retention over 80%.

Acknowledgements

We acknowledge funding from the German Federal Ministry for Research and Education (BMBF) in support of the nanoEES^{3D} project (award number 03EK3013) as part of the strategic funding initiative energy storage framework. The authors thank Prof. Eduard Arzt (INM) for his continuing support, FuMA-Tech (esp. Dr Bauer and Dr Klicpera) for kindly providing membranes and helpful discussions. We also thank Dr Choonsoo Kim, Sathyamoorthi Sethuraman, Pattarachai Srimuk, and Dr Soumyadip Choudhury (all at INM) for useful discussions.

References

- 1 P. Simon and Y. Gogotsi, *Nat. Mater.*, 2008, 7, 845–854.
- 2 B. Dunn, H. Kamath and J.-M. Tarascon, *Science*, 2011, 334, 928–935.
- 3 B. Akinwolemiwa, C. Peng and G. Z. Chen, *J. Electrochem. Soc.*, 2015, 162, A5054–A5059.
- 4 S. T. Senthilkumar, R. K. Selvan and J. S. Melo, *J. Mater. Chem. A*, 2013, 1, 12386–12394.
- 5 E. Frackowiak, M. Meller, J. Menzel, D. Gastol and K. Fic, *Faraday Discuss.*, 2014, 172, 179–198.

- 6 Q. Li, K. Li, C. Sun and Y. Li, *J. Electroanal. Chem.*, 2007, **611**, 43–50.
- 7 G. Lota and E. Frackowiak, *Electrochem. Commun.*, 2009, **11**, 87–90.
- 8 S. Roldán, C. Blanco, M. Granda, R. Menéndez and R. Santamaría, *Angew. Chem., Int. Ed.*, 2011, **50**, 1699–1701.
- 9 D. Gastol, J. Walkowiak, K. Fic and E. Frackowiak, *J. Power Sources*, 2016, **326**, 587–594.
- 10 M. Zeiger, D. Weingarth and V. Presser, *ChemElectroChem*, 2015, **2**, 1117–1127.
- 11 L. Chen, H. Bai, Z. Huang and L. Li, *Energy Environ. Sci.*, 2014, **7**, 1750–1759.
- 12 J. Lee, S. Choudhury, D. Weingarth, D. Kim and V. Presser, *ACS Appl. Mater. Interfaces*, 2016, **8**, 23676–23687.
- 13 Y. Tian, J. Yan, R. Xue and B. Yi, *J. Electrochem. Soc.*, 2011, **158**, A818–A821.
- 14 L. H. Su, L. Y. Gong and Y. Zhao, *Phys. Chem. Chem. Phys.*, 2014, **16**, 681–684.
- 15 L. H. Su, X. G. Zhang, C. H. Mi, B. Gao and Y. Liu, *Phys. Chem. Chem. Phys.*, 2009, **11**, 2195–2202.
- 16 A. Shanmugavani, S. Kaviselvi, K. V. Sankar and R. K. Selvan, *Mater. Res. Bull.*, 2015, **62**, 161–167.
- 17 Z. J. Zhang, Y. Q. Zhu, X. Y. Chen and Y. Cao, *Electrochim. Acta*, 2015, **176**, 941–948.
- 18 H. Yu, J. Wu, L. Fan, S. Hao, J. Lin and M. Huang, *J. Power Sources*, 2014, **248**, 1123–1126.
- 19 J. Wu, H. Yu, L. Fan, G. Luo, J. Lin and M. Huang, *J. Mater. Chem.*, 2012, **22**, 19025–19030.
- 20 E. Frackowiak, K. Fic, M. Meller and G. Lota, *Chemosuschem*, 2012, **5**, 1181–1185.
- 21 J. Lee, B. Krüner, A. Tolosa, S. Sathyamoorthi, D. Kim, S. Choudhury, K.-H. Seo and V. Presser, *Energy Environ. Sci.*, 2016, **9**, 3392–3398.
- 22 B. Krüner, J. Lee, N. Jäckel, A. Tolosa and V. Presser, *ACS Appl. Mater. Interfaces*, 2016, **8**, 9104–9115.
- 23 S.-E. Chun, B. Evanko, X. Wang, D. Vonlanthen, X. Ji, G. D. Stucky and S. W. Boettcher, *Nat. Commun.*, 2015, **6**, 7818.
- 24 B. Evanko, S. J. Yoo, S.-E. Chun, X. Wang, X. Ji, S. W. Boettcher and G. D. Stucky, *J. Am. Chem. Soc.*, 2016, **138**, 9373–9376.
- 25 L.-Q. Mai, A. Minhas-Khan, X. Tian, K. M. Hercule, Y.-L. Zhao, X. Lin and X. Xu, *Nat. Commun.*, 2013, **4**, 2923.
- 26 R. Narayanan and P. R. Bandaru, *J. Electrochem. Soc.*, 2014, **162**, A86–A91.
- 27 A. Z. Weber, M. M. Mench, J. P. Meyers, P. N. Ross, J. T. Gostick and Q. Liu, *J. Appl. Electrochem.*, 2011, **41**, 1137–1164.
- 28 A. Laheäär, P. Przygocki, Q. Abbas and F. Béguin, *Electrochem. Commun.*, 2015, **60**, 21–25.
- 29 K. Fic, M. Meller and E. Frackowiak, *J. Electrochem. Soc.*, 2015, **162**, A5140–A5147.
- 30 S. Brunauer, P. H. Emmett and E. Teller, *J. Am. Chem. Soc.*, 1938, **60**, 11.
- 31 G. Y. Gor, M. Thommes, K. A. Cychosz and A. V. Neimark, *Carbon*, 2012, **50**, 1583–1590.
- 32 J. Lee, D. Weingarth, I. Grobelsek and V. Presser, *Energy Technol.*, 2015, **4**, 75–84.
- 33 D. Weingarth, M. Zeiger, N. Jäckel, M. Aslan, G. Feng and V. Presser, *Adv. Energy Mater.*, 2014, **4**, 1400316.
- 34 V. Presser, J. McDonough, S. H. Yeon and Y. Gogotsi, *Energy Environ. Sci.*, 2011, **4**, 3059–3066.
- 35 J. D. Donaldson and W. Moser, *J. Chem. Soc.*, 1960, **789**, 4000–4003.
- 36 W. B. Schaap, J. A. Davis and W. H. Nebergall, *J. Am. Chem. Soc.*, 1954, **76**, 5226–5229.
- 37 F. Séby, M. Potin-Gautier, E. Giffaut and O. F. X. Donard, *Geochim. Cosmochim. Acta*, 2001, **65**, 3041–3053.
- 38 A. J. Berry, *Qualitative Inorganic Analysis*, Cambridge University Press, 2016.
- 39 B. Giannetti, P. Sumodjo and T. Rabockai, *J. Appl. Electrochem.*, 1990, **20**, 672–676.
- 40 S. S. Abd El Rehim, H. H. Hassan and N. F. Mohamed, *Corros. Sci.*, 2004, **46**, 1071–1082.
- 41 B. Stirrup and N. Hampson, *Surf. Technol.*, 1977, **5**, 429–462.
- 42 D. Weingarth, A. Foelske-Schmitz and R. Kötz, *J. Power Sources*, 2013, **225**, 84–88.
- 43 M. Kaus, J. Kowal and D. U. Sauer, *Electrochim. Acta*, 2010, **55**, 7516–7523.
- 44 J. Kowal, E. Avaroglu, F. Chamekh, A. Šenfelds, T. Thien, D. Wijaya and D. U. Sauer, *J. Power Sources*, 2011, **196**, 573–579.
- 45 L. García-Cruz, P. Ratajczak, J. Iniesta, V. Montiel and F. Béguin, *Electrochim. Acta*, 2016, **202**, 66–72.
- 46 H. A. Andreas, *J. Electrochem. Soc.*, 2015, **162**, A5047–A5053.
- 47 S. Fleischmann, N. Jäckel, M. Zeiger, B. Krüner, I. Grobelsek, P. Formanek, S. Choudhury, D. Weingarth and V. Presser, *Chem. Mater.*, 2016, **28**, 2802–2813.
- 48 N. Jäckel, D. Weingarth, A. Schreiber, B. Krüner, M. Zeiger, A. Tolosa, M. Aslan and V. Presser, *Electrochim. Acta*, 2016, **191**, 284–298.

Supporting Information

Asymmetric tin-vanadium redox electrolyte for hybrid energy storage with nanoporous carbon electrodes

Juhan Lee,^{a,b} Aura Tolosa,^{a,b} Benjamin Krüner,^{a,b} Nicolas Jäckel,^{a,b}
Simon Fleischmann,^b Marco Zeiger,^{a,b} Daekyu Kim,^{a,c} Volker Presser^{a,b,*}

^a INM – Leibniz Institute for New Materials, Campus D2 2, 66123 Saarbrücken, Germany

^b Department of Materials Science and Engineering, Saarland University, Campus D2 2, 66123 Saarbrücken, Germany

^c School of Energy, Materials and Chemical Engineering, Korea University of Technology and Education, Chungjeol-ro 1600, 31253 Cheonan, Republic of Korea

* Corresponding author's eMail: volker.presser@leibniz-inm.de

Electrochemical performance of the $\text{SnSO}_4\text{-VO}_2$ redox electrolyte system with activated carbon electrodes

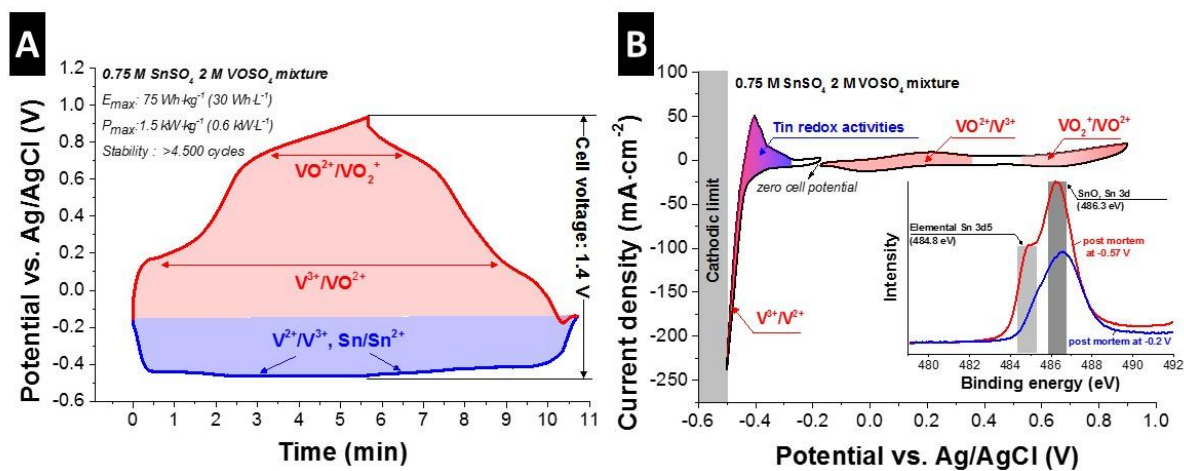


Figure S1: (A) The potential development of the positive and the negative electrodes obtained from 0.75 M SnSO_4 2 M VOSO_4 mixture system in $0.1\text{ M H}_2\text{SO}_4$. (B) The cyclic voltammograms obtained for 0.75 M SnSO_4 2 M VOSO_4 system in $0.1\text{ M H}_2\text{SO}_4$ in the potential range of either the negative or the positive electrode. The inset shows the post mortem XPS data from the negative electrode charged at -0.57 V and -0.2 V . For more information on this system, also see Ref. ¹.

Post mortem analysis of activated carbon electrodes operated with the SnSO_4 - VO_2 redox electrolyte system

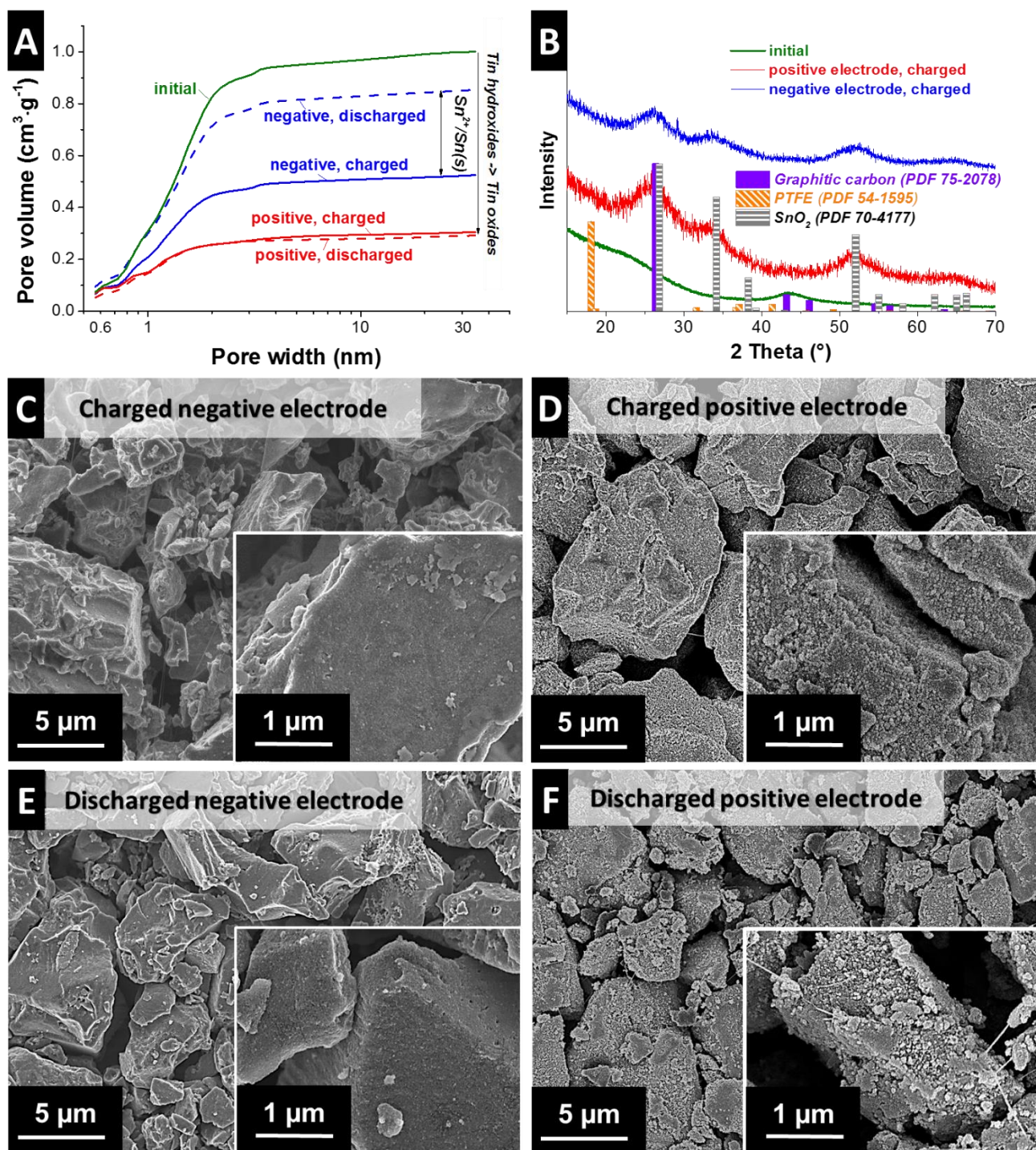


Figure S2: Post mortem analyses of electrodes operated using 0.75 M SnSO_4 2 M VO_2 mixture electrolyte. (A) Pore size distribution pattern calculated by quenched solid density functional theory analysis of nitrogen sorption data. (B) X-ray diffraction patterns. (C-F) Scanning electron micrographs.

Three-electrode experiments (half-cell)

For the three-electrode half-cell experiments, a spring-loaded two-piston cell was used with Ag/AgCl reference electrode (saturated, 3 M NaCl). As current collectors, two graphite pistons were applied for the working and counter electrodes while GF/A glassy fiber filter (Whatman) was located in between to prevent the short circuit and to reserve electrolyte. Working electrode was prepared with 4 mm diameter and 200 μm thickness while a double stack of porous carbon electrode was used as counter electrode (12 mm diameter, 500 μm thickness).

Figure S3B shows the reversible hydrogen storage at the carbon micropores (YP-80F activated carbon bound with 5 mass% PTFE) as the potential is scanned from -0.5 V to +0.6 V. At a potential lower than -0.5 V, hydrogen storage does not seem to be reversible anymore.

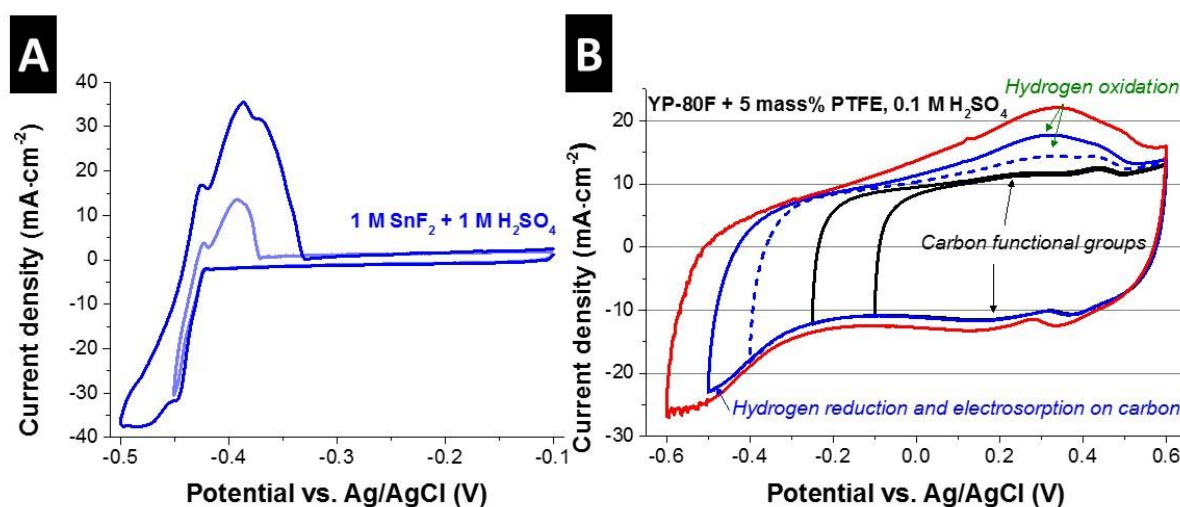


Figure S3: Cyclic voltammograms of 1 M SnF₂ + 1 M H₂SO₄ system (A) and 0.1 M H₂SO₄ system (B) at 1 mV·s⁻¹.

Rate behavior and the cycling stability test with full cell configuration

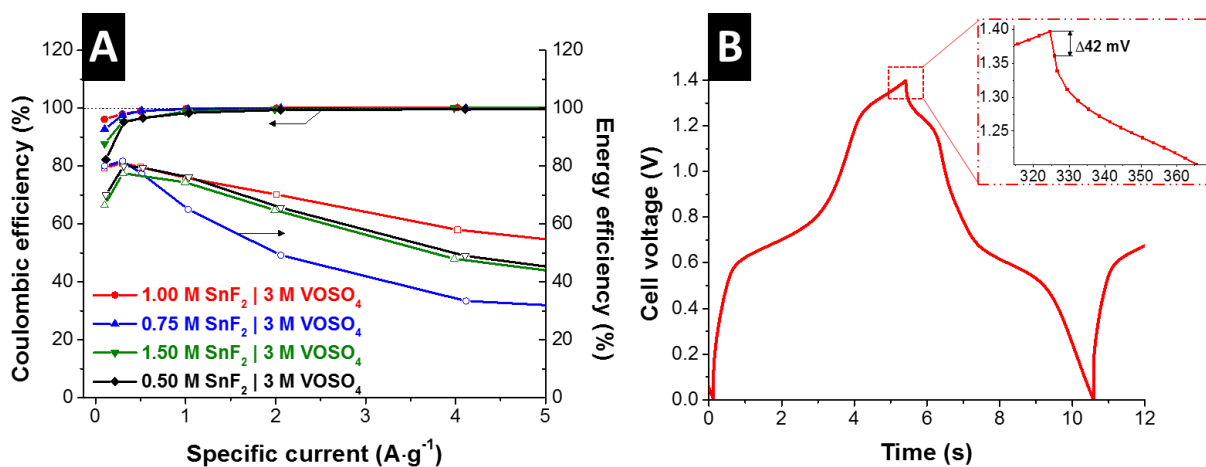


Figure S4: (A) Coulombic and energy efficiency of the asymmetric electrolyte system with SnF₂ and VOSO₄ in 1 M H₂SO₄ at various specific current. (B) GCPL curves obtained after applying 100 cycles at 1 A·g⁻¹. The inset shows the iR drop.

Ragone plot

For the gravimetric Ragone plot (**Figure S5A**), the values are normalized to the active mass of the electrode excluding the mass of the separator, electrolyte, current collector, and device outer housing. However, this active mass normalization can mislead when the values are compared to that of commercial products which are generally normalized by the total device mass. For a fair comparison, a wet normalization was suggested which considers the mass of the electrolyte and electrode.² The suggested normalization technique requires the skeletal density of the electrode and the electrolyte density which allows the calculation of the electrolyte mass which are confined in porous carbon electrode. Following the procedures described in Ref.², the maximum specific energy for the asymmetric electrolyte system (1 M SnF₂ | 3 M VOSO₄) is calculated to be around 17.2 Wh·kg⁻¹. On the contrary, when the performance of a double-layer capacitor (1 M Na₂SO₄) is normalized to the mass of the electrode and electrolyte, the specific energy is only about 1.2 Wh·kg⁻¹.

For the volumetric Ragone plot (**Figure S5B**), the values are normalized to the volume of the electrode, separator, and electrolyte.

For the areal Ragone plot (**Figure S5C**), the values are normalized to the area of the separator in the cell. The specific energy of the asymmetric electrolyte system (1 M SnF₂ | 3 M VOSO₄) is about 12 times higher than that of a double layer capacitor (1 M Na₂SO₄). This indicates that the use of anion exchange membrane is beneficial in terms of specific energy despite its high price as long as the price of the anion exchange membrane does not exceed the 12-fold price of the conventional porous separator applied for double-layer capacitors.

The promising features of the asymmetric electrolyte system (1 M SnF₂ | 3 M VOSO₄) can be seen in all Ragone plots with various normalizations exhibiting significant enhancement for energy storage while keeping a high power performance close to that of a double-layer capacitor (1 M Na₂SO₄).

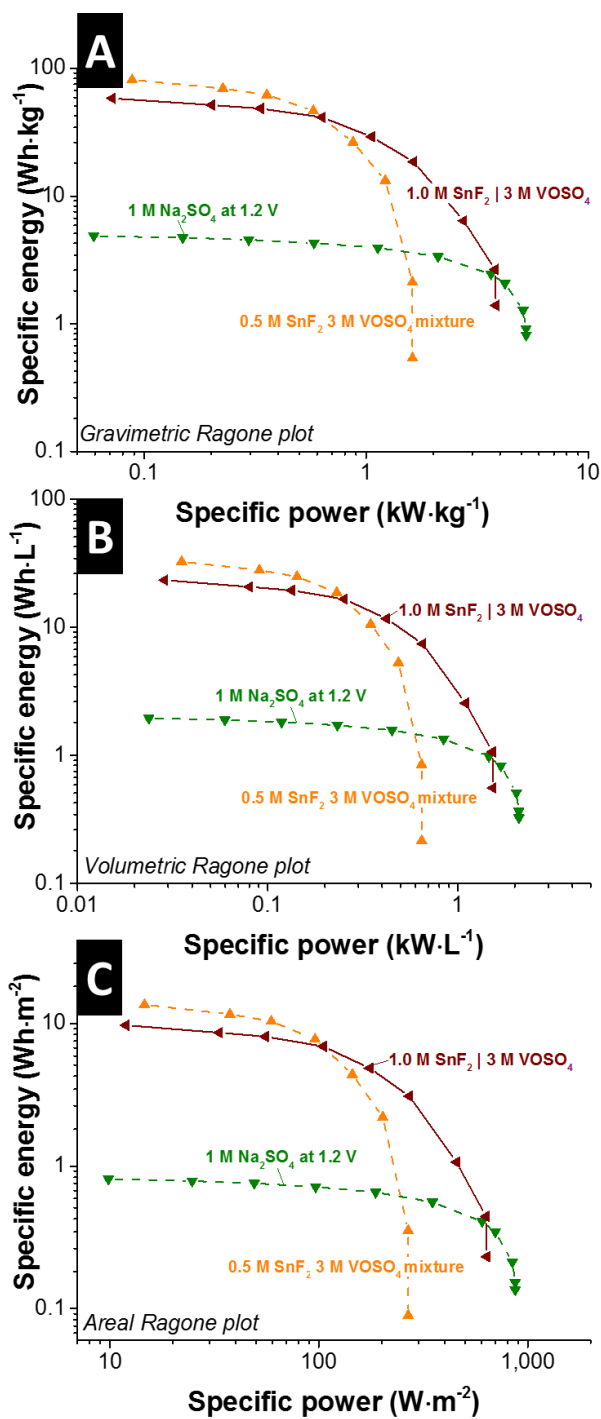


Figure S5: Ragone plot for the comparison of a mixture electrolyte (0.5 M SnF₂ 3 M VOSO₄ mixture), asymmetric electrolyte (1 M SnF₂ | 3 M VOSO₄), and a double layer capacitor (1 M Na₂SO₄) with gravimetric (A), volumetric (B), and areal (C) normalization.

Pore distribution from nitrogen gas sorption and thermogravimetric analysis

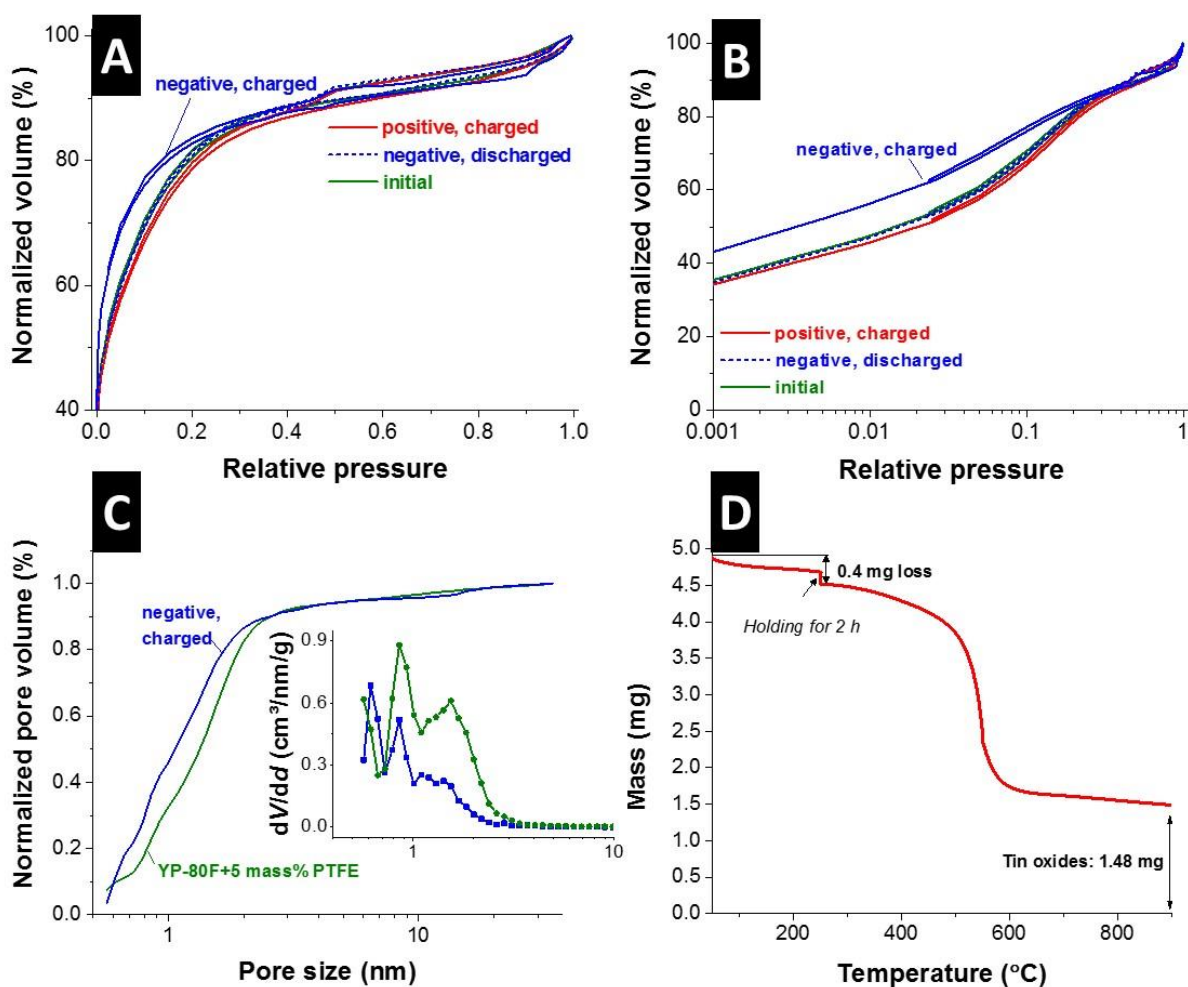


Figure S6: Normalized isotherms in different scales (A-B) and normalized cumulative pore volume vs. pore size plot (C) as normalized to the maximum value of each samples while the inset shows the dV/dd plot. (D) Mass loss data for charged negative electrode from thermogravimetric analysis is plotted as a function of applied temperature. At 200 °C, the temperature was held for 2 h.

Selected area electron diffraction (SAED)

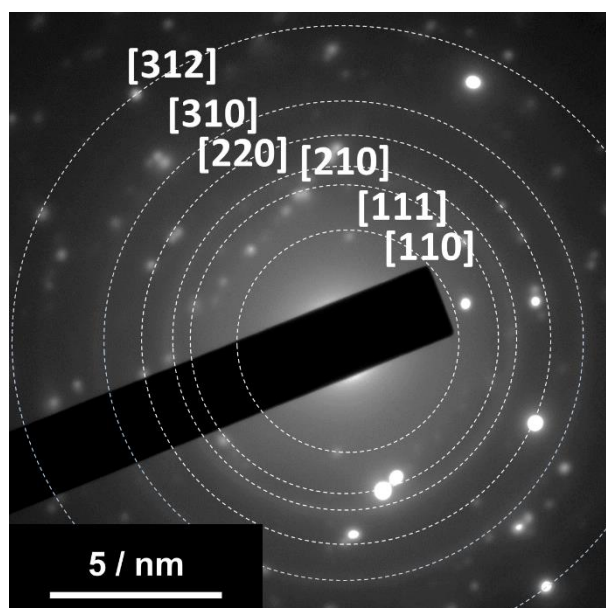


Figure S7: Selective area diffraction patterns obtained for the negative electrode in charged state for 1 M SnF₂ | 3 M VOSO₄ in 1 M H₂SO₄ system. The indices correspond with rutile-type SnO₂ planes.

Supporting references

1. Lee, J.; Krüner, B.; Tolosa, A.; Sathyamoorthi, S.; Kim, D.; Choudhury, S.; Seo, K.-H.; Presser, V., Tin/vanadium redox electrolyte for battery-like energy storage capacity combined with supercapacitor-like power handling. *Energ Environ Sci* **2016**, 9, (11), 3392-3398.
2. Chun, S.-E.; Evanko, B.; Wang, X.; Vonlanthen, D.; Ji, X.; Stucky, G. D.; Boettcher, S. W., Design of aqueous redox-enhanced electrochemical capacitors with high specific energies and slow self-discharge. *Nat Commun* **2015**, 6.

3.6. Porous carbon as a quasi-reference electrode in aqueous electrolytes

**Juhan Lee,^{1,2} Nicolas Jäckel,^{1,2} Daekyu Kim,^{1,3} Mathias Widmaier,^{2,5}
Sethuraman Sathyamoorthi,^{1,4} Pattarachai Srimuk,^{1,2} Simon Fleischmann,²
Marco Zeiger,^{1,2} and Volker Presser^{1,2,*}**

¹ INM - Leibniz Institute for New Materials, Campus D2 2, 66123 Saarbrücken, Germany

² Saarland University, Campus D2 2, 66123 Saarbrücken, Germany

³ School of Energy, Materials and Chemical Engineering, Korea University of Technology and Education, Chungjeol-ro 1600, 31253, Cheonan, Republic of Korea

⁴ Electrochemical Process Engineering Division, CSIR-Central Electrochemical Research Institute, Karaikudi, 630 006, India

⁵ Robert Bosch GmbH, Postfach 10 60 50, 70049 Stuttgart, Germany

Citation:

Lee, J.; Jäckel, N.; Kim, D.; Widmaier, M.; Sathyamoorthi, S.; Srimuk, P.; Kim, C.; Fleischmann, S.; Zeiger, M.; Presser, V., Porous carbon as a quasi-reference electrode in aqueous electrolytes. *Electrochimica Acta* **2016**, 222, 1800-1805.

Own contributions:

Design, planning, writing, cell design, experimental plan, electrochemical analyses

Abstract

This study examines the performance of porous carbon as quasi-reference electrode (QRE) in aqueous media and evaluates their suitability. The performance of activated carbon and carbon black as QRE was investigated in acidic (H₂SO₄) and neutral (Na₂SO₄, NaCl, Li₂SO₄) solutions and compared to platinum metal wire and Ag/AgCl reference electrode. In neutral and acidic electrolyte, the porous carbon based QREs exhibited a notable stability and reliability with low level of potential drift (1 mV per day) and potential deviation of less than 10 mV. These results can contribute to the further development in porous carbon based QREs leading to novel opportunities in electrochemical analysis.



Porous carbon as a quasi-reference electrode in aqueous electrolytes

J. Lee^{a,b,1}, N. Jäckel^{a,b,1}, D. Kim^{a,c}, M. Widmaier^{b,e}, S. Sathyamoorthi^{a,d}, P. Srimuk^{a,b},
C. Kim^a, S. Fleischmann^b, M. Zeiger^{a,b}, V. Presser^{a,b,*}

^a INM – Leibniz Institute for New Materials, 66123 Saarbrücken, Germany

^b Department of Materials Science and Engineering, Saarland University, 66123 Saarbrücken, Germany

^c School of Energy, Materials, and Chemical Engineering, Korea University of Technology and Education, Cheonan 330-708, Republic of Korea

^d Electrochemical Process Engineering Division, CSIR-Central Electrochemical Research Institute, Karaikudi, 630 006, India

^e Robert Bosch GmbH, Postfach 10 60 50, 70049 Stuttgart, Germany

ARTICLE INFO

Article history:

Received 21 September 2016

Received in revised form 24 November 2016

Accepted 25 November 2016

Available online 26 November 2016

Keywords:

acidic solution
aqueous solution
quasi-reference electrode
redox electrolytes
supercapacitors

ABSTRACT

This study examines the performance of porous carbon as quasi-reference electrode (QRE) in aqueous media and evaluates their suitability. The performance of activated carbon and carbon black as QRE was investigated in acidic (H₂SO₄) and neutral (Na₂SO₄, NaCl, Li₂SO₄) solutions and compared to platinum metal wire and Ag/AgCl reference electrode. In neutral and acidic electrolyte, the porous carbon based QREs exhibited a notable stability and reliability with low level of potential drift (1 mV per day) and potential deviation of less than 10 mV. These results can contribute to the further development in porous carbon based QREs leading to novel opportunities in electrochemical analysis.

© 2016 Elsevier Ltd. All rights reserved.

1. Introduction

Aqueous media are attracting much attention in the advancement of electrochemical energy storage technologies due to their lower cost, environmental friendliness, and high operation safety [1,2]. However, in energy storage systems using aqueous media, electrochemical analysis has suffered from the lack of a suitable reference electrodes (RE) [3] because the conventional REs including standard hydrogen electrodes, silver/silver chloride, and saturated calomel electrodes trigger analytical inaccuracy in aqueous media. These result from liquid junction potential due to the boundary between two solutions, contamination of the electrolyte in the RE through diffusion, instability for large pressures and high temperatures, and difficulties in miniaturizing the cell design, particularly micro cell design [3–5].

In order to overcome the limitation of conventional REs, platinum (Pt) and polytetrafluoroethylene (PTFE) bound porous carbon film electrodes as quasi-reference electrodes (QREs) have emerged as alternatives. In general, QREs do not provide a reference potential which can be universally applied to various

solutions; however, they could exhibit a reproducible and stable reference potential, while the absolute potential varies from solution to solution. When the reference potential of a QRE is calibrated and validated by applying an internal reference like the ferrocene/ferrocenium (Fc/Fc⁺) redox couple, the QRE can be effectively applied to the system where the use of the conventional reference electrodes is limited or impossible [6]. Although platinum (Pt) has been considered as a promising QRE [3,4,7–9], its application as QRE was, unfortunately, limited because of unexpected potential drift based on electrochemical condition changes, such as surface oxidation processes [3,5]. On the other hand, the PTFE bound porous carbon film electrodes have successfully demonstrated remarkably stable and reliable performance with potential shifts below 1 mV per day in organic media and ionic liquids [7,8]. Nevertheless, there has been no systematic study investigating the long-term stability and the accuracy of porous carbon as QRE in aqueous electrolytes, and thus, the effective use of PTFE bound porous carbon film electrodes as QRE in electrochemical analysis is inhibited. Therefore, the aim of this study is to examine the feasibility of porous carbons bound with PTFE as QRE in aqueous media.

* Corresponding author at: INM – Leibniz Institute for New Materials, 66123 Saarbrücken, Germany.

E-mail address: volker.presser@leibniz-inm.de (V. Presser).

¹ ISE member.

2. Experimental

2.1. Materials

The electrolytes were prepared in deionized water with sulfuric acid (1 M H₂SO₄, 95–98 % purity), sodium sulfate (1 M Na₂SO₄, ≥99.0% purity), sodium chloride (1 M NaCl, ≥99.0% purity), and lithium sulfate (1 M Li₂SO₄, ≥99.0% purity). Potassium ferricyanide (K₃[Fe(CN)]₆, ≥99.0% purity) was added as a trace redox media for the pH neutral electrolytes with 0.1 M concentration.

For the free-standing flexible electrodes, two different carbon materials were employed: type YP80-F activated carbon (Kuraray, called AC) and type ENSACO350 carbon black (Imerys Graphite & Carbon, called CB). The carbon powder was mixed with ethanol and PTFE, rolled, and dried in a vacuum oven at 120 °C for 48 h at 2·10³ Pa. The mass ration of carbon to PTFE was 95:5 for the AC electrode and 90:10 for the CB electrode.

2.2. Material characterization

Elemental chemical analysis was performed with a Vario Micro Cube (Elementar GmbH) by pressing the powder carbon samples into tin boats. The temperature of the reduction tube was 850 °C and the combustion tube was heated to 1150 °C. An average chemical composition of three measurements was determined for each powder. The oxygen content was calculated by difference. Calibration was performed by five times measuring sulfanilamide with known elemental composition.

Nitrogen gas sorption measurements were carried out with an Autosorb iQ system (Quantachrome) at the temperature of liquid nitrogen (−196 °C) after degassing at 100 Pa and 150 °C for 10 h. For the measurements, the relative pressure (P/P₀) was varied from 5·10^{−7} to 1.0 in 68 steps. The specific surface area (SSA) was calculated with the ASiQwin-software using the Brunauer-Emmett-Teller (BET) equation in the linear relative pressure range of 0.01–0.2. We also calculated the SSA and pore size distribution (PSD) via quenched-solid DFT (QSDFT) with assuming a slit pore shape model between 0.56 and 37.5 nm.

2.3. Electrochemical measurements

In neutral solution, a platinum disk (1.13 cm², 100 μm thickness) was employed as a working electrode (WE) with a Pt wire (1 mm diameter) current collector. A double stack of oversized AC film electrodes (1.13 cm², 500 μm for each electrode) with graphite current collectors was employed as counter electrode

(CE). In acidic solution, AC film electrodes with equal electrode thickness (200 μm) and mass (ca. 10 mg) were selected as WE and CEs with a graphite current collector.

In order to examine electrochemical properties, cyclic voltammetry was conducted with a VMP300 potentiostat/galvanostat (Bio-Logic) using custom-built cells with a three-electrode configuration (detailed description in Ref. [10]). A time-dependent reference potential was obtained from two cycles of cyclic voltammograms (CV), which were carried out every 30 min for the first 10 h and every 1 h for the rest of the operation. For some of the cells, a commercially available Ag/AgCl reference electrode (saturated in 3 M NaCl, BASi) was mounted at the side of the cell. The potential of the Ag/AgCl was measured vs. Hg/Hg₂SO₄ reference electrode (saturated K₂SO₄) to convert the measured potential containing liquid junction potential to the values vs. SHE.

3. Results and discussion

The nitrogen sorption isotherm at −196 °C of AC powder shows a type I(b) shape (Fig. 1A) being characteristic for microporous materials with pores smaller than 2.5 nm [11]. CB powder exhibits a mixture of type I(b) and type IV(b) shapes with a slight H4 hysteresis (characteristic for mesopores) indicating the material has predominantly both micro- and mesopores, and exhibits interparticle voids in the macropore range, as indicated by the strong nitrogen uptake close to atmospheric pressure [12]. The pore structure of the AC and CB carbon powder is shown in Fig. 1B. AC shows a high pore volume of 1.15 cm³ g^{−1} and a specific surface area (SSA) of 1756 m² g^{−1} by QSDFT having a majority of micropores (<2 nm) with a minor amount of mesopores. In case of CB, well distributed micro- and mesopores contribute to a slightly lower pore volume of 0.77 cm³ g^{−1} and much lower SSA (QSDFT) of 715 m² g^{−1} as compared to AC powder (Table 1). As demonstrated by Ruch et al. and Weingarth et al. [7,8], porous carbon with high specific surface area can be applied as QRE in organic solutions and ionic liquids with long-term reliability and stability. The reason for the high reliability and stability of the porous carbon QREs was explained by their high double-layer capacitance, which can reduce the potential shift of the QRE. For that reason, the high specific surface area of AC and CB is expected to be beneficial for also providing a reliable and stable QRE potential in aqueous electrolytes.

Fig. 2A shows the ferricyanide/ferrocyanide redox reaction examined by the CVs of Pt and Ag/AgCl RE. Around 60 h after cell assembly, the cathodic and anodic peak positions are shifted to the positive value for Pt QRE indicating that the reference potential (E_r)

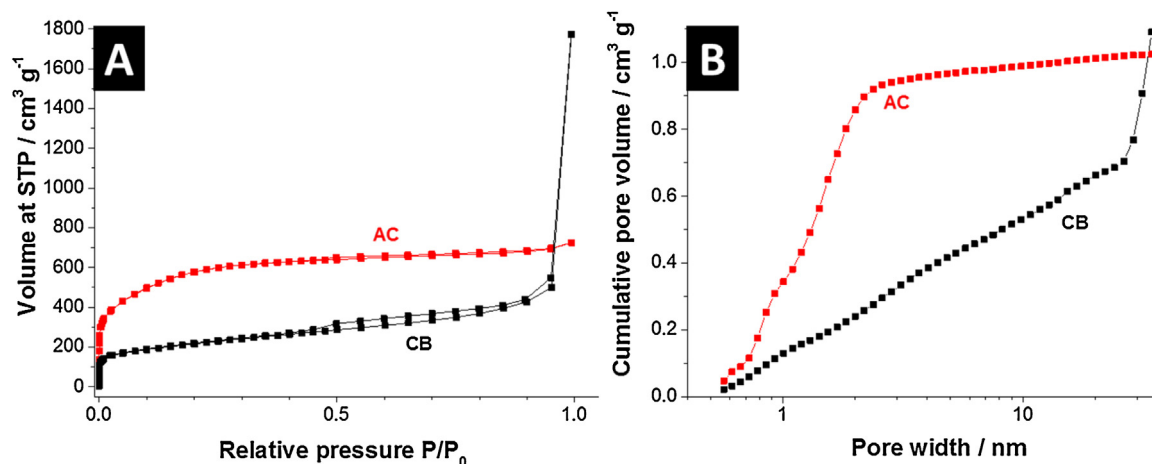


Fig. 1. Nitrogen sorption isotherms (A) and pore volume distribution (B) of AC and CB electrodes.

Table 1
Specific surface area of AC and CB powder materials without binder, as well as pore volume and average pore size.

Material	BET SSA (m ² /g)	QSDFT SSA (m ² /g)	Pore volume (cm ³ /g)	Average pore size (nm)
AC	2347	1756	1.15	1.6
CB	770	715	0.77	14

of Pt QRE is shifted to the negative potential, while the Ag/AgCl RE shows less potential shift. The stability of the reference potential can be quantitatively investigated by following the half-wave potential from the CV, which is the middle position between anodic and cathodic peaks. The half-wave potential is continuously shifting by ca. 13 mV per day to the positive value (negative potential shifting of E_p) in case of the Ag/AgCl electrode (Fig. 2B), indicating its instability for long-term measurement. This potential shift can be explained by the cross contaminations between the RE system (3 M NaCl) and the cell system (1 M Na₂SO₄ with 0.1 M potassium ferricyanide), which is supported by the color change of the electrolyte in the Ag/AgCl RE (Fig. 2B, inset). The blue color change implies the deposition of Prussian blue on the RE [13]. These results suggest that the Ag/AgCl electrode is not suitable as RE in aqueous solutions, particularly when containing high concentrations of redox couple species [14–17].

Fig. 3A presents the long-term stability examined by the half-wave potential of the Pt and AC QREs. Initially, the half-wave potentials are greatly shifting or drifting for the first 30 h after cell assembly. The large initial potential shifts could originate from time-dependent wetting condition change of porous carbon [18–21], the presence of ferricyanide/ferrocyanide [5,9], and/or preferable ion adsorption on the WE and the QREs [22]. About 30 h after the cell assembly, we see that the half-wave potentials converge to around 30 mV for all tested QREs; afterwards, only slight potential shifts (<1 mV/day) can be observed. In particular, the E_p values measured after 5 days are reproducible with a slight deviation of 1–3 mV and 2–6 mV for AC and Pt, respectively (Table 2). The results indicate that Pt and AC QREs can be effectively applied for electrochemical analysis by giving enough stabilization time without any specific treatments. In fact, we assembled a cell with AC QRE and investigated the stability 30 h after the cell assembly. For the subsequent 6 days of measurements, the AC QRE shows a very stable performance without any signs of drifting or shifting of the reference potential (Fig. 3B).

For more realistic and precise investigations of QREs, trace redox species should be excluded to prevent their influence on the

system. Therefore, we applied a modified analytical method to characterize the reference potential of the QREs. A symmetric two electrode cell was built with AC film electrodes as WE and CE, while a QRE was mounted at the side of the cell and the conventional RE (Ag/AgCl) at the other side of the cell. The WE was operated in an electrode potential window up to 0.4 V vs. QRE at a specific current of 100 mA g⁻¹ while applying a resting time of 1 min (Fig. 3C). During the cell operation, the open circuit potential (OCP) of the QRE was measured versus conventional Ag/AgCl reference electrodes; the OCP, in this case, corresponds to the reference potential of the tested QRE. The measured reference potential of the QREs includes the liquid junction potential due to the different mobility of the Na⁺ and Cl⁻ ions. However, as long as a constant and reproducible liquid junction potential is expected for a certain solvent system, the applied Ag/AgCl is still a reasonable choice for the validation of the stable and reproducible reference potential of QREs as shown in many other studies [23–25]. The OCPs of various QREs are plotted in Fig. 3D as a function of operation time. In case of Pt QRE in Na₂SO₄ solution, the reference potential of Pt QRE is initially shifting with a negative slope and seems to be stabilizing (4.5 mV/day) to a value of around 250 mV vs. Ag/AgCl; however, irregular fluctuations can be seen through the entire period. Moreover, the reference potential of the other Pt QREs (Pt #2, Pt #3) show a large deviation (ca. 220 mV) as recorded after 5 days. This indicates that Pt QREs could possibly provide a reliable reference potential 30 h after the cell assembly; however, the irregular fluctuation of ca 16 mV and the irreproducible potential should be considered. On the contrary to Pt QRE, AC QRE provides a very stable (0.4 mV/day) and reproducible reference potential (± 10 mV) in 1 M Na₂SO₄ solution (Table 2).

For acidic media (1 M H₂SO₄), the reference potentials of AC and CB QREs are measured vs. Ag/AgCl without introducing redox trace species following the method described in Fig. 3C. The results are plotted in Fig. 4A as a function of operation time. In general, we found large irregular fluctuations (>50 mV) of the Pt reference potential most probably due to surface modification of Pt in proton rich environment. Interestingly, CB and AC QREs show initial

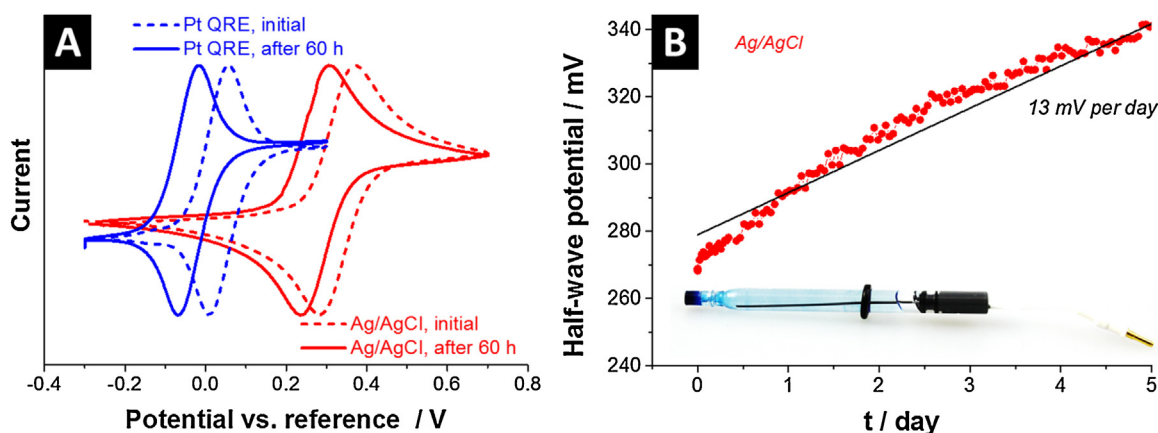


Fig. 2. (A) CVs obtained for Pt and Ag/AgCl reference electrodes in 1 M Na₂SO₄ with 0.1 M potassium ferricyanide aqueous solution. (B) Half-wave potential of the ferri- and ferrocyanide redox reaction measured vs. Ag/AgCl reference electrode. The inset shows the contamination of the Ag/AgCl reference electrode after the operation for 5 days (blue discoloration).

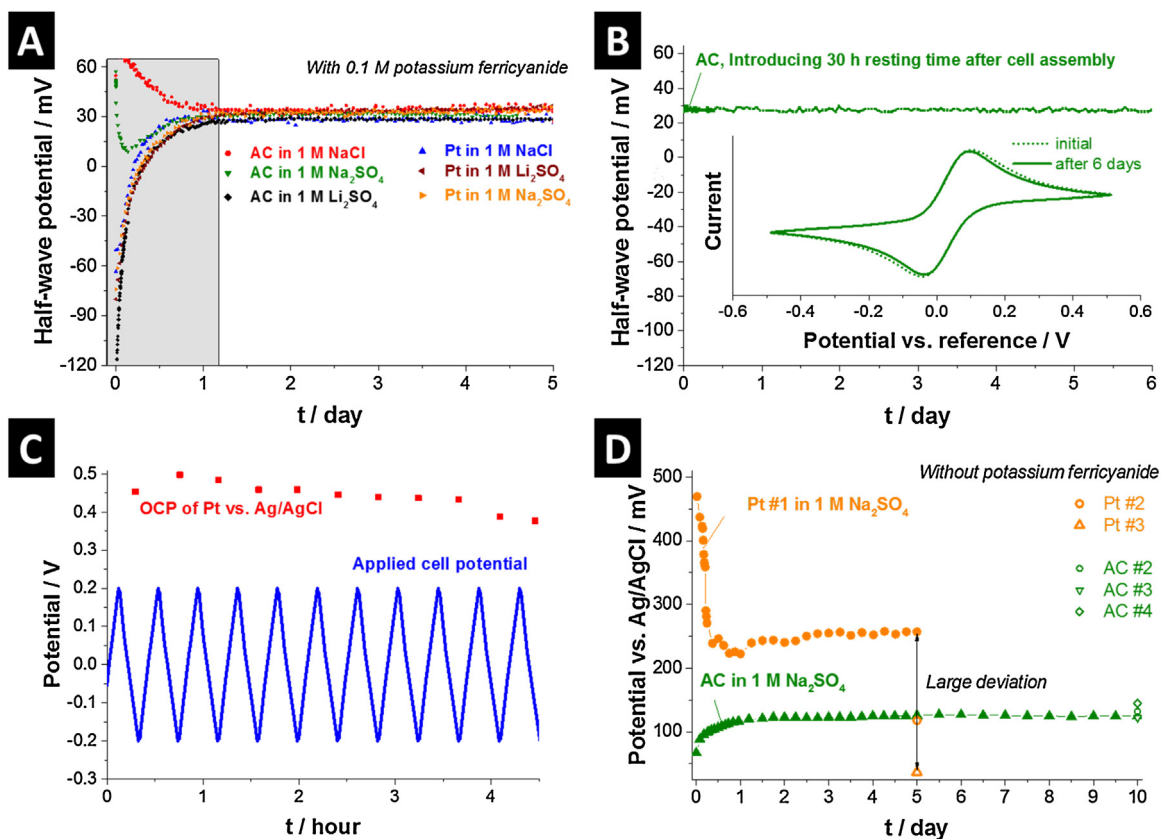


Fig. 3. (A) Half-wave potential of potassium ferri- and ferrocyanide measured vs. Pt and PTFE bound AC electrodes in various neutral solutions for 5 days. (B) The half-wave potential of the AC is measured by introducing 30 h initial resting time after the cell assembly. Inset shows the initial cyclic voltammogram as well as the one obtained after 6 days. (C) A new analytical method to investigate QREs. The AC film electrode was operated in a total potential window of 0.4 V via a quasi-reference electrode at a specific current of 100 mA/g with a resting time of 1 min while measuring the OCP of the quasi-reference electrode vs Ag/AgCl. (D) Reference potential of Pt and AC QREs measured in 1 M Na₂SO₄ solution without introducing potassium ferricyanide.

reference potential shifting to the positive value, similarly to the case of neutral solutions. After 30 h stabilization time for CB QRE and 85 h for AC QRE, relatively stable reference potentials (<5 mV per day) can be seen in 1 M H₂SO₄. Considering a low level of potential shifting (<1 mV per day) and a much shorter stabilization time, CB QRE is preferable for acidic solutions compared to AC QRE, which requires longer stabilization time (85 h) with slightly higher potential shifting rate (3.5 mV per day). Possibly, the very low oxygen content of the CB (ca. 0.51 atom%, Table 3) could be responsible for the lower level of reference potential shifting as compared to that of AC (ca. 2.27 atom%). As investigated by cyclic voltammetry in half-cell configuration (Fig. 4B), the AC electrode exhibits a slight redox activity at the potential around 280–290 mV vs. Ag/AgCl which is most probably due to the oxygenated carbon functional groups, for instance quinone-like functional groups as

reported in Ref. [15]. On the contrary, the CB electrode shows only a negligible redox contribution of oxygenated carbon functional groups due to its low oxygen content. When the carbon electrode with oxygenated functional groups is immersed into the proton rich electrolyte, the oxygenated carbon functional groups can interact with protons which could possibly polarize the electrode positively. The much lower proton uptake of CB compared to AC (reported in Ref. [12]) is also corresponding to the low level of oxygen containing carbon functional groups which is also in line with the positive shifting direction of the reference potential.

4. Conclusions

Our study provides the feasibility of porous carbon as a quasi-reference electrode as tested 1) in neutral solutions (Na₂SO₄, NaCl,

Table 2
Summary of the reference potential of PTFE bound AC, CB, and Pt.

Electrolyte	Na ₂ SO ₄	Na ₂ SO ₄	Li ₂ SO ₄	Li ₂ SO ₄	NaCl	NaCl	Na ₂ SO ₄	Na ₂ SO ₄	H ₂ SO ₄	H ₂ SO ₄
Trace redox	PFC	PFC	PFC	PFC	PFC	PFC	Ag/AgCl	Ag/AgCl	Ag/AgCl	Ag/AgCl
Material	AC	Pt	AC	Pt	AC	Pt	Pt	AC	AC	CB
Stabilization time (h)	30	30	30	30	30	30	30	30	85	30
Potential shift (mV/day)	0.1	0.2	0.2	0.6	0.1	0.1	4.5	0.4	3.5	1
E _r vs. trace redox (mV)	36	32	34	32	37	21	80	131	470	460
E _r vs. SHE (converted, mV) ^a	440	444	442	444	439	455	289	362	701	691
E _r deviation (mV)	±1.1	±3.5	±2.4	±2.4	±0.5	±6	±112	±10	±12	±10

^a E_r values were converted per the reference potential of Ag/AgCl filled with 3 M NaCl and the redox potential of ferricyanide/ferrocyanide (ca. 273 mV vs. Ag/AgCl). The reference potential of Ag/AgCl (3 M NaCl) is about 231 mV vs. SHE in 1 M Na₂SO₄ and 203 mV in 1 M H₂SO₄ including the liquid junction potential.

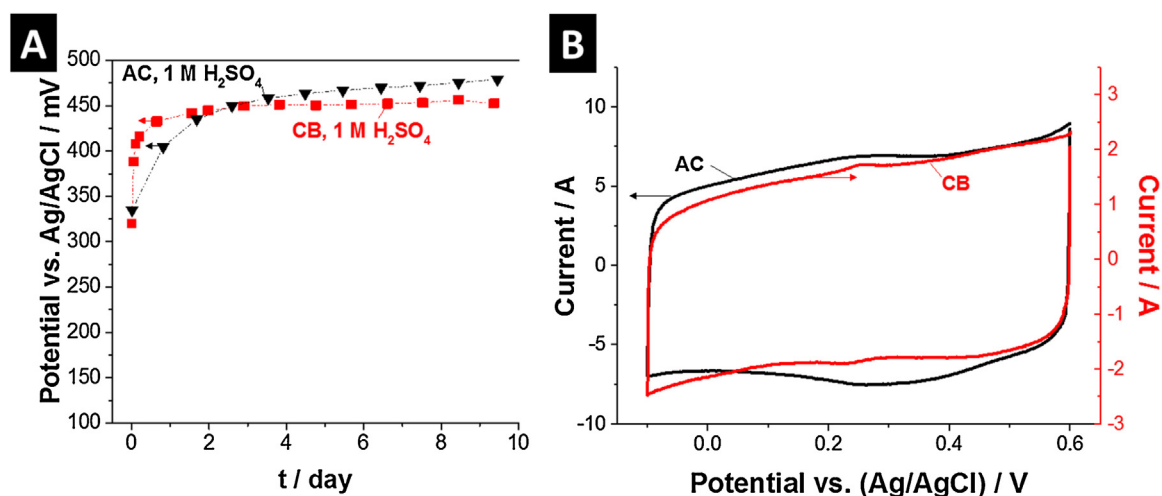


Fig. 4. (A) The reference potential of various quasi-reference electrodes in 1 M H₂SO₄ acidic solution. (B) Cyclic voltammograms obtained for AC and CB in 1 M H₂SO₄ acidic solution in three electrode configuration.

Table 3

Chemical compositions of AC and CB powder materials via CHNS elemental analysis.

Material	C (atom%)	H (atom%)	N (atom%)	S (atom%)	O (atom%)
AC	91.6 ± 0.1	6.05 ± 0.4	n.d.	n.d.*	~2.3
CB	94.9 ± 0.5	4.31 ± 0.6	n.d.	n.d.*	~0.5

* Not detectable.

and Li₂SO₄) with [Fe(CN)₆]⁴⁻/[Fe(CN)₆]³⁻ as an internal reference, 2) in Na₂SO₄ solution without internal reference, and 3) in H₂SO₄ acidic solution without internal reference.

After a varying stabilization time, PTFE bound AC and Pt QREs provide a stable reference potential of around 35 mV vs. [Fe(CN)₆]⁴⁻/[Fe(CN)₆]³⁻ in Na₂SO₄, NaCl, and Li₂SO₄ neutral aqueous solution with a potential shift below 1 mV/day, and a low level of deviation of ca 5 mV. As further investigated in Na₂SO₄ solution without introducing [Fe(CN)₆]⁴⁻/[Fe(CN)₆]³⁻ redox couple, Pt QRE exhibits relatively stable performance (4.5 mV/day) with slight fluctuation (ca. 10 mV) in reference potential but with highly irreproducible values. On the other hand, AC QRE showed a stable (0.4 mV/day) and reproducible reference potential (±10 mV) as investigated without introducing any internal reference. Therefore, we could conclude that AC QRE can be considered as a promising QRE candidate for neutral solution as verified in Na₂SO₄ solution. The validation of QRE reference potential should be carefully carried out when trace redox species are introduced into the testing system.

In case of H₂SO₄ acidic solution, PTFE bound carbon black provides an acceptable level of potential shift (1 mV per day) with the reference potential around 460 mV vs. Ag/AgCl (3 M NaCl); however, the deviation of ca 10 mV should be taken into account when an accurate analysis is required.

Our study demonstrates that porous carbon can be effectively applied to acidic and neutral solutions as a QRE with stable and reproducible potential by soaking them into an electrolyte for 30 h prior to their use or by employing 30 h of stabilization time after the cell assembly. However, validation and calibration are recommended before porous carbon QREs are applied in any other conditions than reported here, namely, 1 M concentrated NaCl, Na₂SO₄, Li₂SO₄, and H₂SO₄.

Acknowledgements

We acknowledge funding from the German Federal Ministry for Research and Education (BMBF) in support of the nanoEES^{3D} project (award number 03EK3013) as part of the strategic funding initiative energy storage framework. The authors thank Prof. Eduard Arzt (INM) for his continuing support. We also thank Friedrich Kaasik and Anna Schreiber (all at INM) for useful discussions and technical support.

References

- [1] Z. Yang, J. Zhang, M.C.W. Kintner-Meyer, X. Lu, D. Choi, J.P. Lemmon, J. Liu, *Electrochemical Energy Storage for Green Grid*, *Chem. Rev.* 111 (2011) 3577–3613.
- [2] T. Janoschka, N. Martin, U. Martin, C. Friebe, S. Morgenstern, H. Hiller, M.D. Hager, U.S. Schubert, An aqueous, polymer-based redox-flow battery using non-corrosive, safe, and low-cost materials, *Nature* 527 (2015) 78–81.
- [3] J. Ghilane, P. Hapiot, A.J. Bard, Metal/Polypyrrole Quasi-Reference Electrode for Voltammetry in Nonaqueous and Aqueous Solutions, *Anal. Chem.* 78 (2006) 6868–6872.
- [4] K.K. Kasem, S. Jones, Platinum as a reference electrode in electrochemical measurements, *Platinum Met. Rev.* 52 (2008) 100–106.
- [5] J.H. Han, S. Park, H. Boo, H.C. Kim, J. Nho, T.D. Chung, Solid-State Reference Electrode Based on Electrodeposited Nanoporous Platinum for Microchip, *Electroanalysis* 19 (2007) 786–792.
- [6] A.J. Bard, L.R. Faulkner, *Electrochemical Methods: Fundamentals and Applications*, 2nd Edition, John Wiley & Sons, 2000.
- [7] P.W. Ruch, D. Cericola, M. Hahn, R. Kötzt, A. Wokaun, On the use of activated carbon as a quasi-reference electrode in non-aqueous electrolyte solutions, *J. Electroanal. Chem.* 636 (2009) 128–131.
- [8] D. Weingarh, A. Foelske-Schmitz, A. Wokaun, R. Kötzt, PTFE bound activated carbon—A quasi-reference electrode for ionic liquids, *Electrochem. Commun.* 18 (2012) 116–118.
- [9] A. Tasaka, E. Morimoto, A. Mimoto, A. Inoue, M. Inaba, Stability and Thermodynamic Analysis of Pt and NiO_xF_y/Ni Reference Electrodes in a Dehydrated Melt of NH₄F·2HF, *J. Electrochem. Soc.* 154 (2007) E172–E177.
- [10] J. Lee, B. Krüner, A. Tolosa, S. Sethuraman, D. Kim, S. Choudhury, K.H. Seo, V. Presser, Tin/vanadium redox electrolyte combining battery-like energy storage capacity with supercapacitor-like power handling, *Energ Environ Sci* (2016).
- [11] K. Sing, D. Everett, R. Haul, L. Moscou, R. Pierotti, J. Rouquerol, T. Siemieniowska, Physical and biophysical chemistry division commission on colloid and surface chemistry including catalysis, *Pure Appl. Chem* 57 (1985) 603–619.
- [12] N. Jäckel, D. Weingarh, A. Schreiber, B. Krüner, M. Zeiger, A. Tolosa, M. Aslan, V. Presser, Performance evaluation of conductive additives for activated carbon supercapacitors in organic electrolyte, *Electrochim. Acta* 191 (2016) 284–298.
- [13] A.A. Karyakin, Prussian Blue and Its Analogues: Electrochemistry and Analytical Applications, *Electroanalysis* 13 (2001) 813–819.
- [14] S.T. Senthilkumar, R.K. Selvan, J.S. Melo, Redox additive/active electrolytes: a novel approach to enhance the performance of supercapacitors, *J. Mater. Chem. A* 1 (2013) 12386–12394.

- [15] K. Fic, M. Meller, E. Frackowiak, Interfacial Redox Phenomena for Enhanced Aqueous Supercapacitors, *J. Electrochem. Soc.* 162 (2015) A5140–A5147.
- [16] B. Akinwolemiwa, C. Peng, G.Z. Chen, Redox Electrolytes in Supercapacitors, *J. Electrochem. Soc.* 162 (2015) A5054–A5059.
- [17] B. Krüner, J. Lee, N. Jäckel, A. Tolosa, V. Presser, Sub-micrometer Novolac-Derived Carbon Beads for High Performance Supercapacitors and Redox Electrolyte Energy Storage, *ACS Appl. Mater. Interfaces* 8 (2016) 9104–9115.
- [18] J. Lee, D. Weingarth, I. Grobelsek, V. Presser, Use of Surfactants for Continuous Operation of Aqueous Electrochemical Flow Capacitors, *Energy Technology* 4 (2016) 75–84.
- [19] M. Aslan, D. Weingarth, P. Herbeck-Engel, I. Grobelsek, V. Presser, Polyvinylpyrrolidone/polyvinyl butyral composite as a stable binder for castable supercapacitor electrodes in aqueous electrolytes, *J. Power Sources* 279 (2015) 323–333.
- [20] K. Fic, G. Lota, E. Frackowiak, Electrochemical properties of supercapacitors operating in aqueous electrolyte with surfactants, *Electrochim. Acta* 55 (2010) 7484–7488.
- [21] K. Fic, G. Lota, E. Frackowiak, Effect of surfactants on capacitance properties of carbon electrodes, *Electrochim. Acta* 60 (2012) 206–212.
- [22] M.M. Goldin, V.A. Kolesnikov, M.S. Khubutiya, A.G. Volkov, G.J. Blanchard, A.K. Evseev, M.M. Goldin, Open circuit potential shifts of activated carbon in aqueous solutions during chemical and adsorption interactions, *J. Appl. Electrochem.* 38 (2008) 1369–1374.
- [23] T. Nann, S.K. Ibrahim, P.-M. Woi, S. Xu, J. Ziegler, C.J. Pickett, Water Splitting by Visible Light: A Nanophotocathode for Hydrogen Production, *Angew. Chem. Int. Ed.* 49 (2010) 1574–1577.
- [24] R.S. Jayashree, J.S. Spendelow, J. Yeom, C. Rastogi, M.A. Shannon, P.J.A. Kenis, Characterization and application of electrodeposited Pt, Pt/Pd, and Pd catalyst structures for direct formic acid micro fuel cells, *Electrochim. Acta* 50 (2005) 4674–4682.
- [25] D.R. Bond, D.E. Holmes, L.M. Tender, D.R. Lovley, Electrode-Reducing Microorganisms That Harvest Energy from Marine Sediments, *Science* 295 (2002) 483–485.

3.7. Nanoconfinement of redox reactions enables rapid zinc iodide energy storage with high efficiency

Juhan Lee,^{1,2} Pattarachai Srimuk,^{1,2} Simon Fleischmann,^{1,2} Alexander Ridder,^{1,2} Marco Zeiger,^{1,2} and Volker Presser^{1,2,*}

¹ INM - Leibniz Institute for New Materials, Campus D2 2, 66123 Saarbrücken, Germany

² Saarland University, Campus D2 2, 66123 Saarbrücken, Germany

Citation:

Lee, J.; Srimuk, P.; Fleischmann, S.; Ridder, A.; Zeiger, M.; Presser, V., Nanoconfinement of redox reactions enables rapid zinc iodide energy storage with high efficiency. *J. Mater. Chem. A* **2017**, 5 (24), 12520-12527.

Own contributions:

Design, planning, writing, cell design, experimental plan, electrochemical analyses, N₂ sorption analysis, and SEM measurements

Abstract

A key challenge for present-day electric energy storage systems, such as supercapacitors and batteries, is to meet the world's growing demand for high performances, low cost, and environmental-friendliness. Here, we introduce a hybrid energy storage system combining zinc iodide (ZnI₂) as redox electrolyte with a nanoporous activated carbon fiber (ACF) cathode and a zinc disk anode. We found that the nanopores (<1 nm) of ACF lead to a strong adsorption behavior of iodide and triiodide. Hence, this system exhibits low self-discharge rates without applying an ion selective membrane. The high power performance (20.0 kW/kg) originates from the enhanced redox kinetics of the iodide system as evidenced by electrochemical analysis. Considering the high specific energy (226 Wh/kg), the ACF/Zn ZnI₂ battery represents an alternative for lead acid, Ni-Zn, and Ni-Cd batteries, while providing a supercapacitor-like power performance in the range of seconds to minutes charging times.

Cite this: *J. Mater. Chem. A*, 2017, 5,
12520Received 26th April 2017
Accepted 25th May 2017

DOI: 10.1039/c7ta03589f

rsc.li/materials-a

Nanoconfinement of redox reactions enables rapid zinc iodide energy storage with high efficiency†

Juhan Lee,^{ab} Pattarachai Srimuk,^{ab} Simon Fleischmann,^{ab} Alexander Ridder,^{ab}
Marco Zeiger^{ab} and Volker Presser^{ab*}

A key challenge for present-day electric energy storage systems, such as supercapacitors and batteries, is to meet the world's growing demand for high performances, low cost, and environmental-friendliness. Here, we introduce a hybrid energy storage system combining zinc iodide (ZnI₂) as redox electrolyte with a nanoporous activated carbon fiber (ACF) cathode and a zinc disk anode. We found that the nanopores (<1 nm) of ACF lead to a strong adsorption behavior of iodide and triiodide. Hence, this system exhibits low self-discharge rates without applying an ion exchange membrane. The high power performance (20.0 kW kg⁻¹) originates from the enhanced redox kinetics of the iodide system as evidenced by electrochemical analysis. Considering the high specific energy (226 W h kg⁻¹), the ACF/ZnI₂ battery represents an alternative for lead acid, Ni–Zn, and Ni–Cd batteries, while providing a supercapacitor-like power performance in the range of seconds to minutes charging times.

1. Introduction

The growing global demand for electric energy storage (EES) has been driving science and technologies for the development of new materials and systems.^{1,2} The ultimate goals for next generation EES systems pertain to cost-effectiveness, environmental-friendliness, performance durability, rapid charging, and facile scalability.³ In that regard, energy storage using nanoporous carbons (like in supercapacitors) and redox electrolytes (like in redox flow batteries) is promising due to the simplicity of the system architecture, prospective low production cost, high power performance, and robust longevity.^{4–7}

Fundamentally, redox electrolyte systems capitalize on the synergy of fast ion physisorption confined in carbon nanopores *via* electric double-layer formation and the accelerated faradaic redox species in an electrolyte.⁸ Hence, the energy storage mechanism of redox electrolytes differs from ion intercalation in battery systems such as LiCoO₂, LiFePO₄, and graphite which causes low power and reduced cycling stability due to slow ion intercalation kinetics and the corresponding volume change.⁹ Redox electrolytes enable fast ion mobility and rapid charge transfer with a high performance stability.¹⁰ The fast kinetics of nanoporous carbon electrodes distinguishes (non-flow) redox electrolyte systems from bulk redox flow battery technologies with meso-/macroporous electrodes.¹¹ In particular, systems

employing iodide are promising as they provide a specific energy over 30 W h kg⁻¹, high specific power over 10 kW kg⁻¹, and cyclic life time over 5000 cycles when paired with nanoporous carbon.^{10,12–14}

To avoid rapid self-discharge, most redox electrolytes, such as vanadium complexes^{15,16} and ferricyanide/ferrocyanide,¹⁷ require an ion exchange membrane (IEM). Without such membranes, oxidized ionic species in the electrolyte shuttle to the opposite electrode. In 2015, a novel concept was reported by applying an iodine solution as catholyte and a methyl viologen anolyte.¹⁸ In the absence of an IEM, this system showed a slow self-discharge rate as benefited by a favorable adsorption of the iodine system inside the carbon nanopores.¹⁸ As an alternative to viologen, a Zn containing anolyte can be a promising candidate for a capacity balance to the iodine catholyte because of its high energy storage capacity (>50 W h L⁻¹).¹⁹ Further, the redox kinetics of Zn²⁺/Zn_(solid) are much faster compared to larger viologen molecules.^{20,21}

While few studies have investigated Zn anolyte and iodine catholyte, known as the ZnI₂ battery;^{19,22–29} the use of nanoporous carbon as cathode has not yet been explored. Instead, modified iodine-polymers have mostly been applied as cathode material. Earlier studies have been focusing on galvanic cells instead of rechargeable secondary batteries due to the high self-discharge rate and relatively low coulombic efficiencies of 40%.^{23–25} In such works, the use of cation exchange membranes prevented the shuttling of I₃⁻ to the negative electrode.²³ Herein, we report a hybrid energy storage system employing zinc iodide (ZnI₂) redox electrolyte with nanoporous activated carbon fiber (ACF) cathode and zinc disk anode. This feature is enabled by favorable sorption of iodide within nanoporous

^aINM – Leibniz Institute for New Materials, 66123 Saarbrücken, Germany. E-mail: volker.presser@leibniz-inm.de

^bDepartment of Materials Science and Engineering, Saarland University, 66123 Saarbrücken, Germany

† Electronic supplementary information (ESI) available. See DOI: 10.1039/c7ta03589f

carbon. The adsorption behavior of iodine in porous carbon was investigated with respect to different pore sizes with regards to self-discharge rate and reversible hydrogen reduction. Successful operation of this system without an IEM was demonstrated. We investigated the origin of the high power performance further by electrochemical analysis with a rotation disk electrode. Finally, the specific power and energy will be discussed by normalization considering the mass and volume of the electrode, electrolyte, and separators in the cell.

2. Experimental description

2.1. Materials

For the carbon fiber electrodes, ACC-507-15, ACC-507-20 and ACC-507-25 (Kynol Europe GmbH) were used as received. The last two digits of the sample indicate the activation degree as determined by the process parameters chosen by the company, while the three digits (507 for all samples) in the middle of the label indicate the type of phenolic precursor applied for the synthesis. For the free-standing carbon film electrodes, type YP-80F activated carbon powder (Kuraray Europe GmbH; called AC-1.4 in this paper, with 1.4 being the average pore size) was mixed with polytetrafluoroethylene (PTFE, Sigma-Aldrich) and ethanol, rolled to $200 \pm 6 \mu\text{m}$ thickness, and dried in a vacuum oven (120°C , 20^3 Pa) for 48 h while controlling the final mass ratio of carbon to PTFE to be 95 : 5. For the zinc electrodes, zinc sheets with the thickness of $1 \mu\text{m}$ and $100 \mu\text{m}$ (GoodFellow) were used. For the electrolytes, potassium iodine (Bio Ultra >99.5%, Sigma-Aldrich), potassium ferricyanide (BioUltra $\geq 99.0\%$, Sigma-Aldrich) zinc iodine (purum p.a. $\geq 98.0\%$, Sigma-Aldrich) were dissolved in deionized water at different concentrations.

For the preparation of MWCNT paper, 40 mg of NC7000 MWCNTs (Nanocyl SA) were dispersed in 1 mass% of Triton X-100 surfactant in 80 mL of de-ionized water. Next, they were sonicated for 30 min with ice-bath assistance. Then, the mixture was filtered through hydrophilic PVDF membrane filter ($0.22 \mu\text{m}$ pore size, 47 mm diameter, Millipore). The MWCNT paper formed in this step was washed multiple times with copious amount of de-ionized water to get rid of any surfactant. Afterwards, the MWCNT paper was washed with 50 mL of methanol and dried at 60°C for 12 h under vacuum. Finally, the MWCNT paper was peeled off from the membrane.

All carbon electrodes were characterized by nitrogen gas sorption analysis (GSA) with a Quantachrome Autosorb iQ system. Before measurement, the electrodes were degassed at 150°C for ca. 20 h at a relative pressure of 0.1 Pa. All experiments were carried out in liquid nitrogen at -196°C in the relative pressure range from 1×10^{-6} to 1.0 in 56 steps. The specific surface areas (SSA) of the activated carbon (AC) and activated carbon fiber (ACF) electrodes were calculated both (i) by applying quenched-solid density functional theory (QSDFT) with a slit pore model and (ii) by Brunauer–Emmett–Teller (BET) equation in the linear regime of the measured isotherms *via* ASiQwin-software 3.0. For the MWCNT paper, non-local density functional theory (NLDFIT) with a hybrid model of slit and spherical pores was applied for the calculation of SSA while

providing BET SSA for comparison. The ACF electrodes are labeled according to the measured average pore size; ACF-0.7 for ACC-507-15, ACF-0.8 for ACC-507-20, and ACF-1.1 for ACC-507-25. Detailed information about nitrogen GSA can be found in ESI† at Section 1.

2.2. Cell design and assembly

For the half-cell experiments, a double stack of YP-80F electrodes ($200 \mu\text{m}$ thickness, 12 mm diameter) was used as counter electrode while Ag/AgCl reference electrode or YP-80F QRE was mounted at the side of the cell having a close contact to both working and counter electrodes; the scheme of the cell design (D-Cell) can be found elsewhere.³⁰ Two graphite pistons were applied as current collectors and the working (12 mm diameter) and counter electrode were separated by GF/A glassy fiber filter (Whatman). After the cell assembly, electrolyte was injected by vacuum backfilling.

For full-cell configurations, two different cell designs were applied: (i) the D-cell which allows the observation of the individual potential developments *via* spectator reference electrode while the amount of electrolyte is not controlled. (ii) Cells which limits the excess volume of the electrolyte (L-cell); here, excess volume means the volume of the electrolyte in the cell beyond the geometrical volume of the electrode. The drawing of L-cell can be found in our previous reports.^{12,16,17} For the L-cell, the electrolyte was dropped to the gasket channel having a size of 1.33 cm^2 where the electrode (13 mm diameter) was placed above the glassy carbon current collectors, and the cell was sealed afterwards. For the prevention of the electrolyte shortage *via* the electrolyte adsorption during the electrochemical operation, the electrodes were previously soaked in the electrolyte and degassed by applying vacuum for 10 min. For both cell designs, a double stack of surfactant coated polypropylene separator (Celgard3501) was located to the cathode side to prevent the short circuit *via* Zn dendrite formation while GF/A glassy fiber filter was located at the anode side as electrolyte reservoir.

2.3. Electrochemical characterization

For the electrochemical characterizations, a VMP300 potentiostat/galvanostat (Bio-Logic) was used while cells were stored at 25°C in a climate chamber.

For the evaluation of self-discharge rate in KI aqueous solution, the working electrodes were oxidized with the capacity limit of 0.2 mA h at 10 mA cm^{-2} (ca. 720 mA g^{-1}) in half-cell configuration, rested for various time, and reduced at 10 mA cm^{-2} . The potential of the working electrode was carefully controlled so that it was always positively charged than the counter electrode. During the oxidation, a potential plateau appeared which implies the oxidation of iodides while the oxidized iodine and polyiodides are reduced back at the reduction current until the potential range was far below the potential plateau. Hence, the coulombic efficiency of this cycle indicates the amount of self-discharged species oxidized iodine *via* diffusion of oxidized iodine and reduction at the counter electrode, also known as redox shuttling. In the case of ZnI_2

aqueous solution, full-cell configuration was applied with ACF-0.8 as cathode while varying anode materials to characterize the self-discharge rate of anode materials in ZnI_2 solution. The cells were charged at 10 mA cm^{-2} (ca. 720 mA g^{-1}) with the capacity limit of 0.94 mA h , rested for various time, and reduced at 10 mA cm^{-2} . For the average and standard deviation values, three cells were assembled for each configuration.

For the gravimetric specific energy (E), two different normalization methods were applied *via* eqn (1) to provide a comparative data basis with battery and supercapacitor materials in the literature: (i) a normalization with respect to only the active mass of the electrode or (ii) a normalization with respect to the total mass of the electrode, separator, and electrolyte.

$$E = \frac{i}{m} \int U dt \quad (1)$$

where E_{GC} is the specific energy calculated from galvanostatic charge and discharge mode, U is the cell voltage, and i is the discharge current. For the volumetric specific energy, the calculated energy was normalized to the volume of the, electrode, separator, and electrolyte.

The specific power (P) was calculated by dividing the specific energy (E) by discharging time (Δt_{dis}) at each specific current step *via* eqn (2):

$$P = \frac{E_{\text{GC}}}{\Delta t_{\text{dis}}} \quad (2)$$

C-Rate was obtained by dividing the maximum capacity by the applied current.

For the rate performance test of the full cells, two cells were assembled. As there was no significant difference was found, the results of one cell are plotted in the manuscript while providing the results of both cells in ESI,† Section 4.

3. Results and discussion

3.1. Iodide adsorption of carbon nanopores for cathode

Due to the shuttling of oxidized/reduced ions through the separator between the electrodes, the redox activities of halide ions such as iodide and bromide can only be effectively utilized for energy storage when applying cation exchange membranes.³¹ The strong physisorption of oxidized halide ions in nanoconfined spaces, however, enables low self-discharge rates in the absence of an ion exchange membrane which significantly reduces the cost. As experimentally demonstrated,¹⁸ a very low self-discharge rate was observed for aqueous 1 M potassium iodide (KI) in a nanoporous carbon cathode. However, the influence of the carbon pore structure on the self-discharge performance with halide redox electrolytes has not yet been established.

We first investigated the cathode and employed ACF with different average pore sizes (0.7, 0.8, and 1.1 nm) and MWCNTs (Table 1 and Fig. S1 in ESI†). In Fig. 1a, we show the self-discharge performance in three-electrode configuration with an oversized counter electrode and a porous carbon quasi-

reference electrode (QRE, see Section 3 in ESI†).³² A clear dependency is seen: with larger average pore size, the self-discharge is accelerated. Throughout the experiments, the working electrode potential was controlled by applying a current density of 10 mA cm^{-2} with the oxidation capacity limit of 0.2 mA h . The working electrode potential exhibits a plateau at the iodide redox potential of 7 mV vs. carbon (Fig. 1a). In the case of ACF-0.7 and ACF-0.8, that is, nanoporous carbons with average pore sizes below 1 nm , a high charge retention ($>87\%$) can be observed even after 12 h resting time, evidencing a very low self-discharge (Fig. 1a). Carbon nanopores exceeding 1 nm (ACF-1.1) exhibit a faster self-discharge rate than sub-nanometer pores (ACF-0.8 and ACF-0.7) with a charge retention of around 69% after 12 h resting time. For comparison, multi-wall carbon nanotubes (MWCNTs) show a significant level of self-discharge, retaining only 13% of charge after 12 h resting.

Considering the high reversibility of iodide redox activities in carbon micropore for energy storage,^{10,12} redox shuttling is believed to be the major factor for the self-discharge rate in our study since the type, morphology, and chemical composition of the ACF electrodes were similar. According to the EDX analysis (Table S1 in ESI†), all ACF electrodes exhibit high carbon content over 95 mass\% containing oxygen content lower than 4 mass\% . Hence, the adsorption of iodide at the carbon electrode must be the major influence for the self-discharge rate as it impedes the diffusion of iodide ions. Without adsorption of iodide in nanopores, a high coulombic efficiency over 90% would be impossible to achieve.

As shown in Fig. 1a, ACF-0.8 is the most promising cathode material for the ZnI_2 battery, considering its low self-discharge rate and higher DFT specific surface area ($1638 \text{ m}^2 \text{ g}^{-1}$) compared to that of ACF-0.7 ($1499 \text{ m}^2 \text{ g}^{-1}$), providing a higher active area as well as a larger volume reservoir (total pore volume of $0.66 \text{ cm}^3 \text{ g}^{-1}$ for ACF-0.8 and $0.50 \text{ cm}^3 \text{ g}^{-1}$ for ACF-0.7) for redox reactions. The benefits of high specific surface area and high pore volume were reported for the electric energy storage *via* iodide reaction in carbon micropores.¹² Furthermore, as reported in recent studies,^{10,12} high cyclic stability of nanoporous carbon with iodide redox electrolyte (over 4000 cycles) assures that nanoporous carbon is a promising cathode in ZnI_2 batteries. Most of all, high power performance *via* conductive carbon network and enhanced redox kinetics in nanopores are advantageous for cathode part in ZnI_2 batteries as compared to the poor cyclic lifetime (<1000 cycles) and high resistivity of conducting polymers.^{33,34}

3.2. Anode materials for ZnI_2 battery

We benchmarked different carbons and a zinc disk as anode in a membrane-free setup for the ZnI_2 battery (Fig. 1b), while ACF-0.8 was applied as cathode. To the best of our knowledge, such a membrane-free configuration has not yet been reported. At present, zinc plates are the most reported anode material for ZnI_2 secondary batteries.^{19,23,24} Recently, a carbon felt anode was reported for ZnI_2 flow batteries, which fundamentally differ from our non-flow operation;³⁵ however, membranes are still required

Table 1 Specific surface area and total pore volume of various carbon electrodes as calculated either by density functional theory or BET equation as well average pore size from nitrogen sorption analysis

Sample	SSA DFT (m ² g ⁻¹)	SSA BET (m ² g ⁻¹)	Total pore volume (cm ³ g ⁻¹)	Average pore size (nm)
MWCNTs bucky paper	>218	218	>0.58	>8.7
ACF-0.7	1499	1339	0.50	0.7
ACF-0.8	1638	1694	0.66	0.8
ACF-1.1	1986	2313	0.96	1.1
AC-1.4	1648	2094	1.05	1.4

to maintain high coulombic efficiencies (>96%). In theory, the standard redox potential of Zn²⁺/Zn_(solid) at +0.76 V *vs.* SHE excludes the use of a carbon anode because hydrogen evolution at the carbon surface can occur below the zinc reduction potential. Recently, it was reported that hydrogen gas can be adsorbed in carbon nanopores and be reversibly oxidized at the anode side.^{4,36,37} Therefore, our work first explores the feasibility of applying nanoporous carbon as anode for ZnI₂ battery.

The mesoporous MWCNTs anode shows high coulombic efficiency of around 90% (Fig. 1b) when no resting time was applied. Yet, the capacity retention drops rapidly after 1 h of resting time as the system suffers from a high self-discharge rate. After 3 h resting time, ACF-0.7 and ACF-0.8 completely lost the energy storage capacity. We see a clear trend of faster self-discharge in the case of smaller pores. This is explained by a poor charge reversibility of the porous carbon anode, as the cathodic limit is gradually extended for negative potentials (Fig. 1c).

The irreversibility arises from adsorbed iodides inhibiting the adsorption of evolved hydrogen gas in the micropores.⁴ Therefore, at -0.85 V *vs.* Ag/AgCl, the system shows a large reduction current while only a fraction of the charges (charge retention of 28%) can be returned during the oxidation scan. Obviously, the porous carbon anode is not suitable for the redox activity of Zn²⁺/Zn_(solid) occurring at -0.97 ± 0.03 V *vs.* Ag/AgCl (ESI, † Section 4) since the irreversible hydrogen evolution leads to a low energy storage efficiency. As an alternative for anode materials, Zn disks enhance the performance of the system *via* hydrogen overpotential leading to an effective Zn²⁺/Zn_(solid) redox reaction.³⁸ This is depicted in Fig. 1b where we see a charge retention of ~80% even after 12 h resting time for a zinc disc anode.

3.3. Electrochemical stability

In addition to self-discharge performance, the electrochemical stability window of aqueous solutions was investigated. The potential window in aqueous solutions is theoretically limited to 1.23 V by the oxygen evolution reaction (OER, 1.23 V *vs.* SHE) and the hydrogen evolution reaction (HER, 0 V *vs.* SHE). Broader potential stability windows exceeding 2 V *vs.* SHE can be achieved when electrodes with high hydrogen overpotential are applied, such as Pb, Sn, Zn, or boron-doped diamond.³⁹ For the determination of the anode potential limit of a zinc disk, linear potential sweep curves were obtained at different scan rates in 1 M KI (in order to exclude the influence of Zn²⁺/Zn_(solid)

reaction) by applying a zinc disk as a working electrode (Fig. 2a) since the hydrogen evolution is the major limiting factor.⁴⁰ As determined by the current increase onset from the linear potential sweep, the zinc electrode exhibits an anode limit potential of -1.31 V *vs.* Ag/AgCl (-1.1 V *vs.* SHE). Given that the reduction current decreases as the potential was further scanned to the negative potential, the onset current at -1.31 V originates from the H⁺/H₂(gas) redox reaction. The rapid current increase at a potential below -1.6 V is caused by hydrogen gas formation from water splitting.⁴¹

For the cathode potential limit of the ACF-0.8 nanoporous carbon fiber electrode, the irreversible reaction of iodine/iodate is the main limiting factor (ESI, † Section 2). The cathode potential is not limited by the irreversible oxygen evolution reaction but by the high self-discharge rate of non-ion-selective membranes. In that respect, the cathode potential limit can be quantified from the charge reversibility of the working electrode by extending the applied potential window in small potential steps (Fig. 2b, inset), also known as *S*-value test (stability value test; see ESI, † Section 4).^{30,42} The low *S*-value below 0.4 V indicates that little irreversible charges are transferred, making the redox reaction at the working electrode favorable for energy storage with high coulombic efficiency. The increasing reduction capacity (Fig. 2b) and the redox peaks in the cyclic voltammogram imply that the redox contribution onsets at 0.15 V *vs.* Ag/AgCl while maintaining a high coulombic efficiency (99%, equivalent to *S*-value of 0.008) up to 0.35 V. At 0.4 V, the *S*-value increases because of the onset of unfavorable charge transfer, such as irreversible redox reactions or redox shuttling, which is further supported by the I₂/IO₃⁻ redox peaks arising at 0.38 V (Fig. 2c).

3.4. Electrochemical performance of porous carbon cathode

ZnI₂ cells were benchmarked using a 100 μm thin Zn plate as anode and nanoporous carbon with 0.8 nm pore size (ACF-0.8) as cathode. The latter had shown a very low self-discharge (Fig. 1a) and a high specific surface area (1694 m² g⁻¹, BET). In 1.2 M ZnI₂, a well-defined cell potential plateau (Fig. 3a) can be observed by constant charging and discharging current at 11.3 mA (10 mA cm⁻²) as the charge capacity was limited to 3.75 mA h (3.3 mA h cm⁻²). The potential developments of cathode and anode assure that the cell is in a stable potential window since the anode and the cathode potential limits are about 100 mV and 300 mV, respectively.

At a low current of 3 mA (2.26 mA cm⁻²), the volume limited full cell exhibits the maximum cell capacity of *ca.* 3 mA h (64

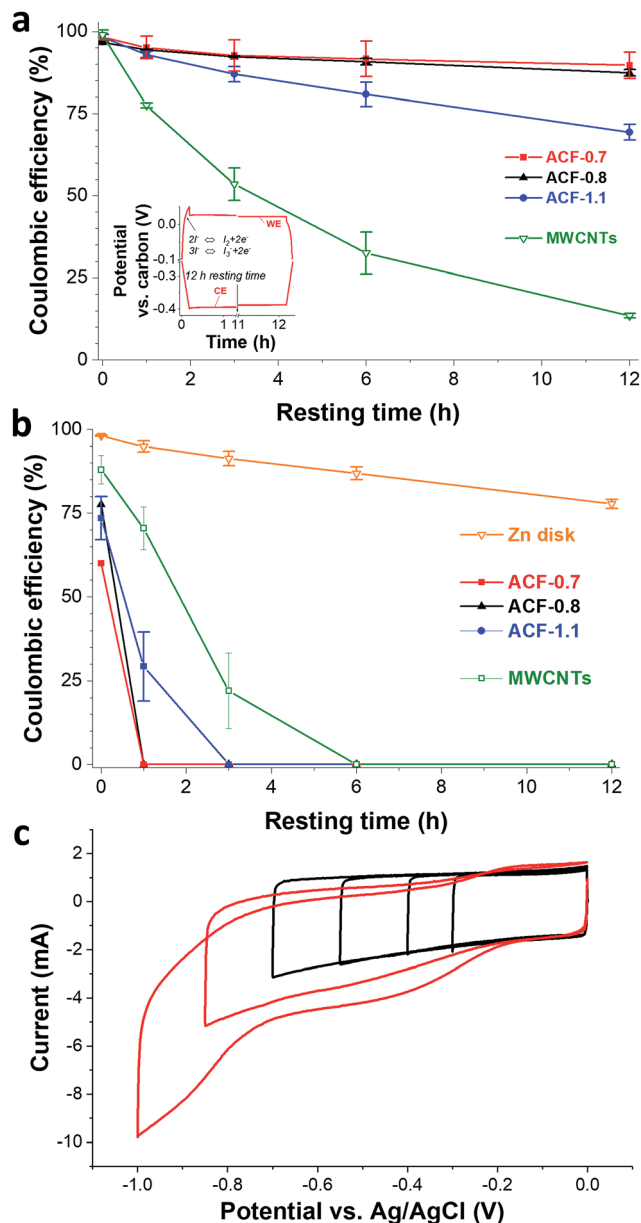


Fig. 1 Adsorption characteristics of iodine containing solution (1 M KI) in terms of self-discharging. (a) Self-discharging rate of different cathode materials in half-cell configuration. Inset shows the electrochemical procedure applied for the measurements. (b) Self-discharging rate of different anode materials in full-cell configuration as balanced with ACF-0.8 cathode. (c) Cyclic voltammograms were obtained with various potential window for ACF-0.8 in half-cell configuration.

mA h cm⁻³) showing overcharge as characterized by a sharp cell voltage increase during charging and a rapid cell voltage drop during discharging (Fig. 3b). The energy of the cell is about 3.6 mW h (77.8 W h L⁻¹ normalized to the combined volume of the electrode, electrolyte, and separators) at a rate of 1C, leading to a coulombic efficiency of 96% and an energy efficiency of 92%. The system shows a high power performance of 400 mA (301 mA cm⁻², 133C rate), still maintaining a cell capacity of over 1 mA h with an energy efficiency of 52%. For comparison: ZnI₂ batteries

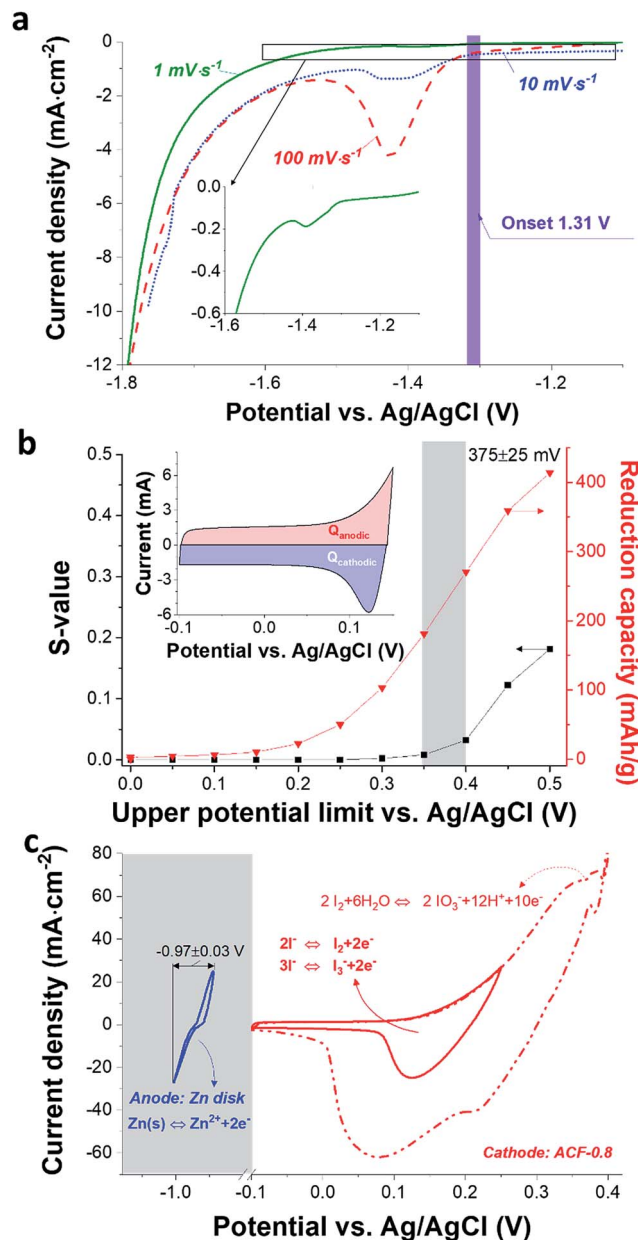


Fig. 2 Cathode and anode potential limits were determined by electrochemical analyses. (a) Linear potential sweep for Zn disk in 1 M KI. (b) S-Value analysis for ACF-0.8 in 1.2 M ZnI₂ (c) cyclic voltammograms were obtained from S-value analysis.

based on conducting polymers show limited power performance; capacity retention of about 60% at 10C rate and large overpotential (over 300 mV) at 4.8 mA cm⁻².^{19,27}

The rate handling performance is summarized in Table 2 and Fig. 3c. In terms of stability, the ACF/Zn ZnI₂ battery performance does not suffer after sweeping through different C-rates from 1C to 133C (Fig. 3c). The performance durability testing at a rate of 1C reproducibly demonstrates the ability of ACF/Zn ZnI₂ to maintain 86% of the initial capacity retention after 500 cycles (Fig. S8b in ESI†). While the stability of the ZnI₂ battery have been poorly explored so far, the ACF/Zn ZnI₂ battery is the most robust system among reported ZnI₂ studies.

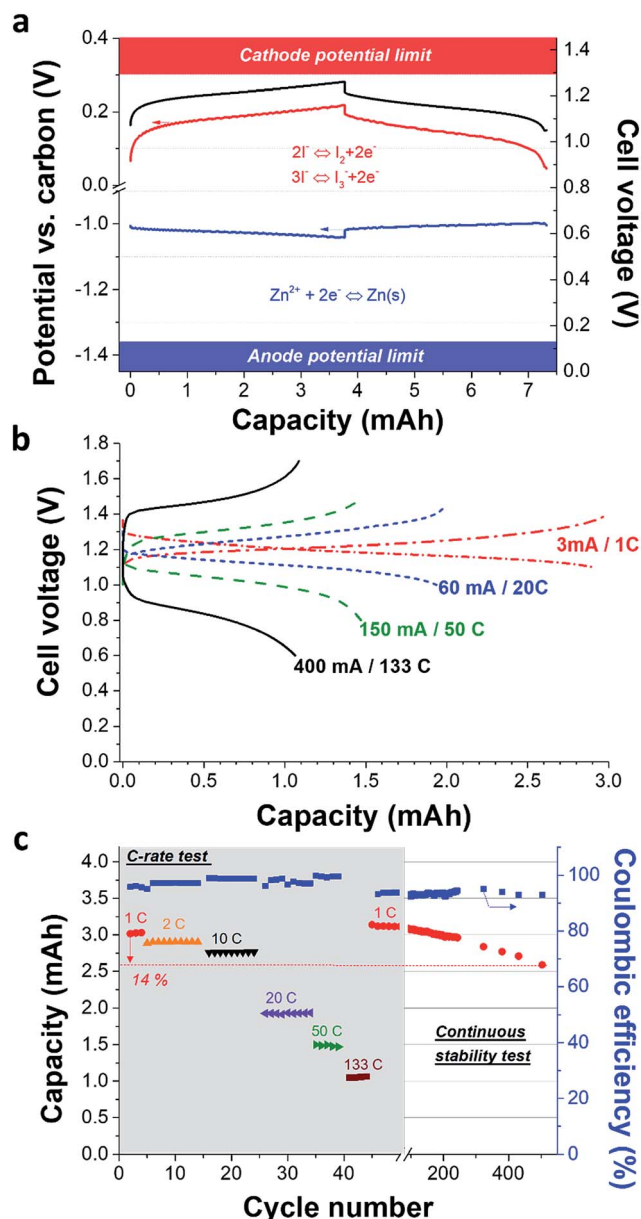


Fig. 3 Electrochemical characterizations for ACF-0.8/Zn ZnI₂ battery with full-cell configuration in 1.2 M ZnI₂. (a) Charge and discharge potential profiles obtained at 11.3 mA (10 mA cm⁻²) as the charge capacity was limited to be 3.75 mA h (3.3 mA h cm⁻²). (b) Charge and discharge potential profiles obtained at different currents. (c) Rate handling performance and cyclic stability.

Tsutsumi *et al.* reported the coulombic efficiency of 50 cycles without discussion about the capacity retention.²⁹ About 300 cycles were carried out at 2 mA cm⁻² by Yamamoto *et al.* and the capacity retention of 75% is reported. The robustness of the ACF/ZnI₂ battery is due to the high stability of the iodide redox reaction in the carbon micropores as reported in a few cases;^{10,12-14} yet, thorough and detailed understanding of the degradation performance of ACF/ZnI₂ battery seems to be necessary *via in situ* or post mortem analysis for the further development of the system.

Table 2 Electrochemical energy storage performance of ACF-0.8/Zn 1.2 M ZnI₂ at different C-rates in terms of energy efficiency and specific energy. For the normalization, the volume of the electrode, electrolyte, and separators are considered

C-Rate	1	2	10	20	50	133
Energy efficiency (%)	92	92	92	84	77	52
Specific energy (W h L ⁻¹)	77.8	74.1	69.4	46.2	31.8	18.3

3.5. Volumetric and gravimetric device performance

As pointed out by Chun *et al.*,¹⁸ comparing the specific energy and power performance of the system in a Ragone plot can be misleading, particularly when the performance of a system is normalized only to the mass or volume of the active electrode. The main problem with such comparison is that the performance metrics of commercial products were evaluated per mass and volume of the device while the claimed performances are mostly normalized excluding the volume and the mass of the separator, current collector, electrolyte, and outer housing. There are difficulties in reporting device performance on laboratory scale since the volume of the inactive energy storage material such as current collectors and cell body, in general, is 10–100 times larger and heavier than the electrode material.⁴³ Yet, the volume and the mass of the outer housing and current collectors can be significantly reduced by either upscaling or engineering. Therefore, reporting normalized values including the volume and the mass of the electrode, separator, and electrolyte is reasonable for comparing laboratory cells with commercial products. In that regard, the ACF/Zn ZnI₂ cell performances are normalized (see ESI,† Section 5) considering the mass and the volume of electrode and separator, as well as the electrolyte; in that case, thin Zn foil (1 μm, 0.3 mg) was applied as anode. We see in the Ragone plot normalized by volume (Fig. 4a) or mass (Fig. 4b) that the ACF/Zn ZnI₂ cells exhibit an energy density of 77.8 W h L⁻¹ and a specific energy of 50.9 W h kg⁻¹. Considering cell scale normalization, the specific power performance of ACF/Zn ZnI₂ cell (5.3 kW L⁻¹, 4.7 kW kg⁻¹) is superior than that of an aqueous supercapacitor (activated carbon, 1 M Na₂SO₄) and a redox electrolyte aided hybrid system (activated carbon, 1 M K₃(Fe(CN)₆)) with a similar cell design and dimension. At such high-power ratings, the ACF/Zn ZnI₂ system still exhibits a specific energy of 12.2 W h kg⁻¹ (18.3 W h L⁻¹).

The origin of the high-power performance of the ACF/Zn ZnI₂ battery is the fast redox kinetic of iodide and zinc surface redox reaction since the system exhibits a similar *iR* drop compared to that of aqueous supercapacitors with the same cell dimension. This indicates that the ACF/Zn ZnI₂ battery does not suffer from diffusion limited redox feature (Fig. 4c). As shown in ESI,† Section 2, employing nanoporous activated carbon (AC) as a cathode for the ZnI₂ system is beneficial in two aspects. First, the confinement of the redox ions in nanoporous carbon leads to thin layer diffusion rather than to conventional planar diffusion.^{8,44-46} Therefore, the high power of the ACF/Zn ZnI₂ battery is enabled *via* enhanced redox kinetics of iodide/triiodide in confined carbon nanopores. Second, halides

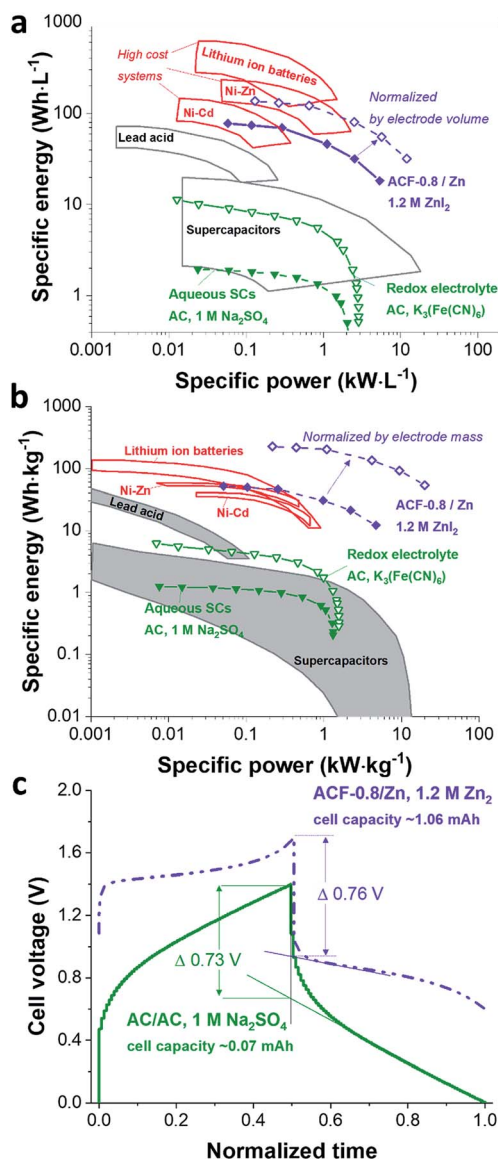


Fig. 4 Electrochemical performance of ACF-0.8/Zn 1.2 M ZnI₂ battery as compared to the other systems. (a) Volumetric Ragone plot where values are adapted from ref. 47. (b) Gravimetric Ragone plot where values are adapted from ref. 48. (c) *iR* drop comparison between aqueous double-layer capacitor and ACF-0.8/Zn ZnI₂ battery.

prefer to adsorb on carbon surfaces which could block the active reaction site of a flat carbon electrode, leading to an ineffective ion diffusion kinetic. This limiting feature was not observed in the case of activated carbon (ESI,† Section 2). Since most redox ions were confined in the carbon nanopores with a high total pore volume (*ca.* 1 cm³ g⁻¹), most of the redox reactions relate to nanoconfined ions. Therefore, the redox reaction rate with AC was largely decoupled from ion transportation from the bulk solution to the electrode surface.

The ACF/Zn ZnI₂ battery has a much higher capacity (1.06 mA h) than the AC/AC supercapacitor (0.07 mA h) at the same current density (400 mA cm⁻²). The superiority of the specific power performance of ACF/Zn ZnI₂ compared to supercapacitors originates from nanoporous carbon

capitalizing on the fast iodide redox couple (see detailed kinetic data in ESI,† Section 2). Furthermore, our ZnI₂ system exhibits specific energy values very close to that of commercially available Ni–Zn (50 W h L⁻¹) and Ni–Cd (38 W h L⁻¹) batteries.

4. Conclusions

The adsorption behavior of iodine and triiodide on porous carbon strongly depends on the size of the pores. In the case of the ZnI₂ battery system, sub-nanometer pores enable low self-discharge *via* iodine and triiodide adsorption in carbon nanopores (charge retention of 78% after 12 h resting time), which was achieved without applying an ion exchange membrane. Rotating disk electrode analysis proved that the unprecedentedly high power performance (20.0 kW kg⁻¹) of the ACF/Zn ZnI₂ battery is enabled by the enhanced kinetics of iodide within carbon nanopores.

Acknowledgements

We acknowledge funding from the German Federal Ministry for Research and Education (BMBF) in support of the nanoEES^{3D} project (award number 03EK3013) as part of the strategic funding initiative energy storage framework. The authors thank Prof. Eduard Arzt (INM) for his continuing support. We also thank Soumyadip Choudhury, Anna Schreiber, Ingrid Grobelsek, Benjamin Krüner, and Hwirim Shim (all at INM) for useful discussions and support.

References

- 1 M. R. Lukatskaya, B. Dunn and Y. Gogotsi, *Nat. Commun.*, 2016, **7**, 12647.
- 2 M. Salanne, B. Rotenberg, K. Naoi, K. Kaneko, P.-L. Taberna, C. Grey, B. Dunn and P. Simon, *Nat. Energy*, 2016, **1**, 16070.
- 3 Z. Yang, J. Zhang, M. C. W. Kintner-Meyer, X. Lu, D. Choi, J. P. Lemmon and J. Liu, *Chem. Rev.*, 2011, **111**, 3577–3613.
- 4 K. Fic, M. Meller and E. Frackowiak, *J. Electrochem. Soc.*, 2015, **162**, A5140–A5147.
- 5 B. Akinwolemiwa, C. Peng and G. Z. Chen, *J. Electrochem. Soc.*, 2015, **162**, A5054–A5059.
- 6 S. T. Senthilkumar, R. K. Selvan and J. S. Melo, *J. Mater. Chem. A*, 2013, **1**, 12386–12394.
- 7 B. Evanko, S. J. Yoo, S.-E. Chun, X. Wang, X. Ji, S. W. Boettcher and G. D. Stucky, *J. Am. Chem. Soc.*, 2016, **138**, 9373–9376.
- 8 R. Narayanan and P. R. Bandaru, *J. Electrochem. Soc.*, 2014, **162**, A86–A91.
- 9 V. Etacheri, R. Marom, R. Elazari, G. Salitra and D. Aurbach, *Energy Environ. Sci.*, 2011, **4**, 3243–3262.
- 10 E. Frackowiak, M. Meller, J. Menzel, D. Gastol and K. Fic, *Faraday Discuss.*, 2014, **172**, 179–198.
- 11 A. Z. Weber, M. M. Mench, J. P. Meyers, P. N. Ross, J. T. Gostick and Q. Liu, *J. Appl. Electrochem.*, 2011, **41**, 1137–1164.
- 12 B. Krüner, J. Lee, N. Jäckel, A. Tolosa and V. Presser, *ACS Appl. Mater. Interfaces*, 2016, **8**, 9104–9115.

- 13 G. Lota, K. Fic and E. Frackowiak, *Electrochem. Commun.*, 2011, **13**, 38–41.
- 14 G. Lota and E. Frackowiak, *Electrochem. Commun.*, 2009, **11**, 87–90.
- 15 J. Lee, A. Tolosa, B. Krüner, N. Jäckel, S. Fleischmann, M. Zeiger, D. Kim and V. Presser, *Sustainable Energy & Fuels*, 2017, **1**, 299–307.
- 16 J. Lee, B. Krüner, A. Tolosa, S. Sathyamoorthi, D. Kim, S. Choudhury, K.-H. Seo and V. Presser, *Energy Environ. Sci.*, 2016, **9**, 3392–3398.
- 17 J. Lee, S. Choudhury, D. Weingarth, D. Kim and V. Presser, *ACS Appl. Mater. Interfaces*, 2016, **8**, 23676–23687.
- 18 S.-E. Chun, B. Evanko, X. Wang, D. Vonlanthen, X. Ji, G. D. Stucky and S. W. Boettcher, *Nat. Commun.*, 2015, **6**, 7818.
- 19 M. Hishinuma, T. Iwahori, H. Sugimoto, H. Sukawa, T. Tanaka, T. Yamamoto, Y. Yanagisawa, Y. Yoda and S. Yoshida, *Electrochim. Acta*, 1990, **35**, 255–261.
- 20 C. L. Bird and A. T. Kuhn, *Chem. Soc. Rev.*, 1981, **10**, 49–82.
- 21 M. Chamoun, B. J. Hertzberg, T. Gupta, D. Davies, S. Bhadra, B. Van Tassell, C. Erdonmez and D. A. Steingart, *NPG Asia Mater.*, 2015, **7**, e178.
- 22 T. Yamamoto and T. Kanbara, *Inorg. Chim. Acta*, 1988, **142**, 191–193.
- 23 T. Yamamoto, M. Hishinuma and A. Yamamoto, *Inorg. Chim. Acta*, 1984, **86**, L47–L49.
- 24 T. Yamamoto and S.-I. Kuroda, *J. Electroanal. Chem. Interfacial Electrochem.*, 1983, **158**, 1–11.
- 25 T. Yamamoto, S.-I. Kuroda and A. Yamamoto, *Inorg. Chim. Acta*, 1982, **65**, L175–L176.
- 26 T. Yamamoto, *J. Chem. Soc., Chem. Commun.*, 1981, 187–188, DOI: 10.1039/c39810000187.
- 27 G. Mengoli, M. M. Musiani, D. Pletcher and S. Valcher, *J. Appl. Electrochem.*, 1987, **17**, 525–531.
- 28 G. Mengoli, M. M. Musiani, R. Tomat, S. Valcher and D. Pletcher, *J. Appl. Electrochem.*, 1985, **15**, 697–704.
- 29 H. Tsutsumi and Y. Matsuda, *Electrochim. Acta*, 1993, **38**, 1373–1375.
- 30 J. Lee, D. Weingarth, I. Grobelsek and V. Presser, *Energy Technol.*, 2016, **4**, 75–84.
- 31 L. Chen, H. Bai, Z. Huang and L. Li, *Energy Environ. Sci.*, 2014, **7**, 1750–1759.
- 32 J. Lee, N. Jäckel, D. Kim, M. Widmaier, S. Sathyamoorthi, P. Srimuk, C. Kim, S. Fleischmann, M. Zeiger and V. Presser, *Electrochim. Acta*, 2016, **222**, 1800–1805.
- 33 G. Wang, L. Zhang and J. Zhang, *Chem. Soc. Rev.*, 2012, **41**, 797–828.
- 34 I. Shown, A. Ganguly, L.-C. Chen and K.-H. Chen, *Energy Sci. Eng.*, 2015, **3**, 2–26.
- 35 B. Li, Z. Nie, M. Vijayakumar, G. Li, J. Liu, V. Sprenkle and W. Wang, *Nat. Commun.*, 2015, **6**, 6303.
- 36 K. Fic, M. Meller, J. Menzel and E. Frackowiak, *Electrochim. Acta*, 2016, **206**, 496–503.
- 37 E. Frackowiak and F. Béguin, *Carbon*, 2002, **40**, 1775–1787.
- 38 S. Higashi, S. W. Lee, J. S. Lee, K. Takechi and Y. Cui, *Nat. Commun.*, 2016, **7**, 11801.
- 39 C. L. Bentley, A. M. Bond, A. F. Hollenkamp, P. J. Mahon and J. Zhang, *Electrochim. Acta*, 2013, **109**, 554–561.
- 40 G. Juhel, B. Beden, C. Lamy, J. M. Leger and R. Vignaud, *Electrochim. Acta*, 1990, **35**, 479–481.
- 41 C. Chakkaravarthy, A. K. A. Waheed and H. V. K. Udupa, *J. Power Sources*, 1981, **6**, 203–228.
- 42 D. Weingarth, H. Noh, A. Foelske-Schmitz, A. Wokaun and R. Kötz, *Electrochim. Acta*, 2013, **103**, 119–124.
- 43 Y. Gogotsi and P. Simon, *Science*, 2011, **334**, 917–918.
- 44 K. R. Ward, L. Xiong, N. S. Lawrence, R. S. Hartshorne and R. G. Compton, *J. Electroanal. Chem.*, 2013, **702**, 15–24.
- 45 M. C. Henstridge, E. J. F. Dickinson, M. Aslanoglu, C. Batchelor-McAuley and R. G. Compton, *Sens. Actuators, B*, 2010, **145**, 417–427.
- 46 I. Streeter, G. G. Wildgoose, L. Shao and R. G. Compton, *Sens. Actuators, B*, 2008, **133**, 462–466.
- 47 J. H. Pikul, H. Gang Zhang, J. Cho, P. V. Braun and W. P. King, *Nat. Commun.*, 2013, **4**, 1732.
- 48 P. Simon and Y. Gogotsi, *Nat. Mater.*, 2008, **7**, 845–854.

Supplementary Information

Nanoconfinement of redox reactions enables rapid zinc iodide energy storage with high efficiency

*Juhan Lee,^{ab} Pattarachai Srimuk,^{ab} Simon Fleischmann,^{ab}
Alexander Ridder,^{ab} Marco Zeiger,^{ab} and Volker Presser^{ab*}*

^a INM - Leibniz Institute for New Materials, 66123 Saarbrücken, Germany

^b Department of Materials Science and Engineering, Saarland University, 66123 Saarbrücken, Germany

* Corresponding author's eMail: volker.presser@leibniz-inm.de

Section 1: Material characterizations

Nitrogen sorption isotherms (**Fig. S1a**) recorded at $-196\text{ }^{\circ}\text{C}$ of ACF-1.1 and YP-80F (AC-1.4) can be classified as type I(b) shape. The isotherms for ACF-0.7 and ACF-0.8 are type I(a) implying that ACF-0.7 and ACF-0.8 have narrower pores ($<1\text{ nm}$) than ACF-1.1 and AC-1.4. The pore size distribution (PSD) patterns of AC and ACF were calculated with quenched-solid density functional theory (QSDFT) assuming slit pores. For multi-walled carbon nanotubes (MWCNTs), we applied non-local functional theory (NLDFT) with a hybrid model of slit and spherical pores because this yielded the best fit for the measured data. As can be seen from **Fig. S1b**, all three ACF samples are predominately microporous, whereas AC-1.4 also shows a small mesopore volume, and multi-walled carbon nanotubes (MWCNTs) are exclusively mesoporous. The pore structure parameters (surface area / pore volume / average pore size) can be found in the main manuscript (**Table 1**).

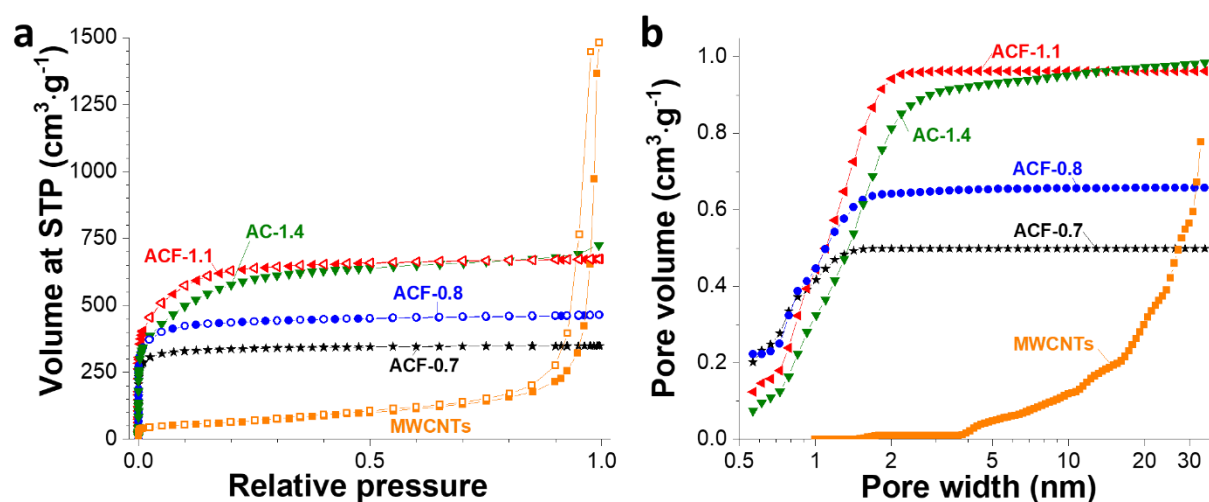


Fig. S1: Nitrogen gas sorption analysis of the carbon electrodes applied for this work. a) Nitrogen gas sorption isotherms at $-196\text{ }^{\circ}\text{C}$. b) Cumulative pore size distribution per volume.

The morphology of the carbon electrodes was examined by a JEOL JSM 7500F field emission scanning microscope (FE-SEM) at 3 kV (**Fig. S2**). The chemical composition of the carbon electrodes was determined by energy dispersive X-ray spectroscopy (EDX) with an X-Max-150 detector (Oxford Instruments) attached to the SEM chamber (**Table S1**). The spectra of ten spots were measured using an accelerating voltage of 10 kV and averaged; for the calibration, silicon crystal was applied. ACF samples show a highly-intertwined network of porous carbon fibers with an average diameter of about 5 μm and a length of up to several centimeters. The fibers themselves show a high internal porosity, as seen on the fiber surfaces and fracture cross-sections (**Fig. S2a-c**). MWCNT electrodes also form an intertwined network (**Fig. S2d**), whereas the tubes themselves show no internal porosity, as evidenced by GSA. Activated carbon of type AC-1.4 consists of particles in the size of several microns, which are connected by PTFE fibers (**Fig. S2e**). These particles show large, visible pores of up to 1 μm on the surface, which lead to a hierarchical, interparticle pore network.

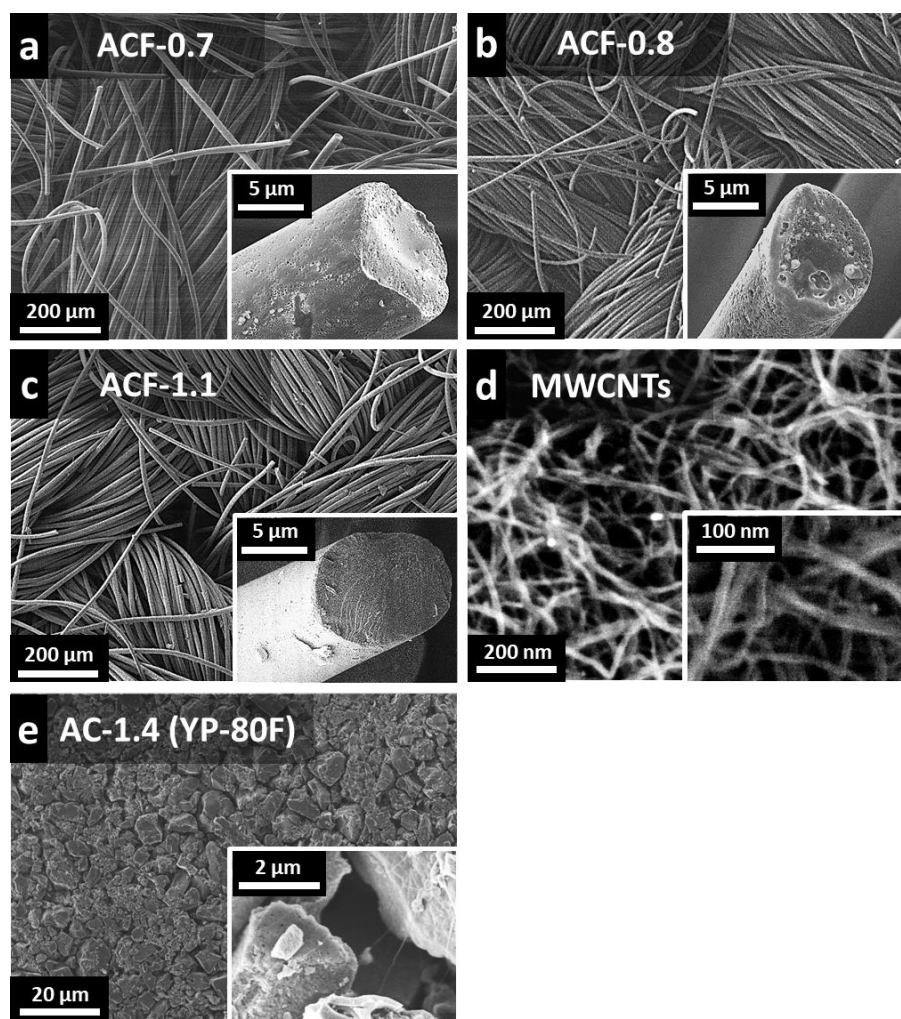


Fig. S2: Scanning electron micrographs of the different carbon electrode materials.

Table S1: Chemical composition of the carbon electrodes determined by EDX.

Sample	C (mass%)	O (mass%)	Al, F, Na, K, Si (mass%)
MWCNTs	>91	4-6	<4
ACF-0.7	>95	2-4	<1
ACF-0.8	>95	2-4	<1
ACF-1.1	>98	<2	<1
AC-1.4	>95	4-5	<1

Raman spectroscopy was carried out with a Renishaw inVia Raman microscope applying an Nd:YAG laser (532 nm) with a power of ca. 0.25 mW. With a grating of 2400 lines·mm⁻¹, yielding a spectral resolution of approximately 1.2 cm⁻¹. The spot size on the sample was about 2 μm with a numeric aperture of 0.9. Spectra were recorded for various carbon electrodes with an acquisition time of 30 s and 10 accumulations. D- and G-band deconvolution was carried out with baseline-subtracted, D-band normalized Raman spectra, employing four Voigt peaks.¹ The quantitative results are found in **Table S2**, Raman spectra are given in **Fig. S3**.

Peak deconvolution reveals a decreasing I_D/I_G ratio of 2.86, 2.79, and 2.61 for ACF-0.7, ACF-0.8, and ACF-1.1, respectively. Similarly, the FWHM values for the D-signal drop in the same order for these samples, from 141 to 109 cm⁻¹. Both a higher I_D/I_G ratio, as well as a higher FWHM of the D-signal are generally associated with an increase in structural carbon disorder that is linked to defects in the hexagonal graphite structure.² These defects originate mainly from micropores that disrupt the graphitic carbon lattice. The smallest micropores are found in ACF-0.7, causing quantitatively more carbon defects per volume of material, which leads to the highest I_D/I_G ratio and D-signal FWHM of this sample. AC-1.4, which exhibits a porosity comparable to ACF-1.1, leading to the same I_D/I_G of 2.61, the lower FWHM of the D-signal can be associated with a slightly lower fraction of micropores below 1 nm (**Fig. S1b**). MWCNTs have virtually no intraparticle pores, defects in the graphitic structure are mainly related to vacancies or non-hexagonal carbon rings.³ Therefore, they exhibit a less defective graphite structure, which leads to by far the lowest I_D/I_G (2.06) and FWHM of the D-signal (64 cm⁻¹).

Table S2: Results of Raman D- and G-band deconvolution Position and full width at half maximum (FWHM) are given, as well as the areal intensity ratio.

Sample	D-mode		G-mode		I_D/I_G ratio
	Position (cm^{-1})	FWHM (cm^{-1})	Position (cm^{-1})	FWHM (cm^{-1})	
MWCNTs	1353	64	1600	67	2.06
ACF-0.7	1337	141	1604	54	2.86
ACF-0.8	1338	126	1604	53	2.79
ACF-1.1	1335	109	1604	49	2.61
AC-0.8	1337	96	1602	55	2.61

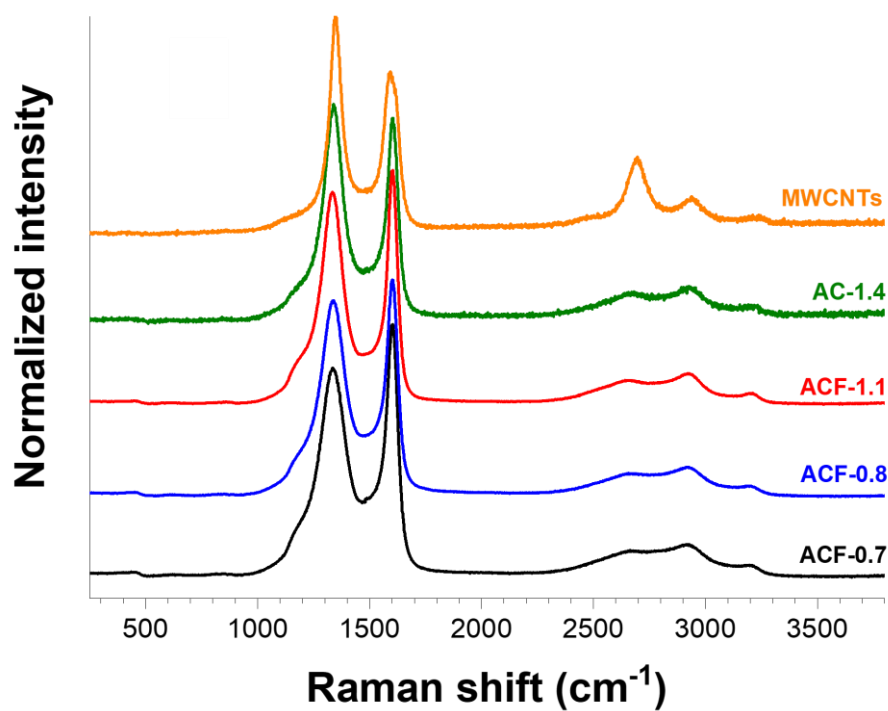


Fig. S3: Raman spectra of samples ACF-0.7, ACF-0.8, ACF-1.1, AC-1.4, and MWCNT.

Section 2: Redox kinetics of potassium ferricyanide and iodide in nanoporous carbon

To investigate the kinetic of redox electrolyte in nanoporous carbon electrodes, we first benchmarked a well-established standard redox couple with one electron transfer, namely 1 M of potassium ferricyanide, PFC. The inset in **Fig. S4a** illustrates cyclic voltammograms of a flat surface electrode (5 mm diameter glassy carbon, GC, ALS GmbH) and nanoporous activated carbon (AC-1.4) coated on GC at a scan rate of $100 \text{ mV}\cdot\text{s}^{-1}$. The detailed preparation of the carbon coated GC can be found in Ref.⁴. The CVs of GC and AC-1.4 electrodes exhibit half-wave potential of +0.26 V and +0.21 V vs. Ag/AgCl, respectively, with different oxidation and reduction current response. The reduction currents of GC and AC-1.4 electrodes versus scan rate follow a power law ($y=ax^e+b$) with an exponent of 0.3 for GC and 1.0 for AC-1.4 (**Fig. S4a**). Therefore, the redox kinetics in AC-1.4 electrode seems to follow the recently suggested thin layer diffusion electrochemistry (exponent close to 1) than the planar diffusion electrochemistry (exponent close to 0.5).⁵⁻⁷

So far, the thin layer diffusion electrochemistry has been studied mostly with the carbon nanotubes with various arrangement for different type of pore space between the tubes. After the pioneering modeling and simulation work for the thin layer electrochemistry,⁵⁻⁷ enhanced redox kinetics in porous carbon electrode were reported in case of macroporous and mesoporous carbons via diffusion-less redox reactions and fast ion diffusion in the confined carbon pores, respectively.^{8,9} Our results of microporous activated carbon electrode (AC-1.4) strongly support the electrochemical thin layer process from previous reported meso- and macroporous carbon studies. However, since the contribution of electric double-layer (EDL) formation is reported to be significant for high surface carbon electrode in case ferricyanide/ferrocyanide redox couple,¹⁰ the conventional electrochemical analyses could be misleading when the influence of ELD is not considered. Therefore, the influence of the electric double-layer must be excluded for the analysis. The implementation of rotating disk electrode (RDE, RRDE-3A, ALS GmbH) allows us to investigate the redox kinetic in nanoporous carbon since the contribution of electric double-layer can be kept at a constant scan rate while kinetic condition is varied via rotational speed of the electrode.

The bulk hydrodynamic diffusion generated via the spinning of the electrode leads to a thin and constant diffusion layer. Hence, the rate is limited mostly to the diffusion of redox species near the charges transfer zone. **Fig. S4b-c** shows cyclic voltammograms at $100 \text{ mV}\cdot\text{s}^{-1}$ with different rotational speed. By increasing the rotational speed of electrode from 200 rpm to 3200 rpm, the $\text{Fe}(\text{CN}_6)^{4-}$ ions in bulk regime are transported faster into the diffusion layer. Therefore, the reduction current is increasing as a function of increasing rotational speed. This phenomenon is explained by Koutecky-Levich equation,^{4, 11}

$$\frac{1}{j} = \frac{1}{j_k} + \frac{1}{j_L} = \frac{1}{B} \omega^{-0.5} + \frac{1}{nFKC} \quad (\text{Eq. S1})$$

where, j is the measured current, j_k the intrinsic kinetic limit current, j_L is the mass transfer limit current, F is Faraday constant, C is bulk concentration, and n is number of electron involved in the reaction which is the proportional to the square root of angular velocity (ω) of RDE electrode. The proportionality is defined as B ,

$$B = 0.62D^{2/3}\nu^{-1/3}nFC \quad (\text{Eq. S2})$$

where, ν is the kinematic viscosity of the electrolyte and D is diffusion coefficient of reactant. We assume j_k to be constant at certain potential with rate constant (k).

As shown in **Fig. S4d**, the linear relation between response current and angular speed is obtained. The slope of the graph (B^{-1}) corresponds to the diffusion coefficient. The diffusion coefficient was calculated by using $\nu = 0.00921 \text{ cm}^2\cdot\text{s}^{-1}$, $n=1$, $F=96485 \text{ mol}^{-1}$, and $C=0.001 \text{ mol}\cdot\text{cm}^{-3}$. In case of nanoconfined redox ions (AC-1.4), the diffusion coefficient of $2.1\cdot 10^{-7} \text{ cm}^2\cdot\text{s}^{-1}$ was obtained while the diffusion coefficient for GC flat electrode was calculated to be $1.6\cdot 10^{-7} \text{ cm}^2\cdot\text{s}^{-1}$. The higher diffusion coefficient of the nanoporous carbon than that of GC flat electrode confirms the redox kinetic is enhanced in nanoporous carbon as enabled by the fast diffusion of redox ions in the confinement of carbon nanopores.

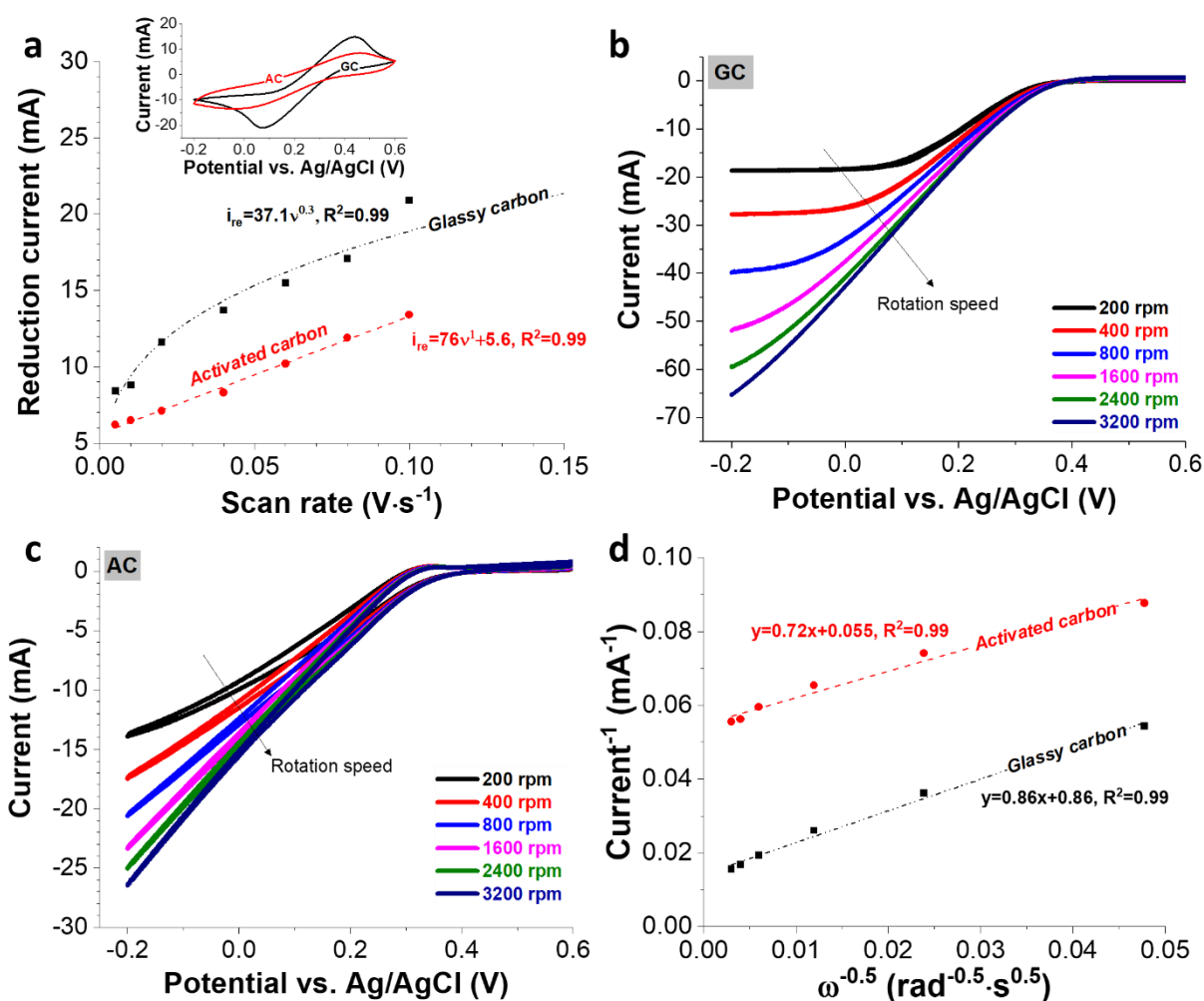


Fig. S4: Kinetic study of redox couple (1 M potassium ferricyanide) with cyclic voltammetry under static and dynamic condition. Dynamic condition was given by rotation disk electrode. a) the reduction current versus scan rate corresponding result from cyclic voltammogram (inset) in 1 M potassium ferricyanide, b-c) cyclic voltammogram of GC and AC-1.4 electrode with different rotational speed and d) Koutecky-Levich relation plot.

The same strategy is applied to study kinetic of potassium iodide (KI). Iodide is the complex redox reaction which undergo oxidation by donating two electrons to form iodine/and triiodide at standard potential of 0.54 V vs SHE, afterward the resulting iodine can be reacted with water to form iodate ion at potential of 1.2 V vs SHE. The latter is an irreversible reaction (inset **Fig. S5a**) consuming the iodide ions leading to poor charge efficiency particularly. Therefore, we avoid the second reaction by limiting potential lower than 0.6 V vs. SHE (0.4 V vs. Ag/AgCl):



Fig. S5a shows the cyclic voltammograms of AC-1.4 and GC electrode in 0.1 M KI and 0.5 M K₂SO₄. In the case of GC, the onset oxidation potential of iodide (I⁻) ion was observed to be at +0.12 V vs. Ag/AgCl. The oxidation current is sharply increase up to 0.15 mA at +0.3 V vs. Ag/AgCl; afterwards, the electrode was backward scanned, leading to reduction of triiodide/iodine(I₂/I₃⁻). The ratio of oxidation and reduction current (I_{re}/I_{ox}) is 0.57 suggesting irreversible process possibly due to redox shuttling and precipitation of I₂.^{12, 13} The latter is strongly depended on the identity of electrode such as microstructure and surface chemistry. The cyclic voltammogram of 0.1 M KI and 0.5 M K₂SO₄ performs differently in AC-1.4 compared to the flat electrode (GC). The onset oxidation potential was observed to be 0.12 V vs. Ag/AgCl, which is 0.18 V lower than in GC electrode possibly via the higher local concentration which trapped inside pores and thin layer diffusion.⁸ The I_{re}/I_{ox} of AC-1.4 is 0.98, confirming that nanoporous carbon mitigate the redox shuttling and favor to form triiodide instead of iodine resulting high degree of reversible reaction. **Fig. S5b** illustrates the reduction current of triiodine on AC-1.4 and GC electrode plotted against the scan rate. By fitting the curve with a power law, the kinetic limit can be identified (**Fig. S5b**): AC-1.4 exhibits an exponent of 0.4 and the GC flat electrode of 0.2. Because the oxidation potential was not scanned till the peak current appears, the low exponent numbers (<0.5) do not necessarily indicate slow redox kinetics in both cases. The reduction current is rather reduced due to the larger peak separation at higher scan rate than the kinetic limitations since the non-equilibrium state of the reaction to the oxidation peak current is growing as the peak separation is getting broader in a fixed potential window for the scanning. Because the thin layer electrochemistry in carbon pores is also featured by the narrow peak separation with less distortion in shape,⁵⁻⁸ the lower exponent number for AC-1.4 than that of GC flat electrode still implies that the redox kinetics of iodide system in nanopores is faster than on the flat electrode.

Further studies with RDE in 0.1 M KI and 0.5 M K₂SO₄ (**Fig. S5c**) show that the reduction current for AC-1.4 is slightly increased by increasing of rotating speed being good align with Koutecky-Levich equation (**Fig. S5d**). The slope of curve was 1.26, translating to a diffusion coefficient of $5.3 \cdot 10^{-3} \text{ cm}^2 \cdot \text{s}^{-1}$. As compared to a previous study, the diffusion coefficient of I⁻ on GC electrode estimated from static condition is between $1.6 \cdot 10^{-5}$ and $2.6 \cdot 10^{-7} \text{ cm}^2 \cdot \text{s}^{-1}$ depending on the concentration.^{13, 14} These values are much lower than that of AC-1.4 electrode. In addition, the RDE result in GC electrode does not fit to the Koutecky-Levich since we observed no change of reduction and oxidation current when the electrode rotation speed is increased. This is possible when the formation of triiodide ions is dominated by deposition/adsorption of iodine/iodide leading to continuous shuttling process of oxidized triiodide/iodine ion. Since the redox reactions are confined in the case of porous carbons in narrow pores,⁸ this active site blocking does not play an influential role in case of AC-1.4. Considering the specific adsorption behavior of iodide,¹⁵ confining iodide into the carbon micropores seems to be crucial for enhanced redox kinetics as well as high reversibility enabled by low-degree of redox shuttling.

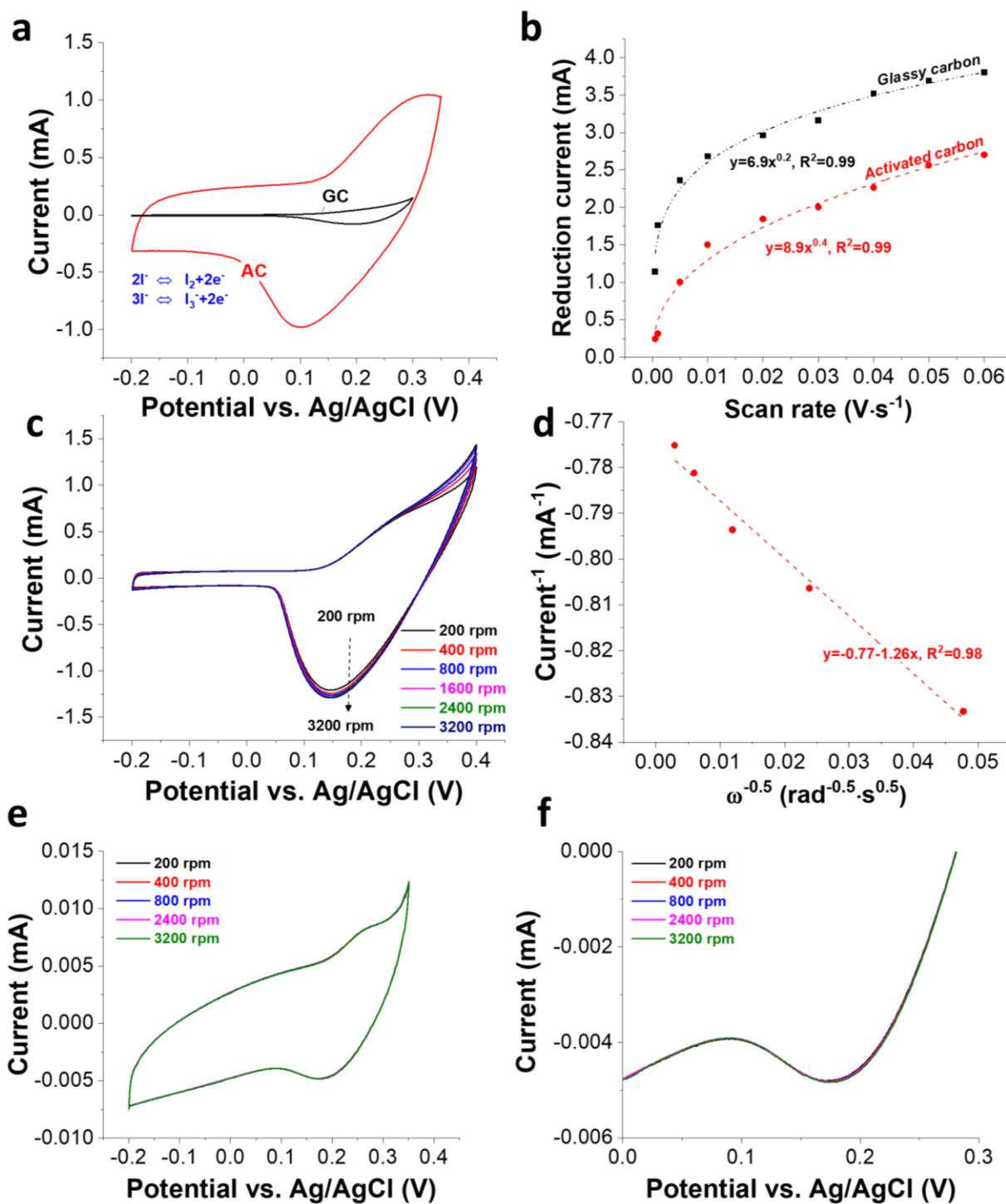


Fig. S5: The kinetic study of iodide on GC and AC electrode with cyclic voltammetry under static and dynamic condition. a) Cyclic voltammogram of GC and AC electrode in 0.1 M KI and 0.5 M K_2SO_4 , b) plot of reduction current versus scan rate respecting result from cyclic voltammogram, c) cyclic voltammogram of AC electrode in 0.1 M KI and 0.5 M K_2SO_4 with different rotational speed, d) Koutecky-Levich relation plot, e) and f) cyclic voltammogram of GC electrode in 0.1 M KI and 0.5 M K_2SO_4 with different rotational speed.

Section 3: Validity of carbon quasi-reference electrode

Porous carbon for use as a quasi-reference electrode has been demonstrated by us in previous work (Ref. ¹⁶). In short, porous carbon can be effectively applied to aqueous electrochemistry when a reproducible reference potential of the applied carbon quasi-reference electrode (QRE) is validated in a certain system with the acceptable stability for the experimental time frame. Considering the scope of our work, the reproducible reference potential within the range of 50 mV is reasonable when the reference potential is stable for at least 48 h; this corresponds with the time required for the characterization of ACF/Zn ZnI₂ batteries and the self-discharge rate of 1 M KI solution with various cathodes in half-cell configuration.

For the determination of the reference potential of the applied carbon QRE (YP-80F with 5 mass% PTFE), activated carbon fiber electrodes (ACF-0.8) were charged to 0.2 mAh at 1.1 mA·cm⁻² in half-cell configuration vs. carbon QRE and the OCP of the ACF-0.8 was measured by subtracting the iR drop (**Fig. S6**, inset). After the OCP period, the cell is discharged until the potential plateau disappeared. By this way, we have ensured that the iodine and triiodide are completely in a reduced state. In this manner, OCPs were measured after various resting time after the cell assembly. We note a small standard deviation of ca. 11 mV from three cells. A particularly stable reference potential can be seen after 30 h which also aligns with our previous observations with potassium ferricyanide containing neutral aqueous solutions.¹⁶ Given that the measured OCP does not shift more than 10 mV for 2.5 d measurement, the applied carbon QRE is considered to be valid for the scope of our work.

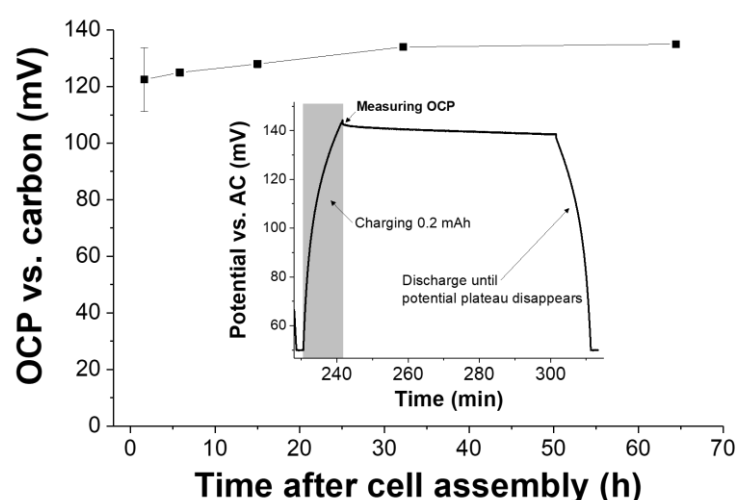


Fig. S6: Validity test for porous carbon quasi-reference electrode in 1 M KI solution. The reproducibility and the stability of the reference potential was measured by observing open circuit potential after charging the working electrode up to 1 mAh with the capacity limit of 0.2 mAh.

Section 4: Stability (S-value) analysis in charge reversibility point of view

Quantitative data analysis of cyclic voltammograms via S-value testing (**Fig. S7**, inset) is an effective analytical method to quantify i) the onset potential window of the chemical decomposition potential or irreversible electrochemical reaction by thorough investigation on the reversibility of the charge,^{17, 18} ii) charge storage capacity at the applied voltage window, and iii) cyclic voltammograms containing information about the redox reactions.

The S-value is defined per Ref. ¹⁷ as:

$$S = \frac{Q_{char}}{Q_{dis}} - 1 \quad (\text{Eq. S6})$$

where Q_{char} is the charge accumulated during charging (i.e., oxidation in our case) and Q_{dis} is the amount of charge released during discharging (i.e., reduction in our case). The comprehensive data from S-value testing can directly be converted in a plot of specific capacity vs. maximum applied cell voltage (**Fig. S7**). The limit for the stable cell voltage can be determined either by the upper S-value limit of 0.1 or by the exponent increase in S-value, which corresponds to irreversible Faradaic reaction.^{17, 19} In **Fig. S7**, the maximum stable potential window for ACF-0.8 cathode is determined to be 375 mV (marked gray) where S-value starts increase exponentially. While conducting the S-value analysis, also the potential of the Zn disk was measured (**Fig. S7**). In the stable potential range of the cathode, the Zn disk potential was fluctuating with the amplitude of ca. 0.06 V around 0.97 V implying that the redox potential of $Zn^{2+}/Zn(s)$ on Zn disk is in that range.

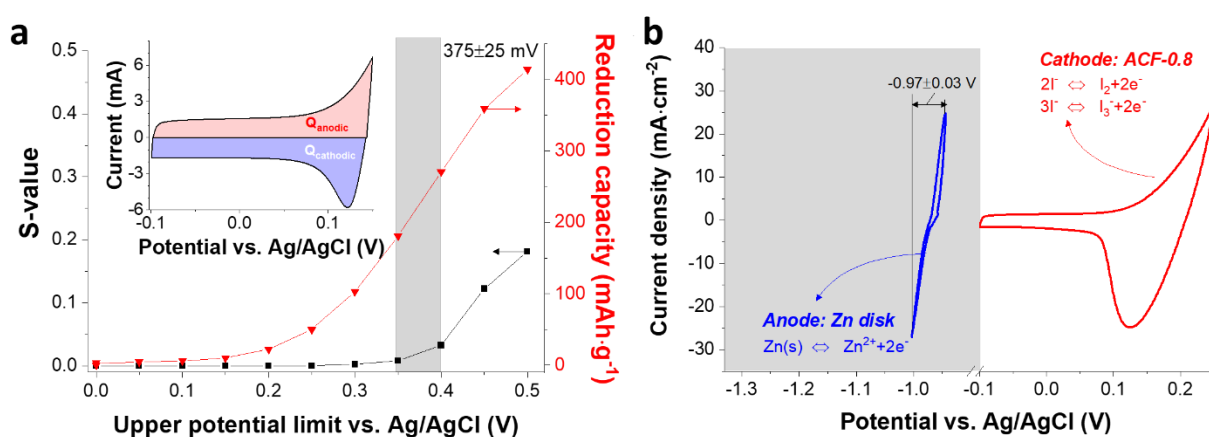


Fig. S7: Electrochemical analysis of an ACF/Zn battery in 1.2 M ZnI₂ solution. a) S-value results and reduction capacities are plotted as a function of upper potential limit. Inset shows the cyclic voltammogram obtained as the upper potential limit was set to 0.15 V vs. Ag/AgCl. b) Cyclic voltammograms obtained for ACF-0.8 working electrode as operated by Ag/AgCl reference electrode while recording the potential of the Zn disk counter electrode.

Section 5: Normalization for Ragone plot

For the evaluation of electrochemical energy storage materials, the most common normalization method is to consider only the mass or volume of the electrode excluding the electrochemically inactive materials such as separators, binder materials, and electrolyte.²⁰ For the comparison with the other systems, volumetric or gravimetric Ragone charts are often used; however, such comparisons can be misleading since the performance of the commercially available energy storage systems is commonly normalized to the entire cell volume and mass, while the claimed performance is mostly normalized only by the active mass of the electrode.¹⁵ Considering that volume and the mass of the current collectors and the outer housing can be significantly minimized by state of the art engineering techniques, particularly, when the size of the system is getting bigger, normalization to the total mass or volume of the electrode, separator, and electrolyte is a reasonable solution for the comparison to the commercially available systems in Ragone chart. As reported in Ref. 15, a complexity arises for the estimation of the electrolyte mass in porous carbon while volumetric normalization can be easily done by considering the geometrical volume of the electrode, electrolyte, and separator. Following the procedures described in Ref. 15 we calculated the volume of the electrolyte which is filled in the porous carbon via Equation (S7),

$$V_{free} = V_{geo} - \frac{m_c}{\rho_{skel}} \quad (\text{Eq. S7})$$

where V_{free} is the free volume in the porous carbon filled with electrolyte, V_{geo} is the geometric volume of the electrode compartment, m_c is the mass of the activated carbon fiber, and ρ_{skel} is the skeletal density of the activated carbon electrode which is $2.1 \text{ g}\cdot\text{cm}^{-3}$.

For the electrolyte volume in the separators, the following equation is applied.

$$V_{freeS} = V_{geoS} \cdot P_{sep} \quad (\text{Eq. S8})$$

where V_{freeS} is the free volume in the separator filled with electrolyte, V_{geoS} is the geometric volume of the separator, and P_{sep} is the porosity of the separator. For the glassy fiber separator, the porosity was 0.9 and for Celgard 3501 it was 0.55.

Since our volume limited cell does not have space for the electrolyte except the geometric volume of the separator and the electrode, the mass of the total electrolyte (m_{el}) in the cell was derived via:

$$m_{el} = (V_{freeS} + V_{free}) \cdot \rho_{el} \quad (\text{Eq. S9})$$

where ρ_{el} is the measured electrolyte density.

For comparison, the power and energy storage performance are also normalized only by the mass of the electrode (**Fig. S8a**).

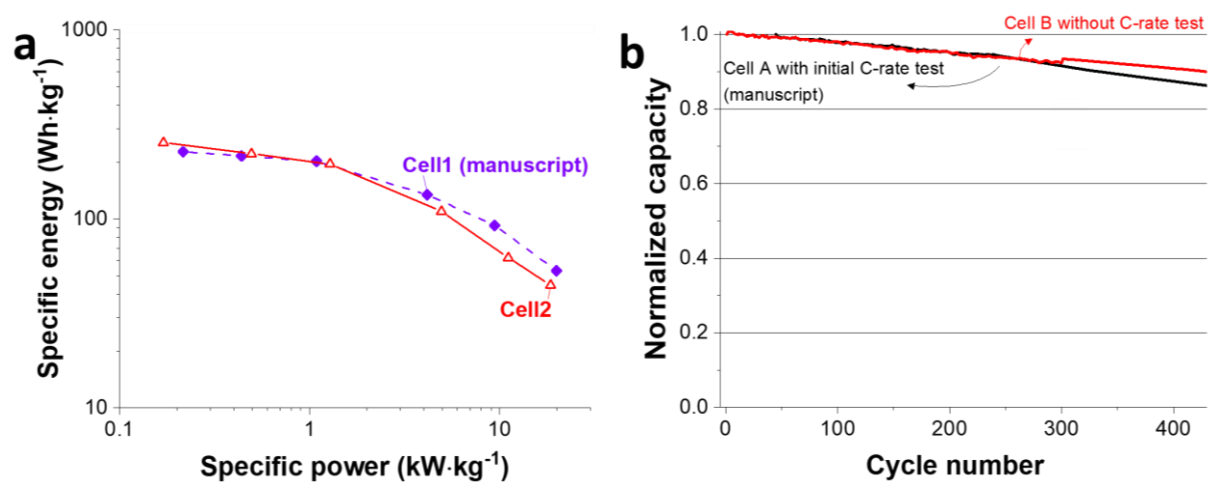


Fig. S8: Electrochemical performance of ACF/Zn 1.2 M ZnI₂ battery cells. a) Specific power and energy from two ACF/Zn 1.2 M ZnI₂ battery cells as normalized only by the mass of the electrode. b) Cyclic stability of two ACF/Zn 1.2 M ZnI₂ battery cells. Cell A was characterized with the initial C-rate test while Cell B was characterized without C-rate test. Here, the normalized capacities are shown only from the 1 C-rate results.

References for Supporting Information

1. M. Zeiger, N. Jäckel, D. Weingarh and V. Presser, *Carbon*, 2015, **94**, 507-517.
2. J. Cebik, J. K. McDonough, F. Peerally, R. Medrano, I. Neitzel, Y. Gogotsi and S. Osswald, *Nanotechnology*, 2013, **24**, 205703.
3. Y. E. Lozovik, S. Ogarkov and A. Sokolik, *Phys. Rev. B*, 2012, **86**, 045429.
4. P. Srimuk, L. Ries, M. Zeiger, S. Fleischmann, N. Jackel, A. Tolosa, B. Krüner, M. Aslan and V. Presser, *RSC Adv.*, 2016, **6**, 106081-106089.
5. K. R. Ward, L. Xiong, N. S. Lawrence, R. S. Hartshorne and R. G. Compton, *J. Electroanal. Chem.*, 2013, **702**, 15-24.
6. M. C. Henstridge, E. J. F. Dickinson, M. Aslanoglu, C. Batchelor-McAuley and R. G. Compton, *Sens. Actuators, B*, 2010, **145**, 417-427.
7. I. Streeter, G. G. Wildgoose, L. Shao and R. G. Compton, *Sens. Actuators, B*, 2008, **133**, 462-466.
8. R. Narayanan and P. R. Bandaru, *J. Electrochem. Soc.*, 2014, **162**, A86-A91.
9. S. Chathoth, E. Mamontov, S. Dai, X. Wang, P. Fulvio and D. Wesolowski, *Europhys. Lett.*, 2012, **97**, 66004.
10. J. Lee, S. Choudhury, D. Weingarh, D. Kim and V. Presser, *ACS Appl Mater Interfaces*, 2016, **8**, 23676-23687.
11. P. Srimuk, M. Zeiger, N. Jäckel, A. Tolosa, B. Krüner, S. Fleischmann, I. Grobelsek, M. Aslan, B. Shvartsev and M. E. Suss, *Electrochim. Acta*, 2017, **224**, 314-328.
12. E. I. Rogers, D. S. Silvester, L. Aldous, C. Hardacre and R. G. Compton, *The Journal of Physical Chemistry C*, 2008, **112**, 6551-6557.
13. C. L. Bentley, A. M. Bond, A. F. Hollenkamp, P. J. Mahon and J. Zhang, *Electrochim. Acta*, 2013, **109**, 554-561.
14. C. L. Bentley, A. M. Bond, A. F. Hollenkamp, P. J. Mahon and J. Zhang, *J. Phys. Chem. C*, 2015, **119**, 22392-22403.
15. S.-E. Chun, B. Evanko, X. Wang, D. Vonlanthen, X. Ji, G. D. Stucky and S. W. Boettcher, *Nat Commun*, 2015, **6**, 7818.
16. J. Lee, N. Jäckel, D. Kim, M. Widmaier, S. Sathyamoorthi, P. Srimuk, C. Kim, S. Fleischmann, M. Zeiger and V. Presser, *Electrochim. Acta*, 2016, **222**, 1800-1805.
17. D. Weingarh, H. Noh, A. Foelske-Schmitz, A. Wokaun and R. Kötz, *Electrochim. Acta*, 2013, **103**, 119-124.
18. J. Lee, D. Weingarh, I. Grobelsek and V. Presser, *Energy Technol.*, 2016, **4**, 75-84.
19. K. Xu, S. P. Ding and T. R. Jow, *J. Electrochem. Soc.*, 1999, **146**, 4172-4178.
20. Y. Gogotsi and P. Simon, *Science*, 2011, **334**, 917-918.

4. Conclusions and outlook

This PhD thesis has investigated REHES systems to advance both the fundamental understanding and the electrochemical energy storage performance. While revisiting the known systems like AC|K₃Fe(CN)₆|AC and AC|KI|AC, a couple of systems are introduced as a new generation of electric energy storage devices such as Zn|ZnI₂|AC batteries and AC|SnF₂|VOSO₄|AC hybrid energy storage device. The basic understanding of the REHES systems enabled a significant enhancement of the device performance throughout this PhD work (**Fig. 17A**) compared to the state-of-the-art.

The redox-active surfactant (tetrapropylammonium iodide) modified redox electrolyte from the initial work exhibited only 81 F/g (ca. 4 Wh/kg at 1.2 V) while the higher values were achieved, namely: 28.3 Wh/kg for AC|K₃Fe(CN)₆|AC, 33 Wh/kg for AC|KI|AC, 75 Wh/kg for AC|VOSO₄+SnSO₄|AC, and 226 Wh/kg for Zn|ZnI₂|AC as normalized by m_a . Rapid redox reactions in nanoconfinement of carbon pores smaller than 1 nm give access to high power applications. For example, Zn|ZnI₂|AC exhibits a specific power of 20 kW/kg (**Fig. 17A**, normalized by m_a), which is even higher than that of state of the art AC|AC aqueous double-layer capacitor (5.2 kW/kg, normalized by m_a). This breaks with the paradigm that power must always be traded for energy storage capacity, and vice versa. All results indicate that the REHES systems are very promising for the new generation of electric energy storage not only because of high device performances (**Fig. 17B**) but also because of simplicity of the system. The redox electrolyte can be readily applied to the porous electrodes commonly used for electrical double-layer capacitors. Furthermore, the possibility for its low production cost is attractive as compared to other expensive battery materials like nickel, cadmium, and cathode materials for lithium-ion batteries.

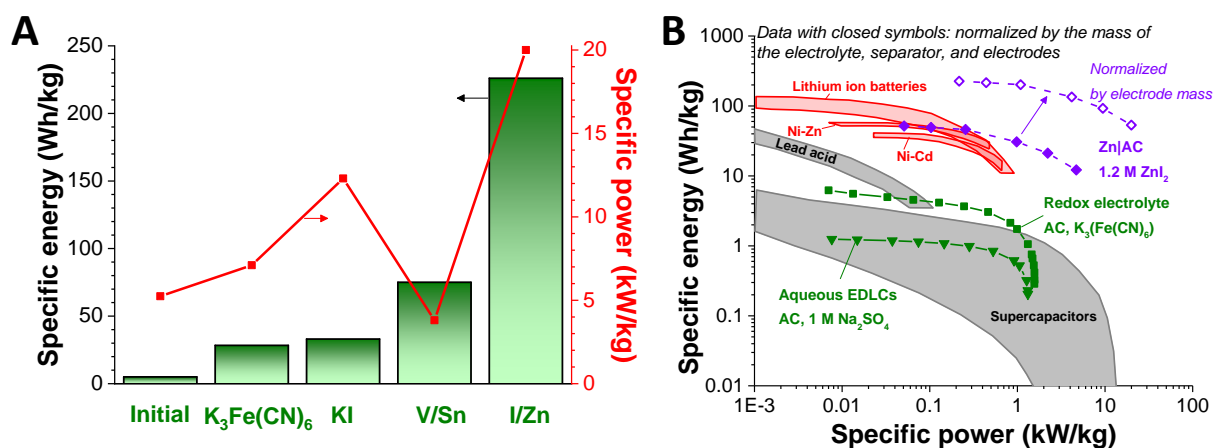


Figure 17 Overview of the REHES device performance through this PhD work. (A) Specific energy and power performance of the REHES systems. (B) Ragone plot for the comparison with other commercially available electric energy storage devices. Adapted from Ref. [40] with permission from The Royal Society of Chemistry.

The performance improvements achieved in this work were only possible by a rigorous understanding of the fundamental electrochemistry of REHES systems and their electrode materials. It was of high importance to adequately design a device considering the charge balance between positive and negative electrodes while keeping the potentials of both electrodes within the electrochemical stability windows. In this regard, reversible hydrogen storage at the negative electrode can be used to achieve charge balancing in response to the redox-enhanced charge storage capacity at the positive electrode. For high reversibility of the hydrogen reaction, microporous carbons play an essential role by enabling high charge storage capacity as well as the high specific energy of the device through the upper operating cell voltage around 1.2-1.8 V. Such values are exceeding the theoretical water splitting cell voltage of 1.23 V. To identify the electrochemical stability window, we found the *S*-value analysis to be particularly useful. It requires relatively short measuring time as compared to other methods like floating and GCPL tests.

The major drawback of the reversible hydrogen storage is low energy efficiency due to high overpotential of the reaction. Hence, the design of the redox systems other than hydrogen reaction had been highly required at the negative electrode. As alternatives, redox electrolytes based on $Sn(s)/Sn^{2+}$ and $Zn(s)/Zn^{2+}$ were applied at the negative electrode. In this case, the charge can be easily balanced by adjusting the concentration ratio of the redox couples for positive and negative electrodes.

Another important aspect is the need to optimize the carbon pore structure. For the optimization of carbon pore structure, we found the most important aspects are to understand the fundamentals of diffusion and adsorption of redox ions in carbon micropores. The diffusion of redox ions plays essential roles for:

- i) potential redistribution of the cell by the diffusion of oxidized/reduced redox ions,
- ii) diffusion-less redox reaction by the confinement of redox ions in carbon micropores, and
- iii) self-discharge by redox shuttling through the diffusion of oxidized or reduced ions.

First, we found that the confinement of redox ions prevents the loss of cell voltage during the resting time which occurs by the inhomogeneous oxidation state of redox ions in the entire electrolyte. When the cell is rapidly charged, the oxidation states are different at the electrode and the bulk electrolyte, and the potential drops quickly according to the Nernst equation as the diffusion redistributes the ions. For the prevention of the latter, the ions can be confined to narrow carbon pores.

Second, the nanoconfinement of the redox ions in carbon micropores enables the high power performance of REHES systems through diffusion-less redox kinetics. For the investigation of redox kinetics, not only the redox electrochemistry must be considered but also the contribution of the double-layer formation. When the influence of the latter is non-negligible, the conventional analysis with Randles-Ševčík equation becomes inaccurate. As suggested from the last part of this PhD work with ZnI_2 redox electrolyte, the diffusion and kinetics of redox ions in microporous carbon can be effectively studied by rotating disk electrode by applying the Koutechky-Levich equation. So far, the most reliable way to describe these effects is based on the thin-layer electrochemistry (TLE). However, TLE modeling and simulations so far assumed a constant diffusion coefficient throughout the system. As shown by recent works, the diffusion coefficient may considerably vary throughout the space in the electrode and the bulk electrolyte. Possibly, it depends on the shape and the size of the pores as well as the chemical composition of the electrode surface. Likewise, the local concentration[136] and the adsorption energy of ions could also rely on these parameters[40]. Therefore, there is a strong need for the further improvement of reliable models considering the influence of pore size on local ion concentration, diffusion coefficient, and the adsorption energy.

Third, the application potential for REHES systems would remain severely limited due to the redox shuttling through the diffusion of oxidized or reduced ions. For the prevention of the redox shuttling, ion selective membranes are often necessary. However, their rigorous use would be a severe cost driver, particularly, for large-scale applications. New perspectives to overcome the need of such membranes arise by studying the adsorption of redox ions in carbon nanopores. Immobilizing the redox ions by strong adsorption, the systems with the micropores carbon electrodes do not require the use of ion selective membrane to hinder the notorious redox shuttling. As demonstrated by this PhD work with carbon fiber electrode with various average pore size, the adsorption of iodide was found to be stronger in sub-nanometer pores (<1 nm), but to be much weaker in larger pores.

Considering the diffusion-less fast redox reaction, narrower pores are beneficial, while the charge storage capacity requires a large pore volume. Therefore, for the optimized performance of REHES systems, the pore volume is recommended to be maximized while keeping the high portion of narrow pores. The larger pores are expected to bring negative influence through the diffusion-controlled charge redistribution of the electrolyte.

Compared to the aqueous redox electrolyte systems, non-aqueous redox electrolyte systems remain ill-explored. They offer the key benefit of enabling a high operating cell voltage (1.2-4 V), while their general drawback is lower power performance in comparison to the aqueous systems due to low ionic conductivity. In the future, non-aqueous REHES systems with improved ion mobility may play an important role as a bridge between aqueous REHES systems for power management and battery systems for energy management.

References

- [1] E. Pomerantseva, Y. Gogotsi, Two-dimensional heterostructures for energy storage, *Nat. Energy*, 2 (2017) 17089.
- [2] J.R. Miller, A.F. Burke, Electrochemical capacitors: challenges and opportunities for real-world applications, *Electrochem. Soc. Interface*, 17 (2008) 53.
- [3] J.R. Miller, P. Simon, Electrochemical Capacitors for Energy Management, *Science*, 321 (2008) 651-652.
- [4] M.R. Lukatskaya, B. Dunn, Y. Gogotsi, Multidimensional materials and device architectures for future hybrid energy storage, *Nat. Commun.*, 7 (2016) 12647.
- [5] D. Linden, T.B. Reddy, *Handbook of Batteries*. 3rd, McGraw-Hill, 2002.
- [6] L.J. Krause, T. Brandt, V.L. Chevrier, L.D. Jensen, Surface Area Increase of Silicon Alloys in Li-Ion Full Cells Measured by Isothermal Heat Flow Calorimetry, *J. Electrochem. Soc.*, 164 (2017) A2277-A2282.
- [7] L.J. Krause, L.D. Jensen, V.L. Chevrier, Measurement of Li-Ion Battery Electrolyte Stability by Electrochemical Calorimetry, *J. Electrochem. Soc.*, 164 (2017) A889-A896.
- [8] G.Z. Chen, Supercapacitor and supercapattery as emerging electrochemical energy stores, *Int. Mater. Rev.*, 62 (2017) 173-202.
- [9] A. Mukhopadhyay, B.W. Sheldon, Deformation and stress in electrode materials for Li-ion batteries, *Prog. Mater. Sci.*, 63 (2014) 58-116.
- [10] B. Evanko, S.W. Boettcher, S.J. Yoo, G.D. Stucky, Redox-Enhanced Electrochemical Capacitors: Status, Opportunity, and Best Practices for Performance Evaluation, *ACS Energy Lett.*, 2 (2017) 2581-2590.
- [11] L. Xia, L. Yu, D. Hu, G.Z. Chen, Electrolytes for electrochemical energy storage, *Mater. Chem. Front.*, 1 (2017) 584-618.
- [12] J. Lee, B. Krüner, A. Tolosa, S. Sathyamoorthi, D. Kim, S. Choudhury, K.-H. Seo, V. Presser, Tin/vanadium redox electrolyte for battery-like energy storage capacity combined with supercapacitor-like power handling, *Energy Environ. Sci.*, 9 (2016) 3392-3398.
- [13] V. Augustyn, P. Simon, B. Dunn, Pseudocapacitive oxide materials for high-rate electrochemical energy storage, *Energy Environ. Sci.*, 7 (2014) 1597-1614.
- [14] E. Herrero, L.J. Buller, H.D. Abruña, Underpotential Deposition at Single Crystal Surfaces of Au, Pt, Ag and Other Materials, *Chem. Rev.*, 101 (2001) 1897-1930.
- [15] N. Yoshida, Y. Yamada, S.-i. Nishimura, Y. Oba, M. Ohnuma, A. Yamada, Unveiling the origin of unusual pseudocapacitance of $\text{RuO}_2 \cdot n\text{H}_2\text{O}$ from its hierarchical nanostructure by small-angle x-ray scattering, *J. Phys. Chem. C*, 117 (2013) 12003-12009.
- [16] W. Sugimoto, Ruthenium Oxides as Supercapacitor Electrodes, *Encyclopedia of Applied Electrochemistry*, Springer 2014, pp. 1813-1821.
- [17] T. Brousse, D. Bélanger, J.W. Long, To be or not to be pseudocapacitive?, *J. Electrochem. Soc.*, 162 (2015) A5185-A5189.
- [18] P. Simon, Y. Gogotsi, B. Dunn, Where Do Batteries End and Supercapacitors Begin?, *Science*, 343 (2014) 1210-1211.
- [19] W. Wang, Q. Luo, B. Li, X. Wei, L. Li, Z. Yang, Recent progress in redox flow battery research and development, *Adv. Funct. Mater.*, 23 (2013) 970-986.
- [20] L. Li, S. Kim, W. Wang, M. Vijayakumar, Z. Nie, B. Chen, J. Zhang, G. Xia, J. Hu, G. Graff, J. Liu, Z. Yang, A Stable Vanadium Redox-Flow Battery with High Energy Density for Large-Scale Energy Storage, *Adv. Energy Mater.*, 1 (2011) 394-400.
- [21] A.Z. Weber, M.M. Mench, J.P. Meyers, P.N. Ross, J.T. Gostick, Q. Liu, Redox flow batteries: a review, *J. Appl. Electrochem.*, 41 (2011) 1137-1164.
- [22] B. Li, Z. Nie, M. Vijayakumar, G. Li, J. Liu, V. Sprenkle, W. Wang, Ambipolar zinc-polyiodide electrolyte for a high-energy density aqueous redox flow battery, *Nat. Commun.*, 6 (2015) 6303.

- [23] P. Alotto, M. Guarnieri, F. Moro, Redox flow batteries for the storage of renewable energy: A review, *Renewable Sustainable Energy Rev.*, 29 (2014) 325-335.
- [24] B. Akinwolemiwa, C. Peng, G.Z. Chen, Redox Electrolytes in Supercapacitors, *J. Electrochem. Soc.*, 162 (2015) A5054-A5059.
- [25] F. Béguin, V. Presser, A. Balducci, E. Frackowiak, Carbons and electrolytes for advanced supercapacitors, *Adv. Mater.*, 26 (2014) 2219-2251.
- [26] P.R. Bandaru, H. Yamada, R. Narayanan, M. Hofer, Charge transfer and storage in nanostructures, *Mat Sci Eng R*, 96 (2015) 1-69.
- [27] Y. Yue, H. Liang, Micro- and Nano-Structured Vanadium Pentoxide (V_2O_5) for Electrodes of Lithium-Ion Batteries, *Adv. Energy Mater.*, 7 (2017) 1602545.
- [28] V. Aravindan, J. Gnanaraj, Y.-S. Lee, S. Madhavi, Insertion-Type Electrodes for Nonaqueous Li-Ion Capacitors, *Chem. Rev.*, 114 (2014) 11619-11635.
- [29] M. Widmaier, N. Jäckel, M. Zeiger, M. Abuzarli, C. Engel, L. Bommer, V. Presser, Influence of carbon distribution on the electrochemical performance and stability of lithium titanate based energy storage devices, *Electrochim. Acta*, 247 (2017) 1006-1018.
- [30] M. Widmaier, B. Krüner, N. Jäckel, M. Aslan, S. Fleischmann, C. Engel, V. Presser, Carbon as Quasi-Reference Electrode in Unconventional Lithium-Salt Containing Electrolytes for Hybrid Battery/Supercapacitor Devices, *J. Electrochem. Soc.*, 163 (2016) A2956-A2964.
- [31] S. Porada, J. Lee, D. Weingarh, V. Presser, Continuous operation of an electrochemical flow capacitor, *Electrochem. Commun.*, 48 (2014) 178-181.
- [32] V. Presser, C.R. Dennison, J. Campos, K.W. Knehr, E.C. Kumbur, Y. Gogotsi, The Electrochemical Flow Capacitor: A New Concept for Rapid Energy Storage and Recovery, *Adv. Energy Mater.*, 2 (2012) 895-902.
- [33] K.B. Hatzell, M. Beidaghi, J.W. Campos, C.R. Dennison, E.C. Kumbur, Y. Gogotsi, A high performance pseudocapacitive suspension electrode for the electrochemical flow capacitor, *Electrochim. Acta*, 111 (2013) 888-897.
- [34] J. Lee, D. Weingarh, I. Grobelsek, V. Presser, Use of Surfactants for Continuous Operation of Aqueous Electrochemical Flow Capacitors, *Energy Technol.*, 4 (2016) 75-84.
- [35] T. Nguyen, M.F. Montemor, Redox active materials for metal compound based hybrid electrochemical energy storage: a perspective view, *Appl. Surf. Sci.*, 422 (2017) 492-497.
- [36] S.T. Senthikumar, R.K. Selvan, J.S. Melo, Redox additive/active electrolytes: a novel approach to enhance the performance of supercapacitors, *J. Mater. Chem. A*, 1 (2013) 12386-12394.
- [37] E. Frackowiak, M. Meller, J. Menzel, D. Gastol, K. Fic, Redox-active electrolyte for supercapacitor application, *Faraday Discuss.*, 172 (2014) 179-198.
- [38] J. Lee, S. Choudhury, D. Weingarh, D. Kim, V. Presser, High Performance Hybrid Energy Storage with Potassium Ferricyanide Redox Electrolyte, *ACS Appl Mater Interfaces*, 8 (2016) 23676-23687.
- [39] R. Narayanan, P.R. Bandaru, High Rate Capacity through Redox Electrolytes Confined in Macroporous Electrodes, *J. Electrochem. Soc.*, 162 (2014) A86-A91.
- [40] J. Lee, P. Srimuk, S. Fleischmann, A. Ridder, M. Zeiger, V. Presser, Nanoconfinement of redox reactions enables rapid zinc iodide energy storage with high efficiency, *J. Mater. Chem. A*, 5 (2017) 12520-12527.
- [41] B. Krüner, J. Lee, N. Jäckel, A. Tolosa, V. Presser, Sub-micrometer Novolac-Derived Carbon Beads for High Performance Supercapacitors and Redox Electrolyte Energy Storage, *ACS Appl. Mater. Interfaces*, 8 (2016) 9104-9115.
- [42] J. Lee, A. Tolosa, B. Krüner, N. Jäckel, S. Fleischmann, M. Zeiger, D. Kim, V. Presser, Asymmetric tin-vanadium redox electrolyte for hybrid energy storage with nanoporous carbon electrodes, *Sustainable Energy & Fuels*, 1 (2017) 299-307.
- [43] E. Frackowiak, K. Fic, M. Meller, G. Lota, Electrochemistry Serving People and Nature: High-Energy Ecocapacitors based on Redox-Active Electrolytes, *Chemsuschem*, 5 (2012) 1181-1185.

- [44] T. Yamamoto, Use of Polymer-Iodine Adducts as Positive Electrodes of Cells, *J Chem Soc Chem Comm*, (1981) 187-188.
- [45] T. Yamamoto, S.-I. Kuroda, A. Yamamoto, Iodine cells: iodine adducts of 6-nylon as cathodes of galvanic cells, *Inorg. Chim. Acta*, 65 (1982) L175-L176.
- [46] T. Yamamoto, S.-I. Kuroda, Iodine-polymer adducts as active materials for positive electrodes of galvanic cells, *J. Electroanal. Chem. Interfacial Electrochem.*, 158 (1983) 1-11.
- [47] T. Yamamoto, M. Hishinuma, A. Yamamoto, Zn|ZnI₂|iodine secondary battery using iodine-nylon-6 adduct as positive electrode, and its charge-discharge performance, *Inorg. Chim. Acta*, 86 (1984) L47-L49.
- [48] G. Mengoli, M.M. Musiani, D. Pletcher, S. Valcher, Studies of Zn|ZnX₂| polyaniline batteries. II. X=I, *J. Appl. Electrochem.*, 17 (1987) 525-531.
- [49] G. Mengoli, M.M. Musiani, D. Pletcher, S. Valcher, Studies of Zn| ZnX₂| polyaniline batteries. IX= Cl and Br, *J. Appl. Electrochem.*, 17 (1987) 515-524.
- [50] G. Mengoli, M.M. Musiani, R. Tomat, S. Valcher, D. Pletcher, On the use of pyrrole black in zinc-halogen batteries, *J. Appl. Electrochem.*, 15 (1985) 697-704.
- [51] T. Yamamoto, T. Kanbara, Porous and electrically conducting clay-carbon composite as positive electrodes of zinc-oxygen primary cells and zinc-iodine secondary cells, *Inorg. Chim. Acta*, 142 (1988) 191-193.
- [52] M. Hishinuma, T. Iwahori, H. Sugimoto, H. Sukawa, T. Tanaka, T. Yamamoto, Y. Yanagisawa, Y. Yoda, S. Yoshida, Zinc Iodine Secondary Cell Using 6-Nylon or Poly(Ether) Based Electrode - Basic Research for Industrial Use of the Secondary Cell, *Electrochim. Acta*, 35 (1990) 255-261.
- [53] J. Manassen, I. Cabasso, Nonflow Zinc/Halogen Storage Cell Made of Thin Film Composite, *J. Electrochem. Soc.*, 136 (1989) 578-579.
- [54] H. Tsutsumi, Y. Matsuda, Electrochemical behavior of ferrocene-deoxycholic acid 1:2 inclusion compound and its application to positive material of zinc-iodine secondary batteries, *Electrochim. Acta*, 38 (1993) 1373-1375.
- [55] G. Wang, L. Zhang, J. Zhang, A review of electrode materials for electrochemical supercapacitors, *Chem. Soc. Rev.*, 41 (2012) 797-828.
- [56] I. Shown, A. Ganguly, L.-C. Chen, K.-H. Chen, Conducting polymer-based flexible supercapacitor, *Energy Sci. Eng.*, 3 (2015) 2-26.
- [57] Q. Li, K. Li, C. Sun, Y. Li, An investigation of Cu²⁺ and Fe²⁺ ions as active materials for electrochemical redox supercapacitors, *J. Electroanal. Chem.*, 611 (2007) 43-50.
- [58] G. Lota, E. Frackowiak, Striking capacitance of carbon/iodide interface, *Electrochem. Commun.*, 11 (2009) 87-90.
- [59] G. Lota, K. Fic, E. Frackowiak, Alkali metal iodide/carbon interface as a source of pseudocapacitance, *Electrochem. Commun.*, 13 (2011) 38-41.
- [60] S. Roldan, M. Granda, R. Menendez, R. Santamaria, C. Blanco, Mechanisms of Energy Storage in Carbon-Based Supercapacitors Modified with a Quinoid Redox-Active Electrolyte, *J. Phys. Chem. C*, 115 (2011) 17606-17611.
- [61] S. Roldán, C. Blanco, M. Granda, R. Menéndez, R. Santamaría, Towards a Further Generation of High - Energy Carbon - Based Capacitors by Using Redox - Active Electrolytes, *Angew. Chem. Int. Ed.*, 50 (2011) 1699-1701.
- [62] Y. Tian, J. Yan, R. Xue, B. Yi, Capacitive Properties of Activated Carbon in K₄Fe(CN)₆, *J. Electrochem. Soc.*, 158 (2011) A818-A821.
- [63] L.H. Su, X.G. Zhang, C.H. Mi, B. Gao, Y. Liu, Improvement of the capacitive performances for Co-Al layered double hydroxide by adding hexacyanoferrate into the electrolyte, *Phys. Chem. Chem. Phys.*, 11 (2009) 2195-2202.
- [64] M. Tachibana, Y. Tsukada, T. Ohishi, H. Yamagishi, M. Murakami, New High Capacity Electric Energy Storage Device with an Electrolyte that Contains a Conducting Polymer, *KOBUNSHI RONBUNSHU*, 66 (2009) 259-265.

- [65] G. Sun, K. Li, C. Sun, Electrochemical performance of electrochemical capacitors using Cu(II)-containing ionic liquid as the electrolyte, *Microporous Mesoporous Mater.*, 128 (2010) 56-61.
- [66] S.J. Yoo, B. Evanko, X. Wang, M. Romelczyk, A. Taylor, X. Ji, S.W. Boettcher, G.D. Stucky, Fundamentally Addressing Bromine Storage through Reversible Solid-State Confinement in Porous Carbon Electrodes: Design of a High-Performance Dual-Redox Electrochemical Capacitor, *J. Am. Chem. Soc.*, 139 (2017) 9985-9993.
- [67] B. Evanko, S.J. Yoo, S.-E. Chun, X. Wang, X. Ji, S.W. Boettcher, G.D. Stucky, Efficient Charge Storage in Dual-Redox Electrochemical Capacitors through Reversible Counterion-Induced Solid Complexation, *J. Am. Chem. Soc.*, 138 (2016) 9373-9376.
- [68] S.E. Chun, B. Evanko, X. Wang, D. Vonlanthen, X. Ji, G.D. Stucky, S.W. Boettcher, Design of aqueous redox-enhanced electrochemical capacitors with high specific energies and slow self-discharge, *Nat Commun*, 6 (2015) 7818.
- [69] S.M. Cha, G. Nagaraju, S.C. Sekhar, J.S. Yu, A facile drop-casting approach to nanostructured copper oxide-painted conductive woven textile as binder-free electrode for improved energy storage performance in redox-additive electrolyte, *J. Mater. Chem. A*, 5 (2017) 2224-2234.
- [70] K. Chen, S. Song, D. Xue, An ionic aqueous pseudocapacitor system: electroactive ions in both a salt electrode and redox electrolyte, *RSC Adv.*, 4 (2014) 23338-23343.
- [71] L. Chen, Y. Chen, J. Wu, J. Wang, H. Bai, L. Li, Electrochemical supercapacitor with polymeric active electrolyte, *J. Mater. Chem. A*, 2 (2014) 10526-10531.
- [72] Z. Ahmad, *Principles of corrosion engineering and corrosion control*, Elsevier Science 2006, pp. 49.
- [73] J. Lee, P. Srimuk, K. Aristizabal, C. Kim, S. Choudhury, Y.C. Nah, F. Mücklich, V. Presser, Pseudocapacitive Desalination of Brackish Water and Seawater with Vanadium-Pentoxide-Decorated Multiwalled Carbon Nanotubes, *ChemSusChem*, 10 (2017) 3611-3623.
- [74] B. Baranowski, S. Zaginaichenko, D. Schur, V. Skorokhod, A. Veziroglu, *Carbon Nanomaterials in Clean Energy Hydrogen Systems*, Springer Netherlands 2008, pp. 283.
- [75] Y. Cheng, S.P. Jiang, Advances in electrocatalysts for oxygen evolution reaction of water electrolysis -from metal oxides to carbon nanotubes, *Prog Nat Sci-Mater*, 25 (2015) 545-553.
- [76] M. Miles, M. Thomason, Periodic variations of overvoltages for water electrolysis in acid solutions from cyclic voltammetric studies, *J. Electrochem. Soc.*, 123 (1976) 1459-1461.
- [77] K. Qu, Y. Zheng, X. Zhang, K. Davey, S. Dai, S.Z. Qiao, Promotion of Electrocatalytic Hydrogen Evolution Reaction on Nitrogen-Doped Carbon Nanosheets with Secondary Heteroatoms, *ACS Nano*, 11 (2017) 7293-7300.
- [78] Y. Li, H. Wang, L. Xie, Y. Liang, G. Hong, H. Dai, MoS₂ nanoparticles grown on graphene: an advanced catalyst for the hydrogen evolution reaction, *J. Am. Chem. Soc.*, 133 (2011) 7296-7299.
- [79] L.Q. Mai, A. Minhas-Khan, X. Tian, K.M. Hercule, Y.L. Zhao, X. Lin, X. Xu, Synergistic interaction between redox-active electrolyte and binder-free functionalized carbon for ultrahigh supercapacitor performance, *Nat Commun*, 4 (2013) 2923.
- [80] K. Fic, M. Meller, J. Menzel, E. Frackowiak, Around the thermodynamic limitations of supercapacitors operating in aqueous electrolytes, *Electrochim. Acta*, 206 (2016) 496-503.
- [81] M. He, K. Fic, E. Frackowiak, P. Novák, E.J. Berg, Influence of aqueous electrolyte concentration on parasitic reactions in high-voltage electrochemical capacitors, *Energy Storage Materials*, 5 (2016) 111-115.
- [82] C. Vix-Guterl, E. Frackowiak, K. Jurewicz, M. Friebe, J. Parmentier, F. Béguin, Electrochemical energy storage in ordered porous carbon materials, *Carbon*, 43 (2005) 1293-1302.
- [83] E. Frackowiak, F. Béguin, Electrochemical storage of energy in carbon nanotubes and nanostructured carbons, *Carbon*, 40 (2002) 1775-1787.

- [84] M. He, K. Fic, E. Frckowiak, P. Novak, E.J. Berg, Ageing phenomena in high-voltage aqueous supercapacitors investigated by in situ gas analysis, *Energy Environ. Sci.*, 9 (2016) 623-633.
- [85] Q. Abbas, F. Béguin, High voltage AC/AC electrochemical capacitor operating at low temperature in salt aqueous electrolyte, *J. Power Sources*, 318 (2016) 235-241.
- [86] K. Fic, G. Lota, M. Meller, E. Frackowiak, Novel insight into neutral medium as electrolyte for high-voltage supercapacitors, *Energy Environ. Sci.*, 5 (2012) 5842-5850.
- [87] B.E. Conway, E. Gileadi, Kinetic theory of pseudo-capacitance and electrode reactions at appreciable surface coverage, *Trans. Faraday Soc.*, 58 (1962) 2493-2509.
- [88] K. Fic, M. Meller, E. Frackowiak, Interfacial Redox Phenomena for Enhanced Aqueous Supercapacitors, *J. Electrochem. Soc.*, 162 (2015) A5140-A5147.
- [89] V. Khomenko, E. Raymundo-Pinero, E. Frackowiak, F. Béguin, High-voltage asymmetric supercapacitors operating in aqueous electrolyte, *Appl. Phys. A: Mater. Sci. Process.*, 82 (2006) 567-573.
- [90] L. Demarconnay, E. Raymundo-Pinero, F. Béguin, A symmetric carbon/carbon supercapacitor operating at 1.6 V by using a neutral aqueous solution, *Electrochem. Commun.*, 12 (2010) 1275-1278.
- [91] Q. Gao, L. Demarconnay, E. Raymundo-Pinero, F. Béguin, Exploring the large voltage range of carbon/carbon supercapacitors in aqueous lithium sulfate electrolyte, *Energy Environ. Sci.*, 5 (2012) 9611-9617.
- [92] P. Ratajczak, K. Jurewicz, P. Skowron, Q. Abbas, F. Béguin, Effect of accelerated ageing on the performance of high voltage carbon/carbon electrochemical capacitors in salt aqueous electrolyte, *Electrochim. Acta*, 130 (2014) 344-350.
- [93] P. Ratajczak, K. Jurewicz, F. Béguin, Factors contributing to ageing of high voltage carbon/carbon supercapacitors in salt aqueous electrolyte, *J. Appl. Electrochem.*, 44 (2014) 475-480.
- [94] A. Laheäär, P. Przygocki, Q. Abbas, F. Béguin, Appropriate methods for evaluating the efficiency and capacitive behavior of different types of supercapacitors, *Electrochem. Commun.*, 60 (2015) 21-25.
- [95] M. Tachibana, T. Ohishi, Y. Tsukada, A. Kitajima, H. Yamagishi, M. Murakami, Supercapacitor using an electrolyte charge storage system, *Electrochemistry*, 79 (2011) 882-886.
- [96] L. Chen, H. Bai, Z. Huang, L. Li, Mechanism investigation and suppression of self-discharge in active electrolyte enhanced supercapacitors, *Energy Environ. Sci.*, 7 (2014) 1750-1759.
- [97] L. Qian, X. Tian, L. Yang, J. Mao, H. Yuan, D. Xiao, High specific capacitance of CuS nanotubes in redox active polysulfide electrolyte, *RSC Adv.*, 3 (2013) 1703-1708.
- [98] H.J. Yu, J.H. Wu, L.Q. Fan, Y.Z. Lin, S.H. Chen, Y. Chen, J.L. Wang, M.L. Huang, J.M. Lin, Z. Lan, Y.F. Huang, Application of a novel redox-active electrolyte in MnO₂-based supercapacitors, *Sci. China: Chem.*, 55 (2012) 1319-1324.
- [99] H. Yu, L. Fan, J. Wu, Y. Lin, M. Huang, J. Lin, Z. Lan, Redox-active alkaline electrolyte for carbon-based supercapacitor with pseudocapacitive performance and excellent cyclability, *RSC Adv.*, 2 (2012) 6736-6740.
- [100] S. Senthilkumar, R.K. Selvan, Y. Lee, J. Melo, Electric double layer capacitor and its improved specific capacitance using redox additive electrolyte, *J. Mater. Chem. A*, 1 (2013) 1086-1095.
- [101] K. Sun, E. Feng, H. Peng, G. Ma, Y. Wu, H. Wang, Z. Lei, A simple and high-performance supercapacitor based on nitrogen-doped porous carbon in redox-mediated sodium molybdate electrolyte, *Electrochim. Acta*, 158 (2015) 361-367.
- [102] D. Weingarh, A. Foelske-Schmitz, R. Kötz, Cycle versus voltage hold – Which is the better stability test for electrochemical double layer capacitors?, *J. Power Sources*, 225 (2013) 84-88.
- [103] K. Xu, S.P. Ding, T.R. Jow, Toward reliable values of electrochemical stability limits for electrolytes, *J. Electrochem. Soc.*, 146 (1999) 4172-4178.

- [104] D. Weingarh, H. Noh, A. Foelske-Schmitz, A. Wokaun, R. Kötz, A reliable determination method of stability limits for electrochemical double layer capacitors, *Electrochim. Acta*, 103 (2013) 119-124.
- [105] P.W. Ruch, D. Cericola, a. Foelske, R. Kötz, a. Wokaun, A comparison of the aging of electrochemical double layer capacitors with acetonitrile and propylene carbonate-based electrolytes at elevated voltages, *Electrochim. Acta*, 55 (2010) 2352-2357.
- [106] H.A. Andreas, Self-Discharge in Electrochemical Capacitors: A Perspective Article, *J. Electrochem. Soc.*, 162 (2015) A5047-A5053.
- [107] J. Niu, B.E. Conway, W.G. Pell, Comparative studies of self-discharge by potential decay and float-current measurements at C double-layer capacitor and battery electrodes, *J. Power Sources*, 135 (2004) 332-343.
- [108] A.T. Hubbard, Study of the kinetics of electrochemical reactions by thin-layer voltammetry, *J. Electroanal. Chem. Interfacial Electrochem.*, 22 (1969) 165-174.
- [109] A.T. Hubbard, F.C. Anson, Linear Potential Sweep Voltammetry in Thin Layers of Solution, *Anal. Chem.*, 38 (1966) 58-61.
- [110] C.R. Christensen, F.C. Anson, Chronopotentiometry in Thin Layer of Solution, *Anal. Chem.*, 35 (1963) 205-209.
- [111] I. Streeter, G.G. Wildgoose, L. Shao, R.G. Compton, Cyclic voltammetry on electrode surfaces covered with porous layers: an analysis of electron transfer kinetics at single-walled carbon nanotube modified electrodes, *Sens. Actuators, B*, 133 (2008) 462-466.
- [112] M.C. Henstridge, E.J.F. Dickinson, M. Aslanoglu, C. Batchelor-McAuley, R.G. Compton, Voltammetric selectivity conferred by the modification of electrodes using conductive porous layers or films: The oxidation of dopamine on glassy carbon electrodes modified with multiwalled carbon nanotubes, *Sens. Actuators, B*, 145 (2010) 417-427.
- [113] G.P. Keeley, M.E. Lyons, The effects of thin layer diffusion at glassy carbon electrodes modified with porous films of single-walled carbon nanotubes, *Int. J. Electrochem. Sci*, 4 (2009) 794-809.
- [114] K.R. Ward, L. Xiong, N.S. Lawrence, R.S. Hartshorne, R.G. Compton, Thin-layer vs. semi-infinite diffusion in cylindrical pores: A basis for delineating Fickian transport to identify nano-confinement effects in voltammetry, *J. Electroanal. Chem.*, 702 (2013) 15-24.
- [115] T. Liu, W.G. Pell, B.E. Conway, Self-discharge and potential recovery phenomena at thermally and electrochemically prepared RuO₂ supercapacitor electrodes, *Electrochim. Acta*, 42 (1997) 3541-3552.
- [116] J. Black, H.A. Andreas, Effects of charge redistribution on self-discharge of electrochemical capacitors, *Electrochim. Acta*, 54 (2009) 3568-3574.
- [117] B.W. Ricketts, C. Ton-That, Self-discharge of carbon-based supercapacitors with organic electrolytes, *J. Power Sources*, 89 (2000) 64-69.
- [118] A. Lewandowski, P. Jakobczyk, M. Galinski, M. Biegun, Self-discharge of electrochemical double layer capacitors, *Phys. Chem. Chem. Phys.*, 15 (2013) 8692-8699.
- [119] B.E. Conway, *Electrochemical Supercapacitors: Scientific Fundamentals and Technological Applications*, Springer US2013.
- [120] I.S. Ike, I. Sigalas, S. Iyuke, Understanding performance limitation and suppression of leakage current or self-discharge in electrochemical capacitors: a review, *Phys. Chem. Chem. Phys.*, 18 (2016) 661-680.
- [121] B.E. Conway, W.G. Pell, T.C. Liu, Diagnostic analyses for mechanisms of self-discharge of electrochemical capacitors and batteries, *J. Power Sources*, 65 (1997) 53-59.
- [122] S. Ban, J. Zhang, L. Zhang, K. Tsay, D. Song, X. Zou, Charging and discharging electrochemical supercapacitors in the presence of both parallel leakage process and electrochemical decomposition of solvent, *Electrochim. Acta*, 90 (2013) 542-549.
- [123] M. Kaus, J. Kowal, D.U. Sauer, Modelling the effects of charge redistribution during self-discharge of supercapacitors, *Electrochim. Acta*, 55 (2010) 7516-7523.

- [124] A. Shanmugavani, S. Kaviselvi, K.V. Sankar, R.K. Selvan, Enhanced electrochemical performances of PANI using redox additive of $K_4[Fe(CN)_6]$ in aqueous electrolyte for symmetric supercapacitors, *Mater. Res. Bull.*, 62 (2015) 161-167.
- [125] I.S. Ike, I. Sigalas, S.E. Iyuke, The Effects of Self-Discharge on the Performance of Symmetric Electric Double-Layer Capacitors and Active Electrolyte-Enhanced Supercapacitors: Insights from Modeling and Simulation, *J. Electron. Mater.*, 46 (2017) 1163-1189.
- [126] J. Kowal, E. Avaroglu, F. Chamekh, A. Šenfelds, T. Thien, D. Wijaya, D.U. Sauer, Detailed analysis of the self-discharge of supercapacitors, *J. Power Sources*, 196 (2011) 573-579.
- [127] W. Pell, B. Conway, Voltammetry at a de Levie brush electrode as a model for electrochemical supercapacitor behaviour, *J. Electroanal. Chem.*, 500 (2001) 121-133.
- [128] R. De Levie, On porous electrodes in electrolyte solutions: I. Capacitance effects, *Electrochim. Acta*, 8 (1963) 751-780.
- [129] J. Kowal, E. Avaroglu, F. Chamekh, A. Šenfelds, T. Thien, D. Wijaya, D.U. Sauer, Detailed analysis of the self-discharge of supercapacitors, *J. Power Sources*, 196 (2011) 573-579.
- [130] D.A. Brownson, C.E. Banks, *The handbook of graphene electrochemistry*, Springer 2014.
- [131] J.E.B. Randles, A cathode ray polarograph. Part II.—The current-voltage curves, *Trans. Faraday Soc.*, 44 (1948) 327-338.
- [132] A. Ševčík, Oscillographic polarography with periodical triangular voltage, *Collect. Czech. Chem. Commun.*, 13 (1948) 349-377.
- [133] D.M. Anjos, J.K. McDonough, E. Perre, G.M. Brown, S.H. Overbury, Y. Gogotsi, V. Presser, Pseudocapacitance and performance stability of quinone-coated carbon onions, *Nano Energy*, 2 (2013) 702-712.
- [134] S. Chathoth, E. Mamontov, S. Dai, X. Wang, P. Fulvio, D. Wesolowski, Fast diffusion in a room temperature ionic liquid confined in mesoporous carbon, *Europhys. Lett.*, 97 (2012) 66004.
- [135] E. Mourad, L. Coustan, P. Lannelongue, D. Zigah, A. Mehdi, A. Vioux, S.A. Freunberger, F. Favier, O. Fontaine, Biredox ionic liquids with solid-like redox density in the liquid state for high-energy supercapacitors, *Nat Mater*, 16 (2017) 446-453.
- [136] P.M. Biesheuvel, R. Zhao, S. Porada, A. van der Wal, Theory of membrane capacitive deionization including the effect of the electrode pore space, *J. Colloid Interface Sci.*, 360 (2011) 239-248.
- [137] J. Lee, N. Jäckel, D. Kim, M. Widmaier, S. Sathyamoorthi, P. Srimuk, C. Kim, S. Fleischmann, M. Zeiger, V. Presser, Porous carbon as a quasi-reference electrode in aqueous electrolytes, *Electrochim. Acta*, 222 (2016) 1800-1805.

Curriculum vitae

Juhan Lee

Contact details

E-Mail juhan.lee@leibniz-inm.de
Date of birth August 9th, 1985
Nationality Korean
Military duty Fulfilled for 2 years (2006-2008), Sergeant



Education

- 2014 – 2017 **PhD Student**, Saarland University, Saarbrücken, Germany
- Energy Materials Group (Prof. Volker Presser), INM - Leibniz Institute for New Materials, Saarbrücken, Germany
- 2012 – 2014 **Joint European Master Program AMASE, Advanced Material Science and Engineering**
- Saarland University, Saarbrücken, Germany
 - Luleå University of Technology, Sweden
 - Master Thesis: Static and continuous operation of an electrochemical flow capacitor (Energy Materials Group, INM - Leibniz Institute for New Materials, Saarbrücken, Germany)
- 2004 – 2011 **Korea University of Technology and Education**
- Master Graduate in Mechanical Engineering, Automobile-Energy
 - Pedagogy coursework for the teaching profession (15 credits)
 - Exchange student at Ruhr University in Bochum, Germany

Relevant experience

- since 2015 **The Korean Scientists and Engineers Association in the FRG**, Energy committee head
Responsibilities: organizing local workshops and annual meeting for energy division, Coordinating Europe-Korea conference in Germany.
- 01/2012–
04/2012 **Biomagnetik Park (Korea)**, Engineer at technical transfer Department
Responsibilities: Acquiring the technology of magnetocardiography from the center for biosignals (Dr. Yong Ho Lee) in KRISS (Korea Research Institute of Standards and Science); particularly, SQUID sensor, Dewar, and mechanical systems.
- 09/2010–
07/2011 **The chair of production systems at Ruhr University (Germany)**, intern
Responsibilities: Operation of 6-axis industrial robots for various experiments and Modeling 3D data, supervised by Dr. Volker Smukala.
- 05/2009–
02/2010 **Nifco Korea Inc. Industrial-educational Cooperation**, lab project student
Responsibilities: Performing strength analysis of mechanical elements and selected Materials, designing 3D models.

Peer-reviewed publications and patent

Analytical electrochemistry

1. Lee, J.; Jäckel, N.; Kim, D.; Widmaier, M.; Sathyamoorthi, S.; Pattarachai, S.; Kim, C.; Fleischmann, S.; Zeiger, M.; Presser, V., *Porous carbon as a quasi-reference electrode in aqueous electrolytes*. *Electrochim. Acta* 222(1) (2016) 1800-1805.

Electric energy storage: capacitors, batteries, and hybrids

2. Lee, J., Badie, S., Srimuk, P., Ridder, A., Shim, H., Choudhury, S., Nah, Y., Presser, V., *Electrodeposition of hydrated vanadium pentoxide on nanoporous carbon cloth for hybrid energy storage*. *submitted*
3. Lee, J.; Srimuk, P.; Fleischmann, S.; Ridder, A.; Zeiger, M.; Presser, V., *Nanoconfinement of redox reactions enables rapid zinc iodide energy storage with high efficiency*. *J. Mater. Chem. A* 2017, 5 (24), 12520-12527.
4. Lee, J.; Tolosa, A.; Krüner, B.; Jäckel, N.; Fleischmann, S.; Zeiger, M.; Kim, D.; Presser, V., *Asymmetric tin-vanadium redox electrolyte for hybrid energy storage with nanoporous carbon electrodes*. *Sustainable Energy Fuels* 2017, 1 (2), 299-307.
5. Lee, J.; Krüner, B.; Tolosa, A.; Sathyamoorthi, S.; Kim, D.; Choudhury, S.; Seo, K.-H.; Presser, V., *Tin/vanadium redox electrolyte for battery-like energy storage capacity combined with supercapacitor-like power handling*. *Energy Environ. Sci.* 2016, 9 (11), 3392-3398. *cover*
6. Lee, J.; Choudhury, S.; Weingarh, D.; Kim, D.; Presser, V., *High performance hybrid energy storage with potassium ferricyanide redox electrolyte*. *ACS Appl Mater Interfaces* 2016, 8 (36), 23676-87.
7. Lee, J.; Weingarh, D.; Grobelsek, I.; Presser, V., *Use of surfactants for continuous operation of aqueous electrochemical flow capacitors*. *Energy Technology* 2016, 4 (1), 75-84.
8. Krüner, B.; Lee, J.; Jäckel, N.; Tolosa, A.; Presser, V., *Sub-micrometer novolac-derived carbon beads for high performance supercapacitors and Redox Electrolyte Energy Storage*. *ACS Appl. Mater. Interfaces* 2016, 8 (14), 9104-9115.
9. Porada, S.; Lee, J.; Weingarh, D.; Presser, V., *Continuous operation of an electrochemical flow capacitor*. *Electrochem. Commun.* 2014, 48, 178-181.

Electrochemical water desalination

10. Srimuk, P.; Lee, J.; Fleischmann, S.; Aslan, M.; Kim, C.; Presser, V.; *Potential-dependent ion selectivity in aqueous media using a binder-free titanium disulfide electrode*, *submitted*
11. Srimuk, P.; Halim, J.; Lee, J.; Tao, Q.; Rosen, J., Presser, V.; *Two-dimensional molybdenum carbide (MXene) with divacancy ordering for brackish and sea water desalination via cation and anion intercalation*. *submitted*
12. Lee, J.; Srimuk, P.; Aristizabal, K.; Kim, C.; Choudhury, S.; Nah, Y. C.; Mücklich, F.; Presser, V., *Pseudocapacitive Desalination of Brackish Water and Seawater with Vanadium-Pentoxide-Decorated Multiwalled Carbon Nanotubes*. *ChemSusChem* 2017, 10 (18), 3611-3623.
13. Srimuk, P.; Lee, J.; Tolosa, A.; Kim, C.; Aslan, M.; Presser, V., *Titanium disulfide: a promising low-dimensional electrode material for sodium ion intercalation for sea water desalination*. *Chem. Mater.* 2017. DOI: 10.1021/acs.chemmater.7b03363
14. Kim, C.; Srimuk, P.; Lee, J.; Fleischmann, S.; Aslan, M.; Presser, V., *Influence of pore structure and cell voltage of activated carbon cloth as a versatile electrode material for capacitive deionization*. *Carbon* 2017, 122 (Supplement C), 329-335.
15. Srimuk, P.; Lee, J.; Fleischmann, S.; Choudhury, S.; Jäckel, N.; Zeiger, M.; Kim, C.; Aslan, M.; Presser, V., *Faradaic deionization of brackish and sea water via pseudocapacitive cation and anion intercalation into few-layered molybdenum disulfide*. *J. Mater. Chem. A* 2017, 5 (30), 15640-15649.
16. Kim, C.; Srimuk, P.; Lee, J.; Aslan, M.; Presser, V., *Semi-continuous capacitive deionization using multi-channel flow stream and ion exchange membranes*. *Desalination* 2018, 425 (Supplement C), 104-110.
17. Kim, C.; Srimuk, P.; Lee, J.; Fleischmann, S.; Aslan, M.; Presser, V., *Influence of pore structure and cell voltage of activated carbon cloth as a versatile electrode material for capacitive deionization*. *Carbon* 2017, 122 (Supplement C), 329-335.

Material characterization

18. Noël, M.; Ananev, S.; Mases, M.; Devaux, X.; Lee, J.; Evdokimov, I.; Dossot, M.; McRae, E.; Soldatov, A. V., *Probing structural integrity of single walled carbon nanotubes by dynamic and static compression*. *physica status solidi (RRL) - Rapid Research Letters* 2014, 8 (11), 935-938.

Patent

19. Noh, H.K.; Jeong, J.E.; Song, S.H.; Moon, K.H.; Lee, J., *Rotating air vent for automobile*. KR Patent WO2012053824 A2: 2012.

Presentations at international conferences

Invited oral presentation

1. **68th Annual Meeting of International Society of Electrochemistry**, 2017, Redox-enabling nanoporous carbons for high-performance energy Storage, Providence, the United States

Oral presentations

2. **International Conference on Capacitive Deionization**, Electrosorption & Electrodialysis, 2017, Pseudocapacitive desalination of high concentrated saline water via vanadium pentoxide decorated multiwall carbon nanotubes, Seoul, South Korea
3. **67th Annual Meeting of International Society of Electrochemistry**, 2016, High performance hybrid energy storage with potassium ferricyanide redox electrolyte, The Hague, The Netherland
4. **11th International Symposium on Electrochemical Micro & Nanosystem Technologies**, 2016, A new generation of hybrid energy storage system exploring the boundary between battery and supercapacitor technologies, Brussels, Belgium
5. **Europe-Korea Conference on Science and Technology**, 2016, A new generation of hybrid energy storage system exploring the boundary between battery and supercapacitor technologies, Berlin, Germany
6. **66th Annual Meeting of International Society of Electrochemistry**, 2015, Hybrid electrochemical energy storage: synergy of double-layer formation and soluble redox couple for advanced power applications, Taipei, Taiwan
7. **World Conference on Carbon**, 2015, Performance and optimization of a flow capacitor with surfactants under continuous flow operation, Dresden, Germany
8. **Europe-Korea Conference on Science and Technology**, 2015, Performance and optimization of a flow capacitor with surfactants under continuous flow operation, Strasbourg, France
9. **4th International Symposium on Enhanced Electrochemical Capacitors**, 2015, Use of ion exchange membranes instead of porous separators for aqueous electrolyte supercapacitors, Montpellier, France

Post presentation

10. **Europe-Korea Conference on Science and Technology**, 2017, Redox electrolytes for high performance electric energy storage, Stockholm, Sweden
11. **Europe-Korea Conference on Science and Technology**, 2015, Electrochemical flow capacitor under static and continuous operation, Vienna, Austria (*poster award*)

Scientific supervision in the INM Energy Materials Group

2017	Jaehoon Choi , <i>Bachelor intern</i> , Synthesis and optimization of two-dimensional material for electrochemical water desalination
2017	Sidonie Carpier , <i>Master intern</i> , Nanoconfinement Faradaic reaction at carbon pores for electrochemical water desalination
2017	Rose Zwingelstein , <i>Master intern</i> , Synthesis and optimization of metal oxide for electrochemical water desalination
2016 – 2017	Alexander Ridder , <i>Master intern</i> , Nanoconfinement of redox reactions enabled rapid zinc iodide energy storage with high efficiency (<i>published, see the publication list</i>)
2016 – 2017	Sylvain Badie , <i>Master intern</i> , Electrodeposition of hydrated vanadium pentoxide on nanoporous carbon cloth for hybrid energy storage (<i>submitted, see the publication list</i>)
2015 – 2016	Daekyu Kim , <i>Bachelor intern</i> , Feasibility of porous carbon as a quasi-reference electrode in aqueous electrolytes (<i>published, see the publication list</i>)

Scientific qualifications and expertise

Characterizations and analysis

Aqueous and organic electrochemistry
Electrochemical water deionization
In operando inductively coupled plasma analysis
Scanning electron microscopy
Energy-dispersive X-ray spectroscopy
X-ray diffraction
Thermogravimetric analysis
Gas sorption analysis
Raman spectroscopy

Material synthesis

Electrochemical depositions of metal oxides on porous carbon materials
Hydrothermal process on porous carbon materials

Language skills*

	Listening	Reading	Speaking	Writing	Certificate
ENGLISH	C1	C1	C1	C1	94 Points of TOEFL IBT
GERMAN	C1	C1	C1	B2	DSH B2

* Common European Framework of Reference for Languages

Awards and scholarship

- 07/2014 Poster award, EU-Korea Conference on Science and Technology, Vienna (Austria)
- 2012-2014 AMASE Scholarship, Erasmus Mundus Masters Course Nr. 2012-0184; Full coverage scholarship for two years.